J. Soils and Crops 33 (2) 317-323, December 2023

ISSN 0971-2836 (Print)
ISSN 2582-2756 (Online)

INFLUENCE OF ELECTROTHERAPY AND SALT PRIMING TO IMPROVE GERMINATION AND VIGOUR OF WHEAT SEEDS

Arindam Mandal[1] and Niranjan Bala[2]

ABSTRACT

In this current study seeds of wheat (*Triticum aestivum*) primed with salts solution [1:1 (v/v) of 0.05% KNO_3 and 0.05% $Ca(NO_3)_2$] and an electric stimulus (DC 300V & 400mA) was passed for 6 minutes (EC6) and 11 minutes (EC11) between two electrodes in a horizontal casting container containing the same salt mixture. Effects of these seed priming treatments on germination %, speed of germination, TR values, shoot length, root length, vigour index, mass accumulation, electrical conductivity, peroxidase and alpha-amylase activities were measured and compared with non-primed control seeds. Electrotherapy (EC6) for six minutes on pre-sown soaked seeds enhanced the physiological and biochemical parameters by establishing a vigorous seedling within a stipulated time. Salt priming also established a vigorous seedling but significantly lower than treatments EC6 and EC11, but it was significantly enhanced all parameters studied when compared with control and water treatments. Electric stimulus and salt priming may be suitable for better germination and vigour of wheat seeds for rain fed cultivation.

(Key words. Electrotherapy, *Triticum aestivum*, germination, vigour, agriculture, alpha-amylase)

INTRODUCTION

The consciousness of the significance of better crop growth and its expression in productivity was happening from the pre-historical era. Until today, various aspects of better productivity of crops and their proper utilization were studied worldwide in different crops. Quality seed plays a vital role in this feature which is not to be considered as a crop growth planning due to its unavailability. To compensate for the demand for quality seed in addition to soil and environmental constraints, crop growth can be adapted in different ways of which seed treatment is one of them.

Wheat (*Triticum aestivum*) is considered a fundamental food item next to rice. It contributes to a large extent to national food safety by providing above 50% of the total calories to the people who generally depend on it. Starchy endosperm in cereal grain acts as a reservoir of storage compounds mobilized during germination to provide nutrients for the growth of germinating seedlings (Fincher, 1989). Mobilization of these storage compounds depends on the secretion and synthesis of hydrolytic enzymes from the aleurone layer and scutellum under the control of growth-promoting hormones (Dominguez and Francisco, 1995).

In West Bengal, the productivity of wheat and quality of seed is limited due to short winter spells and delayed sowing, particularly in rainfed which is recovered through upgrading the crop growth behaviour (Mukherjee, 2012). Presently, wheat cultivation occupies a large area of more than 27 million hectares. Bread wheat contributes approximately 95% to total production while another 4% comes from *Durum* wheat and *Dicoccum* share in wheat production remains only 1%. For cultivation in relation to quantity and quality, the differences related to constraints can be thrashed by selecting an appropriate technique under the seed treatment route. The inclusion of the technique can be optimized for the cultivation practice, especially in rainfed varieties which is more practical in West Bengal due to the exploitation of soil water and saving of underground water level.

After Green Revolution, India has incredibly advanced in wheat cultivation where the productivity and production increased to the tune of 523%, 460%, 559%, 606% and 780% respectively by the year 2000-01, 2005-06, 2010-11, 2015-16 and 2020-21 as compared to 1965-66 (Anonymous, 2021). The success story behind the bloom of wheat production mainly depends on the irrigation schedule. The wheat production is not stabilized during 2000-01 to 2008-09 depicting a growth rate of 1.77 due to unfavourable weather conditions. Hence, the emphasis must be given to limited irrigation and rainfed or accurate management of irrigation by consumption of appropriate techniques (Singh and Kumar, 2022). At present, the productivity of wheat is 35 q ha^{-1} in India though the cultivated high-yielding varieties have a strength of as much as 55–60 q ha^{-1}. The claim projection of wheat for 2025 has been anticipated to be about 109 million tons (Anonymous,

1. Asstt. Professor of Botany, Bejoy Narayan Mahavidyalaya, Hooghly, 712147, WB, India
2. Asstt. Professor of Botany, Sreegopal Banerjee College, Hooghly, 712148, WB, India

2007). At present, the productivity of wheat is 35 q ha^{-1} in India though the cultivated high-yielding varieties have a strength of as much as 55-60 q ha^{-1}. The claim projection of wheat for 2025 has been anticipated to be about 109 million tons (Anonymous, 2007). Population bloom will push the price of essential food items beyond the purchasing power of 696 million people below the poverty line (Anonymous, 2021). If the fluctuating production inclination continues, then achieving the target of wheat by 2025 will remain a difficult task. Different attempt has been made in different seed treatments in which electrotherapy on pre-sowing seed are one of them to surmount these crises. In the production of rainfed high-yielding wheat varieties, the establishment of seedlings is vital in a short duration which is very much compatible with the West Bengal situation due to late planting. The delayed establishment or poor establishment of a crop can create a configuration of low harvest index and yield. The establishment of poor and undersized seed shows an immediate effect and low storability, viability and vigour as a future effect for the coming season when it is utilized as seed material. The establishment of a good crop at the initial level increases the photosynthetic ability specifically depending on flag leaves and their effective tiller number (Fabre *et al.*, 2016). Many countries are engaged in scientific research relating to new varieties of plants and methods of their cultivation like genetic engineering, multi-seasonal selection, the protection of yields with the use of special plants and insects, bio-stimulation using external spectrums such as infra-red, ultra-violet, laser rays, ultrasounds, electric, magnetic and electromagnetic fields (Borisjuk *et al.*, 2019; Blûmmel *et al.*, 2016; Dorchester, 1935). Laser and magnetic field stimulation seem to be especially promising. This method does not cause any environmental changes, so it is desirable for ecological reasons (Mandal and Maity, 2013; Aladjadjiyan, 2007). Research work on the effect of magnetic fields on plant development and yielding has started in the last century. Electro-culture or electrotherapy is the use of electric current to promote the growth of plants. This cultural technique is known today but the idea is dated back to the 17th century. Dr. Von Maimbray of Edinburgh, Scotland observed for the first time that the rapid growth of myrtles tree was induced by an electrical field (Barman and Bhattacharya, 2016). Bose (1902) observed plant responses to electric current treatment, yet; so far it has not been fully exploited for commercial purposes. Electrical stimulus (electrotherapy) to pre-sowing seed is an innovative area of research and emerged as a magic tool that improves the yield of crops in an unprecedented manner which has not been achieved by any other technologies. Although this technology was first applied in cucurbitaceous plants to improve yield, now it has been extended to other crops like vegetables, cereals, pulses, oilseeds, etc. (Bera and Maity, 2004; Bera *et al.*, 2006; Pati, 2007). Electric current (EC) treatment may initiate physiological and biochemical changes which reflect growth and development processes in plants and ultimately the yield (Wahab *et al.*, 1980). Several workers reported yield improvement in various crops by application of this technology (Rahman and Yasmin, 1994; Zang and Hashinaga, 1997). It has been evident that cell proliferation including the synthesis of DNA and RNA also induced by the application of an electromagnetic field (Ruediger, 2009). The application of electrical impulse decreases the time of dormancy and has shown significant improvement in seed germination and seedling growth (Gandhare and Samir, 2014; Zadeh *et al.*, 2014; Aguilara *et al.*, 2015).

The effect of electrotherapy on high-yielding Wheat variety (Genotype C-306) has been attempted to study in detail. Further electric current-mediated changes in germination profile, seedling growth parameters and seed biochemistry have been critically analyzed to develop early crop establishment for optimum production as well as its production of superior seeds for maintaining to achieve the projected production curve. The effect of electrotherapy on pre-sowing seeds of wheat was observed *in vivo* for checking the seedling quality to predict their future aspects.

MATERIALS AND METHODS

Seed samples

The experiment was conducted during the period from November to March of 2018-19 in the subtropical region of West Bengal. For the experiment high yielding varieties of *Triticum aestivum* having a genotype of C-306 collected from Bidhan Chanda Krishi Viswavidyalaya, Kalyani, India were used. Untreated self-pollinated air-dried seeds were used as control. Seeds soaked in distilled water for 4 hours were considered as water treatment. For salt treatment seeds were initially soaked in distilled water for 4 hours and then placed in a mixture of the electrolyte solution of 0.05% KNO_3 and 0.05% $Ca(NO_3)_2$ (1:1). To the water-soaked seeds an electrical stimulus containing DC 300V and 400 mA was passed for 6 minutes between two electrodes in a horizontal casting container containing the same salt mixture was treated as EC6. Treatments for EC11 were the same as EC6 but the electrical stimulus was passed for 11 minutes. For experimental purposes, all the treated seeds were air-dried properly. As there was no or minimum infestation of pests and disease, no plant protection measures were taken.

Experimental design

The experiment was laid out in a completely randomized design (CRD) having five treatments *viz.*, water, salt, and electric therapy for 6 minutes (EC6) and electric therapy for 11 minutes (EC11) with one control (untreated seeds) and replicated four times. The surface sterilized glass plate method was followed for the evaluation of seedling parameters. Seed treatments were done following a standard protocol (Chakraborty, 1998). The whole setup was then placed in the germinator at 27-30 °C. Statistical analysis was performed in the CRD fashion as suggested by Krzywinski and Altman (2014).

Seedling quality parameters

Twenty-five (25) seeds were randomly selected from each seed sample. Seed quality parameters were analyzed in laboratory conditions according to standard methods (Dahiya *et al.*, 1997). Germination percentage (%) was calculated on the 10th day by the formula, Germination % = Number of seeds germinated leading to normal seedling/ Total number of seeds used in the experiment x 100 (Hatzade *et al.*, 2022). The speed of germination was calculated with the help of the formula,Speed of Germination = Ó (n/t), Where, n= Number of seeds germinated, t= Time (days) from sowing. The first count was calculated by counting the number of germinated seeds (leading to normal seedlings) 3 days after placing them for germination test. On the 10th day, the average length of the root and shoot of the normal seedlings were measured and expressed in centimeter (cm). Vigour Index was calculated with the help of the formulae VI = SL × G, where, VI = Vigour Index, SL= Seedling Length (root length + shoot length), and G = Standard Germination Percentage (Abdul-Baki and Anderson, 1973).

Electrical Conductivity (EC)

Electrical Conductivity was measured from water containing leachate of seeds soaked in deionized water at 25° C for 24 hours in a beaker. EC of the water containing leachates of different treatments was measured from a direct reading of the conductivity meter (Model No. Systronics-306) with dip cell having a cell constant of 1.0 and was compared with a control set without any seeds (deionized water) (Humphreys *et al.*, 2004). Electrical Conductivity is expressed by micro-Siemen (iS Sec.$^{-1}$).

Estimation of peroxidase activity

Peroxidase activity was measured according to Nakano and Asada (1981) using o-dianisidine as the substrate. Absorbance was recorded at 430 nm in Systronics-105 Spectrophotometer. Peroxidase activity = ÄA min.$^{-1}$ g^{-1} of imbibed seed. Where ÄA = difference in absorbance (0 min. to 1 min.)

Estimation of á-amylase

Extraction of â- amylase and the estimation of enzyme activities were done as per method suggested by Bernfield (1955). The enzyme activity was expressed as mcg (microgram) of maltose formed min.$^{-1}$ g^{-1} of fresh weight.

RESULTS AND DISCUSSION

In immediately harvested seeds germination % was non-significant. But it was maximum in treatments EC6 (electrical stimulus of DC 300V and 400 mA was applied for 6 minutes in water-soaked seeds), EC11 (same electrical stimulus was applied for 11 minutes), Salt (seeds were soaked in 1:1 mixture of 0.05% KNO_3 and 0.05% $Ca(NO_3)_2$) and water (seeds were soaked for 4 hours in water) over control (untreated). After 1 month of storage, a significant difference in germination was found between treatments salt, EC6 and EC11 as compared to the control (Table 1). The highest germination % was observed in treatments EC6 and EC11 followed by salt. After 4 months and 6 months of storage same patterns of germination was observed as observed in 1 month harvested seeds treatment. Treatment EC6 attributed a promising germination in all storage conditions and the next best was treatment EC11 followed by salt treatment. The germination % was gradually declined in different storage period, but electrotherapy improved the germination % which was highest in treatment EC6 followed by treatments EC11 and salt. Electric stimulus and salt priming mediated significant enhancement in germination was previously supported by the work of Wahab *et al.* (1980) and Feghhenabi *et al.* (2020).

Speed of germination in treatments EC6, EC11 and salt enhanced significantly over control in all storage periods (Table 2). In the case of immediate harvest, highest value observed in treatment EC6 which was non-significant to treatment EC11. At 1-month storage condition, there was no significant difference between salt and EC11 treatments but EC6 treatment always maintained a significant difference with the others representing the highest status. In the 4th month of storage period, there was a significant increase in speed of germination in treatment EC6 over all treatments. There was no significant difference between treatments EC6, EC11 and salt which was significantly higher than control and water. Significant increase in speed of germination was observed in treatment EC6 only over controls after 6 months of storage. The significant enhancement in first count % (TR value) was observed in freshly harvested seeds treated with treatment EC6 (72.32%) over other treatments except for the treatment EC11 (71.40%) (Table 3). The treatment EC11 also maintains a significant increased values over control, where as other treatments were indicated non-significant results. One month after storage again treatment EC6 showed the highest results which was significantly superior over treatment water and control. After 4 months of storage, an non-significant difference was found among the treatments salt, EC6, and EC11 but, these treatments were significantly higher than the treatments of water and control. The same trend was observed for different treatments in 6 months of storage, where treatment EC6 was showed their significance over all other treatments. Salt priming and electric current does a better job in the enhancement of TR value (Feghhenabi *et al.*, 2020; Bera and Maity, 2004). The different isozymes and other assumed defense enzymes *viz.*, endochitinase, exochitinase, protease, lectins, etc. are also found in seeds and may work together as a multi-component defense system to protect seeds during imbibition and germination (Lv *et al.*, 2016).

Immediately after harvest, no significant differences in the root length was observed among treatments EC6, EC11 and Salt (Table 4). Treatment EC6 recorded significantly higher root length followed by treatments salt and EC11 over control. After 1 month and 4 months of storage, only the treatment water showed the significantly lowest root length in comparison to other

treatments. In 6 months of storage condition treatments EC6, salt and EC11 indicated significantly more root length over control and water treatment, but the highest value was maintained by treatment EC6.

There was no significant difference between all treatments in freshly harvested seeds for shoot length, but the highest performance was reflected by treatment EC6 followed by treatments EC11 and salt (Table 5). After 1 month and 6 months of storage, significantly more shoot length was observed in treatments EC6, EC11 and salt over control and water treatment. In 4th month of storage, there was no significant difference among all treatments, but treatment EC6 showed the highest shoot length followed by treatments EC11 and salt respectively.

The vigour index of the freshly harvested seeds increased significantly in all treatments over control and the highest value was observed in treatment EC6 followed by treatments EC11, salt and water (Table 6). After 1 and 4 months of storage, the treatment EC6 created a significant and maximum outcome where an insignificant divergence was found between treatments salt and EC11. The vigour index was very low in 6th month of the storage period where significant diversity was found among all treatments but, the highest value was maintained by treatment EC6. Salt priming with electric stimulus and salt priming alone enhanced root length, shoot length which resulted superior vigour (Bera and Maity, 2004; Bera *et al.*, 2006).

Significant enhancement in fresh weight of all treatments were observed over control except water, whereas treatment EC6 showed the highest results in immediately harvested seeds (Table 7). There was no significant difference found between the treatments and the control but the highest fresh weight was achieved by treatment EC6 after 1 month of storage. After 4 and 6 months of storage period, significantly maximum fresh weight was observed in treatment EC6 over water and control treatments. The dry weight of immediately harvested seeds showed non-significant relationship with the control where salt represented the highest fresh weight followed by treatments EC6 and EC11 (Table 8). Significant enhancement in fresh weight of all treatments were observed over control except water, where treatment EC6 showed the highest fresh weight after one month of storage. During the 4 months of storage, dry weight of treatments EC6 and EC11 increased significantly over other treatments and noticeably treatment EC6 showed highest value. After 6 months of storage a significant array for all the treatments over control was observed except water treatment, whereas treatment EC6 showed the utmost outcome.

Table 1. Evaluation of germination % after harvest

Treatments	Immediate	1 month	4 month	6 month
Control	83.94	70.23	57.26	47.01
Water	83.95	70.35	57.58	51.06
Salt	84.46	75.73	62.73	51.07
EC 6	85.95	74.76	60.33	56.18
EC 11	85.20	75.73	61.18	54.65
Mean	84.70	73.36	59.82	52.00
SE (m)±	0.93	1.36	0.38	0.80
CD at 5%	2.78	4.07	1.13	2.39

Table 2. Evaluation of speed of germination after harvest

Treatments	Immediate	1 month	4 month	6 month
Control	2.82	2.71	2.50	2.17
Water	3.02	2.62	2.47	2.20
Salt	3.25	2.93	2.55	2.22
EC 6	3.33	3.04	2.66	2.27
EC 11	3.29	2.96	2.62	2.26
Mean	3.14	2.85	2.56	2.22
SE (m)±	0.02	0.02	0.01	0.02
CD at 5%	0.059	0.059	0.029	0.059

Table 3. Evaluation of first count % after harvest

Treatments	Immediate	1 month	4 month	6 month
Control	68.17	59.89	57.42	54.33
Water	68.11	59.22	56.80	55.52
Salt	68.29	63.80	59.19	58.06
EC 6	72.32	64.53	59.68	59.35
EC 11	71.40	63.26	59.03	58.05
Mean	69.66	62.14	58.42	57.2
SE (m)±	1.07	0.83	0.60	0.40
CD at 5%	3.20	2.48	1.79	1.19

Table 4. Evaluation of average length of root (cm) after harvest

Treatments	Immediate	1 month	4 month	6 month
Control	14.87	12.33	11.87	7.4
Water	14.93	11	10.33	7.23
Salt	15.33	12.63	12.03	8.07
EC 6	15.57	12.3	12.13	8.23
EC 11	15.37	12.5	11.97	8.03
Mean	15.21	12.15	11.67	7.79
SE (m)±	0.10	0.15	0.19	0.09
CD at 5%	0.29	0.44	0.56	0.26

Table 5. Evaluation of average length of shoot (cm) after harvest

Treatments	Immediate	1 month	4 month	6 month
Control	11.57	11.27	9.57	5.73
Water	11.63	10.6	8.87	5.5
Salt	11.9	13.13	10	6.43
EC 6	12.47	13.20	10.1	6.63
EC 11	12.43	13.17	9.83	6.47
Mean	12.00	12.27	9.67	6.15
SE (m)±	0.32	0.20	0.23	0.11
CD at 5%	0.95	0.59	0.68	0.32

Table 6. Evaluation of vigour index after harvest

Treatments	Immediate	1 month	4 month	6 month
Control	2559	2360.25	1506.25	696
Water	2647.25	2414.75	1356.5	761.5
Salt	2705	2426.5	1652.25	868
EC 6	2782	2447.75	1748.25	1019
EC 11	2754.75	2430.5	1663.5	958.5
Mean	2689.6	2415.95	1585.35	860.6
SE (m)±	25.71	3.70	20.61	18.29
CD at 5%	76.87	11.06	61.62	54.69

Table 7. Evaluation of fresh weight of seedling after harvest

Treatments	Immediate	1 month	4 month	6 month
Control	1.35	1.30	1.14	0.73
Water	1.35	1.2	1.12	0.77
Salt	1.48	1.29	1.21	0.82
EC 6	1.51	1.31	1.21	0.84
EC 11	1.49	1.3	1.19	0.82
Mean	1.44	1.28	1.17	0.79
SE (m)±	0.03	0.02	0.01	0.01
CD at 5%	0.089	0.059	0.04	0.029

Table 8. Evaluation of dry weight of seedling after harvest

Treatments	Immediate	1 month	4 month	6 month
Control	260.5	257	212.5	161
Water	259	254.5	212	159.5
Salt	268	264	214.5	173
EC 6	266.5	266.5	224.25	176.2
EC 11	264.25	263.5	221.5	175
Mean	263.65	261.1	216.95	168.9
SE (m)±	3.19	1.19	1.52	2.69
CD at 5%	9.54	3.56	4.54	8.04

Table 9. Evaluation of electric conductivity after harvest

Treatments	Immediate	1 month	4 month	6 month
Control	234.25	250.35	330.33	337.7
Water	231.25	255	273.43	279.5
Salt	205	230.65	266.75	277.5
EC 6	198	221	249.53	265
EC 11	199	225.7	262.75	275
Mean	213.5	236.05	276.56	287
SE (m)±	0.77	0.37	0.79	1.17
CD at 5%	2.30	1.10	2.36	3.50

Table 10. Estimation of peroxidase activity in seed after harvest

Treatments	Immediate	1 month	4 month	6 month
Control	0.70	0.43	0.36	0.28
Water	0.72	0.52	0.35	0.29
Salt	0.72	0.62	0.45	0.34
EC 6	0.77	0.63	0.45	0.39
EC 11	0.75	0.61	0.43	0.36
Mean	0.73	0.56	0.41	0.33
SE (m)±	0.004	0.011	0.009	0.003
CD at 5%	0.0119	0.032	0.026	0.008

Table 11. Estimation of á- amylase activity in seed after 24 hours after harvest

Treatments	Immediate	1 month	4 month	6 month
Control	164.72	140.51	122.38	112.71
Water	169.1	156.56	139.90	131.81
Salt	178.21	156.96	140.24	134.49
EC 6	226.33	189.57	183.18	162.41
EC 11	205.13	185.023	180.35	155.89
Mean	188.70	165.72	153.21	139.46
SE (m)±	1.13	0.16	0.11	0.11
CD at 5%	3.378	0.478	0.328	0.328

Table 12. Estimation of á- amylase activity in seed after 72 hours after harvest

Treatments	Immediate	1 month	4 month	6 month
Control	361.38	309.41	281.32	257.26
Water	372.27	314.19	282.70	264.65
Salt	397.60	330.95	299.55	281.38
EC 6	440.7	399.91	377.40	326.57
EC 11	411.82	382.3	328.01	311.49
Mean	396.75	347.35	313.80	288.27
SE (m)±	0.11	0.35	11.18	0.10
CD at 5%	0.32	1.04	33.43	0.29

Due to maintaining the normal storage condition in all cases, the seeds existed in equal micro-atmospheric conditions. Therefore, the studies on various seedling parameters are now crucial and mainly linked with the seedling quality for early establishment of the crop and crop quality liable for grain filling. Most of the treatments showed a significant effect (Table 1-8) on germination parameters, root-shoot length, vigour index, fresh weight and dry weight under different treatments over control. The same inclination was observed in treatments EC6, EC11 and salt for seedling growth and in mass accumulation. Significant superior value was always reflected by electric stimulus though the salt and water were also maintaining a significant distinction over control in most cases. Sometimes the lower dose and water spray are not showing a significant tendency. The effect of both electric and salt treatments retained likeness in most cases where water showed a significant downward outcome, particularly with the treatment EC6. Therefore, a critical observation of biochemical activity was very essential, particularly on rainfed wheat genotypes.

Significantly decrease in electric conductivity was observed in treatments EC6, EC11 and salt over control and water treatments in immediately harvested seeds (Table 9). In the 1 and 4 months of storage, the E.C. showed same trend i.e. control maintained a significant difference with respect to other treatments though water treatment showed the highest result after 1 month. The lowest result was displayed in treatment EC6. The treatments of water, salt and EC11 were indicating an insignificant difference among them but they were significantly superior to treatment EC6 and inferior to the control after 6 months of storage. The estimation of Electrical Conductivity (E.C.) of stored seed was the easiest method for evaluation of seed quality. Seeds of lower vigour leach out a greater quantity of solutes and it would show a higher value of E.C. The increasing E.C. due to aging showed a significant negative correlation with vigour index and germination (Thakur *et al.*, 2005; Zhang *et al.*, 2021).

In immediately harvested seed, treatment EC6 significantly increased peroxidase activity over control followed by treatments EC11, salt and water respectively (Table 10). This pattern was same in one month and 4 months of seed storage, where electric stimulus and salt treatments maintained a non-significant divergence within them but significant with the other treatments. It was observed that peroxidase activity in the seed was much higher in treatments EC6 than EC11 followed by salt treatment. Although after 6 months peroxidase activity enhanced significantly in treatment EC6 over all other treatments. Among the different storage periods, peroxidase activity slowly declined but it was always higher in treatment EC6 irrespective to storage periods of seed. The biochemical nature i.e. peroxidase activity was increased by electric stimulus corroborates the work of Pati *et al.* (2007) which has an indispensable role in preventing the accumulation of H_2O_2 in addition to the buildup the tolerance against stress.

A significant increase in á-Amylase activity at 24 hours was observed in all treatments over control for immediate harvested seeds (Table 11). The highest place was achieved by treatment EC6 followed by treatments EC11, salt, water and control. This trend of á-Amylase activities was followed by seeds after one, 4 and 6 months of storage, where most of the treatments maintained a clear significant difference. The electric treatments always showed a higher result and the control maintained the lowest value.

Treatment EC6 enhanced á-Amylase activity significantly at 72 hours for immediately harvested seeds over all treatments (Table 12). After 1 month of storage treatment EC6 maintained a significantly increased value followed by treatments EC11, salt respectively over control. Seeds stored for 4 months were exhibited significant increase in á-Amylase activity at 72 hours in treatment EC6 over all other treatments. There was no significant difference found between control, water and salt treatments. In the 6 months of storage significantly highest á-Amylase activity was observed in treatment EC6 followed by treatments EC11, salt and water treatments over control. The activity of á-amylase increased with the progress of germination. The equivalent scenario was observed in the present investigation where the highest result was found in Electrotherapy in every stage of storage. Actually, the application of electric potential increased the glucose 6 phosphate dehydrogenase (G-6-PD) activity in the shoot apex of the spinach plant (Montavon *et al.*, 1987).

Priming is the foremost influencing treatment of seed for better crop growth under normal and stressful situations, particularly under rainfed conditions. From the above study it can be inferred that, electrotherapy especially treatment EC6 followed by EC11 and salt priming treatment on pre-sown soaked seed significantly enhanced the germination and biochemical parameters by establishing a vigorous seedling within a stipulated time and finally in mass accumulation. Cellular protein denaturation and loss of membrane integrity are the major factors responsible for dehydration injury to plants under water deficit. The gain of healthy seedlings at the initial stage and their proper establishment is one of the key factors playing a significant role in the production system. Hence, seed treated with an electric stimulus and salt priming for a predetermined time influenced the role of physiological and biochemical activities that leads to enhanced growth of seedlings.

REFERENCES

Abdul-Baki, A.A. and J.D. Anderson, 1973. Vigor determination in soybean seed by multiple criteria. Crop Sci. **13**: 630-633.

Aguilara, J.O., D.S. Riverob, A.E. Puentesa, P.E.V. Perillaa and A.M.S. Navarro, 2015. Comparison of the effects in the germination and growth of corn seeds (*Zea mays* L.) by exposure to magnetic, electrical and electromagnetic fields, Chem. Eng. Trans. **43**: 169-174.

Aladjadjiyan, A. 2007. The use of physical methods for plant growing stimulation in Bulgaria, J. Cent. Eur. Agric. **8**:369-380.

Anonymous, 2007. Annual Report, Directorate of Weed Research, Indian Council of Agricultural Research.

Anonymous, 2021. Annual Report, Directorate of Weed Research, Indian Council of Agricultural Research.

Anonymous, 2021. Global Poverty Monitoring Technical Note, World Bank. https://blogs.worldbank.org/opendata/march-2021-global-poverty-update-world-bank.

Barman, P. and R. Bhattacharya, 2016. Impact of electric and magnetic field exposure on young plants-a review, Int. J. Curr. Res. Aca. Rev. **4**(2): 182-192.

Bera, A.K. and U. Maity, 2004. Enhancing yield potential in rice by pre-sowing electric current treatment of rice grains, Plant Arch. **4**: 17-24.

Bera, A.K., M.K. Pati and P. Ghanti, 2006. Effect of presowing electrical stimulus of seed on growth and yield of ridge gourd (*Luffa acutangula* Roxb.) and snake gourd (*Trichosanthes anguina* L.), Indian J. Plant Physiol. **11**: 291-294.

Bernfeld, P. 1955. Amylase á and â, Meth. Enzymol. **1**: 149-158.

Blûmmel, M. 2016. Opportunities from multi-dimensional crop improvement and the supporting role of Near Infrared Spectroscopy (NIRS) networks, Presented 11 November 2016. International Livestock Research Institute, Nairobi, Kenya.

Borisjuk, N., O. Kishchenko, S. Eliby, C. Schramm, P. Anderson, S. Jatayev, A. Kurishbayev and Y. Shavrukov, 2019. Genetic modification for wheat improvement: from transgenesis to genome editing, Biomed. Res. Int. **2019**: 6216304.

Bose, J.C. 1902. Electric response in ordinary plants under mechanical stimulus, Bot. J. Linn. **35**(245): 275-304.

Chakraborty, P. 1998. Heterosis for oil content and fatty acid composition in sesame under salinity stress, J. Oilseeds Res. **15** (2): 213-218.

Dahiya, O.S., R.P.S. Tomer and A. Kumar, 1997. Evaluation of viability and vigour parameters with respect to field emergence in chickpea (*Cicer arietinum* L.), Seed Res. **25**:19- 24.

Dominguez, F. and J. Francisco, 1995. Pattern of endoproteolysis following wheat grain germination Cejudo. Physiol. Plant. **95**: 253-259.

Dorchester, C.S. 1935. A study of the effect of electric current on certain crop plants, Retrospective Theses and Dissertations. 13499. https://lib.dr.iastate.edu/rtd/13499.

Fabre, D., D.E. Adriani, M. Dingkuhn, T. Ishimaru, B. Punzalan, T. Lafarge, A.C. Vidal and D. Luquet, 2016. The qTSN4 effect on flag leaf size, photosynthesis and panicle size, benefits to plant grain production in rice, depending on light availability, Front. Plant Sci. **7**: 623.

Feghhenabi,F., H. Hadi, H. Khodaverdiloo and M.T.V. Genuchten, 2020. Seed priming alleviated salinity stress during germination and emergence of wheat (*Triticum aestivum* L.), Agric. Water Manag. **231**: 106022.

Fincher, G.B. 1989. Molecular and cellular biology associated with endosperm mobilization in germinating cereal grains, Annu. Rev. Plant Physiol. Plant Mol. Biol. **40**: 305–345.

Gandhare, W.Z. and M. Samir, 2014. A new approach of electric field adoption for germination improvement, J. Power Energy Eng. **2**: 13-18.

Hatzade, R.V., S.S. Mahajan, E.G. Lal, S.A. John and P.K. Shukla, 2022. Correlation and regression analysis of standard germination and field emergence with various viability and vigour tests in tetraploid and diploid cotton, J. Soils and Crops. **32**(2): 305-311.

Humphreys, M.T., W.R. Raun, K.L. Martin, K.W. Freeman, G. V. Johnson and M.L. Stone, 2004. Indirect estimates of soil electrical conductivity for improved prediction of wheat grain yield, Commun. Soil Sci. Plant Anal. **35**(17-18): 2639-2653.

Krzywinski, M. and N. Altman, 2014. Two-factor designs, Nat. Methods, **11**: 1187–1188.

Lv, Y., S. Zhang, J. Wang and Y. Hu, 2016. Quantitative proteomic analysis of wheat seeds during artificial ageing and priming using the isobaric tandem mass tag labeling. PLoS One. **11**(9): e0162851.

Mandal, S.K. and A. Maity, 2013. Applications of laser in agriculture - a critical review, Elixir. Mech. Engg. **63**: 18740-18745.

Montavon, M., M.E.L. Toukhi, G. Auderset and H. Greppin, 1987. Effect of photoperiod and electrical potentials applied to petioles on the glucose-6-phosphate dehydrogenase activity used as marker of floral induction in shoot apices of spinach, Ann. Bot. **60**: 225- 230.

Mukherjee, D. 2012. Effect of different sowing dates on growth and yield of wheat (*Triticum aestivum*) cultivars under mid hill situation of West Bengal, Indian J. Agron. **57**(2): 152-156.

Nakano, Y. and K. Asada, 1981. Hydrogen peroxide is scavenged by ascorbate-specific peroxidase in spinach chloroplasts, Plant Cell Physiol. **22**: 867-880.

Pati, M.K. 2007. Effect of pre-sowing electrical stimulus on growth and yield of bottle gourd (*Lagenaria siceraria* Mol. Standl.), Ph.D. Thesis, Bidhan Chandra Krishi Viswavidyalaya, West Bengal, India.

Rahman, M.A. and F.Yasmin, 1994. Performance of electric current treated seeds of Bottle gourd (*Lagenaria siceraria* (Mol.) standl.) on growth, sex expression and yield, Bangladesh J. Bot. **23**(1): 67-72.

Ruediger, H.W.R. 2009. Genotoxic effects of radiofrequency electromagnetic fields. Pathophysiol. **16**: 89-102.

Singh, G and R. Kumar, 2022. Crop and water productivity under different sowing methods and irrigation schedules of Wheat (*Triticum aestivum* L.), J. Soil and Crops.**32**(2): 322-325.

Thakur, A.S., P.S. Thakur and R. Mehta, 2005. Effect of pre-treatments on seed germination in *Berberis aristate*, Indian J. Plant Physiol. **10**(4): 338-343.

Wahab, A.M.A. A.F. Omran, E. Elkholy and H. Hafez, 1980. Studies on the effect of treating watermelon and snake cucumber seeds with electric current, Seed Sci. Technol. **8**(1): 95-102.

Zadeh, E., A. Majd and S. Arbabian, 2014. Effects of electromagnetic fields on seed germination in *Urtica dioica* L, Int. J. Sci. Technol. Res. **3** (4): 365-368.

Zang, H. and F. Hashinaga, 1997. Effect of high electric field on the quality of satsuma mandarin fruits, Shokubutsu Kojo Gakkaishi. **9**(2): 107-113.

Zhang, K., Y. Zhang, J. Sun, J. Meng and J. Tao, 2021. Deterioration of orthodox seeds during ageing: Influencing factors, physiological alterations and the role of reactive oxygen species, Plant Physiol. Biochem. **158**: 475-485.

Rec. on 02.05.2023 & Acc. on 17.05.2023

Applied Physics A (2023) 129:672
https://doi.org/10.1007/s00339-023-06954-x

Applied Physics A
Materials Science & Processing

Superparamagnetic $Ni_{0.5}Zn_{0.5}Fe_2O_4$ nanoparticles prepared by ball-milling

Sk Mohammad Yasin[1]

Received: 15 July 2023 / Accepted: 23 August 2023

Abstract
$Ni_{0.5}Zn_{0.5}Fe_2O_4$ ferrite nanoparticles were synthesized by high-energy ball-milling using binary oxide precursors, followed by a subsequent heat treatment at comparatively lower temperature (500 °C for 1 h) to promote the redistribution of the cations to their equilibrium positions. Although, several articles are available on Ni–Zn ferrite nanoparticles, the magnetic data of ball-milled sample has hardly been analysed based on existing theoretical models to extract useful information. The samples were characterized by X-ray diffraction, scanning electron microscopy and dc magnetization study. The average crystallite sizes estimated from the structural data (using Scherrer equation) are found to be around 14.4 nm. The temperature and field variation of magnetic data suggests a superparamagnetic nature with a distribution of particle sizes. The zero field cooled and field cooled magnetization data are analysed based on a theoretical model of superparamagnetic particles with a log-normal distribution, resulting in an average particle size of 24.4 nm (width parameter of 0.23). The Langevin function adequately describes the field variation of magnetization (M–H) data at room temperature, in addition to a paramagnetic contribution, suggesting the existence of significant spin disorder. The above fit yields an average magnetic moment of 7860 μ_B. The results of the magnetic study corroborate well with the structural and morphological characteristics.

Keywords Ferrites · Magnetic nanoparticle · Superparamagnetism · Zero field cooled and field cooled magnetization

1 Introduction

Magnetic materials such as transition metal oxides, ferrites, mixed-valence manganites and their composites have been the focus of attention of researchers for many decades due to the variety of interesting physical phenomena exhibited by them and the possibility of exploiting these for useful device applications [1–5]. The advent of nano science and technology in the early part of this century has added a new dimension to the research on magnetic materials. Nowadays, magnetic nanoparticles are of great interest for their applications in memory storage, biomedicine, MRI, sensors, activators etc. [6, 7].

The ferrites are most versatile magnetic materials for general use. Among different ferrites the Ni–Zn ferrites are important due to their wide range of potential applications such as high-density information storage devices, microwave devices, transformer cores, NEM/MEMs, magnetic fluids, etc. [4]. The Ni–Zn ferrites exhibit low magnetic coercivity and high electrical resistivity which greatly reduce eddy current losses at high frequencies. The electromagnetic properties of Ni–Zn ferrite are dependent on their cation distributions [8, 9]. The structure, morphology and the size distribution of the complex oxides and ferrites nanoparticles have great influence on their electronic and magnetic properties [10–18]. Mainly, they exhibit superparamagnetism, weak ferromagnetism, spin canting, surface spin effects etc. [10–14].

It is widely believed that the physical properties are very sensitive to the method of synthesis. Various synthesis methods have been used to form nano-sized Ni–Zn ferrites (or similar kind of ferrites) and other oxide films. These include, hydrothermal [19, 20], chemical co-precipitation [11, 15, 21], sol–gel [22], reverse micelle [23], ball-milling and mechanochemical synthesis [16, 24–27], spin coating [28] and electrochemical deposition [29] etc. Several reports are available on the methods of synthesis and characterization of nickel-zinc ferrite nanoparticles [10, 11, 15, 20, 22–24, 27,

✉ Sk Mohammad Yasin
yasin@bnmv.ac.in; yasin3587@gmail.com

[1] Department of Physics, Bejoy Narayan Mahavidyalaya, The University of Burdwan, Itachuna, Hooghly, West Bengal 712147, India

Published online: 04 September 2023

Year 12 : Issue 1, January-June 2024 I S S N : 0975-6256

ललिता कवि-भारती

(LALITĀ KAVI-BHĀRATĪ)

U. G. C. CARE LISTED JOURNAL

(पीयर-रिव्यू षाण्मासिकी शोध-पत्रिका)

किशोर-विद्या-निकेतनम्
बी-2/236-ए-1, (भारतीय स्टेट बैंक अस्सी शाखा)
भदैनी, वाराणसी-221001

विषयानुक्रमणिका

ईशोपनिषदि श्रीबलदेवभाष्यभास्करोदयेन पञ्चमुख्यतत्त्वानामनुसन्धानम्

श्री सन्तु कुमार पाल

असिस्टेन्ट प्रोफेसर

विजय नारायण महाविद्यालय, इटाचूना-७१२१४७

जिला हुगली, पश्चिमबङ्गाल

श्रीपाद्बलदेवविद्याभूषणैः अचिन्त्यभेदाभेदतत्त्वं ईशोपनिषदि कथं प्रतिष्ठापितं तदत्र अनुसन्धीयते। अचिन्त्यभेदाभेदसम्प्रदाये बहूनि महत्त्वपूर्णानि तत्त्वानि सन्ति। तेषु तत्त्वेषु पञ्च मुख्यतत्त्वानि सन्ति। जीवपादा अपि एतानि मुख्यपञ्चतत्त्वानि स्वीकुर्वन्ति। ननु कानि तानि मुख्यतत्त्वानि। अचिन्त्यवैष्णव-सम्प्रदाये ईश्वरजीवप्रकृतिकालकर्माणि इत्येतानि पञ्च मुख्यतत्त्वानि। अचिन्त्यभेदाभेदसम्प्रदाये बलदेवविद्याभूषणः मुख्याचार्य आसीत्। प्रबन्धेऽस्मिन् बलदेवविद्याभूषणभाष्येण इशोपनिषदि एतेषां पञ्चतत्त्वानां स्वरूपम् अनुसन्धीयते। किञ्च कथम् एतेषां तत्त्वानां इशोपनिषदि समन्वयः भवति तदत्र प्रदर्श्यते। किञ्च एतैः मुख्यतत्त्वैः अचिन्त्यभेदाभेदतत्त्वस्यापि प्रकाशनं कथं भवति। किञ्च एतेषां तत्त्वस्थापनात् अद्वैतादिसम्प्रदायानां विरोधः चेत् कथं समन्वयः तदत्र प्रदर्श्यते। किञ्च यद्यपि अचिन्त्यभेदाभेदतत्त्वैः साकम् अन्येषां सम्प्रदायानां विरोधः अस्ति तथापि दोषः नास्ति। अतः विरोधे सत्त्वेऽपि कथं दोषो नास्ति तदपि विचार्यते। प्रबन्धोऽयं छात्राणाम् बोधाय न तु विदुषां कृते। प्रसिद्धाचार्यबलदेवविद्याभूषणैः कथं स्वसम्प्रदायमतस्थापनापुरस्सरं कथं ईशोपनिषदः भाष्यविरचनं कृतं तदत्र आलोच्यते। अनेन छात्राणां चित्तविभ्रमदोषः न भवति। यतो हि अद्वैतादिभाष्यग्रन्थबलात् तेषां चितविभ्रमः दोषः भवति। कस्य सम्प्रदायस्य साधुत्वं कस्य सम्प्रदायस्य मतम् ग्राह्यम् इति चिन्ता जायते। अस्य निवारणमत्र क्रियते।

अचिन्त्यभेदाभेदवादाः -

श्रीश्रीकृष्णचैतन्यचरणानुचरगौडीयवैष्णवाचार्यपादगणाः सर्ववेदान्तसारभूतसर्वसिद्धान्तः श्रीमद्भागवत-रसामृतसिन्ध्वन्तर्गतः। अतर्क्यसहस्रशक्त्यद्भुतज्ञानतत्त्वं तच्छक्तिवैचित्रवस्तुसमूह सम्बन्ध-ज्ञापकसर्वतन्त्रसिद्धान्तं प्रकोटीचक्रुः तदेव अचिन्त्यभेदाभेदवादः नाम्ना अभिधीयते। अचिन्त्यानन्त-शक्तिसम्पन्नपरतत्त्वेन[1] सह परतत्त्वस्य यः अचिन्त्ययुगपत्भेदाभेदसम्बन्धः तदेव अचिन्त्यभेदाभेदवाद इति। भगवान् श्रीकृष्णचैतन्यदेवः सर्ववेदैकफलरूपश्रीमद्भागवतमेव ब्रह्मसूत्रस्य अकृत्रिमभाष्यमिति सूचितवान्।[2] श्रीमद्भागवतं द्वैतस्य वा भेदाभेदवादस्य प्रतिपादकं न भवति। किञ्च मायातः भयमुत्पद्यते। अतः अद्वितीयपरतत्त्वं भयसंसारनिवर्तकमेव श्रीमद्भागवतम्। निर्विशेषवस्तैक्याभेदवादस्य श्रीमद्भागवतं न प्रतिपादकम्।[3] अतएवाऽचिन्त्यतत्त्वप्रतिपादकपरं भागवतमिति फलितम्। गौडीयदार्शनिक-सिद्धान्तानुसारं शक्तिमतः शक्तिं पृथक् कर्तुमशक्यत्वात् शक्तिशक्तिमन्तौ मिलित्वा अभेदरूपाद्वितीयवस्तु प्रतिपाद्यते। वस्तु विशेष्यं वस्तुशक्तिः विशेषणम्। विशेषणगुणवृक्त-विशेष्यमेव वस्तु। अत्र प्रश्नो भवति यत् विशेष्यविशेषणयोः मेलनेन एव यदि वस्तु भवति तर्हि विशेषणात् विशेष्यं शक्तिमातः शक्तिं पृथक् कर्तुं न शक्यते। अतः शक्तेः स्वीकारस्य आवश्यकता एव नास्ति। प्रसङ्गेऽस्मिन् श्रीजीवपादैः प्रोक्तं वस्तु सत्त्वेपि मन्त्रमहौषधादिप्रभावेण शक्तिः दुर्बला भवति। किञ्च हस्तः अदग्धश्चेदपि अग्निः अग्नितः तस्य दाहिकाशक्तिः पृथक् इति युक्तियुक्तम्। अत्र यद्यपि वस्तुतत्त्वं तु एकमेव न द्वयम्। स्वाभाविकशक्तिवैचित्र्यात् शक्तिमतः अद्वयतत्त्वस्य व्याघातो न भवति। अतः स्वरूपात् अभिन्नरूपे शक्तेः चिन्ता असम्भवा इति कारणात् भेदः इति। अपि च भिन्नरूपेऽपि चिन्ता अशक्या इति अभेदः। अतः शक्तिशक्तिमतो र्भेदाभेदः स्वीकृतः। तदेव अचिन्त्यं तर्केण अगम्यं परन्तु शास्त्रगम्यं शब्दमूलकम्।[4]

गौडीयवैष्णवदार्शनिकैः अतीन्द्रियतत्त्वं वा तच्छक्तेः अलौकिकत्वनिरूपणे अचिन्त्य इति पदस्य प्रयोगः क्रियते। परन्तु शङ्करचार्यः तु मायातत्त्वनिरूपणे अनिर्वचनीयम् उक्तवान्। अचिन्त्यानिर्वाच्ययोः अभेदः न भवति। शब्दप्रमाणगम्यतत्त्व-निर्देशकाचिन्त्यशब्दः इति। अचिन्त्यमित्यस्य प्रयोगः श्रुतौ, श्रीमहाभारते, श्रीगीतायां, श्रीविष्णुसहस्रनामग्रन्थे, श्रीविष्णुपुराणे, श्रीभागवतपुराणे दरीदृश्यते। अचिन्त्यशब्दस्य तात्पर्यं तु श्रुतेस्तु शब्दमूलत्वात्[४] इति ब्रह्मसूत्रेण प्रतिपादितम्। आचार्यशङ्करैरपि उक्तसूत्रभाष्ये अङ्गीकृतम्[५] अचिन्त्यशक्तिः एव परब्रह्म इति। विष्णुसहस्रनामस्तोत्रे अचिन्त्यशब्दस्य प्रयोगः दृश्यते। श्रीशङ्करचार्यः अपि अचिन्त्यमित्यस्य अर्थं लिखितवान् यत् प्रमाणादिसाक्षित्वेन सर्वप्रमाणागोचरत्वादचिन्त्यः।[६] अयमीदृशः इति विश्वप्रपञ्चविलक्षणत्वेन चिन्तयितुमशक्यत्वात् वा अचिन्त्यम्[७] इति। श्रीधरस्वामिपादैः श्रीजीवगोस्वामिपादैः तु अचिन्त्यशब्दस्य अर्थः क्रियते यत् शब्दमूलकश्रुतार्थापत्ति-ज्ञानगोचरः[८] इति। यद्यपि भेदाभेदयोः युगपदवस्थानमुभयोः समभावेन नित्यानित्यमिति अबोध्यमचिन्त्यम् प्रतीयमानं मनुष्यबुद्धौ तथापि शास्त्रोपष्टिमवश्यमङ्गीकर्तव्यमिति। श्रीविष्णुपुराणे[९] श्रीमैत्रेयः श्रीपराशरं प्रपच्छ यत् सत्त्वादिगुणरहितदेशकालाद्यपरिच्छिन्नप्राकृतदेहहीनरागादि-शुन्यब्रह्मणः कथं जगत्सर्जनं भवति। श्री पराशरः अवोचत् यत् हे भगवन् यथा समस्तभावपदार्थस्य शक्तिसमूहः अचिन्त्यज्ञानगोचरः तथैव ब्रह्मणः जगत्सृष्ट्यादिशक्तिसमूहः अचिन्त्यज्ञानगोचरः इति। एतच्च अग्नेः उष्णताशक्तिः इव स्वभावसिद्धम्।

बलदेवभाष्यपुरस्सरं पञ्चतत्त्वानां विवेकः-

ईशोपनिषदि अचिन्त्यभेदाभेदतत्त्वस्य समन्वयार्थं श्रीपादपरमवैष्णवाचार्येण श्रीमद्बलदेवविद्या-भूषणेन ईशोपनिषत्मन्त्रस्य भाष्यरचनात् पूर्वं मङ्गलाचारणं आचरितम्। -

वेदास्तथा स्मृतिगिरो ह्यमचिन्त्यशक्तिं सृष्टिस्थितिप्रलयकारणमामनन्ति।

तं श्यामसुन्दरमविक्रियमात्ममूर्तिं सर्वेश्वरं प्रणतिमात्रवशं भजामः।।इति।।[१०]

मङ्गलश्लोकेन अनेन आचार्यबलदेवविद्याभूषणेन अचिन्त्यभेदाभेददर्शनस्य स्वरूपं दार्शनिकतत्त्वम् अनुबन्धचतुष्टयञ्च आलोचितम्। यद्यपि मङ्गलं सम्प्रदायेषु दृश्यते शिष्यशिक्षार्थं विघ्नादिनाशाय[११] तथाप्यत्र मङ्गलाचारणेन आचार्येण अचिन्त्यभेदाभेददर्शनस्य प्रकृष्टस्वरूपं प्रदर्शितम्। श्लोकेऽस्मिन् मोक्षदातुः भगवतः श्रीकृष्णस्य स्वरूपद्वयं दृश्यते। तद्यथा एकं स्वरूपलक्षणम् अपरञ्च तटस्थलक्षणमिति। यद्यपि अचिन्त्यभेदाभेदसम्प्रदाये स्वरूपतटस्थयोः अङ्गीकारः नास्ति तथापि मङ्गलश्लोकपर्यालोचनेन एतल्लक्षणद्वयं स्पष्टं दृश्यते। तद्यथा श्लोके आत्ममूर्तिमविक्रियमचिन्त्यशक्तिमित्यादिभिः पदैः आचार्यः भगवतः श्रीकृष्ण-व्रजेन्द्रनन्दनस्य स्वरूपलक्षणं प्रकटीचकार। अवशिष्टांशेन भगवतः तटस्थलक्षणं प्रदर्शितम्। किञ्च भगवतः व्रजेन्द्रनन्दनस्य सविशेषस्वरूपमेव बलदेवैः प्रतिपाद्यते। तदेव अचिन्त्यभेदाभेदवादस्य मूलम्। यतो हि श्रीवैष्णवाः श्रीकृष्णस्य निर्विशेषत्वं न स्वीकुर्वन्ति। किञ्च श्रीकृष्णः एव सृष्टिस्थितिप्रलयरूपजगतः कारणम्। जगज्जीवौ ब्रह्मणः शक्तिस्वरूपौ। समस्तवेदराशिः[१०] स्मृतिवाक्यसमूहः[११] यस्य प्रतिपादकाः। श्रीगौडीयदर्शने अचिन्त्यशक्तेः मनुष्यबुद्ध्या चिन्तयितुम-शक्यत्वात् केवलशब्दप्रमाणगम्यमिति उच्यते।[१२] अनेन अचिन्त्यतत्त्वस्य शब्दमात्रप्रमाणगम्यत्वं सूचितम्। किञ्च समस्तवेदराशिः इत्वनेन अचिन्त्यतत्त्वस्य वेदमूलत्वमपि दर्शितम्। नैतत् कपोलकल्पितत्त्वं वेदमूलत्वात्। किञ्च श्रुतिस्मृतिभ्यां अचिन्त्यतत्त्वस्य प्रामाण्यमपि दर्शितम्। अपि च अचिन्त्यशक्तिमिति पदेन साक्षात् स्वसम्प्रदायस्य अचिन्त्यतत्त्वस्य प्रतिपादनं चकार आचार्यः। अचिन्त्यानन्तशक्तिसम्पन्न-परतत्त्वेन सह परतत्त्वस्य य अचिन्त्ययुगपद्भेदाभेदयुक्तसम्बन्धः तदेव अचिन्त्यभेदाभेदतत्त्वम् इति। श्रीपाद्बलदेवमते ब्रह्मणः त्रिविधा शक्तयः सन्ति। ताः शक्तयः परापराविद्या चेति।[१३] ननु का नाम परा शक्तिरिति चेत् उच्यते आचार्येण विष्णुशक्तिरेव स्वरूपशक्तिः परशक्तित्वेन कल्प्यते। अपरा नाम क्षेत्रज्ञाख्या जीवशक्तिः इति। मायाशक्तिस्तु अविद्याशक्तिः तमोरूपा कर्मस्वरूपा इत्यभिधीयते। श्रीपाद्बलदेवैः प्रोक्तं यत् ब्रह्म परास्यशक्तिमद्रूपेण जगतः निमित्तकारणं भवति। ब्रह्म जीवशक्तिमायाशक्तिभ्यां तु जगतः

उपादानकारणं भवति। अतः एव ब्रह्म शक्त्या जगतः उभयकारणं[14] भवति। अपराशक्तितः जीवस्य अविद्याशक्तितः जगतः उत्पत्तिः भवति। निमित्तकारणरूपेण ब्रह्म नित्यं कूटस्थमपरिमेयमपरिवर्तनीयम्। उपादानकारणरूपेण ब्रह्म परिणामिनित्यं जगद्रूपेण नित्यम्। परन्तु परिणतो भूत्वापि ब्रह्म अविकृतापरिवर्तितरूपेन तिष्ठति। श्रीबलदेवेन पुनः परब्रह्मणः पराशक्तेः त्रिविधाः वृत्तयः प्रदर्शिताः। तद्यथा सन्धिनी संवित् ह्लादिनी[15] चेति। आचार्यबलदेवैः संवित्प्रधानवृत्तिः वाग्देवी इति अभिधीयते। किञ्च ह्लादप्रधानावृत्तिः लक्ष्मी इति उच्यते। अनेन सिद्धान्तेन एव आचार्यैः श्रीविष्णोः स्वशक्तिः श्रीलक्ष्याः जीवकोटित्वशक्तेः पृथक् इति ज्ञापितम्।[16] किञ्च परतत्त्वं यदा रसास्वादनिमित्तेन ह्लादिनीशक्तेः सर्वानन्दातिशायिनीवृत्त्या तस्यैव शक्त्यंशरूपं भक्तजनानां हृदि सञ्चारयति तदा सा वृत्तिः कृष्णप्रीतिरूपवैचित्र्यं धारयित्वा परममास्वादनचमत्कारितां प्राप्नोति।[17] अतः भक्तिभक्तकोटिं प्रविश्य भगवान्भक्तयोः आह्लादित्वात् एव भगवच्छक्तिविशेषः[18] इत्यपि उच्यते। एतादृशाचिन्त्यशक्तिविशिष्ट-श्यामसुन्दर एव जगत्कर्ता। स एव परमब्रह्म। आचार्यैः श्यामसुन्दर इत्यनेन पदेन श्रीकृष्णस्य सविशेषभक्ति-व्यङ्गरूपम् एव प्रकाश्यते। अचिन्त्यभेदाभेदसम्प्रदायिकाः सविशेषत्वमेव अङ्गीकुर्वन्ति परब्रह्मणः। जगतः सृष्टिस्थितिप्रलयकारणं अचिन्त्यशक्तिः एव। श्रीकृष्णः शक्तिमान्, जगत् जीवसमूहः तस्य शक्तिः। उभयोः मध्ये भेदाभेदः स्पष्टः। किन्तु युगपद्भेदाभेदः केन प्रकारेण एकस्मिन्नेवाधारे तिष्ठतीति चिन्तातीतमतः अचिन्त्यम्। किञ्च मङ्गलश्लोके अचिन्त्यशक्तिं इत्यनेन ब्रह्मजीवयोः सम्बन्धः अचिन्त्यः इति द्योत्यते। अविक्रियमिति पदेन परमब्रह्मणः क्षयरहित्वं वर्णितम्। अनेन एव नित्यत्वं ख्यापितम्। आत्ममूर्तिमित्यनेन सच्चिदानन्दविग्रहविशिष्टश्रीव्रजेन्द्रनन्दनस्य सविशेषस्वरूपत्वरूपं प्रकाश्यते। सर्वेश्वरम् इत्यनेन अखिलस्य जगतः ईश्वनकर्ता इति। प्रणतिमात्रवशमित्यनेन भक्त्या एव लब्धुं शक्यते इति द्योत्यते। भजामः इत्यनेन भजनाद्यनुष्ठानेन श्रीकृष्णप्रीतिरुत्पद्यते। भजनेन एव शरणागतिः भवति मनुष्याणाम्।

मुक्तिः पुरुषोत्तमसाक्षात्कारः[19] एव परमप्रयोजनम्। अशेषसंसारबन्धदोषविनाशपूर्वपरतत्त्वश्रीकृष्ण-साक्षात्कारः भगवच्छरणागतिः एव मोक्षः। भक्तिभजनाद्यनुष्ठानेन भगवान्श्रीश्यामसुन्दरव्रजेन्द्रनन्दस्य चरणाश्रयप्राप्तिः एव प्रयोजनम्।[20] तत्तु अचिन्त्यतत्त्वज्ञानेन जायते।

मन्त्रव्याख्यानात्पूर्वम् उपोद्घातभाष्ये श्रीपाद्वैष्णवाचार्यमद्वलदेवविद्याभूषणः स्वसम्प्रदायनिहितसिद्धान्तस्य अचिन्त्यभेदाभेदवादतत्त्वस्य प्रतिष्ठापनाय पूर्वपक्षत्वेन बहूनां सम्प्रदायानां सिद्धान्तवर्णनपुरस्सरं ततत्सिद्धान्त-खण्डनाय स्वसिद्धान्तं अवोचत्। न चेत् स्वसिद्धान्तस्य किं गुरुत्वं तत् स्पष्टतया न ज्ञायेत। किञ्च अचिन्त्यभेदाभेदतत्त्वस्य प्रतिष्ठापने का आवश्यकता तत्तु न ज्ञायते। किञ्च पूर्वपक्षत्वेन श्रीवैष्णवसम्प्रदायान्तर्ग-ताचार्याणां सिद्धान्ता न गृहीताः। केवलं मीमांसाशास्त्रे[21] सांख्यशास्त्रम्[22] अद्वैतवेदान्तशास्त्रं[23] च स्वीकृतानि। अनेन एव ज्ञायते तस्मिन् समये मीमांसादिशास्त्राणां प्रभावः अधिकः आसीत्। किञ्च द्वैतादिशास्त्राणामुल्लेखः नास्ति। अपि च अचिन्त्यभेदाभेदतत्त्वस्य स्थापनाय एतेषां शास्त्राणां खण्डनमत्यन्तमावश्यकमासीत्।

ततः सिद्धान्तरूपेण प्रोक्तमाचार्यैः यत् परस्य विष्णोरिह स्वातन्त्र्यसर्वकर्तृत्वसार्वज्ञत्वपुमर्थत्वादि-धर्मकत्वज्ञानसुखस्वरूपत्वं निरूप्यते इति। अत्र ग्रन्थस्य आरम्भः किमर्थं क्रियते तत्प्रोक्तवान्। परतत्त्वरूपेण विष्णोः उल्लेखः कृतः आचार्येण अनेन माध्वमतश्रीवैष्णवमतयोः समन्वयितुमिच्छतीति प्रतीयते। यतो हि आचार्यः पूर्वाश्रमे माध्वसम्प्रदायी आसीत्। किञ्च माध्वसम्प्रदाये नारायणः विष्णुरेव परमब्रह्म[24] इति अङ्गीक्रियते। किञ्च स्वातन्त्र्यसर्वकर्तृत्वादिगुणविशिष्टविशेषणैः सविशेषत्वं परस्य ब्रह्मणः सूचितम्। अचिन्त्यभेदाभेदसम्प्रदाये सविशेषत्वं ब्रह्मणः अङ्गीक्रियते। सुखस्वरूपत्वमित्यनेन मुक्तेः स्वरूपं ख्यापितम्। श्रीवैष्णवाः तु श्रीकृष्णप्रेमलक्षणमेव प्रयोजनमिति ब्रुवन्ति। अत सिद्धान्तख्यापनेन एव अचिन्त्यभेदाभेद-वादस्य बीजम् स्थापितवान् आचार्यः।

मन्त्रभाष्यस्य रचनात् पूर्वमेव आचार्यः स्वाचिन्त्यभेदाभेदसम्प्रदायाभिमतानि तत्त्वानि ख्यापितानि। तेनैव श्रीवैष्णवाचिन्त्यसम्प्रदायस्य मुख्यतत्त्वानि कानि तेषां स्वरूपविषये ज्ञानं भवति। येन ग्रन्थपाठकानाम्

अचिन्त्यभेदाभेदसम्प्रदायविषये ज्ञानम् उत्पद्यते। अधः श्रीबलदेवविद्याभूषणस्य सिद्धान्तपुरस्सरम् तानि तत्त्वानि आलोच्यन्ते।

तद्यथा ईश्वरजीवप्रकृतिकालकर्माणि चेति पञ्चमौलिकतत्त्वानि श्रीबलदेवमते। अत्र जीवेश्वरौ अजड़ौ ज्ञानस्वरूपौ। अन्तिमत्रयं जड़ं ज्ञानहीनम्। किञ्च प्रथमचतुष्टयं नित्यानाद्यनन्तस्वरूपम्। अवशिष्टतत्त्वमनित्य-मनादिः परन्तु अनन्तस्वरूपं न भवति। किञ्च प्रथमतत्त्वं नियन्ता तद्व्यतिरिक्तम् अन्यत्सर्वं नियन्त्रितम्। नियन्त्रितेषु जीवः भोक्ता, प्रकृतिः भोग्या, कालः भोगस्य निमित्तकारणमिति। जीवप्रकृतिकालकर्माणि एतानि चत्वारि ब्रह्मणः शक्तिरूपाणि। अतः शक्तिमान् ब्रह्म अद्वितीयवस्तु[24] इति।

ईश्वरः- ईश्वरः स्वतन्त्रः सर्वकर्ता सर्वज्ञः मुक्तिदाता विज्ञानस्वरूपः। किञ्च ईश्वरः विभुचैतन्यं नित्यज्ञानादिगुण-विशिष्टस्मदर्थवाच्यस्वरूपः इति। प्रकृतिषु अनुप्रवेशनियमनाभ्यां जगत्सर्जनं कृत्वा जीवोपभोगमुक्तिविधानं चकार सर्वशक्तिमान् स्वतन्त्र ईश्वरः। किञ्च ईश्वरः एकः अभिन्नः सन्नपि गुणगुणिभावेन देहदेहिभावेन ज्ञानवतः प्रतीतिगोचरो भवति। ईश्वरः यद्यपि अव्यक्तं तथापि भक्तिग्राह्यः। एकरसः भूत्वा चिदानन्दस्वरूपं दधदि भक्तानाय। सर्वव्यापी भूत्वापि जीवान्तस्थदेवतारूपेण तिष्ठति। वैषम्यरहितः सन्नपि भक्तपक्षपातकारी। जगतः उपादानकारणं सन्नपि परिणामरहितः परिवर्तनहीनः। अंशहीनोऽपि स्वांशः। परमेश्वरे एवं बहवः विरुद्धगुणाः दृश्यन्ते। परमब्रह्मणः गुणशक्तिसमूहाः स्वाभिन्नाः। परन्तु अभिन्नः सन्नपि लोकव्यवहाराय भिन्नत्वेन व्यवह्रियते। एष एव लोकाचारसम्मतभेदविषयः परमात्मनः। परमात्मस्वशक्त्योः मध्ये भेदो नास्ति परन्तु विशेषः अस्ति। विशेषः भेदप्रतिनिधिः भूत्वा प्रकृतिभेदसृष्ट्या आपातभेदप्रतीतिं[25] प्रदर्शयति। परमेश्वरः युगपत् सत् सत्तावान्, ज्ञानं ज्ञाता, आनन्दः आनन्दमयः, धर्मः धर्मी, शक्तिः शक्तिमान् च भवति। यथा सर्पः एवं कुण्डलाकृत्या कुण्डलं सर्पस्य विशेषणं भवति तथैव ब्रह्म ज्ञानात्मकः सन्नपि तस्य ज्ञानं गुणः धर्मरूपेण कल्पयितुं शक्यते। अनेन अचिन्त्यभेदाभेदसम्प्रदायानुसारं सविशेषत्वं प्रतिपाद्यते। ब्रह्म सजातीयविजातीयस्व-गतभेदरहितम्। यतो हि शक्तिभिन्नः ब्रह्मणः वस्त्वन्तरं नास्ति। अतः तस्य सजातीयविजातीयभेदोऽपि न भवति। अपि च श्रीविग्रहस्य प्रत्येकं अवयवाः यस्मात् आनन्दमयरूपाः अतः स्वगतभेदोऽवि न भवति। अतः परमात्मनि यद्यपि अभेदः तथापि भिन्नवस्तुव्यवहारबोधकशब्द इव ज्ञानानन्दहस्तपादप्रभृतिभिन्नशब्दानां व्यवहारस्तु अचिन्त्यविशेषस्वभावात् भवति। तद्यथा एकस्मादेव वैदूर्यमणेः नीलपीतादिविभिन्नवर्णानां प्रकाशः दृश्यते तद्वत् ब्रह्मणः ज्ञानानन्दादीनां प्रकाशः। मणौ तथा नानावर्णप्रकाश-कारिणी शक्तिरस्ति तथैव परब्रह्मणि नानाविर्भावसंघटनपटीयसी विशेषशक्तिः वर्तते। अनेनैव विशेषस्वभावेन अभिन्नज्ञानानन्दप्रभृतीनां भिन्नवत्प्रकाशो भवति। स्वरूपतः अभिन्नज्ञानानन्दादीनाम् आविर्भावभेददर्शनेन भेदाभेदपक्षमपि स्वीकर्तुम् अयोग्यम्। यतो हि श्रुत्या तु भेददर्शिनां नरकपातः सूच्यते।

जीवः- नियामकस्य ईश्वरस्य नियम्यः जीवः अणुचैतन्यविशिष्टः। जीवात्मानः बहवः विविधावस्थापन्नाः। किञ्च जीवः स्वरूपतः भगवद्दासः। ईश्वरवैमुख्यात् बन्धकारणम्। बन्धः द्विविधः तत्स्वरूपावरणम् तद्-गुणावरणरूपम्। एतत् द्विविधबन्धकारणमोचनपूर्वकं ईश्वरानुग्रहेण स्वरूप-साक्षात्कारो भवति। ईश्वरस्य शक्तिः जीवः, शक्तिमान् ईश्वरः इति बलदेवविद्याभूषणसिद्धान्तः। यद्यपि भोगविषये मुक्तः जीवोऽपि ब्रह्मसमानः तथापि स्वरूपतः सामर्थ्यतः नित्यभेदः उभयोः वर्तते। जीवाः अपि परस्परभिन्नाः साधनतारतम्यात्। तद्यथा भक्त्यतारतम्यात् मुक्तजीवाः एव नित्यमुक्तः बद्धमुक्तः बद्धाः इति त्रिधा भिन्नाः भवन्ति। जीवस्य ब्रह्मनिष्टत्वात् ब्रह्मण्यप्यहेतुत्वात् ब्रह्मात्मकता नु वस्तुतः जीवः स्वयं ब्रह्म[26] इति। मुक्तावस्थायामपि जीवाः श्रीहरेः नित्योपासकाः भवन्ति। अतः जीव परमेश्वरतः भिन्नः नित्यचेतनः भगवद्दासः[27] इति।

प्रकृतिः- सांख्यप्रसिद्धा सत्वरजस्तमसां साम्यावस्था प्रकृतिः एव अचिन्त्यभेदाभेदवादिभिः अङ्गीकृता। तथाहि अचार्यबलदेवैः प्रोक्तं स्वभाष्ये यत् प्रकृतिः सत्त्वादिगुणसाम्यावस्थातमोमाया-दिशब्दवाच्या तदीक्षणावाप्तसामर्थ्या अविद्यारूपा विचित्रजगज्जननी इति। तमोमयादिशब्दवाच्या प्रकृतिः ईश्वरस्य ईक्षणेन चेतनवती भूत्वा अखिलं जगत् ससर्ज। परन्तु सांख्यानामिव अचिन्त्यभेदाभेदमते प्रकृतिः स्वतन्त्रा चेतनवती न

भवति। परन्तु नित्या प्रकृतिः ईश्वराश्रिता ईश्वरवश्या भवति। प्रकृतिः ब्रह्मणः शक्तिः। अत्र बलदेवविद्याभूषणेन सांख्यमतानुसारं महत्तत्त्वमहङ्कारतत्त्वं स्वीक्रियते।[२९]

कालः- त्रैगुण्यशून्य जड ईश्वरस्य चेष्टाशक्तिविशेषः कालः। भूतभविष्यद्वर्तमानप्रभृतिशब्द-व्यवहारहेतुः। क्षणादिपरार्धान्तचक्रवत्परि-वर्तमानप्रलयसर्गनिमित्तभत-जड़द्रव्यविशेषस्य नाम काल इति। कालः नित्यः ईश्वराधीनः।[३०]

कर्म- कर्मणः लक्षणवर्णनप्रसङ्गे आचार्येण बलदेवेन प्रोक्तं यत् कर्म जडम् अदृष्टादिशब्दवाच्यं अनादि शब्द वाच्यम् नाश्यम् इति। कर्म परमेश्वरशक्तिभूतम्।[३१] तस्मात् एतानि एव जीवादिचत्वारिमुख्यतत्त्वानि परमेश्वरस्य शक्तिमत्त्वात् शक्तिमद्ब्रह्म इति अद्वैतवाक्ये अपि सङ्गतिः भवतीति श्रीपाद्बलदैवैः प्रोक्तम्। शक्तिमद्ब्रह्मप्रतिपादनमेव अचिन्त्यभेदाभेदवादस्य उद्देश्यम्। आचार्येण स्वमतेन साकम् शक्तिमद्ब्रह्म इत्युक्त्वा अद्वैतस्य समन्वयं साधितवान्। अतः आचार्येण सूचितं यत् शक्तिमद्ब्रह्म निरूपयितुम् आचार्यरूपा श्रुतिः आह- ईशेत्यादि। ईशवास्यमन्त्रस्य व्याख्यानात् पूर्वम् आचार्यश्रीपाद्बलदेवभूषणैः गदितं यत् आत्मयाथात्मप्रकाश-कत्वेन मन्त्राणां कार्यस्वविनियोगः परन्तु उपासनायां विनियोगः अविरोधात् इति। अत्र उपासना नाम तु **जीवपरयोः सम्बन्धविशेषसाधनं भजनमिति।** सम्बन्धो हि जीवे परसाम्मुख्यमिति। अत्रापि अचिन्त्यतत्त्वस्य प्रतिष्ठा कृता आचार्येण। यतो हि अचिन्त्यभेदाभेदवादमते तु भक्त्या एवं भगवत्प्रीतिः उत्पद्यते। तेन परतत्त्वेन सह साक्षात्कारो भवति। किञ्च आचार्यबलदेवविद्याभूषणः अचिन्त्यशक्तिं विशेषत्वेन वक्ति। तस्मात् एव प्रोक्तं टीकाकारैः सम्बन्धविशेषसाधनं भजनमिति।[३२] अपि च वैष्णवसम्प्रदाये भक्तिविशेष एव परमात्मनुशीलनं वा योग इति अभिधीयते। भक्तिरपि अचिन्त्यभेदाभेदसम्प्रदाये शक्तिविशेषः।[३३] जीवे परसाम्मुख्यम् इति कथनेन जीवात्मपरमात्मनोः भेदः कथितः। परन्तु भेदः चिन्तयितुम् अशक्यः चेदपि मुक्तावस्थायां भेदस्तु वर्तते। न चेत् परसाम्मुख्यमित्यस्य व्यर्थता स्यात्। अतः भक्तिलब्धाचिन्त्य-तत्त्वप्रतिपादनाय एव संक्षेपतः मन्त्रार्थान् व्याख्यास्यामि अयं भावः द्योत्यते।

उपसंहारः-श्रीपाद्बलदेवविद्याभूषणरचितैः ईशोपनिषद्भाष्यैः श्रीवैष्णवसम्प्रदायस्य श्रीचैतन्यमहाप्रभुकालतः यत् अचिन्त्यतत्त्वस्य प्रतिपादनं प्राचलत् तस्यैव परिपूर्णता स्थाप्यते। श्रीगौणीयचैतन्यसम्प्रदायिकाचार्यैः न स्वसम्प्रदायप्रतिपादनपरभाष्यं टीका ग्रन्थः चेति लिखिताः। अतः तत्कालस्थपण्डितैः श्रीचैतन्यसम्प्रदायस्य भिन्नस्तन्त्रसम्प्रदायकत्वेन अस्तित्वं नाङ्गीकृतम्। अतः श्रीपाद्बलदेवाचार्यः पञ्चमस्तन्त्रवैष्णवसम्प्रदायस्य प्रतिष्ठापनाय ब्रह्मसूत्रस्य उपनिषदः भाष्यं रचितवान्। ततः स्वकीयभाष्यबलादेव एव अचिन्त्यभेदाभेदतत्त्वं प्रतिष्ठाप्य भारतीयवैष्णवदर्शनेषु अन्यतमस्थानं प्रापितवान्। किञ्च अचिन्त्यसम्प्रदायस्य यद्यपि शङ्कराचार्यैः ईषोपनिषद्भाष्येण जगति यत् अद्वैततत्त्वं स्थापितं तथापि आचार्येण सुव्याख्याकौशलेन मनसि अचिन्त्यतत्त्वप्रतिपादनं मया करणीयम् इति विधाय भाष्यं लिखितम्। भाष्यं पर्यालोच्य अचिन्त्यभेदाभेद-तत्त्वप्रतिपादनशीलस्य आचार्यबलदेवस्य स्वसम्प्रदायात् किञ्चित् नावीन्यं प्रदर्शितं तद्दृश्यते।

व्याख्यातृणामनेकार्थत्वे चित्तविभ्रमदोषनिवारणम्-

व्याख्यायाः अनेकार्थत्वे भ्रमः इति चेत् न उपासकानां साधकानां अध्यात्माधिकारिणां वैचित्र्यात् उपास्यविषयस्य च दुर्विज्ञेयत्वात् च प्राचीनैः शास्त्रकारैः व्यवहारे नैके लक्ष्यप्राप्त्यनुमार्गाः प्रदर्शिताः। इदमुक्तम् अप्पय्यदीक्षितैः सिद्धान्तलेशसंग्रहग्रन्थे -

''प्राच्यैर्व्यवहारसिद्धविषयेष्वात्मैक्यसिद्धौ परं
सन्नह्याद्भिरनादरात् सरणयो नानाविधा दर्शिताः।।
तन्मूलानिह सङ्ग्रहेण कतिचित् सिद्धान्तभेदान् भिय-
श्शुद्धये सङ्कलयामि तातरणव्याख्यावत्रः ख्यापितान्।।इति।।''[३४]

अतः अत्र अध्यात्ममार्गे अकल्पितार्थवस्तुप्रतिपादनानुकूलतया कल्पिताः नानामार्गाः प्रदर्शिताः शास्त्र-व्याख्यातृभिः इति भूषणमेव न दूषणम्। अतः प्रकृतेः ब्रह्मसूत्रमाश्रित्य द्वैताद्वैतरूपमार्गभेदः साधकोपयोगितया नानाप्रकारैः उपदिष्टः।

भारतीयसंस्कृतिः अनेकेषु एकत्वं साधयितुमिच्छति। सनातनसंस्कृतवाङ्मये अनन्तशास्त्रम् अगणित-तद्भाष्यव्याख्यानानि विलसन्ति। तत्र सर्वेषां शास्त्राणां विषयः, साध्यं(उद्देश्यम्), अधिकारी इत्यादयः अर्थाः मिथो भिन्नाः। एवं सति शास्त्रेषु विषयाधिकारिमुखेन परस्परभेदः अस्ति चेदपि सर्वेषु शास्त्रेषु मध्ये किञ्चित् विलक्षणसमन्वयसूत्रं टीकाकृद्भिः सुकौशलं प्रकाशितम्। अस्माकं संस्कृतौ सर्वमपि शास्त्रमितरशास्त्र-सहकृतं सत् स्वलक्ष्यं साधयति। न किञ्चिद् शास्त्रे सर्वात्मना इतरशास्त्रासहकृतम् सत् श्रेष्ठत्वं साधयति इति न दृष्टम्। अतः शास्त्रव्याख्याकाराः स्वस्वटीकाटिप्पण्यादिषु तत्तच्छास्त्रस्य इतरशास्त्रोपेक्षितत्वं कस्मिन् प्रसङ्गे कथमस्ति इति सप्रमाणं प्रदर्शयन्ति। सर्वस्य पर्यालोचनेन अस्माभिः दृष्टं यत् विना ईशोनिषनिषद्भाष्ये यद् अचिन्त्यभेदाभेदतत्त्व-मालोचितम् आचार्यैः तत्तु यथार्थमेव यत्र न संशयः।

अन्तःटिप्पणी

१. श्रीरूपगोस्वामिकृतस्तवमालायां उत्कलिकावल्लरी नामकस्तवस्य स्तवमालाविभूषणनामटीकायाः उपसंहारे श्रीबलदैवैः लिखितं यत् षडशीत्युत्तरषोडशशतीगणिते तस्य (१६८६)शाके तु टीकायाः निष्पत्तिः इति (श्रीस्तवमाला श्रीबलदेवविरचितभाष्यसमेता, मुम्बई निर्णयसागरः १९०३ क्रीस्ताब्दे)

२. श्रीभक्तिविनोदठाकुरसम्पादिता श्रीसज्जनतोषणीपत्रिका सिद्धान्तरत्न(९म वर्षः, १०म संख्या, १३०८ वङ्गाब्दः)

३. श्रीसज्जनतोषणीपत्रिका, द्वितीयवर्षः१२९२ वङ्गाब्दः। श्रीरसिकानन्दमुरारिवेशोद्भवश्रीविश्वम्भरानन्द-गोस्वामि-रचित श्रीयुक्तबलदेवविद्याभूषणजीवनीशीर्षकप्रबन्धतः ज्ञायते।

४. अतर्कत्यसहस्रशक्ति-भाः ३/३३/३।

५. चैतन्यचरितामृतः-२५/८९/९८।

६. एकात्मवादस्य भगवदनभिमतत्वात्। यदुक्तं तृतीये भगवतैव-सारार्थदर्शिना ४/२८/६२।

७. स्वरूपादभिन्नत्वेन चिन्तयितुमशक्यत्वाद्भेदः, भिन्नत्वेन चिन्तयितुमशक्यत्वादभेदश्च प्रतीयते इति शक्तिशक्ति-मतोर्भेदाभेदावेवाङ्गीकृतौ, तौ च अचिन्त्यौ इति। स्वमते त्वचिन्त्यभेदाभेदावेव अचिन्त्यशक्ति-मयत्वादिति। (सर्वसम्वादिनी, वङ्गीयसाहित्यपरिषद् १३२७।

८. ब्रह्मसूत्रम् -२/१/२७।

९. ब्रह्मसूत्रम् -२/१/२७। भाष्यं द्रष्टव्यम्।

१०. अचिन्त्याः खलु ये भावाः न तांस्तर्केण योजयेत्। प्रकृतिभ्यः परं यत्तु तदचिन्त्यस्य लक्षणम्। मः भाः भीष्मपः ५ अः, १२।

११. श्रीविष्णुसहस्रनामस्तोत्रम् -शाङ्करभाष्योपेतम् (संस्कृत प्रेस् डिपोजिटरी, कलिकाताः, १९८५, १०२श्लोकः।

१२. श्रीविष्णुपुराणं-१/३।१२, आत्मप्रकाशटीका द्रष्टव्या

१३. निर्गुणस्याप्रमेयस्य शुद्धस्याप्यमलात्मनः। कर्थं सर्गादिकर्तृत्वं ब्रह्मणेष्युपगम्यते।। ऋक्षयः सर्वभावानाम-चिन्त्यज्ञानगोचराः। यतोतो ब्रह्मणस्तास्तु सर्गाद्या भावशक्तयः। भवन्ति तपतां श्रेष्ठ पावकस्य यथोष्णता।। इति।। विः पुः -१/३.१-२

१४. समाप्तिकामो मङ्गलमाचरेत्, इति श्रुतिः।

१५. अचिन्त्यः स आत्मा स विज्ञेयः -माण्डुक्योपनिषद्

१६. अचिन्त्याः खलु ये भावाः न तांस्तर्केण योजयेत्। प्रकृतिभ्यः परं खलु यत्तु तदचिन्त्यस्य लक्षणम्।। -मः भाः भीष्मः ५अः१२।

१७. श्रुतेस्तु शब्दमूलत्वात् -ब्र-२/१/२७।

१८. तस्य हरेस्तिस्रः शक्तयः सन्ति–पराख्या क्षेत्रज्ञाख्या मायाख्या चेति। परास्य शक्तिर्विविधैव श्रूयते, स्वभाविकी ज्ञानबलक्रिया च, प्रधानक्षेत्रज्ञपतिर्गुणेशः, संसारबद्धस्थितिः मोक्षहेतुः इति श्रुतेः। विष्णुशक्तिः परा प्रोक्ता क्षेत्रज्ञाख्या तथापरा। अविद्या कर्मसंज्ञान्या तृतीया शक्तिरिष्यते।।इति–श्रीविष्णुपुराणाच्च।

१९. स च पराख्याशक्तिमद्रूपेण जगन्निमित्तं क्षेत्रज्ञादिशक्तिमद्रूपेण तु तदुपादानञ्च भवति। तदात्मानं स्वयमकुरुत इत्यादि श्रवणात्। (वेदान्तस्यमन्तकः २/९–१०, श्रीश्यामलालगोस्वामि सं.।)

२०. तावदेकस्यैव तत्त्वस्य सच्चिदानन्दत्वाच्छक्तिरप्येका त्रिधा भिद्यते। तदुक्तं विष्णुपुराणे श्रीध्रुवेण ह्लादिनीसन्धिनी संवित्तय्येका सर्वसंस्थितौ। (श्रीभगवत्सन्दर्भः, १०२, अनु, २५०–५१ पृष्ठ सत्यानन्दः सं)

२१. तत्रैव त्रिवृत् परा कीर्त्यते। अत्र सम्वित्प्रधाना वृत्तिर्गर्दिवी, ह्लादप्रधाना तु लक्ष्मीः। इत्थञ्चास्या जीवकोटित्व निरस्तम्। (वेदान्तस्यमन्तकः २/२१)

२२. तस्या ह्लान्या एव कापि सर्वानन्दातिशायिनी वृत्तिर्नित्यं भक्तवृन्देष्व निक्षिप्यमाणा भगवत्प्रीत्याख्याया वर्तते। अतस्तदनुभवेन श्रीभगवानपि श्रीमद्भक्तेषु प्रीत्यतिशयं भजत इति। प्रीतिसन्दर्भः–६५ अनु

२३. भक्तिर्हि भक्तकोटिप्रविष्टतदार्द्रीभावयितृतच्छक्तिविशेषः (श्रीभक्तिसन्दर्भः, श्रीगौडीयमठ सं, १८० अनु.२०२ पृष्ठ)

२४. पुरुषोत्तमसाक्षात्कार, तथा परस्परहर्षातिशयः प्रयोजनम् –गोः भाः, १.१ उपक्रमः।

२५. श्रीकृष्णप्रेमलक्षणप्रयोजनम्–तत्त्व सः। अनु।

२६. कर्मणो निखलपुमर्थहेतुत्वम्। सगदिः कर्मफलस्य नित्यत्वम् इति बलदेवभाष्यम्।

२७. प्रकृतेश्च स्वतः कर्तृत्वम्–इति बलदेवभाष्यम्।

२८. परिच्छिन्नस्य प्रतिबिम्बितस्य भ्रान्तस्य वा ब्रह्मण एव जीवत्वं चिन्मात्रब्रह्मात्मकत्वधीमात्रादेवास्य–इति बलदेवभाष्यम्।

२९. विष्णुरेव ब्रह्मशब्दवाच्यं–सू भा: १/१/१।

३०. श्री गोविन्दभाष्यस्य प्रारम्भः, श्रीगीताभूषणभाष्यस्य प्रारम्भः द्रष्टव्यः।

३१. श्रीव्यासतीर्थकृतन्यायमृतम् –२ अवच्छेदः, विशेषसमर्थननामकं षोडशप्रकरणं द्रष्टव्यम्।

३२. सिद्धान्तरत्नम् द्रष्टव्यम् –१.१७–१९ (श्रीश्यामलालगोस्वामी सं.)

३३ श्रीगोविन्दभाष्यम् –१/१/१।

३४. सिद्धान्तलेषसंग्रहः –६.२८।

संदर्भ सूची

१. अप्पय्यदीक्षितः। सिद्धान्तलेशसंग्रहः। संपादकः–वारसनाथद्विवेदी। वाराणसी। सम्पूर्णानन्दसंस्कृत–विश्वविद्यालयः। २००५ खिष्टब्दः। मुद्रितम्।

२. ईशाद्यष्टोत्तरशतोपनिषद्। संपादकः–वासुदेवशर्मा। वाराणसी। चौखम्बा विद्याभवनम्। १९९५ खिष्टब्दः। मुद्रितम्।

३. गोस्वामिप्रभुपादलीलभक्तिसिद्धान्तसरस्वती। गौढीयदर्शनम्। संपादकः–गौढीयमिशन्। कलकाता। वागबाजार। २०१५ खिष्टब्दः। मुद्रितम्।

४. प्रमेयरत्नावली। संपादकः–श्रीमद् अक्षयकुमारशर्मा। कलिकाता। १९२७ खिष्टब्दः। मुद्रितम्।

५. वेदान्तसूत्रम्। संपादकः–त्रिदण्डिस्वामी। कलिकाता। संस्कृतपुस्तकभण्डारः। १९६७ खिष्टब्दः। मुद्रितम्।

६. वेदान्तदर्शन(ब्रह्मसूत्रम्)। संपादकः–श्रीश्यामदासः। वृन्दावनम्। व्रजगौरव प्रकाशनम्। २००३ खिष्टब्दः। मुद्रितम्।

७. सिद्धान्तदर्पणः। संपादकः–श्रीहरिदासः। नवद्वीपः। हरिबलकुटीरः। ४५७ गौराब्दः। मुद्रितम्।

८. स्वामीशिवानन्दसरस्वती। ईशोपनिषद्। संपादकः–स्वामी सत्यव्रतानन्दसरस्वती। कलिकाता। उमाचल् प्रकाशनी। १३९२ बङ्गाब्दः(प्रथमप्रकाशनम्)। मुद्रितम्।

९. श्रीमत्सुन्दरानन्दविद्याविनोदः। अचिन्त्यभेदाभेदवादः। संपादकः–सुन्दरानन्दविद्याविनोदः। कलिकाता। गौढीयमिशन्। १९९१ खिष्टब्दः। मुद्रितम्।

Materials Chemistry and Physics 313 (2024) 128765

Contents lists available at ScienceDirect

Materials Chemistry and Physics

journal homepage: www.elsevier.com/locate/matchemphys

Study of magnetic induction heating of $Li_{0.25}Zn_{0.3}Co_{0.15}Fe_{2.3}O$ nanoparticles

Madhumita Dalal [a,d,*], Jean-Marc Greneche [b], Raghumani S. Ningthoujam [c], Pabitra K. Chakrabarti [a,**]

[a] Solid State Research Laboratory, Department of Physics, Burdwan University, Burdwan, 713 104, West Bengal, India
[b] Institut des Molécules et Matériaux du Mans, IMMM UMR CNRS 6283, Le Mans Université, 72085, Le Mans Cedex 9, France
[c] Chemistry Division, Bhabha Atomic Research Centre, Mumbai, 400085, India
[d] Department of Physics, Bejoy Narayan Mahavidyalaya, Itachuna, Hooghly, West Bengal, - 712147, India

HIGHLIGHTS

- Nanoparticles (size ~ 6 nm) of $Li_{0.25}Zn_{0.3}Co_{0.15}Fe_{2.3}O_4$ are prepared by sol gel method in a pure phase.
- Presence of superparamagnetic nanoparticles is confirmed in smaller nanoparticles (size ~ 6 - 12 nm).
- High saturation magnetization with enhanced anisotropy is observed.
- Nanoparticles exhibit significant magnetic induction heating efficiency.
- Hyperthermia temperature is reached within a short interval (~6 min) of switching the external ac magnetic field.

GRAPHICAL ABSTRACT

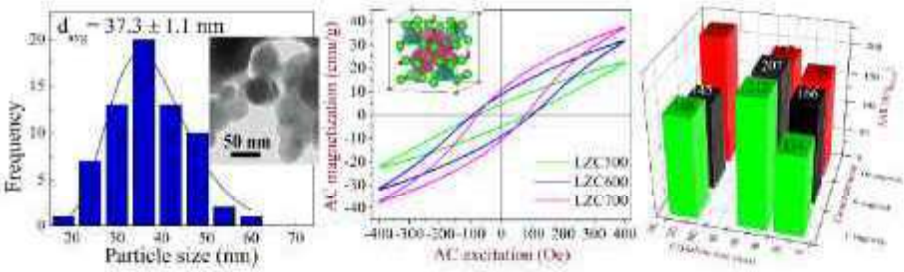

ARTICLE INFO

Keywords:
X-ray diffraction
Electron microscopy
Magnetic properties
Ferrites
Magnetic induction heating

ABSTRACT

Five different batches of $Li_{0.25}Zn_{0.3}Co_{0.15}Fe_{2.3}O_4$ (LZC) nanoparticles were prepared by sol-gel method. Of these five batches, one has a very small mean size of ~6.0 nm and the others have mean sizes of ~11.9, 47.3, 114 and 139 nm. The phase formation of the nanoparticles is confirmed by analysing the X-ray diffraction (XRD) patterns using the Rietveld method. To ensure phase formation, further structural analyses, namely transmission electron microscopy, Raman spectroscopy and x-ray photoemission spectroscopy measurements are performed. Before analysing the magnetic properties of the prepared nanoparticles, Mössbauer spectra are recorded both at room temperature and at 77 K to determine the magnetic nature and hyperfine behaviour of the nanoparticles. The resence of magnetically blocked states is estimated by recording the dynamic hysteresis loops and then to gain insight into the magnetic properties of this particular Li-Zn-Co-ferrite stoichiometry, static M – H loops and field cooled and zero field cooled M-T curves are extracted using a vibrating sample magnetometer. Finally, the applicability of prepared nanoparticles as a heat mediator in magnetic induction heating is studied in an external field of 335 Oe intensity and 290 kHz frequency. The highest specific absorption rate (SAR) is found to be ~212 $W/g_{Ferrite}$ for 47.3 nm nanoparticles at a concentration of only 1 mg/mL.

* Corresponding author. Solid State Research Laboratory, Department of Physics, Burdwan University, Burdwan, 713 104, West Bengal, India.
** Corresponding author.
E-mail addresses: madhumita@bnmv.ac.in (M. Dalal), pkchakrabarti@phys.buruniv.ac.in (P.K. Chakrabarti).

https://doi.org/10.1016/j.matchemphys.2023.128765
Received 9 July 2023; Received in revised form 16 November 2023; Accepted 1 December 2023

1. Introduction

Iron oxides have proved to be potential candidates in various emerging fields of nanomaterials for decades. This group of magnetic nanoparticles, namely Fe_3O_4 and MFe_2O_4 (where M = Zn, Mn, Co, Ni, Li or combination of these) is applicable in a wide area of research which includes biomedical applications, targeted drug delivery, magnetic induction heating (MIH), anode material in lithium-ion and sodium-ion batteries, arsenic removal, antibacterial activities, microwave absorption efficiency and many others [1–8]. In order to improve the properties of these nanomaterials, modification of existing synthesis procedures or sometimes new preparation methodologies are introduced [9–12]. Various well-known methods to prepare nanoparticles include co-precipitation, sol-gel, hydrothermal, ball milling, etc. In choosing a preparation technique, emphasis should be placed on the uniformity of the prepared nanoparticles and a cost effective way to prepare them. Among various preparation techniques, sol-gel method with its other inherent advantages serves all the requirements to prepare nanoparticles in a large scale within a very short period of time. In addition, the sol-gel method is cost effective compared with the hydrothermal method. Moreover, biocompatible organic molecules viz., citric acid are used in the sol-gel method by forming a coating on the nanoparticles and limits the unnecessary growth of the nanoparticles and makes them suitable for biomedical applications by forming a carboxylate group with the Fe−OH molecules present on the nanoparticle surface [13]. Not only the alteration in preparation techniques but also the variation of cations and their proportion in MFe_2O_4 can modify the magnetic properties as well as the magnetic anisotropy of this group of nanomaterials [14–17]. Specifically, when Zn atoms replace a part of Fe in tetrahedral A-site of $(FeO)_A[Fe_2O_3]_B$, enhanced magnetization is observed due to reduction of the antiferromagnetically coupled Fe_A^{3+} by Zn^{2+} doping (20%) while Co is known to enhance the magnetic anisotropy of the system [18,19]. For example, when Zn is introduced in $LiFe_2O_4$, which already has high saturation magnetization, high permeability, high Curie temperature (T_c), magnetization is further improved [20] and the introduction of Co ensures enhancement of anisotropy. Hence the choice of Li, Zn and Co cations could be considered to have improved magnetic properties which are suitable for MIH applications. Moreover, when the size of MFe_2O_4 nanoparticles, which has a spinel structure, is controlled below a certain limit, a very interesting magnetic behaviour is observed, known as superparamagnetism. Superparamagnetic (SPM) nanoparticles are important because these have a high saturation magnetization (M_s) with negligible coercivity (H_c). When SPM nanoparticles are subjected to a low frequency external magnetic field, they undergo Brownian or Néel spin relaxations. Brownian relaxation is the rotation of magnetic nanoparticles caused by Brownian motion and in case of Néel spin relaxation, the magnetic moments flip from one easy axis to another. However, in both cases heat is generated and can be used in many applications, including domestic cooking appliances [21]. One such recent applications of MIH is magnetic fluid hyperthermia (MFH) treatment, where a ferrofluid is used as a heat mediator in a low-frequency ac magnetic field [22–24]. MIH is also used in magnetic induction swing adsorption (MISA) process to control greenhouse gas emissions from industries and power plants [25,26]. Magnetic nanoparticles with enhanced heating capacity and high Tc are used as a susceptor additive for processing thermoplastic and thermoset polymer materials [27]. MIH is sometimes involved in the synthesis process of nanostructures and heat assisted catalytic reactions [28–31]. The main parameter determining the suitability of a material in MIH applications is its specific absorption rate (SAR), defined as the energy amount converted into heat per unit time per unit mass. The SARs of some spinel ferrites, MFe_2O_4 (M = Co, Mn, Li, etc.) are already reported viz., SAR of $MnFe_2O_4$ is 112.18 W/g at a field of 90 Oe and 70 kHz, SAR of cobalt ferrite nanoparticles is 133 W/g at field of 510 Oe and 101 kHz [24,32,33]. Earlier, we have reported SAR of two compositions of Li-Zn-Co ferrite, where we have obtained a maximum SAR of 166 $W/g_{Ferrite}$ for the composition $Li_{0.35}Zn_{0.30}Co_{0.05}Fe_{2.3}O_4$ (1 mg/mL) at a field of 335 Oe and 290 kHz [34] and 379 $W/g_{Ferrite}$ for the composition $Li_{0.30}Zn_{0.30}Co_{0.10}Fe_{2.3}O_4$ (2 mg/mL) at a field of 420 Oe and 300 kHz [35]. It is investigated that SAR increases when the percentage of Co is increased but this percentage could not be increased indefinitely because Co adds toxicity to the prepared nanoparticles and it should be maintained below 5% [36]. Otherwise, lithium ferrite and zinc ferrite are non-toxic [37,38], so lithium zinc cobalt ferrite with a cobalt percentage below 5 % could be considered non-toxic and can be used in biomedical applications also.

In this paper, the MIH efficiency of $Li_{0.25}Zn_{0.3}Co_{0.15}Fe_{2.3}O_4$ (LZC) nanoparticles is discussed and how the size of the nanoparticles alters this efficiency is also analysed. Before discussing MIH, phase formation of the prepared samples is analysed. For this purpose, X-ray diffraction (XRD) patterns are analysed using the Rietveld method and various structural parameters are derived from this analysis. Information from transmission electron microscopy (TEM) and Raman spectroscopy is extracted to support the structural verifications. Mössbauer spectra are recorded to determine whether the nanoparticles are in magnetically blocked or relaxed state. The amount of magnetization and the anisotropy constants are calculated from the M − H loops recorded at various temperatures including room temperature (RT).

2. Experimental details

2.1. Nanoparticles synthesis

Nanoparticles of $Li_{0.25}Zn_{0.3}Co_{0.15}Fe_{2.3}O_4$ are prepared by sol-gel method. High purity nitrate powders of $LiNO_3$ (SRL, 99%), Zn $(NO_3)_2{\cdot}6H_2O$ (Merck, Germany, 99.5%), $Co(NO_3)_2{\cdot}6H_2O$ (Merck, Germany, 98%) and $Fe(NO_3)_3{\cdot}9H_2O$ (Merck, Germany, 98%), are taken as precursor materials. Required nitrate salts are taken in proper stoichiometric ratio and a clear aqueous solution is prepared in a beaker at RT using a magnetic stirrer. In another beaker, aqueous solution of equimolar citric acid is prepared at RT using the magnetic stirrer and this solution is then added slowly to the nitrate solution under vigorous stirring. Stirring is continued for ~14 h at 80 °C until gel is formed and upon gel formation, beaker is transferred soon to a furnace and kept there for ~4 h where temperature is maintained at 100 °C. By this, porous chunks of the sample are formed which is further heated at 200 °C for removal of additional nitrates. Finally, the chunks are mortered to get powdered samples and labeled as LZC200. Then it is annealed at 500, 600, 700 and 800 °C for 5 h each in air atmosphere and the corresponding samples are labeled as LZC500, LZC600, LZC700 and LZC800, respectively.

2.2. Characterization techniques

XRD patterns are recorded by a powder X-ray diffractometer, Model BRUKER D8 Advance with da Vinci, using CuKα radiation (λ = 1.5405 Å). XRD patterns are analysed by the Rietveld method using the MAUD program. A high resolution transmission electron microscope, FEI, Tecnai G^2 F30-ST, operating at 300 kV is used to record the micrographs and the selected area diffraction (SAED) pattern of the samples. The same microscope equipped with a scanning unit, a high-angle annular dark field (HAADF) detector for scanning transmission electron microscopy (STEM-HAADF) and energy dispersive X-ray spectroscopy (EDX), is used to perform elemental analyses. The Raman spectrum of the sample, LZC200, is recorded in HORIBA using a Nd:YAG laser of an excitation wavelength of 532 nm and power of 4 mW. The X-ray photoemission spectroscopy (XPS) measurements are carried out using an Omicron electron spectrometer, equipped with a Scienta omicron sphera analyzer and Al Kα monochromatic source with an energy resolution of 0.5 eV. Mössbauer spectra of samples, LZC200, LZC500 and LZC700 are recorded at two different temperatures using a bath cryostat in a transmission mode with a constant acceleration driving unit using a

^{57}Co/Rh γ-beam source. A standard Fe foil is used to calibrate the spectrometer and the isomer shift (IS) values are given relative to that of the standard Fe foil at 300 K. Dynamic magnetic loops are recorded at 300 K using a digital hysteresis loop tracer supplied by Metis Instruments and Equipments NV, Belgium at a frequency of 50 Hz. The static hysteresis loops of the samples, LZC200 and LZC800 are recorded using a vibrating sample magnetometer (VSM) at a maximum applied field of 5 T. Finally, the MIH is performed using Faraday Power Systems where a 1.5 mL microcentrifuge tube is kept at the centre of the coil having 5 cm diameter with 4 turns without touching the coil. 1, 5 and 10 mg of the samples were suspended in 1 mL of deionized water which was then heated using a magnetic field of 335 Oe and 290 kHz frequency. The rise in temperature is recorded using an optical temperature sensor (model: Photon ControlPalmSense2) with accuracy of ±0.01 °C.

3. Results and discussion

3.1. Structural and microstructure properties

3.1.1. XRD and Rietveld analysis

The structural and microstructure properties of the samples are investigated by analysing the XRD patterns using Rietveld method and the MAUD fitted patterns are shown in Fig. 1. Crystallographic peaks are appeared at $2\theta \cong 30.15°$, 35.49°, 37.16°, 43.16°, 53.38°, 57.06°, 62.59°, 71.32° and 73.95° which correspond to the Fd $\bar{3}$ m cubic phase of Li-Zn ferrite as mentioned in JCPDS file no. 71-1268. In addition to these distinct peaks of spinel ferrite, a small peak attributed to rhombohedral (R $\bar{3}$ c) α-Fe_2O_3 hematite (JCPDS file no. 89-0599) appears at $2\theta \cong 33.16°$ in all samples except LZC200. This small peak points to the segregation of α-Fe_2O_3 phase which is a very common occurrence during the combustion of iron oxides in air [39,40]. However, the small percentage of this impurity phase can be neglected in the present study. Structural and microstructural parameters derived from Rietveld analysis are presented in Table 1. A shrinkage of the lattice structure is noticed with increasing annealing temperature i.e., the lattice parameter of the sample, LZC200 is 8.3912 (±0.0009) Å, that of LZC500 is 8.3829 (±0.0004) Å and those of the rest are 8.3800 (±0.0002) Å. This shrinkage may be due to the possible presence or formation of Fe^{2+} at lower temperatures which decreases with increasing annealing temperature [41]. In addition, lattice strain becomes negligible with the formation of larger crystallites at higher annealing temperatures. The smallest crystallite size (d_{cryst}) among the prepared samples is 8.7 (±0.1) nm which would be very interesting to manifest the SPM behaviour. Crystallite sizes are calculated using Williamson-Hall method [42–44] also to remove the effect of strain and the calculated values of d_{cryst} are 6.0 (±1.2), 11.9 (±1.8), 47.3 (±10.0), 114 (±18) and 139 (±37) nm for samples, LZC200, LZC500, LZC600, LZC700 and LZC800, respectively. The values of d_{cryst} derived from the Rietveld analysis are in agreement with those calculated using Williamson-Hall equation. In spinel ferrites, distribution of cations in tetrahedral (A) and octahedral (B) sites plays an important role in determining the magnetism of the samples. Rietveld analysis in this direction reveals that the occupancy of Zn^{2+} ions in A-site increases with the increase of d_{cryst} (Table 1) which confirms the behaviour of Zn^{2+} ions when approaching nanoscale [45]. However, Li^{1+} and Co^{2+} ions with comparatively larger ionic radii (0.68 and 0.75 Å, respectively) occupy B-site [46,47] because the void of site B (0.81 Å) is larger than that of A-site (0.52 Å). A better fitting (GOF ~ 1) is achieved with this distribution of cations only and with this arrangement of cations, theu-parameter remains almost constant at a value of ~0.370 in all samples.

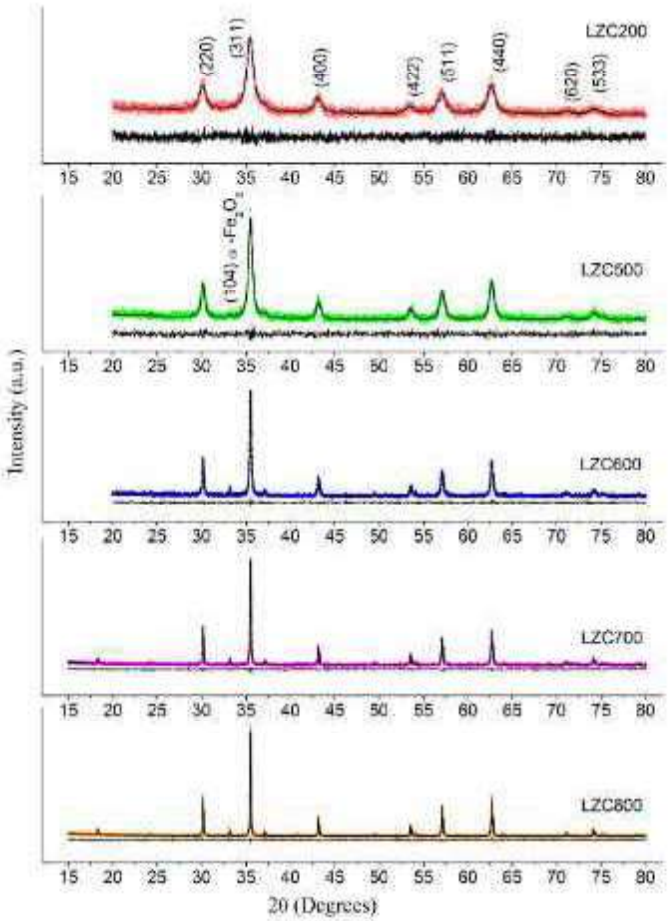

Fig. 1. Experimental XRD patterns and MAUD fitted spectra (dark lines).

3.1.2. TEM analysis

Particle size distribution of four samples, LZC200, LZC500, LZC600 and LZC700 are displayed in Fig. 2 where the corresponding TEM micrographs are shown in inset of the figures. Nanoparticles are mainly spherical in shape and, due to their magnetic attraction properties, they are highly agglomerated. Nanoparticles have a lognormal size distribution (shown by solid lines in Fig. 2) with an average diameter (d_{avg}) of ~10.2 (±0.2), 20.0 (±5.9), 37.2 (±1.1) and 75 (±1.0) nm, respectively which are in agreement with the values of d_{cryst} as derived from the Rietveld analysis (8.7, 15.0, 58.5, 110 nm) or the Williamson-Hall equation (6.0, 11.9, 47.3, 114 nm). Such a fair agreement indicates that the nanoparticles appeared in micrographs are in fact the nanocrystallites of the corresponding samples. Appearance of concentric rings in the SAED pattern indicates that the samples are polycrystalline in nature and that the different diameters correspond to different crystallographic planes. These crystallographic planes are marked in Fig. 3a: they correspond exactly to the crystallographic planes mentioned in the XRD patterns (Fig. 1). This confirms the spinel ferrite phase formation in

Table 1
Results of Rietveld analysis.

Sample	LZC200	LZC500	LZC600	LZC700	LZC800
GOF	1.00	1.01	1.01	1.05	1.05
R_{wp}	9.45	9.56	9.50	10.07	10.04
R_{exp}	9.43	9.43	9.44	9.56	9.57
R_{Bragg}	7.51	7.57	7.43	7.85	7.89
Lattice parameter (Å)(error)	8.391 (0.0009)	8.383 (0.0004)	8.380 (0.0002)	8.380 (0.0001)	8.380 (0.0001)
r.m.s. lattice strain	1.42×10^{-2}	1.27×10^{-2}	5.98×10^{-4}	2.11×10^{-4}	6.54×10^{-5}
Crystallite size (nm)	8.7 ± 0.1	15.0 ± 0.2	58.5 ± 1.1	110 ± 2	212 ± 6
Zn occupancy in A-site	0.11	0.19	0.18	0.26	0.27
u-parameter	0.370	0.370	0.371	0.369	0.368

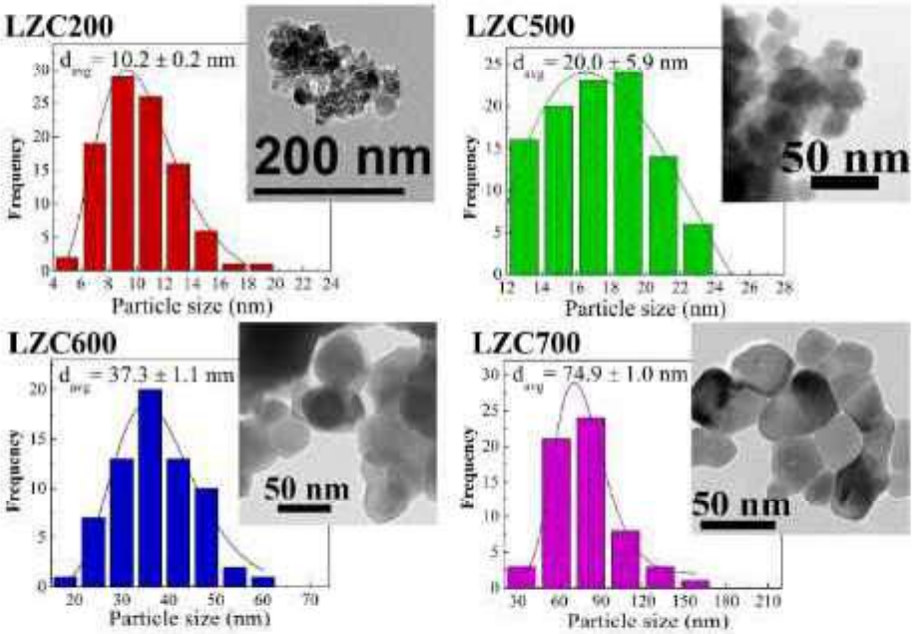

Fig. 2. Particle size histogram alongwith lognormal fitting; Inset: Low magnification TEM images.

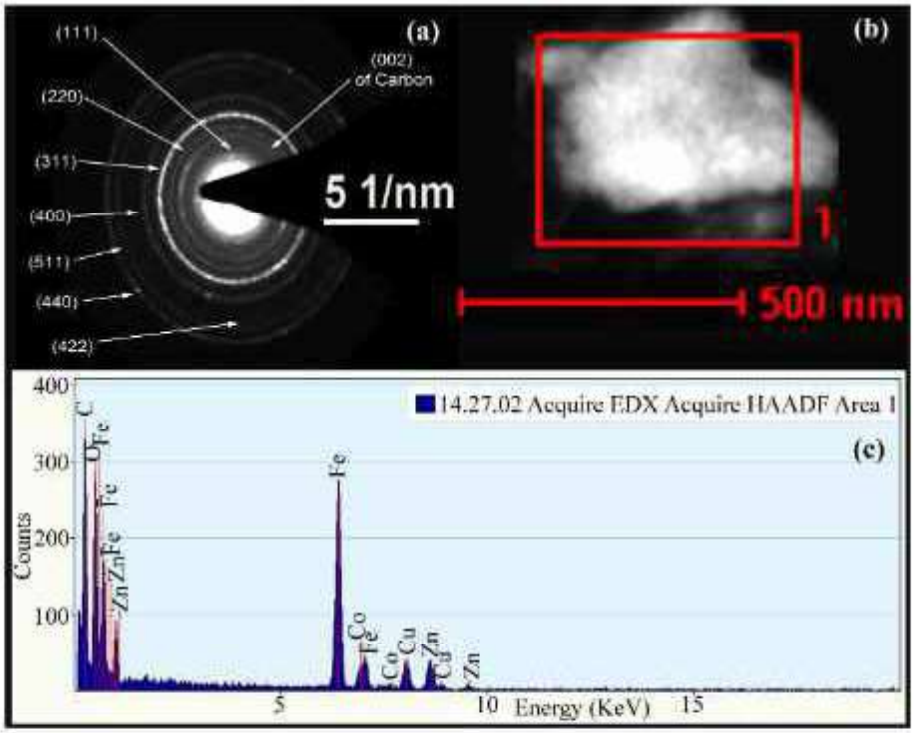

Fig. 3. (a) SAED pattern, (b) STEM-HAADF image, (c) EDX spectrum from area 1 in (b) of sample LZC200.

the prepared nanoparticles.

STEM-HAADF-EDX analysis is performed on one area of the sample, LZC200 (Fig. 3b) to determine the chemical compositions of the sample and the result is displayed in Fig. 3c. Elemental analysis confirms the presence of Fe, Zn, Co and O, but no trace of Li is detected because it is a light element and cannot be easily evidenced by EDX analysis [48]. Additional peaks of C and Cu come from the grid as a C-coated Cu grid used in this study.

3.1.3. Raman analysis

Another reliable method for structural verification is Raman spectroscopy. Spinel ferrites are characterized by five Raman active modes in the 200–800 cm^{-1} wave number range: they are generally denoted as A_{1g}, E_g, T^1_{1g}, T^2_{2g} and T^2_{1g}. Among these five modes, the A_{1g} mode has the highest frequency and the T^1_{2g} mode has the lowest frequency. However, all these Raman active vibration modes are associated with specific atomic motions. Atomic structure of the sample, LZC200, as derived from the Rietveld analysis, is presented in Fig. 4a where the A- and B-sites are shown distinctly. The primitive cell of spinel ferrite is composed

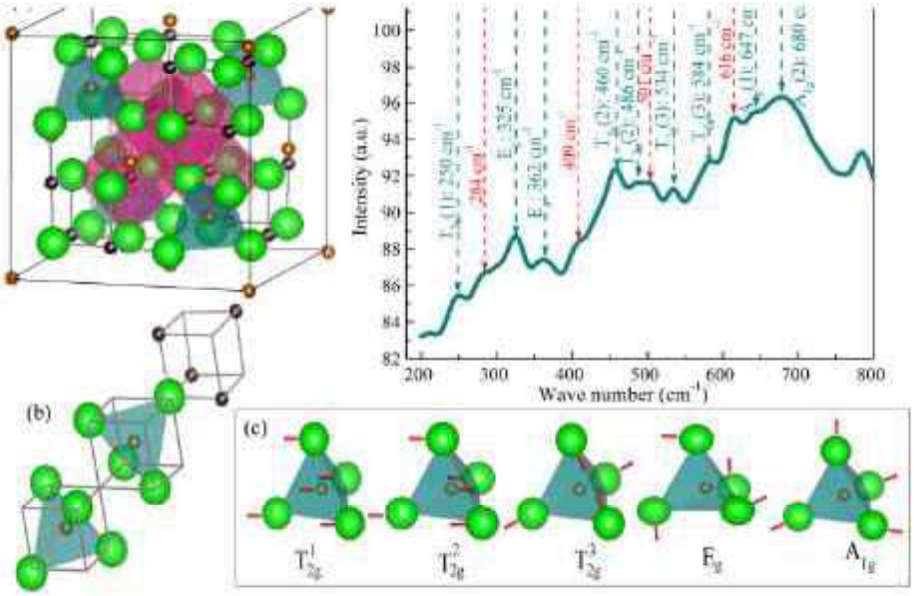

Fig. 4. Sample: LZC200 (a) Atomic structure; (b) Primitive cell; (c) Normal vibrations of the Raman active modes; (d) Raman spectrum.

of two AO_4 tetrahedral units and one B_4 unit as shown in Fig. 4b and contains fourteen atoms. Each O- anion is bonded to three octahedral (B) cations and a single tetrahedral (A) cation. The B- cations are most often considered to be at rest and the vibrational modes are assigned only to movements involving the AO_4 units. However, at higher frequencies the vibrational modes strongly depend on the nature of the B- cations. Origin of these five Raman active modes is explained in Fig. 4c. The T_{2g}^1 mode is assigned to the complete translation of the AO_4 unit; the T_{2g}^2 mode is assigned to the translation along one direction of the lattice where the cation and the O- anions move in opposite directions; the T_{2g}^3 mode is assigned to the asymmetric breathing mode of the AO_4 unit, or to an asymmetric bending of the O- anions bonded to the A-cation; the E_g mode is assigned to the symmetric bending of the O- anions in the AO_4 unit; the A_{1g} mode is assigned to the symmetric breathing mode of the AO_4 unit where the O- anions move away from the A-cation along the directions of the bonds [49]. In normal spinel ferrite (e.g., $ZnFe_2O_4$), the A-site is occupied by M^{2+} ions and the B- site is occupied by Fe^{3+} ions. There is only one type of cation at the A-site and another different but unique type of cation at the B- site. In this normal spinel ferrite only five Raman active modes are generally observed [50]. In inverse spinel ferrite (e.g., $NiFe_2O_4$), the A-site is occupied by Fe^{3+} ions and the B-site is equally shared by M^{2+} and Fe^{3+} ions. Due to this change in the octahedral environment, a splitting of the high frequency vibrational modes is observed [51]. There is also another type of spinel ferrite, called mixed ferrite, which has some degree of inversion. Depending on the nature of cations and the degree of inversion, more than five active Raman modes are visible in some cases [52]. The Raman spectrum of the sample, LZC200 is shown in Fig. 4d where the vibrational modes are assigned accordingly. All modes are split except for the lowest frequency T_{2g}^1 mode. These splittings could be attributed to the distribution of cations at the A- and B- sites as discussed in the Rietveld analysis. Four additional peaks appear at 284, 409, 501 and 616 cm^{-1} (marked by red color in Fig. 4d) which could be assigned to the Raman modes of α-Fe_2O_3 [53]. Thus, the presence of the α-Fe_2O_3 phase in the LZC200 sample is indicated by the Raman analysis which is not derivable from the XRD patterns; however, the peak of α-Fe_2O_3 is seen in the XRD patterns of all other samples annealed at higher temperatures (Fig. 1).

3.1.4. XPS analysis

For further verification of the compositional analysis and to get the trace of Li, an XPS analysis of the sample LZC200 was performed. Fig. 5a shows that the binding energy related to Li 1s is 55.9 eV which agrees the earlier reported value [54] and establishes the presence of Li in the prepared sample. The Zn $2p_{3/2}$ and $2p_{1/2}$ peaks are centred at 1021.4 and 1044.6 eV, respectively (Fig. 5b) which is consistent with the earlier results of Zn ferrite [55]. The spectrum of Co 2p (Fig. 5c) shows two spin-orbit doublets characteristics of Co $2p_{3/2}$ and Co $2p_{1/2}$ and two satellite peaks [56]. The peaks at 782.4 and 796.3 eV correspond to the Co $2p_{3/2}$ and Co $2p_{1/2}$ for Co^{2+} state confirming that the valence state of Co is 2 [57]. The two peaks at 710.8 and 725.1 eV (Fig. 5d) represent the Fe $2p_{3/2}$ and Fe $2p_{1/2}$ for the Fe^{3+} state confirming the valence state of Fe to be 3. The O 1s spectrum shows two peaks located at 529.8 and 531.2 eV which can be assigned to lattice oxygens and native defects of O^{2-} vacancies [55].

3.2. Hyperfine behaviour

A selection of the ^{57}Fe Mössbauer spectra obtained at 77 and 300 K for different samples is presented in Fig. 6. Their hyperfine structures consist of magnetic sextets with broad and asymmetrical lines and a central quadrupolar doublet for some of them. They are examined by fitting the Mössbauer spectra with the MOSFIT program where the magnetic and/or quadrupolar components are described by elementary sextets and/or doublets composed of Lorentzian lines while the refined values of the hyperfine parameters are listed in Table 2. It is important to note that first of all the presence of these sextets or doublets is related to the measurement time (τ_0) window of ^{57}Fe Mössbauer spectrometry and the SPM relaxation time (τ) of the nanoparticles. τ_0 is governed by the Larmor precession time of the ^{57}Fe nucleus which is about 10 ns and $\tau = \tau_0 \cdot \exp\left(\frac{KV}{k_B T}\right)$ [58]. When τ is less than τ_0, the magnetic moments flip randomly from one easy axis to another producing a zero time averaged hyperfine field at the nuclear site and consequently, a doublet or a singlet appears depending on whether the electric field gradient is present at the ^{57}Fe nuclear site or not. When τ is greater than τ_0, sextet pattern appears due to the Zeeman splitting of the ^{57}Fe nucleus in presence of an internal magnetic field. But usually, it remains a very delicate task to prepare nanoparticles of uniform size and shape, and most of the time there is a particle size distributionwhile their shape is not homogeneous (Fig. 2). If there are particles whose sizes are distributed in such a way that both of the above conditions are satisfied, then a mixture of quadrupolar doublet and magnetic sextet pattern is

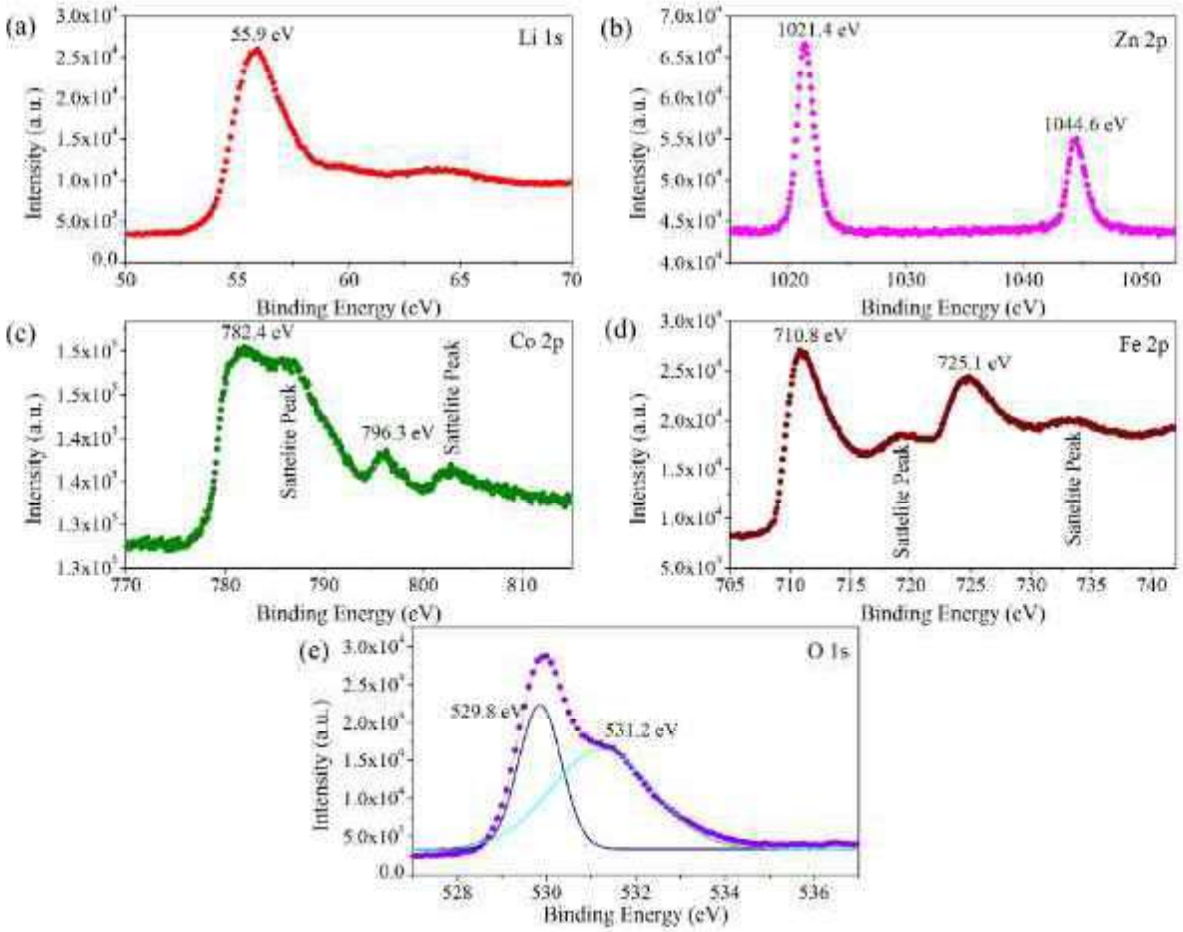

Fig. 5. XPS spectra of LZC200 sample.

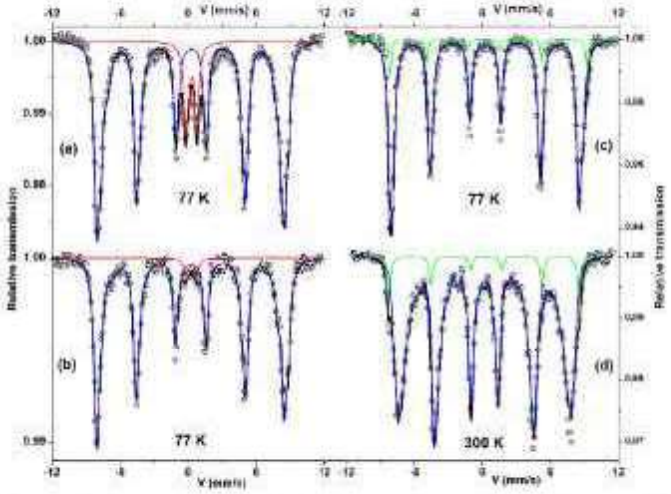

Fig. 6. Mössbauer spectra of (a) LZC200 recorded at 77 K; (b) LZC500 recorded at 77 K; (c) LZC700 recorded at 77 K; (d) LZC700 recorded at 300 K.

found which is called relaxation sextet [59,60]. The Mössbauer spectra of the LZC200, LZC500 and LZC700 samples (Fig. 6) exhibit complex hyperfine structures but the values of isomer shift are unambiguously consistent with the presence of only one valency state, i.e. only Fe^{3+} species: in addition, the values are in agreement with previous results on Li-Zn-Co-ferrites [50–61]. At 77 K, the magnetic component of the spectrum of the sample LZC200, can be well described with at least five components, suggesting the presence of nanoparticles with different sizes, while the quadrupolar doublet (relative area RA of 12%) can be attributed to ultrafine nanoparticles with ultrafast SPM relaxation phenomena [62]. This indicates that LZC200 nanoparticles with a very small $<d_{cryst}>$ ~6 nm but having a distribution of size are likely to be in SPM state at RT (consistent with the hyperfine structure composed of a quadrupolar doublet (35%) and a magnetic hyperfine field (34.6 T; 65%) not shown here). The 77 K spectrum of the LZC500 sample is described by the same fitting model but the proportion of quadrupolar doublet reduces to about 3% while the 300 K spectrum results in a magnetic sextet with strongly broadened lines and a small quadrupolar doublet (not shown here). These results are consistent with an increasing size of the nanoparticles (d_{cryst} ~ 12 nm). The spectrum of the sample,

Table 2
Refined values of hyperfine parameters extracted from the Mössbauer spectra of the samples.

Sample	T (K)	IS (mm/s) ± 0.02	QS or 2ε (mm/s) ± 0.02	B_{hf} (T) ± 0.5	RA (%) ± 2
LZC200	77	<0.46>	<0.01>	<49.9>	86
		0.47	0.90		12
LZC500	77	<0.45>	<0.03>	<50.4>	97
		0.47	0.90		3
LZC700	77	0.43	−0.01	51.3	92
		0.50	0.40	53.8	8
	300	0.31	−0.00	45.5	92
		0.37	−0.23	51.6	8

LZC700 recorded at 77 K is fitted with two distinct magnetic sextets: the larger one is clearly attributed to the magnetically blocked state of the larger ferrite nanoparticles ($d_{cryst.}$ ~ 115 nm) while the smaller one is unambiguously attributed to the presence of hematite (α-Fe_2O_3) with a well crystallize state, according to the present parameters. At 300 K, the spectrum of sample LZC700 is also fitted with two distinct sextets but now the relaxation phenomena are present in the spectrum, suggesting the presence of a small fraction of SPM nanoparticles in this sample. Thus the «Mössbauer blocking temperature » could be considered as well above RT. Finally, the second minor magnetic component (green component in Fig. 6 c, d) is unambiguously due to the presence of α-Fe_2O_3 phase, in agreement with the 77 K spectrum and X-ray diffraction results, as mentioned above: this phase resulting from the thermal treatment could be neglected when considering the magnetic and MIH properties of this sample.

3.3. Magnetic analysis

3.3.1. Dynamic magnetic behaviour

For a preliminary study of the magnetic properties of the prepared samples, dynamic hysteresis loops (Fig. 7a) are recorded at RT for a maximum applied field of ~400 Oe at 50 Hz. None of the loops are saturated at this low value of external field but a trend towards increasing maximum magnetization (B_m) is noticed with increasing $<d_{cryst}>$. The B_m values are 17.8, 22.4, 32.0, 37.6 and 40.7 emu/g for the samples, LZC200, LZC500, LZC600, LZC700 and LZC800, respectively. In the inset of Fig. 7a, H_c is plotted as a function of d_{cryst} which shows that H_c attains a maximum at 47 nm and beyond that H_c falls with increasing $<d_{cryst}>$. We have previously reported the same type of behaviour for $Li_{0.3}Zn_{0.3}Co_{0.1}Fe_{2.3}O_4$ nanoparticles [35] but then we obtained a maximum H_c of ~90 Oe which is a little lower than the maximum H_c (~96 Oe) for the current composition, $Li_{0.25}Zn_{0.3}Co_{0.15}Fe_{2.3}O_4$. This increase in H_c is quite obvious as we have increased the percentage of Co which is known to enhance the magnetocrystalline anisotropy causing an increase in H_c. However, the critical size (D_{cr}) for the transition from a single domain to a multidomain behaviour increases with increasing Co percentage. Now, D_{cr} is ~47 nm (for $Li_{0.25}Zn_{0.3}Co_{0.15}Fe_{2.3}O_4$) which was in the previous case ~ 23 nm (for $Li_{0.3}Zn_{0.3}Co_{0.1}Fe_{2.3}O_4$) [35]. Thus up to 47 nm, surface anisotropy is not the cause of H_c, but rather it comes from magnetocrystalline anisotropy [63]. The remnant magnetizations (B_r) of the samples, LZC200, LZC500, LZC600, LZC700 and LZC800 are 2.2, 4.8, 8.8, 10.8 and 9.9 emu/g, respectively. As discussed earlier, SAR is the main determining factor of a material for the MIH applications and SAR could be calculated from the loop area using the following relation: SAR = Area × frequency [64]. The calculated values of SAR are 11.4, 25.2, 39.1, 39.1 and 33.7 $W/kg_{Ferrite}$ for the samples, LZC200, LZC500, LZC600, LZC700 and LZC800, respectively where ~150 mg of each of the powdered samples are used when recording the dynamic hysteresis loops. Thus, for the samples with $<d_{cryst}>$ up to D_{cr} the magnetocrystalline anisotropy plays an important role in determining the MIH properties of a material and beyond this limit the surface anisotropy reduces the SAR of the material.

3.3.2. Static magnetic behaviour

For a detailed analysis of the magnetic behaviour of $Li_{0.25}Zn_{0.3}Co_{0.15}Fe_{2.3}O_4$, the M – H loops of two samples, LZC200 and LZC800 are recorded at different temperatures for a maximum applied field of 5 T (Fig. 8 a – c). As it can be seen from the graphs, the nature of the M – H loops for the LZC200 and LZC800 samples is different. The loops for the sample LZC800 saturate at a field of ~1.5 T, but for the loops of the sample LZC200, no saturation is found even at field of 5T. This fact clearly calls for the presence of SPM nature in the 6.0 nm nanoparticles of the sample, LZC200 which is blocked in the 139 nm nanoparticles of the sample, LZC800. The H_c value of sample LZC800 is lower than that of the sample LZC200 at all temperatures. The variation of H_c with temperature is shown in Fig. 8d. Although the LZC800 sample has a lower H_c at low temperatures, it is comparable to that of the LZC200 sample at 300 K. As discussed in the previous section, the lower value of H_c suggests the presence of domain boundaries in the LZC800 sample while the LZC200 nanoparticles are single domain nanoparticles. Thus, the increase in magnetic moment with increasing field at higher external fields in the case of the LZC200 sample as well as its H_c value confirms that the LZC200 nanoparticles are single domain SPM nanoparticles. M_s of the LZC200 sample is calculated by fitting initial magnetization curves using the modified Langevin function expressed as, $\mathbf{M} = \mathbf{M_s}|\coth(\mu H/k_BT) - (k_BT/\mu H)| + \chi H$, where the χH represents the paramagnetic contribution. The variation of M_s with temperature is shown in Fig. 8d. At 300 K, M_s of nanoparticles (~6.0 nm) of $Li_{0.25}Zn_{0.3}Co_{0.15}Fe_{2.3}O_4$ (40.8 emu/g) is decreased compared to nanoparticles (~5.8 nm) of $Li_{0.3}Zn_{0.3}Co_{0.1}Fe_{2.3}O_4$ (44.4 emu/g) while H_c of $Li_{0.25}Zn_{0.3}Co_{0.15}Fe_{2.3}O_4$ (782.7 Oe) is much higher compared to $Li_{0.3}Zn_{0.3}Co_{0.1}Fe_{2.3}O_4$ (28.4 Oe) [35]. These changes in M_s and H_c could be attributed to the change in stoichiometry of Li, Co and Zn in the two cases. The magnetic properties of $Li_{0.25}Zn_{0.3}Co_{0.15}Fe_{2.3}O_4$ are compared with the other ferrites in Table 3. Again, the increase in H_c confirms the increase in magnetocrystalline anisotropy of $Li_{0.25}Zn_{0.3}Co_{0.15}Fe_{2.3}O_4$ compared to $Li_{0.3}Zn_{0.3}Co_{0.1}Fe_{2.3}O_4$ which is due to the increased percentage of Co in the former. Alternately, the net magnetization per formula unit of a spinel ferrite is usually calculated by $\mathbf{M} = \mathbf{M_B} - \mathbf{M_A}$, where $\mathbf{M_A}$ and $\mathbf{M_B}$ are magnetizations at A- and B-sites, respectively [69]. According to the cation distribution of LZC200 derived from Rietveld analysis viz., $(Zn_{0.11}Fe_{0.89})[Li_{0.25}Zn_{0.19}Co_{0.15}Fe_{1.41}]O_4$, net magnetization of LZC200 calculated in this way is ~3.05 μ_B which is further converted to M_s using the formula $\mathbf{M_s} = \frac{5585 \times \text{net magnetic moment per formula unit in } \mu_B}{\text{molecular weight}}$ and it is 76.5 emu/g for the sample LZC200. A large difference in this value of M_s from the experimental value (M_s = 59.4 emu/g at 100 K derived using Langevin fitting) could be explained as follows: the formula, $\mathbf{M} = \mathbf{M_B} - \mathbf{M_A}$, is an

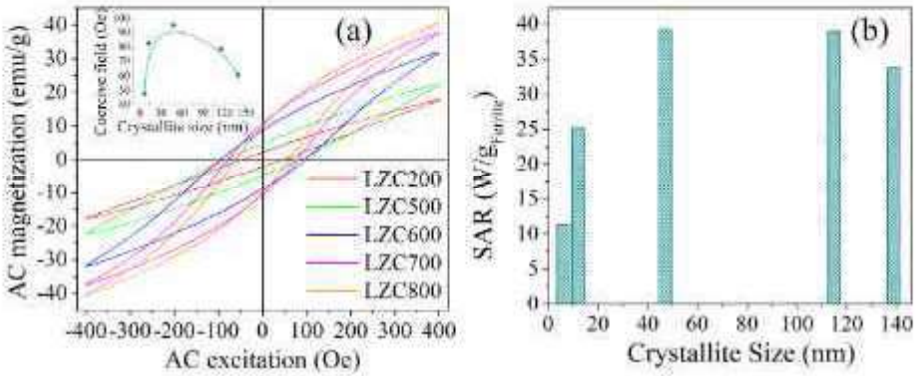

Fig. 7. (a) Dynamic hysteresis loops; Inset: Variation of H_c with $d_{cryst.}$; (b) Column graph of SAR as a function $<d_{cryst.}>$

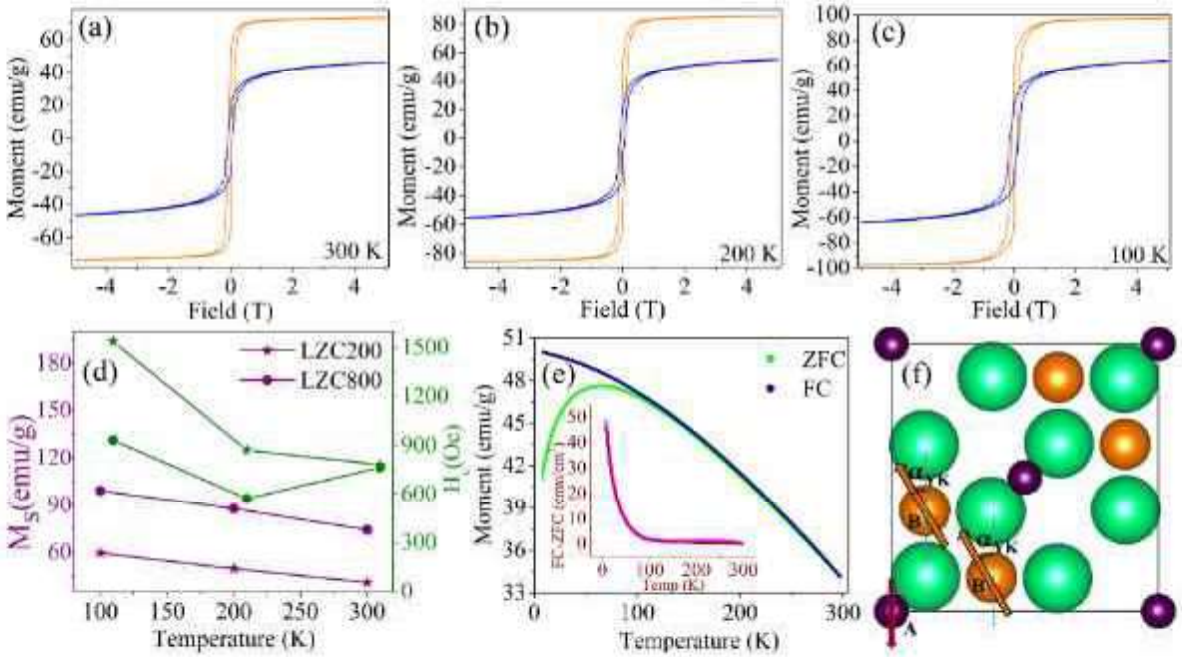

Fig. 8. (a – c) M – H loops; (d) Temperature variation of M_s and H_c; (e) Temperature variation of FC – ZFC magnetizations for LZC200, Inset: Plot of ΔM vs T; (f) Magnetic moments in a formula unit.

Table 3
Summary of magnetic properties of other relevant previously reported ferrite nanoparticles.

Ferrite	Size (nm)	M_s (emu/g)	H_c (Oe)	Reference number
$MnFe_2O_4$	17	526	41	[24]
$Ni_{0.2}Zn_{0.4}Co_{0.2}Fe_2O_4$	30	84	63	[60]
Egg white treated $CoFe_2O_4$	27	51	470	[65]
Apple cider vinegar treated $CoFe_2O_4$	22	59	1039	[66]
$Mn_{0.8}Zn_{0.2}Fe_2O_4$	22	67	168	[67]
$CoFe_2O_4$	28	63	600	[32]
$CoFe_2O_4$	51	66	820	[68]
$Co_{0.95}Fe_2V_{0.05}O_4$	32	61	880	[68]
$MgFe_2O_4$	10–40	34	53	[79]
$Li_{0.5}Fe_{2.5}O_4$	230	61	53	[33]
$Li_{0.25}Zn_{0.30}Co_{0.15}Fe_{2.2}O_4$	6	41	783	This article

oversimplified formula where many parameters viz., surface spins, spin canting, band theory of ferrimagnetism etc., are not considered. Such mismatch in the theoretical and experimental values of M_s is found in most cases [70,71]. However, if canted spin model ($M = M_B \cos \alpha_{YK} - M_A$) is introduced, the Yafet-Kittel angle (α_{YK}) for the sample LZC200 becomes 24.6°. The corresponding values of M, M_s and α_{YK} for the sample LZC800 are 4.65 μ_B, 116.7 emu/g and 23.7°, respectively. To determine the magnetocrystalline anisotropy, the field cooled (FC) and zero field cooled (ZFC) magnetizations of the sample, LZC200 are recorded in a temperature range of 10–300 K at an external field of 5000 Oe. With increasing temperature, ZFC magnetization increases up to $T_P = 63$ K and after that magnetization starts to decrease with further increase in temperature. T_P indicates the average blocking temperature at which the flipping of the magnetic moments of a maximum number of particles is blocked. However, for the entire temperature range, FC magnetization decreases with increasing temperature. The difference in FC and ZFC magnetizations is fitted using the equation, $\Delta M = \frac{20M_S^2H}{6K_{eff}}\left\{1 - \text{erf}\left[\frac{\ln(T/T_B)}{\sqrt{2}\lambda_B} - \frac{\lambda_B}{\sqrt{2}}\right]\right\}$, where $T_B = T_{BO}\exp(\sqrt{2}\lambda_B x)$ and $x = \frac{\ln(T_B/T_{BO})}{\sqrt{2}\lambda_B}$. The error function is introduced as $\int_T^\infty e^{-t^2}dt = (\sqrt{\pi}/2)\text{erfc}(T)$, where $\text{erfc}(T) = 1 - \text{erf}(T)$. The observed difference, ΔM is fitted by systematically varying different parameters viz., T_{BO}, K_{eff}, λ_B, and the fitted curve is shown in the inset of Fig. 8e. The k_{eff} value so derived for an external field of 5000 Oe is 4.14×10^6 erg/cm^3. Previously, k_{eff} of $L_{0.3}Zn_{0.3}Co_{0.1}Fe_{2.3}O_4$ was calculated for an external field of 100 Oe which was 4.8×10^6 erg/cm^3 [35]. Thus, the magnetocrystalline anisotropy of $Li_{0.25}Zn_{0.3}Co_{0.15}Fe_{2.3}O_4$ is enhanced compared to that of $L_{0.3}Zn_{0.3}Co_{0.1}Fe_{2.3}O_4$. This enhancement in anisotropy is reflected in the loop area of the samples. The M – H loop area of the LZC200 and LZC800 samples at 300 K is 14.55 and 21.29 J/kg, respectively which is much larger than that of $L_{0.3}Zn_{0.3}Co_{0.1}Fe_{2.3}O_4$ for the same annealing temperatures (0.21 and 1.44 J/kg, respectively). All these results indicate that $Li_{0.25}Zn_{0.3}Co_{0.15}Fe_{2.3}O_4$ nanoparticles are suitable for MIH applications.

3.4. MIH properties

The MIH efficiency of the samples, LZC500 (d_{cryst} ~ 11.9 nm), LZC600 (d_{cryst} ~ 47.3 nm) and LZC700 (d_{cryst} ~ 114 nm) is studied by recording the time dependent temperature curves at three different concentrations of 1, 5 and 10 mg/mL in an applied ac magnetic field of 335 Oe at 290 kHz. These three samples are chosen in particular because in this size range, 11.9–114 nm, the transition from a single domain to multi-domain occurs. Domain boundaries start to appear from $<d_{cryst}> \geq$ 47.3 nm. Thus, the effect of the domain boundaries on the MIH properties of the material could be studied on these three samples. At a concentration of 10 mg/mL, the temperature increases sharply and reaches 60 °C within 60 s (Fig. 9a). Using these high temperature gradients, the calculated SAR values of the samples, LZC500, LZC600 and LZC700 are 164, 187 and 215 W/$g_{Ferrite}$, respectively. At a concentration of 10 mg/mL, the SAR increases with increasing $<d_{cryst}>$. At this concentration, the domain walls do not have much effect on SAR. At a lower concentration of 5 mg/mL, the SAR of these three samples, LZC500, LZC600 and LZC700 are 166, 207 and 145 W/$g_{Ferrite}$, respectively. Up to D_{cr}, the SAR increases with increasing $<d_{cryst}>$ and then the SAR starts to decrease with further increase of $<d_{cryst}>$. Thus, at low concentration, the domain walls play a significant role in determining the MIH efficiency of a material. Heat generation in the samples with $<d_{cryst}> \leq D_{cr}$

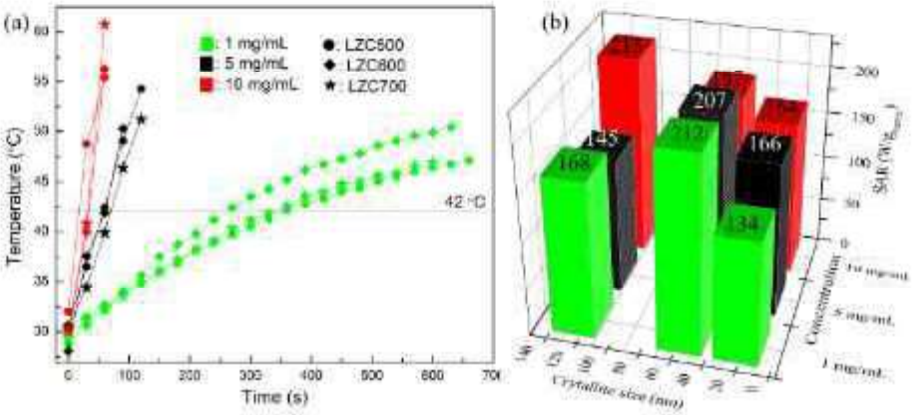

Fig. 9. (a) Time dependent temperature graphs and (b) Plot of SAR as a function of crystallite size at different concentrations.

is due to Brownian and Néel spin relaxations while that in the samples having $<d_{cryst}> > D_{cr}$ is mainly due to hysteresis losses because for Li-Zn-Co ferrite having high resistivity, the losses due to eddy currents can be ignored [72]. Power loss due to Brownian or Néel relaxation is $P = (mH\omega\tau)^2 / |2\tau kT\rho V(1 + \omega^2\tau^2)|$, where m is the magnetic moment of the nanoparticles, H is the strength of the applied ac magnetic field (335 Oe), ω is angular frequency of the applied ac magnetic field ($f = 290$ kHz), τ is the relaxation time, k is the Boltzmann constant, T is the temperature, ρ is the density of the sample, and V is the nanoparticle volume [72]. According to Debye, P is maximal when the condition $\omega\tau = 1$ is satisfied and this could be used to calculate the value of particle size for the maximum power loss due to Néel relaxation ($d_{Néel}$) [73]. Considering $K_{eff} = 4.14 \times 10^8$ erg/cm^3, $\omega = 18.22 \times 10^5$ s^{-1} ($f = 290$ kHz) and T = 300 K the estimated value of $d_{Néel}$ is less than 1 nm. For f = 290 kHz, the estimated hydrodynamic particle size for the maximum power loss due to Brownian relaxation (d_{Brown}) is ~11 nm [72]. Since all the samples considered here have $<d_{cryst}>$ larger than $d_{Néel}$ and d_{Brown}, in these cases the origin of heating is mainly hysteresis loss. Furthermore, the variation of SAR with d_{cryst} (Fig. 9b) is similar to that previously derived from the dynamic hysteresis loops, viz. the SAR of LZC500, LZC600 and LZC700 are 25.2, 39.1 and 39.1 W/$kg_{Ferrite}$, respectively. The SAR values calculated from the dynamic hysteresis loops and time-temperature plots differ significantly because there is a large difference between the frequency of the external fields considered in the two cases (50 Hz and 290 kHz, respectively). Thus to obtain maximum heating efficiency, an optimal size of the nanoparticles is required which should be comparable to D_{cr}. The same trend is followed for much lower concentration as well. For a concentration of 1 mg/mL, the SAR of the samples, LZC500, LZC600 and LZC700 is 134, 212 and 168 W/$g_{Ferrite}$, respectively. Consequently, the SAR of $Li_{0.25}Zn_{0.30}Co_{0.15}Fe_{2.3}O_4$ (212 W/$g_{Ferrite}$) at a concentration of 1 mg/mL and for ac magnetic field parameters (335 Oe, 290 kHz) is much higher than $Li_{0.35}Zn_{0.30}Co_{0.05}Fe_{2.3}O_4$ (166 W/$g_{Ferrite}$) [34] recorded with the same concentration and ac magnetic field parameters although both have comparable $<d_{cryst}>$ (47.3 and 41.0 nm, respectively). Again, the increased SAR of LZC600 compared to other samples of same composition establishes the fact that domain walls play an important role in determining the MIH efficiency of a sample. Large single domain magnetic nanoparticles with enhanced anisotropy are more favourable for MIH applications. TEM micrographs show that the nanoparticles are mainly agglomerated due to a strong dipolar interaction between them and this affects the MIH efficiency by lowering the power losses due to Néel and Brownian relaxations. To avoid agglomeration and achieve colloidal stability, the nanoparticles are often coated by a natural polymer such as chitosan (a polymer composed of glucosamine and N-acetyl-D-glucosamine) [74]. However, here the MIH efficiency of the bare nanoparticles only, is estimated. To compare the results obtained here with the previously reported values, a summary of relevant SAR determination for ferrite nanoparticles is given in Table 4. It is important to mention here thatiron oxide nanoparticles of the same size have a higher magnetization (70.8 emu/g) [75] than that of LZC200 nanoparticles (40.8 emu/g), but despite this fact, LZC200 nanoparticles have a superiority in MIH application because the squareness ratio (0.49) and the effective anisotropy constant (4.14 × 108 erg/cm3) of LZC200 are much above the squareness ratio (0.04) and effective anisotropy constant (7.53 × 105 erg/cm3) of iron oxide nanoparticles [75]. Basically, the magnetocrystalline anisotropy present in a system could be estimated from squareness ratio and at higher values of squareness ratio higher order terms of magnetocrystalline anisotropy start contributing [76]. Moreover, anisotropy is the central parameter optimizing of magnetic hyperthermia as it determines the maximum achievable SAR and controls the influence of the size distribution of nanoparticles on SAR [77]. Some previous work on the MIH properties of iron oxide nanoparticles can be seen in Table 4, among the results iron oxide nanoparticles coated with graphene oxide exhibit comparatively a superior result, but graphene oxide is a very expensive material.

Additionally, at a concentration of 1 mg/mL, these samples show another important and interesting behaviour. In Fig. 9a, the temperature of 42 °C is marked by a dotted line. This temperature is very important in the context of cancer treatment and is known as the hyperthermia temperature [72,78]. At ~42 °C, a pathobiological effect occurs in which the normal structure of proteins, nucleic acids, and phospholipids is altered, resulting deterioration of the cell structure integrity and thus causing damage to the cancer cells. For the three samples considered here, the hyperthermia temperature is reached within 6 min after applying the external field. Therefore, a very small concentration of the prepared nanoparticles can have a great contribution to the cancer treatment.

4. Conclusion

Five different sizes (6–139 nm) of $Li_{0.25}Zn_{0.30}Co_{0.15}Fe_{2.3}O_4$ nanoparticles are prepared by sol-gel method. Cubic Fd 3 m phase formation of spinel ferrites is confirmed by XRD analysis. The cation distribution is estimated from the Rietveld analysis and it is seen that the occupancy of Zn^{2+} ions in A-site increases with increasing $<d_{cryst}>$ while Li^{1+} and Co^{2+} ions occupy B-site. The phase formation is further confirmed by TEM and Raman analyses where the elemental analysis confirms the presence of the constituent elements. XPS analysis confirms the presence of all chosen elements along with their valence states. Mössbauer spectra of the samples confirm the presence of SPM nanoparticles in samples with $<d_{cryst}>$~6.0 and 11.9 nm at RT. For the samples with a larger $<d_{cryst}>$ ~114.5 nm, the nanoparticles are mainly ferromagnetic with B_{hf} ~52 T at 300 K. The presence of SPM relaxations in the smaller nanoparticles is also confirmed by the dynamic and static hysteresis loops. For an external ac field of 400 Oe at 50 Hz frequency, the SAR of

Table 4
Summary of relevant SAR determination of previously reported ferrite nanoparticles.

Ferrite	Concentration (mg/mL)	Coating	H (Oe)	f (kHz)	SAR (W/$g_{Ferrite}$)	Reference number
$MnFe_2O_4$	0.025	PNIPAm-co-GA	90	70	84[a]	[24]
$MgFe_2O_4$	2		335	265	297[a]	[79]
$Mn_{0.4}Fe_{0.8}Fe_2O_4$	20	Fatty acid	251	300	30	[80]
$Mg_{0.282}Mn_{0.718}Fe_2O_4$	16	Lipid	140	100	2170[a]	[81]
$CoFe_2O_4$			510	101	133[a]	[32]
$Li_{0.5}Fe_{2.5}O_4$			1.4	6770	14[a]	[33]
$Ni_{0.4}Zn_{0.4}Co_{0.2}Fe_2O_4$	1		335	290	200	[60]
$Li_{0.30}Zn_{0.30}Co_{0.10}Fe_{2.3}O_4$	2		420	300	379	[35]
$Cu_{0.2}Cd_{0.8}Fe_2O_4$	30 mg (powder)		384	340	0.7	[82]
Magnetite	5	(3-aminopropyl)triethoxysilane	200	252	67.2	[83]
Magnetite	10		334	265	38.4	[84]
	4.15	Poly-ethelene glycol			28.3	
	6.63	Oleic acid			33.5	
Iron Oxide	0.167	Graphene Oxide	408	400	5020	[85]
$Li_{0.25}Zn_{0.30}Co_{0.15}Fe_{2.3}O_4$	1		335	290	212	This article

[a] (W/g).

the five samples with $<d_{cryst}>$ ~6.0, 11.9, 47.3, 114.5 and 139.2 nm are 11.4, 25.2, 39.1, 39.1 and 33.7 W/$kg_{Ferrite}$, respectively. This type of SAR dependency on $<d_{cryst}>$ suggests that nanoparticles with a size comparable to the critical size of single domain should be chosen for MIH applications. In addition, nanoparticles with optimum magneto-crystalline anisotropy are more preferable for MIH applications. The k_{eff} value obtained in this study is 4.14×10^5 erg/cm^3 and the SAR values obtained from time dependent temperature curves for 1 mg/mL concentrations of samples with $<d_{cryst}>$ ~11.9, 47.3 and 114.5 nm are 134, 212 and 168 W/$g_{Ferrite}$, respectively. At this small concentration of the samples, the hyperthermia temperature is also reached in a very short time (within 6 min only) after applying the external ac magnetic field.

CRediT authorship contribution statement

Madhumita Dalal: Conceptualization, Methodology, Data curation, Writing – original draft, Investigation, Software. **Jean-Marc Greneche:** Investigation, Data curation, Validation, Software, Writing – review & editing, Supervision. **Raghumani S. Ningthoujam:** Investigation, Data curation, Software. **Pabitra K. Chakrabarti:** Conceptualization, Supervision, Writing – review & editing.

Declaration of competing interest

The authors declare that they have no known competing financial interests or personal relationships that could have appeared to influence the work reported in this paper.

Data availability

Data will be made available on request.

Acknowledgements

The authors acknowledge the financial assistance provided in the DST-SERB, GOVT OF INDIA (Order no.: EMR/2017/000832, DATED: 19.03.2018). The authors acknowledge the financial support provided by UGC, Govt. of India, through the CAS program (No. F.530/20/CAS-II/2018 (SAP-I), DATED: 25.07.2018), FIST, DST, Govt. of India (Ref. SR/FST/PS-II/2018/52, TPN no.- 19862), and PURSE-II, DST, Govt. of India (No. SR/PURSE Phase-2/34, DATED: 27.02.2017).The authors also acknowledge the UGC-DAE CSR, Kolkata Centre for providing static magnetic measurement facility.

References

[1] I. Khmara, M. Molcan, A. Antosova, Z. Bednarikova, V. Zavisova, M. Kubovcikova, A. Jurikova, V. Girman, E. Baranovicova, M. Koneracka, Z. Gazova, J. Magn. Magn Mater. 513 (2020), 167056, https://doi.org/10.1016/j.jmmm.2020.167056.
[2] R. Liu, Y. Guo, G. Odusote, F. Qu, R.D. Priestley, ACS Appl. Mater. Interfaces 5 (16) (2013) 9167–9171, https://doi.org/10.1021/am402565y.
[3] J.S. Anandhi, G.A. Jacob, R.J. Joseyphus, J. Magn. Magn Mater. 512 (2020), 166992, https://doi.org/10.1016/j.jmmm.2020.166992.
[4] B.H. Hou, Y.Y. Wang, J.Z. Guo, Y. Zhang, Q.L. Ning, Y. Yang, W.H. Li, J.P. Zhang, X.L. Wang, X.L. Wu, ACS Appl. Mater. Interfaces 10 (4) (2018) 3581–3589, https://doi.org/10.1021/acsami.7b16580.
[5] S. Venkateswarlu, D. Lee, M. Yoon, ACS Appl. Mater. Interfaces 8 (36) (2016) 23876–23885, https://doi.org/10.1021/acsami.6b03583.
[6] A. Dong, S. Lan, J. Huang, T. Wang, T. Zhao, L. Xiao, W. Wang, X. Zheng, F. Liu, G. Gao, Y. Chen, ACS Appl. Mater. Interfaces 3 (11) (2011) 4228–4235, https://doi.org/10.1021/am200984p.
[7] X. Meng, W. Yang, G. Han, Y. Yu, S. Ma, W. Liu, Z. Zhang, J. Magn. Magn Mater. 502 (2020), 166518, https://doi.org/10.1016/j.jmmm.2020.166518.
[8] T. Lian, C. Huang, F. Liang, X. Li, J. Xi, ACS Appl. Mater. Interfaces 11 (49) (2019) 45692–45701, https://doi.org/10.1021/acsami.9b16236.
[9] F. Alawiyah, Mufikhah, W.Z. Lubis, G.T. Sulungbudi, Mujamilah, E.G.R. Putra, J. Phys.: Conf. Ser. 1436 (1) (2020), 012067, https://doi.org/10.1088/1742-6596/1436/1/012067.
[10] A. Hajnorouzi, N. Modaresi, J. Magn. Magn Mater. 505 (2020), 166732, https://doi.org/10.1016/j.jmmm.2020.166732.
[11] J. Ma, K. Wang, M. Zhan, ACS Appl. Mater. Interfaces 7 (29) (2015) 16027–16039, https://doi.org/10.1021/acsami.5b04342.
[12] N. Daffé, V. Gavrilov, S. Neveu, F. Choueikani Arrio M.-A., A. Juhin, P. Ohresser, V. Dupuis, P. Sainctavit, J. Magn. Magn Mater. 477 (2019) 226–231, https://doi.org/10.1016/j.jmmm.2019.01.048.
[13] M.E. de Sousa, M.B.F. van Raap, P.C. Rivas, P.M. Zélis, P. Girardin, G. A. Pasquevich, J.L. Alessandrini, D. Muraca, F.H. Sánchez, J. Phys. Chem. C 117 (2013) 5436–5445, https://doi.org/10.1021/jp311556b.
[14] S.F. Mansour, O.M. Hemeda, S.I. El-Dek, B.I. Salem, J. Magn. Magn Mater. 420 (2016) 7–18, https://doi.org/10.1016/j.jmmm.2016.06.062.
[15] M.A. Gabal, A.A. Al-Juaid, S.M. Al-Rashed, M.A. Hussein, F. Al-Marzouki, J. Magn. Magn Mater. 426 (2017) 670–679, https://doi.org/10.1016/j.jmmm.2016.10.147.
[16] A.S. Hameed, H. Bahiraei, M.V. Reddy, M.Z. Shoushtari, J.J. Vittal, C.K. Ong, B.V. R. Chowdari, ACS Appl. Mater. Interfaces 6 (13) (2014) 10744–10753, https://doi.org/10.1021/am502605e.
[17] S.A. Ali, M.A. Matin, M.A. Hakim, M.F. Islam, IOP Conf. Ser. Mater. Sci. Eng. 438 (2018), 012017, https://doi.org/10.1088/1757-899X/438/1/012017.
[18] C. Yao, Q. Zeng, G.F. Goya, T. Torres, J. Liu, H. Wu, M. Ge, Y. Zeng, Y. Wang, J. Z. Jiang, J. Phys. Chem. C 111 (33) (2007) 12274–12278, https://doi.org/10.1021/jp073276s.
[19] X. Tang, L. Jin, R. Wei, X. Zhu, J. Yang, J. Dai, W. Song, X. Zhu, Y. Sun, J. Magn. Magn Mater. 422 (2017) 255–261, https://doi.org/10.1016/j.jmmm.2016.09.022.
[20] P.V.B. Reddy, V.R. Reddy, A. Gupta, R. Gopalan, Ch G. Reddy, Hyperfine Interact. 183 (2008) 81–86, https://doi.org/10.1007/s10751-008-9733-6.
[21] T. Waeckerlé, H. Praissé, B. Boulogne, S.L. Spire, J. Magn. Magn Mater. 304 (2006) 844–846, https://doi.org/10.1016/j.jmmm.2006.03.013.
[22] M.E. de Sousa, A. Carrea, P. M Zéliz, D. Muraca, O. Mykhaylyk, Y.E. Soza, R. G. Goya, F.H. Sanchez, R.A. Dewey, M.B. Fernández van Raap, J. Phys. Chem. C 120 (2016) 7339–7348, https://doi.org/10.1021/acs.jpcc.5b12330.
[23] R. Das, J. Alonso, Z.N. Porshokouh, V. Kalappattil, D. Torres, M.H. Phan, E. Garaio, J.A. Garcia, J.L.S. Llamazares, H. Srikanth, J. Phys. Chem. C 120 (2016) 10086–10093, https://doi.org/10.1021/acs.jpcc.6b02006.
[24] S. Patra, E. Roy, P. Karfa, S. Kumar, R. Madhuri, P.K. Sharma, ACS Appl. Mater. Interfaces 7 (2015) 9235–9246, https://doi.org/10.1021/acsami.5b01786.

[25] L. Menag, M.M. Saiq, S.J.D. Konstas, K. Suzuki, M.R. Hill, J. Mater. Chem. A 7 (2019) 3790–3796, https://doi.org/10.1039/C8TA07789H.
[26] M.M. Saiq, K. Suzuki, M.R. Hill, Chem. Commun. 54 (2018) 2825–2837, https://doi.org/10.1039/C8CC00331A.
[27] T. Bayerl, M. Duhovic, P. Mitschang, D. Bhattacharyya, Composites Part A 57 (2014) 27–40, https://doi.org/10.1016/j.compositesa.2013.10.024.
[28] Y. Tao, G. Huang, H. Li, M.R. Hill, ACS Sustain. Chem. Eng. 7 (2019) 13627–13632, https://doi.org/10.1021/acssuschemeng.9b02323.
[29] C. Gómez-Polo, S. Larumbe, L.F. Barquín, L.R. Fernández, J. Nanoparticle Res. 18 (2016) 118, https://doi.org/10.1007/s11051-016-3428-x.
[30] J.M. Asensio, A.B. Miguel, P.F. Fazzini, P.W.N.M. van Leeuwen, B. Chaudret, Angew. Chem. Int. Ed. 58 (2019) 11306–11310, https://doi.org/10.1002/anie.201904566.
[31] P.M. Mortensen, J.S. Engbæk, S.B. Vendelbo, M.F. Hansen, M. Østberg, Ind. Eng. Chem. Res. 56 (2017) 14006–14013, https://doi.org/10.1021/acs.iecr.7b02331.
[32] E. Mazario, N. Menéndez, P. Herrasti, M. Cañete, V. Connord, J. Carrey, J. Phys. Chem. C117 (2013) 11405–11411, https://doi.org/10.1021/jp4023025.
[33] D.H. Kim, S.H. Lee, K.N. Kim, K.M. Kim, I.B. Shim, Y.K. Lee, J. Magn. Magn Mater. 293 (2005) 320–327, https://doi.org/10.1016/j.jmmm.2005.02.077.
[34] M. Dalal, R.S. Ningthoujam, P.K. Chakrabarti, AIP Conf. Proc. 1942 (2018) 500191–500194, https://doi.org/10.1063/1.5028650.
[35] M. Dalal, J.-M. Greneche, B. Satpati, T.B. Ghzaiel, F. Mazaleyrat, R.S. Ningthoujam, P.K. Chakrabarti, ACS Appl. Mater. Interfaces 9 (2017) 40831–40845, https://doi.org/10.1021/acsami.7b12091.
[36] E. Fantechi, C. Innocenti, M. Zanardelli, M. Fittipaldi, E. Falvo, M. Carbo, V. Shullani, L.D.C. Mannelli, C. Ghelardini, A.M. Ferretti, A. Ponti, C. Sangregorio, P. Ceci, ACS Nano 8 (5) (2014) 4705–4719, https://doi.org/10.1021/nn500454m.
[37] H. Zeng, T. Tao, Y. Wu, W. Qi, C. Kuang, S. Zhou, Y. Chen, RSC Adv. 4 (2014) 23145–23148, https://doi.org/10.1039/C4RA02957G.
[38] X. Yao, J. Kong, C. Zhao, D. Zhou, R. Zhou, X. Lu, Electrochim. Acta 146 (2014) 464–471, https://doi.org/10.1016/j.electacta.2014.08.144.
[39] S. Mukherjee, K. Mukhopadhyay, S. Sutradhar, S. Pati, A.K. Deb, D. Das, P. K. Chakrabarti, J. Phys. Chem. C 117 (2013) 12787–12799, https://doi.org/10.1021/jp311620u.
[40] K. Parekh, R.V. Upadhyay, R.V. Mehta, J. Appl. Phys. 88 (2000) 2799–2804, https://doi.org/10.1063/1.1287222.
[41] G. Sathishkumar, C. Venkataraju, K. Sivakumar, Mater. Sci. Appl. 1 (2010) 19–24, https://doi.org/10.4236/msa.2010.11004.
[42] W.H. Hall, G.K. Williamson, Dead time correction for monitored counters, J. Sci. Instrum. 29 (1952) 132–133, https://doi.org/10.1088/0950-7671/29/4/413.
[43] G.K. Williamson, W.H. Hall, X-ray line broadening from filed aluminium and wolfram, Acta Metall. 1 (1953) 22–31, https://doi.org/10.1016/0001-6160(53)90006-6.
[44] A. Bandyopadhyay, S. Modak, S. Acharya, A.K. Deb, P.K. Chakrabarti, Microstructural, magnetic and crystal field investigations of nanocrystalline Dy^{3+} doped zinc oxide, Solid State Sci. 12 (2010) 448–454, https://doi.org/10.1016/j.solidstatesciences.2009.12.006.
[45] P.K. Chakrabarti, B.K. Nath, S. Brahma, S. Das, K. Goswami, U. Kumar, P. K. Mukhopadhyay, D. Das, M. Ammar, F. Mazaleyrat, J. Phys. Condens. Matter 18 (2006) 5253–5267, https://doi.org/10.1088/0953-8984/18/22/023.
[46] E. Bermejo, C. Lacour, M. Quarton, J. Mater. Sci. Lett. 14 (1995) 1346–1348.
[47] I. Soibam, S. Phanjoubam, C. Prakash, J. Alloys Compd. 475 (2009) 328–331, https://doi.org/10.1016/j.jallcom.2008.07.011.
[48] L.F. Marie, K. Salek, T.S. O'Donovan, Energy Eng. J. Assoc. Energy Eng. 120 (10) (2023) 2193–2209, https://doi.org/10.32604/ee.2023.043075.
[49] J.L. Verble, Physical Review B9 (12) (1974) 5236–5248, https://doi.org/10.1103/PhysRevB.9.5236.
[50] Z. Wang, D. Schiferl, Y. Zhao, H.St.C. O'Neill, J. Phys. Chem. Solid. 64 (2003) 2517–2523, https://doi.org/10.1016/j.jpcs.2003.08.005.
[51] J.H. Kim, I.S. Hwang, Nucl. Eng. Des. 235 (2005) 1029–1040.
[52] V. D'Ippolito, G.B. Andreozzi, D. Bersani, P.P. Lottici, J. Raman Spectrosc. 46 (2015) 1255–1264, https://doi.org/10.1002/jrs.4764.
[53] D.L.A. de Faria, S.V. Silva, M.T. de Oliveira, J. Raman Spectrosc. 28 (1997) 873–878.
[54] R.P. Patil, B.V. Jadhav, P.P. Hankare, Results Phys. 3 (2013) 214–218, https://doi.org/10.1016/j.rinp.2013.09.006.
[55] Y. Guo, N. Zhang, X. Wang, Q. Qian, S. Zhang, Z. Li, Z. Zou, J. Mater. Chem. A 5 (2017) 7571–7577, https://doi.org/10.1039/C6TA11134C.
[56] M.S. Lazarus, R.P. Doyle, T.K. Sham, Chem. Phys. Lett. 57 (4) (1978) 540–546, https://doi.org/10.1016/0009-2614(78)85517-2.
[57] S.R. Naik, A.V. Salker, J. Mater. Chem. 22 (2012) 2740–2750, https://doi.org/10.1039/c2jm15228h.
[58] A. Aharoni, Phys. Rev. B 7 (1973) 1103.
[59] R.A. Brand, Nucl. Instrum. Methods B 28 (1987) 398–416, https://doi.org/10.1016/0168-583X(87)90182-0.
[60] M. Dalal, A. Das, D. Das, R.S. Ningthoujam, P.K. Chakrabarti, J. Magn. Magn Mater. 460 (2018) 12–27, https://doi.org/10.1016/j.jmmm.2018.03.045.
[61] R.K. Sharma, V. Sebastian, N. Lakshmi, K. Venugopalan, V.R. Reddy, A. Gupta, Phys. Rev. B 75 (2007) 144419, https://doi.org/10.1103/PhysRevB.75.144419, 144419-6.
[62] J.M. Greneche, Mössbauer Spectroscopy: the Contribution of 57Fe Mössbauer Spectrometry, Springer-Verlag Berlin Heidelberg, 2013, https://doi.org/10.1007/978-3-642-32220-4.
[63] M. Bmantecón, K. O'Grady, J. Magn. Magn Mater. 296 (2006) 124–133, https://doi.org/10.1016/j.jmmm.2004.11.580.
[64] D. Ortega, Q. Pankhurst, Nanoscience 1 (2013) 60–88, https://doi.org/10.1039/9781849734844-00060.
[65] H.S. Mansoureh, A. Zahra, H. Saeed, S. Amir, J. Sol. Gel Sci. Technol. 106 (2023) 23–36, https://doi.org/10.1007/s10971-023-06073-2.
[66] M. Afshari, A.R.R. Isfahani, S. Hasani, F. Davar, K.J. Ardakani, International Journal of Applied Ceramic Society 16 (4) (2019) 1612–1621, https://doi.org/10.1111/ijac.13224.
[67] M. Shayestefar, A. Mashreghi, S. Hasani, M.T. Rezvan, J. Magn. Magn Mater. 541 (2022), 168390, https://doi.org/10.1016/j.jmmm.2021.168390.
[68] I. Parvin, H. Saeed, S. Amir, F. Atefeh, K. Fatemeh, J.A. Khadijeh, D. Fatemeh, J. Sol. Gel Sci. Technol. 95 (2020) 157–167, https://doi.org/10.1007/s10971-020-05516-w.
[69] S. Humpratub, S. Phokha, P. Kidkhunthod, N. Chanlek, P. Chindaprasirt, Results Phys. 24 (2021) 1041121–1041127, https://doi.org/10.1016/j.rinp.2021.104112.
[70] G. Concas, G. Spano, C. Cannas, A. Musinu, D. Peddis, G. Piccaluga, J. Magn. Magn Mater. 321 (2009) 1893–1897, https://doi.org/10.1016/j.jmmm.2008.12.001.
[71] M. Dalal, A. Mallick, A.S. Mahapatra, A. Mitra, A. Das, D. Das, P.K. Chakrabarti, Mater. Res. Bull. 76 (2016) 389–401, https://doi.org/10.1016/j.materresbull.2015.12.028.
[72] M. Ma, Y. Wu, J. Zhou, Y.K. Sun, Y. Zhang, N. Gu, J. Magn. Magn Mater. 268 (2004) 33–39, https://doi.org/10.1016/S0304-8853(03)00426-8.
[73] P. Debye, The Chemical Catalog Company, NewYork, (1929).
[74] K.H. Bae, M. Park, M.J. Do, N. Lee, J.H. Ryu, G.W. Kim, C.G. Kim, T.G. Park, T. Hyeon, ACS Nano 6 (6) (2012) 5266–5273, https://doi.org/10.1021/nn301046w.
[75] P.T. Phong, V.T.K. Oanh, T.D. Lam, N.X. Phuc, L.D. Tung, N.T.K. Thanh, D. H. Manh, J. Electron. Mater. 46 (4) (2017) 2533–2539, https://doi.org/10.1007/s11664-017-5337-8.
[76] E.V. Gopalan, I.A. Al-Omari, D.S. Kumar, Y. Yoshida, P.A. Joy, M. R. Anantharaman, Appl. Phys. A 99 (2010) 497–503, https://doi.org/10.1007/s00339-010-5573-8.
[77] J. Carrey, B. Mehdaoui, M. Respaud, J. Appl. Phys. 109 (2011), https://doi.org/10.1063/1.3551582, 083921-1 - 083921-17.
[78] K.J. Chen, F.Y. Chaung, S.P. Wey, K.J. Lin, F. Cheng, C.C. Lin, H.L. Liu, H.W. Tseng, C.P. Liu, M.C. Wei, C.M. Liu, H.W. Sung, ACS Nano 8 (2014) 5105–5115, https://doi.org/10.1021/nn501162x.
[79] V.M. Khot, A.B. Salunkhe, N.D. Thorat, M.R. Phadatare, S.H. Pawar, J. Magn. Magn Mater. 332 (2013) 48–51, https://doi.org/10.1016/j.jmmm.2012.12.010.
[80] J. Giri, P. Pradhan, T. Sriharsha, D. Bahadur, J. Appl. Phys. 97 (2005) 10Q9161–10Q9163, https://doi.org/10.1063/1.1855131.
[81] M. Jeun, S. Park, G.H. Jang, K.H. Lee, ACS Appl. Mater. Interfaces 6 (2014) 16487–16492, https://doi.org/10.1021/am5057163.
[82] R. Ghasemi, J. Echeverría, J.I. Pérez-Landazábal, J.J. Beato-Lopez, M. Naseri, C. Gómez-Polo, J. Magn. Magn Mater. 499 (2020), 166201, https://doi.org/10.1016/j.jmmm.2019.166201.
[83] M. Ognjanović, D.M. Stanković, Z.K. Jaćimović, M. Kosović-Perutović, B. Dojcinović, B. Antić, J. Alloys Compd. 884 (2021), https://doi.org/10.1016/j.jallcom.2021.161075, 161075-1 - 9.
[84] R. Ghosh, L. Pradhan, Y.P. Devi, S.S. Meena, R. Tewari, A. Kumar, S. Sharma, N. S. Gajbhiye, R.K. Vatsa, B.N. Pandey, R.S. Ningthoujam, J. Mater. Chem. 21 (2011) 13388–13398, https://doi.org/10.1039/C1JM10092F.
[85] P.J. Sugumaran, X.L. Liu, T.S. Herng, E. Peng, J. Ding, ACS Appl. Mater. Interfaces 11 (2019) 22703–22713, https://doi.org/10.1021/acsami.9b04261.

Nano World Journal

https://doi.org/10.17756/nwj.2024-s1-044

Research Article

Open Access

Study on Structural and Dielectric Behavior of $Li_{0.3}Zn_{0.3}Co_{0.1}Fe_{2.3}O_4$

Madhumita Dalal[1,2*], Sukhendu Sadhukhan[2] and Pabitra K. Chakrabarti[2]

[1]*Department of Physics, Bejoy Narayan Mahavidyalaya, Hooghly, West Bengal, India*
[2]*Department of Physics, Burdwan University, Burdwan, West Bengal, India*

***Correspondence to:**
Madhumita Dalal
Department of Physics,
Bejoy Narayan Mahavidyalaya,
Hooghly, West Bengal, India.

Department of Physics,
Burdwan University,
Burdwan, West Bengal, India.
E-mail: dalal.madhumita@gmail.com

Received: January 03, 2024
Accepted: March 15, 2024
Published: March 20, 2024

Citation: Dalal M, Sadhukhan S, Chakrabarti PK. 2024. Study on Structural and Dielectric Behavior of $Li_{0.3}Zn_{0.3}Co_{0.1}Fe_{2.3}O_4$. *NanoWorld J* 10(S1): S246-S249.

Published by United Scientific Group

Abstract

Nanoparticles of $Li_{0.3}Zn_{0.3}Co_{0.1}Fe_{2.3}O_4$ are prepared by sol-gel method using nitrate salts as precursor materials. Two different sizes (16.9 and 38.9 nm) are obtained by annealing the sample at 500 and 600 °C, respectively. X-ray diffraction (XRD) patterns of the two samples exhibit only the desired peaks of cubic $Fd\bar{3}m$ space group which confirms the pure spinel ferrite phase formation in the samples. Size and root mean square (r.m.s.) lattice strains are obtained by Williamson-Hall method. The r.m.s. lattice strains of the two samples are 1.25×10^{-4} and 1.15×10^{-3}, respectively which confirms that the prepared samples are free from appreciable defects. The dielectric constants of the two samples are studied as functions of temperature and frequency. Dielectric behavior of the samples is explained by the electronic exchange between ferrous and ferric ions. Thermal variation of the dielectric constant shows that there is a phase transition from ferroelectric to paraelectric phase for both the samples at ~ 320 K. Dielectric constant decreases with the increase of frequency which is since beyond a certain frequency of the externally applied electric field, the electronic exchange between the Fe^{2+} and Fe^{3+} ions fail to follow the applied electric field.

Keywords

Ferrite, Sol-gel method, X-ray diffraction, Williamson-Hall method, Dielectric constant

Introduction

Polycrystalline spinel ferrites are widely known for their important structural, magnetic, and dielectric behaviors and interestingly, these properties could be tuned by proper choice of metal cations and by varying the average crystallite size ($\langle d_{cryst} \rangle$). Spinel ferrites have formula unit described by AOB_2O_3 where A- and B- are two lattice voids surrounded by four and six oxygen anions, respectively. Metal cations occupy these voids and depending on the metal cations structural, magnetic, and dielectric behaviors change.

Frequency dependence of dielectric constant of lithium ferrite is studied by Teixeira et al. [1] and the dielectric behavior of substituted lithium ferrites is studied by many researchers which include nickel [2], cobalt [3, 4], cadmium [5], manganese [6] substituted lithium ferrites. Earlier studies indicate that the substituting metals significantly affect the dielectric behavior of the lithium ferrite. In this paper, the frequency dependence and temperature dependence of lithium-zinc-cobalt ferrite is included.

Experimentation

Sample preparation

Polycrystalline ferrite samples of general formula $Li_{0.3}Zn_{0.3}Co_{0.1}Fe_{2.3}O_4$ are prepared by sol-gel method where $LiNO_3$, $Zn(NO_3)_2.6H_2O$, $Co(NO_3)_2.6H_2O$ and $Fe(NO_3)_3.9H_2O$ are used as precursor materials. Nitrate salts are taken in the chosen stoichiometric ratio and dissolved in deionized water by employing a magnetic stirrer. Aqueous solution of equimolar citric acid is added to the aqueous nitrate solution while stirring is maintained. Stirring is continued further until a gel is formed and on gel formation the beaker is shifted to an oven to burn the excess nitrates. The product is then powdered and annealed at two different temperatures (500 and 600 °C) and the samples are named as LZC5 and LZC6, respectively.

Characterizations

XRD patterns of LZC5 and LZC6 samples are recorded in powder X-ray diffractometer, Model BRUKER D8 Advance with da Vinci, using CuKα radiation (λ=1.5405Å). Dielectric measurements of LZC5 and LZC6 samples are recorded by HIOKI 3532–50 LCR HiTESTER over the frequency range of 100 Hz to 5 MHz at different temperatures (300 to 450 K). For dielectric measurement, LZC5 and LZC6 powder samples are pressed into the cylindrical shaped pellets (thickness ~0.05 cm and diameter ~0.8 cm) using hydraulic press and electrodes are formed on the two flat faces of these pellets using silver coating.

Results and Discussion

XRD study

XRD patterns of the samples LZC5 and LZC6 are displayed in figure 1. Diffraction peaks corresponding to the cubic $Fd\bar{3}m$ space group only are appeared in the XRD patterns of both the samples which confirm pure phase formation in the prepared samples. Williamson-Hall method is employed to derive $<d_{crystl}>$ and r.m.s. lattice strain. For this purpose, obtained XRD patterns are fitted with multiple (six) peaks of Gauss type and the βcosθ vs 4sinθ graphs are plotted with the β (full width at half maximum) and θ (peak angle) derived from multiple peaks fitting. Linear fitting is performed on these Williamson-Hall plots (βcosθ vs 4sinθ) and $<d_{crystl}>$ and r.m.s. lattice strains are calculated from the slope and intercept of the fitted straight line. The obtained values of $<d_{crystl}>$ and r.m.s. lattice strain of LZC5 and LZC6 samples are 16.9, 38.9 nm and 1.25 x 10^{-4}, 1.15 x 10^{-3}, respectively which agree with those derived using Rietveld method [7].

Dielectric properties

Variation of dielectric constant with frequency

Dielectric polarization in ferrites occurs through the exchange of electrons between Fe^{2+} and Fe^{3+} ions. Electron exchanges between the $Fe^{2+} \leftrightarrow Fe^{3+}$ results in local displacement of charges which is responsible for polarization in ferrites [3]. In polycrystalline ferrites, the grain boundaries restrict this local displacement of charges and results in high resistivity. Variation of dielectric constant (ε') of LZC5 and LZC6 samples as a function of frequency at different temperatures is displayed in figure 2. Dielectric constant of both the samples decreases with increase of frequency which indicates towards the presence of relaxation in both the samples. But the relaxation deviates from the ideal nature of Debye relaxation and can be explained by Cole-Cole relaxation. According to Cole-Cole relaxation, the dielectric constant is described by equation 1.

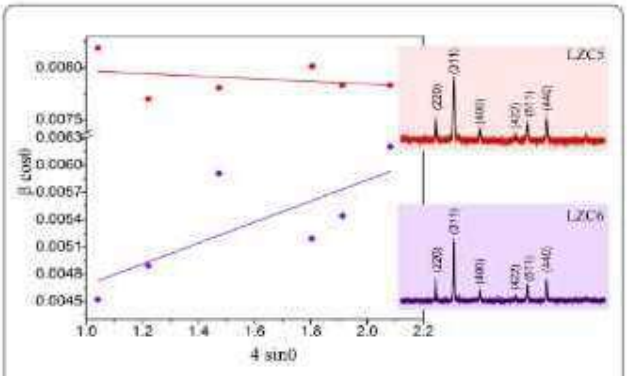

Figure 1: Williamson-Hall plot for the samples LZC5 and LZC6.

$$\varepsilon'(\omega) = \varepsilon_{\infty} + \frac{\Delta\varepsilon\left\{1+(\omega\tau)^{1-\alpha}\sin\left(\frac{\alpha\pi}{2}\right)\right\}}{1+2(\omega\tau)^{1-\alpha}\sin\left(\frac{\alpha\pi}{2}\right)+(\omega\tau)^{2(1-\alpha)}} \quad (1)$$

Where ω is the angular frequency, $\Delta\varepsilon = \varepsilon_0 - \varepsilon_\infty$ is the dielectric relaxation strength, ε_0 and ε_∞ are low frequency and high frequency permittivity limits, respectively, τ is the relaxation time corresponding to the maximum loss and α is the shape parameter [8]. $\alpha = 0$ gives the Debye form of relaxation while non-zero values of α denotes the deviation from Debye form.

In the low frequency region, ε' increases rapidly with the decrease of frequency and has very high value ~3000. The variation of ε' in the low frequency region is dominated by the interfacial polarization effect, which follows the Koop's phenomenological theory and known as the Maxwell-Wagner polarization [4]. Nanoparticles consist of conductive grains bounded by resistive walls which cause to develop polarization at the interface of grain boundaries. At low frequency, this polarization follows the electric field but at high frequencies the polarization can't follow the electric field and causes a sharp drop in the value of ε'. Thus, to avoid the interfacial polarization, the data recorded above the frequency of ~10^3 Hz is considered while fitting by Cole-Cole equation (Equa-

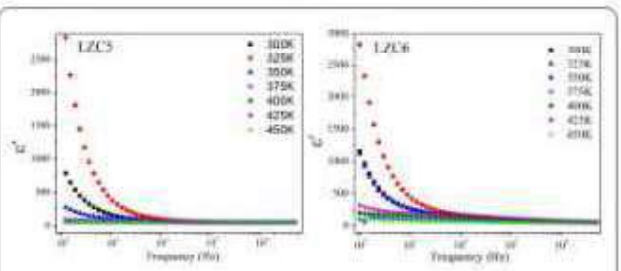

Figure 2: Frequency variation of dielectric constant.

Table 1: Results of Cole-Cole fitting.

Sample	T (K)	ε_s	ε_∞	$\Delta\varepsilon = \varepsilon_s - \varepsilon_\infty$	$\tau \times 10^5$ s	α
LZC5	300	165	49	116	8.28	0.34
	325	320	49	271	6.75	0.26
	350	94	48	46	3.00	0.35
	375	63	48	15	1.63	0.33
LZC6	300	236	43	193	0.96	0.56
	325	637	31	606	53.4	0.67
	350	232	34	198	0.56	0.64
	375	211	20	191	0.36	0.70

tion 1) and fitted parameters are listed in table 1. The dielectric strength ($\Delta\varepsilon$) of LZC6 is higher than that of LZC5 which is because LZC6 having larger $\langle d_{cryst} \rangle$ (= 38.9 nm) compared to LZC5 (16.9 nm) and therefore has larger grain boundaries, i.e. more interfacial polarizations. The shape parameter ranges from 0.26 - 0.70 in the temperature range 300 - 375 K. Above 375 K, ε' becomes very small, so Cole-Cole fitting is avoided above 375 K. High frequency permittivity and relaxation time is relatively higher in LZC5 than LZC6.

Variation of dielectric constant with temperature

Temperature variation of ε' of LZC5 and LZC6 samples recorded at frequencies 1, 10 and 100 kHz is shown in figure 3. At 10 and 100 kHz frequencies, ε' remains independent of temperature but at a frequency of 1 kHz, ε' increases up to a certain temperature and then decreases abruptly with further increase of temperature. Thus, a transition from ferroelectric to paraelectric phase occurs at this temperature (T_c). The value of T_c for LZC5 and LZC6 samples are 319 and 327 K, respectively. Such temperature variation of ε' can also be explained by the presence of grain boundaries in polycrystalline ferrites. At higher temperatures grain boundaries start to disappear, thereby causing a drop in interfacial polarization which in turn results in a drop of ε'. Larger $\langle d_{cryst} \rangle$ of LZC6 causes a larger T_c in this sample.

Variation of loss tangent with frequency

Effect of frequency on the loss tangent (tanδ) of LZC5 and LZC6 samples at different temperatures is shown in figure 4. The sample, LZC5 has very small value of tanδ compared to LZC6 sample, however in both the samples tanδ decreases with the increase of frequency. tanδ represent the energy loss per cycle which comes from two components, one from the polarization part and other from the leakage part. As discussed earlier, the interfacial polarization decreases at high frequencies, thus tanδ decreases at high frequencies. The loss curves at temperatures 300 - 350 K are different from those at other temperatures. None of the curves exhibit a loss peak except for that of LZC5 sample at 325 K. Generally, a loss peak i.e. the maximum value of tanδ occurs at a frequency when the hopping frequency becomes equal to frequency of the applied field. At temperatures above 350 K, tanδ drops abruptly at higher frequency which is due to the disappearance of Maxwell-Wagner polarization above this temperature.

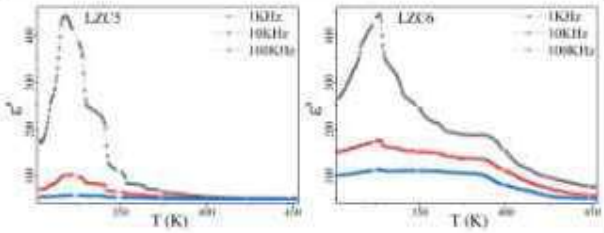

Figure 3: Temperature variation of dielectric constant.

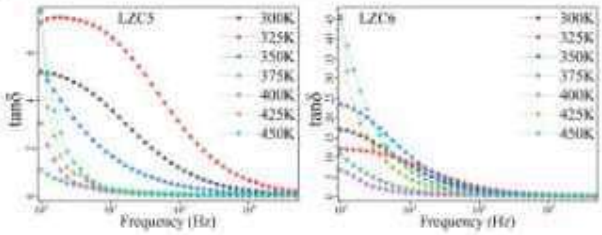

Figure 4: Frequency variation of dielectric loss tangent.

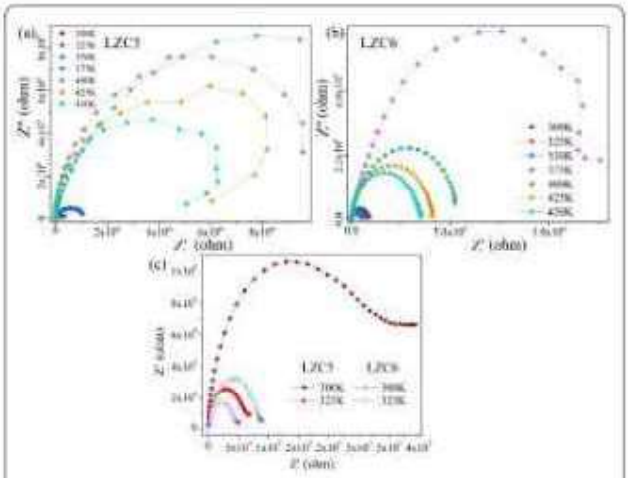

Figure 5: Z' - Z'' plot at different temperatures.

Variation of complex impedances at different temperatures

Z' - Z'' plot of LZC5 and LZC6 samples are shown in figure 5. The plots display some depressed semi-circles with their centres below the real axis, thereby suggesting a non-Debye type relaxation. It is clear from the plots that both the samples have high grain boundary resistance which is a primary requirement for good dielectrics. Additionally, the slope of Z' - Z'' plot of the sample LZC6 is greater than that of LZC5 sample which could be attributed to the drastic change in nanoparticles sizes including the non-uniformity of grain boundaries of the former.

Conclusion

Polycrystalline nanoparticles of $Li_{0.3}Zn_{0.3}Co_{0.1}Fe_{2.3}O_4$ are prepared by sol-gel method and their structural and dielectric properties are studied. Nano-crystallites of sizes 16.9 and 38.9 nm show very small values of r.m.s. lattice strains 1.25

x 10^{-4} and 1.15 x 10^{-3}, respectively which confirm minimized crystal defects in the prepared samples. Dielectric constant of both the samples decreases at higher frequency and high dielectric constant at lower frequency is due to the Maxwell-Wagner type interfacial polarization. At higher temperatures, this polarization decreases abruptly, and loss tangents take a constant value at high temperatures as well as high frequencies. The dielectric strength of LZC6 sample (38.9 nm) at 325 K is maximum (606), so the break down voltage for this sample will be maximum. Hence, nanoparticles of $Li_{0.3}Zn_{0.3}Co_{0.1}Fe_{2.3}O_4$ with $<d_{cryst}>$ of 38.9 nm could be considered as a potential dielectric candidate when dielectric strength will be main concern. But when overall performance is a concern, then considering higher value of impedance, high frequency permittivity, and relaxation time along with lower dielectric loss LZC5 will be a potential dielectric for application cases.

Acknowledgments

Authors want to acknowledge WBDST (292(Sanc.)/ ST/P/S&T/16G-28/2017, Dated: 28.03.2018) for their financial support of this work. Authors wish to acknowledge DST-SERB, Govt. of India (EMR/2017/000832, Dated: 19.03.2018) for the financial assistance. Authors also want to acknowledge the financial support provided by UGC, Govt. of India, through the CAS program (No. F.530/20/CAS-II/2018 (SAP-I), Dated: 25.07.2018), FIST, DST Govt. of India (Ref: SR/FST/PS-II/2018/52, TPN No- 19862,) and PURSE-II, DST, Govt. of India (No. SR/PURSE Phase-2/34, Dated: 27.02.2017).

Conflict of Interest

The authors declare that they have no known competing financial interests or personal relationships that could have appeared to influence the work reported in this paper.

References

1. Teixeira SS, Graça MP, Costa LC. 2012. Dielectric, morphological, and structural properties of lithium ferrite powders prepared by solid state method. *J Non Cryst Solids* 358(16): 1924-1929. https://doi.org/10.1016/j.jnoncrysol.2012.06.003
2. Reddy PV, Reddy VD. 1994. Far-infrared spectral studies of some lithium-nickel mixed ferrites. *J Magn Magn Mater* 136(3): 279-283. https://doi.org/10.1016/0304-8853(94)00321-1
3. Venudhar YC, Mohan KS. 2002. Dielectric behaviour of lithium-cobalt mixed ferrites. *Mater Lett* 54(2-3): 135-139. https://doi.org/10.1016/S0167-577X(01)00551-1
4. Watawe SC, Sarwade BD, Bellad SS, Sutar BD, Chougule BK. 2000. Microstructure, frequency and temperature-dependent dielectric properties of cobalt-substituted lithium ferrites. *J Magn Magn Mater* 214(1-2): 55-60. https://doi.org/10.1016/S0304-8853(00)00033-0
5. Watawe SC, Bamne UA, Gonbare SP, Tangsali RB. 2007. Preparation and dielectric properties of cadmium substituted lithium ferrite using microwave-induced combustion. *Mater Chem Phys* 103(2-3): 323-328. https://doi.org/10.1016/j.matchemphys.2007.02.037
6. Hankare PP, Patil RP, Sankpal UB, Jadhav SD, Mulla IS, et al. 2009. Magnetic and dielectric properties of nanophase manganese-substituted lithium ferrite. *J Magn Magn Mater* 321(19): 3270-3273. https://doi.org/10.1016/j.jmmm.2009.05.074
7. Dalal M, Greneche JM, Satpati B, Ghzaiel TB, Mazaleyrat F, et al. 2017. Microwave absorption and the magnetic hyperthermia applications of $Li_{0.3}Zn_{0.3}Co_{0.1}Fe_{2.3}O_4$ nanoparticles in multiwalled carbon nanotube matrix. *ACS Appl Mater Interfaces* 9(46): 40831-40845. https://doi.org/10.1021/acsami.7b12091
8. Dey CC, Sadhukhan S, Mitra A, Dalal M, Shaw A, et al. 2021. Magnetic energy morphing, capacitive concept for $Ni_{0.3}Zn_{0.4}Ca_{0.3}Fe_2O_4$ nanoparticles embedded in graphene oxide matrix, and studies of wide-band tunable microwave absorption. *ACS Appl Mater Interfaces* 13(39): 46967–46979. https://doi.org/10.1021/acsami.1c10241

J. Soils and Crops 33 (2) 289-292, December 2023

ISSN 0971-2836 (Print)
ISSN 2582-2756 (Online)

PATTERNS OF SEED DEVELOPMENT IN PEA (*Pisum sativum* L.)

Arindam Mandal[1], Prabir Chakraborti[2] and Niranjan Bala[3]

ABSTRACT

The experiment was conducted to evaluate the performance of the developmental pattern of the seed considering the morphological, physiological and biochemical changes. The pea seeds (*Pisum sativum* L.) cv. AP-3 was collected from every 3 replications under RBD fashion in University (BCKV) farms considering consecutive two years (2018-19 and 2019-20). A sufficient number of flowers was tagged on a specific day beginning from the 10th day after anthesis (DAA) to the 45th DAA allowing for 5 days interval. The collected seeds were examined for seed developmental programmes considering seed length, width, fresh and dry seed weight, chlorophyll content, and alpha-amylase activity of the seed. Seed length and width were increased up to 35th DAA. Enrichment of seed dry weight was noted up to 35th DAA though the seed dry weight was increased up to the last stage of maturity. The chlorophyll content and alpha-amylase activity were highest in 20th DAA and 30th DAA, respectively and declined afterwards. In concern of physiological maturity, the second last stage (40th DAA) may be the suitable stage for maturity because maximum dry matter accumulated in the seed at this stage (40th DAA). Hence, this stage may be suitable for seed maturity. From the study, it can be inferred that, the perfect harvesting time of pea pod [*P. sativum* (L.) cv. AP-3] was 40th days after anthesis.

(Key words: Development, pea seed, physiological maturity, seed morphology, *Pisum sativum*)

INTRODUCTION

Field pea (*Pisum sativum* L.) is one of the world's essential and ancient cultivated vegetables. It is *rabi* season pulse vegetables widely cultivated for their green pods worldwide (Kumar *et al.*, 2014; Kindie *et al.*, 2019). The crop is a major source of protein (21% - 25%) with high levels of amino acids, lysine and tryptophan that have high nutritional value (Bhat *et al.*, 2013; Gregory and Hans, 2021, Sunday and Asabar, 2018). It contains a great amount of carbohydrates, a little quantity of fibre and contains 86% to 87% total digestible nutrients creating the crop also an outstanding livestock feed. India is the second largest producer of peas after China. Higher production with enriched nutritional values of peas can be achieved by various agricultural management practices to accomplish the peas demand of the world (Kumar *et al.*, 2022; Lal *et al.*, 2022).

The initial stages of seed expansion are categorised by the advanced accumulation of mass, through cell division, elongation, nutrient accumulation, and water uptake (Atif *et al.*, 2013). It is a very difficult task, to control the quantity and quality of seed simultaneously seeing different food reserves within the seed (Jones *et al.*, 2010; Aghamirzaie *et al.*, 2013). The developmental process is usually alienated into three stages i.e. embryogenesis, expansion, and maturation according to adjustments in seed weight (Ochatt, 2015; Mandal *et al.*, 2017). In the first stage of seed development or embryogenesis, the embryo is differentiated into various types like globular, heart and torpedo that can be terminated at the cotyledon stage, alike somatic embryos (Verdier *et al.*, 2013). Numerous studies have shown that the time for optimum harvest maturity depends on the accumulation of maximum dry matter in seed or physiological maturity for obtaining good quality seed (Mandal *et al.*, 2017). Moreover, the environment plays a vital role in the maturation process in addition to the time taken for a particular crop harvest that adjusts the final seed quality (Weerasekara *et al.*, 2021). The physiological maturity stage for pod and seed may be modified by the diverse nature of the environment, genotypic attitude as well as soil conditions (Li *et al.*, 2017; Raveneau *et al.*, 2011). Generally, good quality is characterized by storability, percentage of germination, seedling vigour, stable appearance in uniformity and establishment of seedlings, improved tolerance to environmental hazards and more constant maturity of the crop (Mandal *et al.*, 2017; Filho, 2015).

In the present situation, the seed development and maturation study are appropriate and important as the seed collection may be perfect to escape ageing and to obtain the optimum quality that kept the standard viability, vigour and ultimate field performance. The physiological maturity along with the specific pattern of seed development considering morphological, physiological and biochemical

1. Asstt. Professor of Botany, Bejoy Narayan Mahavidyalaya, Hooghly, 712147, WB, India
2. Assoc. Professor of Seed Science and Technology, BCKV, Nadia-741252, WB, India
3. Asstt. Professor of Botany, Sreegopal Banerjee College, Hooghly, 712148, WB, India

seed traits may be helpful for succeeding in the seed production of pea.

MATERIALS AND METHODS

The observations were continued on various seed traits like length and width of seed, fresh and dry seed weight, seed chlorophyll content, alpha-amylase activity at 24 hrs. of seed imbibition considering the crop Pea (*Pisum sativum* L.) cv. AP 3. The seeds were collected during seed growth at specific intervals from replicated field plots under AB block Seed Farm, Kalyani, BCKV (Agriculture University), West Bengal considering two consecutive years (2018-19 and 2019-20). A sufficient number of flowers was tagged on a particular day of anthesis under a specific plot to observe the phenology during seed growth. Developing seeds were collected at eight various phases beginning from the 10th day after anthesis (DAA) to the 45th DAA allowing for 5 days interval. D_1, D_2, D_3, D_4, D_5, D_6, D_7 and D_8 refers 10th DAA, 15th DAA, 20th DAA, 25th DAA, 30th DAA, 35th DAA, 40th DAA and 45th DAA respectively. Observations were recorded on 50 seeds of each replication. Chlorophyll was estimated by following the protocol of Arnon (1949) and alpha-amylase activity at 24 hrs. of imbibition (Cui *et al.*, 2002). Seed length, seed width, fresh weight, dry weight, moisture content, chlorophyll content and alpha amylase contents were measured after 10th DAA to 45th DAA at an interval of 5 days following protocols of the International Seed Testing Association (Anonymous, 1976). Statistical analysis was done considering the factorial analysis of 2 factors under CRD fashion (Krzywinski and Altman, 2014).

RESULTS AND DISCUSSION

The observations on seed development progressed in significant differentiation with some exceptions at the end. During seed growth, the seed length showed progression (Table 1) up to D_6 (35th DAA) followed by a small decline at the last two stages of maturity (40th DAA and 45th DAA). Similarly, the width of the seed followed a similar pattern considering the value of subsequent years where significant enhancement was sustained up to D_5 (30th DAA) followed by a significant lessening in seed growth. The fresh and dry weight of pea seeds showed valuable indications regarding seed maturity. The increasing trend was observed up to D_6 (35th DAA) for fresh weight, while the inclination on dry weight was followed up to maturity. The dry matter accumulation evidently indicated its advanced deposition particularly at the last two stages i.e. D_7 (40th DAA) and D_8 (45th DAA) though a non-significant observation was followed in between them. During seed development and maturation, the differentiation in dry matter accumulation was recorded over the years of experimentations indicating its varying response towards differential climatic conditions over the years. An increasing tendency in development was recorded up to stage D_7 (40th DAA) for both the years. Among various phases as treatment, D_6 (35th DAA) exposed the highest effect in fresh weight of seed development with a significant manner that was abruptly declined, it might be due to reduction of seed moisture. A decreasing propensity was followed in seed moisture content favourable for boosting seed maturation. A reduction was determined in every step up to D_8 (45th DAA) though the rate was advanced in later stages with the highest at the ending i.e. D_7 (40th DAA) to D_8 (45th DAA). The dry matter in the seed was slowly added with the progression of seed maturation as the elimination of moisture was supportive to endure the suitable maturation. However, relative humidity may influence seed maturity. The chlorophyll content of the seed was measured carefully as its quantity was dropped after D_5 (30th DAA) to the end. The enzyme alpha-amylase may have a role in seed germination through the utilisation of seed deposition. In the seed developmental stages, it showed differential action of alpha-amylase where significant variation was observed between advanced stages of seed maturity. The alpha-amylase activity was increased with the progression of seed development after D_5 (30th DAA). It was dropped rapidity at the last stages. The important variation was noted in mean values of development phases in continuation of its marked superiority up to D_5 (30th DAA) or D_6 (35th DAA) though all parameters were not truly followed. A sharp decreased was observed in the last stage i.e. D_8 (45th DAA) for both the years. There was a significant variation between Y_1 (1st year i.e. 2018-19) and Y_2 (2nd year i.e. 2019-20) for all characters except in seed length and width (Table 2).

The association among various morphological and biochemical parameters of pea seeds was observed through correlation (Table 3). The morphological characters such as seed length (-0.599), seed width (-0.621), fresh weight of seed (-0.512), dry weight (-0.880) with the moisture content of seed showed a negative correlation but a significant positive association was observed with alpha-amylase (0.508) and chlorophyll content (0.514) indicating moisture favours their actions. Seed length showed a positive correlation with seed width (0.960), fresh weight (0.936) and dry weight of seed (0.808) but the correlation with chlorophyll content was not-significant.

Table 1. Study on various qualitative parameters of seed during seed developmental stages

Characters	D_1(10th DAA)	D_2(15th DAA)	D_3(20th DAA)	D_4(25th DAA)	D_5(30th DAA)	D_6(35th DAA)	D_7(40th DAA)	D_8(45th DAA)	SEm (±)	LSD 0.01
Seed Length (mm)	4.420	5.610	9.110	9.890	10.470	11.140	11.060	10.640	0.012	0.351
Seed Width (mm)	2.585	3.358	5.415	7.527	9.168	9.778	9.112	8.722	0.197	0.571
Fresh weight of seed (g)	0.019	0.256	1.606	3.015	3.702	4.597	3.994	2.848	0.041	0.120
Dry weight of seed (g)	0.003	0.038	0.304	0.701	1.017	1.726	2.087	2.115	0.013	0.038
Moisture content	86.47	85.48	81.08	76.08	72.38	62.45	47.72	16.48	0.510	1.480
Chlorophyll content (mg g^{-1})	0.40	0.56	0.97	0.71	0.62	0.54	0.43	0.37	0.014	0.04
á- amylase (µg g^{-1} m^{-1})	99.5	135.7	181	210.8	257	196.3	131.7	63.0	37.37	12.91

Table 2. Study on various qualitative parameters of different seed growth stages (average throughout the development) considering two years and its interaction effects

Year	Seed Length (mm)	Seed Width (mm)	Fresh weight of seed (mg)	Dry weight of seed (mg)	Moisture content	Chlorophyll content (mg g^{-1})	á- amylase (µg g^{-1} m^{-1})
Y_1 (2018-19)	9.104	6.917	2.495	0.962	67.4	0.588	149.0
Y_2 (2019-20)	8.979	7.000	2.514	1.035	64.7	0.562	169.8
SEm (±)	0.061	0.099	0.021	0.007	0.26	0.007	6.46
LSD 0.01	—	—	—	0.019	0.74	0.020	18.69
Y×D							
SEm (±)	0.171	0.279	0.059	0.019	0.975	0.020	18.26
LSD 0.01	—	—	0.17	0.054	2.842	0.057	—

Table 3. Correlation of different seed parameters through seed development

	Seed Length (mm)	Seed Width (mm)	Fresh weight of seed (mg)	Moisture content	Chlorophyll content (mg g^{-1})	á- amylase (µg $g^{-1}m^{-1}$)
Seed Width (mm)	0.960**					
Fresh weight of seed (mg)	0.936**	0.967**				
Moisture content	-0.599**	-0.621**	-0.512**			
Chlorophyll content (mg g^{-1})	0.108^{NS}	-0.095^{NS}	-0.058^{NS}	0.514**		
á- amylase (µg $g^{-1}m^{-1}$)	0.325*	0.321*	0.387**	0.395**	0.508**	
Dry weight of seed (mg)	0.808**	0.855**	0.815**	-0.880**	-0.446**	-0.113^{NS}

R^2 value= 0.310; * Significant at P > 0.05, ** P > 0.001, NS- Not significant

Seed width showed a positive correlation with fresh weight of seed (0.967) and dry weight of seed (0.855). The observation was supportive through the action of alpha-amylase which indicated a strong positive correlation with fresh weight (0.387), and chlorophyll content (0.508).

In seed formation, various parameters are crucial for the progress of seed in different aspects *viz*, morphological, physiological, biochemical etc. considering the physiological seed maturation. These can be studied through various modifications that were inter-connected in some morphological and physiological characteristics, precisely seed length, width, moisture content, and accrued dry mass content (Filho, 2015). In seed expansion, the content of water plays a vital role and was primarily involved in the way of cell division and enlargement (Bareke, 2018). In seed growth, the number and size of cells can also be regulated by cell division and enlargement (Dante *et al.*, 2014). Therefore, the seeds are confined to a major part of fresh mass at the initiation of growth, due to the huge amount of water inside the cells that will promote formation of various reserves such as carbohydrates, proteins, lipids and minerals (Carvalho *et al.*, 2016). In addition, water plays a vital role in photosynthesis for the development of photosynthates that will be the portion of seed cells or will be deposited as a reserve. In the existing study, the results indicated that the seeds were matured for physiological maturity after D_5 (35th DAA) as the higher values were non-significant or declining at later stages in most cases. The enzyme exhibited rising measure up to D_5 (30th DAA), and then downward drive till to the seed maturity, as its role may be related to the release of the deposited biomolecules for cell activity during cell division and expansion of seed. Alpha-amylase plays a vital role in the hydrolysis of starch during seed germination and maintenance of water potential.

by providing soluble sugars during seed development (Murtaza and Asghar, 2012). The enzyme alpha-amylase is most commonly recognized with the early outbreak of starch granules (He *et al.*, 2019). After entering its peak at D_5 (30th DAA), the activity was reduced up to the seed maturity as the food reserve was in a stable position. The correlation studies on alpha-amylase indicated a strong positive association with all characters except dry weight as the reduced activity of the enzyme stabilises the reserves and quality of the seed. This study on various seed characters may be the indicator of various precise studies on a particular set of characters.

From the above study it is stated that, the development and maturation of seed through the signal of physiological, morphological and biochemical characters probable physiological maturation of pea seed was at 40th DAA considering dependable character seed dry weight with different configuration variable parameters essential to growing good quality seed. Hence, the optimum dry matter depositing stage at D_7 (40th DAA) can be ideal to confirm physiological maturity in contrast to extreme rate moisture reduction with signalling on total chlorophyll content in a declining trend.

REFERENCES

Aghamirzaie, D., M. Nabiyouni, Y. Fang, C. Klumas, L. S. Heath, R. Grene and E. Collakova, 2013. Changes in RNA splicing in developing soybean (*Glycine max*) embryos, Biol., 2(4):1311–1337.

Anonymous, 1976. International Seed Testing Association. Seed. Sci. Technol. 4:51-177.

Arnon, D.I. 1949. Copper enzymes in isolated chloroplasts. Polyphenoloxidase in *Beta vulgaris*. Plant Physiol. 24: 1–15.

Atif, R.M., F. Boulisset, C. Comeux, R. Thompson and S.J. Ochatt, 2013. *In vitro* auxin treatment promotes cell division and delays endoreduplication in developing seeds of the model legume species *Medicago truncatula*. Physiol. Plant. 148(4): 549–559.

Bareke, T. 2018. Biology of seed development and germination physiology. Adv. Plants Agric. Res. 8(4): 336-346.

Bhat, T.A., M. Gupta, M.A. Ganai, R.A. Ahanger, and H.A. Bhat, 2013. Yield, soil health and nutrient utilization of field pea (*Pisum sativum* L.) as affected by phosphorus and biofertilizers under subtropical conditions of Jammu, Int. J. Modern Plant & Anim. Sci. 1(1): 1-8.

Carvalho, E.R., J. A. Oliveira, D. P. da Rosa Mavaieie, H. W. da Silva and C.G. M. Lopes, 2016. Pre-packing cooling and types of packages in maintaining physiological quality of soybean seeds during storage, J. Seed Sci. 38(2): 129-139.

Cui, K.H., S. B. Peng, Y.Z. ZXing, C. G. Xu, S. B. Yuand and Q. Zhang, 2002. Molecular dissection of seedling-vigor and associated physiological traits in rice. Theor. Appl. Genet. 105:745-753.

Dante, R. A., B. A. Larkins and P. A. Sabelli, 2014. Cell cycle control and seed development, Front. Plant Sci. 5: 1-14.

Filho, J. M. 2015. Seed vigor testing: an overview of the past, present and future perspective, Sci. Agric. 72(4): 363-374.

Gregory, E. and K. Hans, 2021. Field Pea Production. NDSU Extension Service, North Dakota State University of Agriculture and Applied Science, A1166: 1–11.

Gutiérrez-Marcos J. F., M.D. Prà, A. Giulini, L.M. Costa, G. Gavazzi, S. Cordelier, O. Sellam, C. Tarout, W. Paul, P. Perez, H. G. Dickinson and G. Consonni, 2007. Empty pericarp4 encodes a mitochondrion-targeted pentatricopeptide repeat protein necessary for seed development and plant growth in maize. Plant Cell. 19(1): 196–210.

He, Y., Y. Lin, C. Chen, M. Tsai and A.H. Lin, 2019. Impacts of Starch and the Interactions Between Starch and Other Macromolecules on Wheat Falling Number, Compr. Rev. Food Sci. Food Saf. 18(3): 641-654.

Jones, S.I., D.O. Gonzalez L.O. and Vodkin, 2010. Flux of transcript patterns during soybean seed development. BMC Genomics. 11:136.

Kindie, Y., A. Bezabih, W. Beshir, Z. Niguse, Z. Asemamaw, A. Adem, B. Tebabele, G. Kebede, T. Alemayehu and F. Assres, 2019. Field pea (*Pisum sativum* L.) variety development for moisture deficit areas of Eastern Amhara, Ethiopia, Adv. Agric. 2019:1-6.

Krzywinski, M. and N. Altman, 2014. Two-factor designs. Nat. Methods. 11, 1187–1188.

Kumar, A. and A. Choudhary, 2014. In book of scientific cultivation of vegetable pea. Indian Agricultural Research Institute, pp. 45-51.

Kumar, A., M. Kumari and S. Sepehya, 2022. Influences of conjoint use of organic and chemical sources of nutrients on soil properties and yield of pea (*Pisum sativum* L.) under sub-montane and low hills subtropical zone of Himachal Pradesh. J. Soils and Crops. 32(2): 256-262.

Lal, M., M. Kaur, S. Singh and T. Chaudhary, 2022. Response of crop geometry and phosphorus levels on field pea (*Pisum sativum* L.) varieties. J. Soils and Crops. 32(2): 240-245.

Li, R., L. chen, Y. Wu, R. Zhang, C.C. Baskin, J. M. Baskin and X. Hu, 2017. Effects of Cultivar and Maternal Environment on Seed Quality in *Vicia sativa*, Plant Sci. 8:1411.

Mandal, A., J. Mandal, S. Roy and P. Chakraborti, 2017. Developmental Archetype of Lentil (*Lens culinaris* Medik) Seed Considering A Few Seed Traits, Int. J. Pure App. Biosci. 5(6): 1153-1158.

Murtaza, G. and R. Asghar, 2012. α-amylase activities during seed development and germination in pea (*Pisum sativum* L.) treated with salicylic acid. Pak. J. Bot. 44(6): 1823-29.

Ochatt, S.J. 2015. Agroecological impact of an in vitro biotechnology approach of embryo development and seed filling in legumes, Agron. Sustain. Dev. 35: 535–552.

Patrick, J.W. and F.L. Stoddard, 2010. Physiology of flowering and grain filling in faba bean, Fld. Crop Res. 115(3):234–242.

Raveneau, M.P., F. Cadre, P. Moreau-Valancogne, I. Lejeune-Hénaut and C. Duc, 2011. Pea and bean germination and seedling responses to temperature and water potential, Seed Sci. Res. 21(3): 205-213.

Ribalta, F. M., P.N. Maria, E. Kylie, J.R. John, S.C. Janine and J.O. Sergio, 2019. Expression pattern of key hormones related to Pea (*Pisum sativum* L.) embryo physiological maturity shift in response to accelerated growth conditions. Front. Plant Sci. 10:1-7.

Sunday, N and K. Asabar, 2018, Response of yield and yield components of field pea (*Pisum sativum* L.) to application of nitrogen and phosphorus fertilizers, Int. J. Sci. Res. Publ. 8(8): 14-19.

Verdier, J., F. Dessaint, C. Schneider and M. A. Darmency, 2013. A combined histology and transcriptome analysis unravels novel questions on *Medicago truncatula* seed coat, J. Exp. Bot. 64(2):459–470.

Weerasekara, I., U.R. Sinniah, P. Namasivayam, M.H. Nazli, S.A. Abdurahman and M.N. Ghazali, 2021. The Influence of Seed Production Environment on Seed Development and Quality of Soybean (*Glycine max* (L.) Merrill). Agron. J. 11(7):1430.

Rec. on 02.03.2013 & Acc. on 31.03.2023

CONTENTS

THIRD CONCEPT
an international journal of ideas. ISSN 0970-7247

Naming of "BHARATA": Through the Ages

Dr. Bani Patua

Abstract

"Bharat" is a Sanskrit term found in scriptures from around 2,000 years ago. On 18th September 1949, the Constituent Assembly deliberated upon various names for the, yet to born, Indian nation – 'Bharatabarsha', 'Jambudwip', 'Hindustan', 'Bharatbhumi' 'Hind'. While 'India' is the most commonly used name for the country, it is often called 'Bharat' and sometimes 'Hindustan' by Indian officials and the public. Adopting a cultural history perspective, this paper considers some of the inherited discourses on "Bharat" both to and at the time of its official equation with 'India' in the Constitution. India has so many names, these are Mahula, Tenjiku, Aryadesha, All-Hind, Jambudwip, India, Bharat, Republic of India, Bharata, Hindusthan etc. In this article, I will discuss about what are the various name of Bharatabarsha. I will also discuss about what significance did the name of Bharatbarsha have in the socio-religious and historical context? This paper examines the significance of the changing meanings of the naming of India and the reasons for its gradual disuse.

Keywords: Mahula, Tenjiku, Aryadesha, All-Hind, Jambudwip, India, Bharat, Republic of India, Bharata, Hindusthan, Bharatbhumi.

INTRODUCTION

Our beloved motherland 'Bharatvarsh' is one of the oldest countries in the world. This holy land is mentioned in ancient literature Ramayana, Mahabharata and various Puranas. India has been famous for its rich cultural heritage since ancient times. In the history of India, many communities have established their supremacy on this plot in different periods, in such a way this country has been known by different names in different periods. In ancient times, from Jambudweep to Aryavartaand from India to being called Hindustan, the history of this country is very interesting and full of surprises. Like the cultural heritage of India, there is a rich history hidden behind the naming of this country. The preamble to the English version of the constitution starts with the words "We, the people of India ..." and then in Part one of the document it states "India, that is Bharat, shall be a Union of States".

Assistant Professor, Department of History, Bejoy Narayan Mahavidyalaya, Itachuna, Hooghly, The University of Burdwan, West Bengal, India
E-mail: bambrata1910@gmail.com

Solid State Communications 392 (2024) 115658

Contents lists available at ScienceDirect

Solid State Communications

journal homepage: www.elsevier.com/locate/ssc

Impact of evolution of structural defects on the ferromagnetic and electrical properties of laser deposited Indium-doped SnO_2 thin films

Shyamsundar Ghosh

Department of Physics, Bejoy Narayan Mahavidyalaya, The University of Burdwan, P.O.-Itachuna, Hooghly, 712147, India

ARTICLE INFO

Communicated by: Saha Bivas

Keywords:
Oxide thin-films
d^0-ferromagnetism
Tin-vacancy defects
Positron annihilation spectroscopy
Raman spectroscopy

ABSTRACT

Impact of non-magnetic cationic-substitution on the evolution of structural defects and correlated ferromagnetic and electrical properties are investigated in series of pulsed laser deposited $Sn_{1-x}In_xO_2$ ($0.0 \leq x \leq 0.12$) thin films. Beyond the nominal doping concentration of 2 at.% (i.e. $x > 0.02$), Indium (In)-doped SnO_2 film switches to exhibit from n-type to p-type electrical conductivity and simultaneously the magnetization (M_S) as well as the Curie temperature (T_C) of the films increase significantly. Estimated values of 'M_S' and 'T_C' are found to achieve as large as 15.21 emu/cm^3 and 540 K respectively when In-doping concentration approaches towards $x = 0.08$ and afterwards tend to decrease abruptly. Various spectroscopic techniques including Positron Annihilation Lifetime Spectroscopy (PALS) have detected the existence of Sn vacancy (V_{Sn}) defects within $Sn_{1-x}In_xO_2$ films arise as the effect of In-substitution at Sn site (In_{Sn}) under O-rich atmosphere. The estimated positron lifetimes and the increase of line-shape *S*-parameter confirm the rise of V_{Sn} defects which serve as the major source of magnetic moments in non-magnetic host SnO_2. Besides, In_{Sn} defects introduce excess holes within SnO_2 lattice and thereby the magnetic spin-spin RKKY interaction between near-by V_{Sn} defects are mediated ferromagnetically through the localized holes. For $x > 0.08$, stabilization of various donor-type defects such as Sn interstitial (Sn_i), indium interstitial (In_i) actually compensates the acceptors that leads to reduce the effective hole density consequently diminishing the strength of ferromagnetism within SnO_2. Hence, tuning of such ferromagnetic and semiconducting properties through non-magnetic cationic substitution in transparent conducting oxides can be very promising in the field of next-generation spintronics.

1. Introduction

In recent years, exploration of defect-induced magnetism (DIM) in low-dimensional (1D/2D) otherwise non-magnetic transparent semiconducting oxides (TCOs) has been drawn immense research attention due to the possibility of intrinsic spin polarization in optically active semiconducting host materials for the next-generation spintronic and opto-spintronic devices [1–3]. In search of room-temperature (RT) dilute magnetic semiconductors (DMSs), oxides like ZnO, TiO_2, SnO_2 etc. have been studied extensively with doping of few percentages of transition-metal (TM) or rare-earth (RE) elements. However, the magnetic properties remains controversial [2,4] and the possibility of existence of magnetic impurity has imposed greatest challenge to the scientists to justify intrinsic nature of the ferromagnetism (FM) [2–8]. On the other hand, existence of DIM in several low-dimensional oxide-based nanostructures [1,2,9–11] paved an alternative way for introducing FM, generally known as d^0 FM, without doping with any magnetic element. The name d^0 appears because the magnetic moment arises without presence of localised *d*-shell electrons. structural defects are generally found to play important role for such robust FM. However, proper control and manipulation of defects within the host material have been quite challenging so far. In many cases, oxygen vacancy (V_O) defects have been attributed to be responsible for such FM [12,13] in oxides. On the other hand, several theoretical reports [14–16] also suggested that cation vacancy defects can introduce larger magnetic moment in oxides which mainly arises from 2p orbital electrons of oxygen surrounding the cation vacancy site. However, proper defect engineering is essential to understand, stabilize and control DIM within oxides nanomaterials and thin films.

SnO_2 has been one of the important TCO material in the field of electronics, optics and potential devices [17]. Earlier, Ogale et al. [6] reported RTFM with giant magnetic moment in transition-metal Co-doped $SnO_{2-\delta}$ thin films. Later Barla et al. [7] reported that Co-*3d* electrons are not directly responsible for the observed ferromagnetism. In fact, even in our previous work [8] also, bulk Co-doped SnO_2 exhibited only paramagnetic behaviour, whereas FM appears only in

E-mail addresses: shyamsundar@bnmv.ac.in, sghoshphysics@gmail.com.

https://doi.org/10.1016/j.ssc.2024.115658
Received 1 April 2024; Received in revised form 13 July 2024; Accepted 15 August 2024
Available online 15 August 2024

case of nanostructures. This signifies structural defects may play animportant role in inducing FM in SnO_2 nanostrutres. Unlike ZnO, DIM in low-dimensional SnO_2-based nanomaterials has not been explored very consistently in literature. Although several factors like oxygen vacancies [18,19], bound magnetic polaron [20], Sn interstials [21], etc. have been reported for the origin of FM in SnO_2 nanostructues and thin films, still the exact origin is not properly understood. In addition, the first principle caculation by Wang et al. [22] and density function theory (DFT) calculations by Rahman et al. [23] suggested tin-vacancy (V_{Sn}) defects can induce large magnetic moment within SnO_2 and it is quite possible to stabilize carier-mediated ferromagnetism exceeding the threshold concentration of V_{Sn} defects. However, the experimental evidence of V_{Sn} vacancy-induced magnetism for SnO_2 is very rare. In addition, Rahman et al. [23] also suggested that the giant magneic moment observed by Ogale et al. [6] might be due to formation of signifcant amount V_{Sn} defects. Howerver due to its high formation energy, stablization of significant amount of cation-vacancy defects are quite challenging in pristine oxides [24]. Theoritcally, it has been predicted [24] that the formation energy of cation-vacancy may decrease during the growth under oxygen-rich atmosphere. In addition, Bouzerar et al. [25] recommended that substitution of few percentage of lower valence non-magnetic element at cation site can also reduce the formation energy of cation-vacancy defects significantly.

In this backdrop, we have deposited pristine and non-magnetic Indium (In)-substituted SnO_2 thin-films under oxygen-rich atmosphere using pulsed laser depostion (PLD) technique. Indium is trivalent and thus the subsitution of In^{3+} at tetravalent Sn stie is expected to introduce holes within SnO_2 lattice. In adition, O-rich atmosphere within PLD chamber may trigger the formation of cation vacancy defects within doped SnO_2 films rather oxygen vacancy. Thus evolution of structural defects upon In-substitution has been analysed dusing various spectroscopic techniques including positron annihilation lifetime spectroscopy (PALS) and correlation the phenomena of d^0 FM of the In-substituted SnO_2 films.

2. Experimental details

High pure SnO_2 and In_2O_3 powders (99.99 %) are mixed with appropriate ratio and grinded properly to prepare a uniform precursor. Then precursor mixture is annealed at high temperature (800 °C) for 8hrs under O_2-rich atmosphere. Then it is converted into a pallet which is used as the source material in pulsed laser deposition (PLD) chamber to fabricate of the series of In-doped SnO_2 thin films on c-axis (0001) sapphire (Al_2O_3) substrate. At first, the PLD chamber evacuated down to pressure of 2×10^{-5} mbar and is filled with pure oxygen gas of partial pressure 10 mbar. Thereafter, different $Sn_{1-x}In_xO_2$ ($0.0 \leq x \leq 0.12$) thin films are fabricated with varying In-doping concentration (x) under O_2-rich atmosphere. During preparation of the films, Kr–F excimer laser has been operated with laser power density ~1.41 J/cm^2 and the pulse repetition rate of 5 Hz. All the pure and In-doped SnO_2 films are deposited for 30 min keeping the substrate temperature fixed at 600 °C. After completion of deposition process, each film is annealed at 600 °C for 10 min at the same atmosphere and then cooled naturally at RT.

The films are characterized by Grazing Incidence X-ray Diffraction (GIXRD, X'Pert Pro, Panalytical), Field Emission Scanning Electron Microscopy (FESEM, FEI Helios Nanolab-600), Transmission electron microscopy (TEM) and associated Energy dispersive spectrum (EDS). Magnetic properties are analysed using superconducting quantum interference devices (SQUIDs), magnetic force microscopy (MFM) and atomic force microscopy (AFM). Dynamics of defects within the host materials are probed using X-ray photoelectron spectroscopy (XPS, PHI 5000 Versaprobe II Scanning XPS microprobe, ULVAC-PHI, USA) with a monochromatic Al-K_α radiation; Raman spectroscopy (LABRAM HR from Horiba Jobin Yvon) and Photoluminescence (PL) spectroscopy (Horiba Jobin Yvon, Fluorolog-3) having Xe lamp source under the excitation wavelength of 330 nm. For electrical characterization, Hall-effect experimental set up and four-probe methods are employed. Finally, to understand the dynamics of defects more in depth, Positron Annihilation Lifetime Spectroscopy (PALS) measurement are performed using the source materials (pallets) in power form. Radioactive ^{22}Na (~10 μCi in strength) deposited on a thin (~2 mg cm^{-2}) nickel foil is used as source positrons. The sample along with the source is kept under vacuum throughout the experiment and covered the source to ensure full capture and annihilation of the positrons from the source within the sample itself. Using a slow-fast coincidence spectrometer, the γ rays are detected with time resolution 170 ps obtained as full width at half-maximum of the ^{60}Co γ-ray coincidence spectrum. Under each positron lifetime spectrum about 1.5 million counts were collected having peak to background ratio better than 10000:1. High pure germanium (HPGe) detectors of resolution 1.27 and 1.33 at 511 keV are used for CDBS measurement. In order to avoid any kind of magnetic contamination of the films, extreme precautions are adopted in every step during performing experiments including the sample fabrication. In fact, non-magnetic tweezers, non-magnetic containers etc. are used to handle the samples during the entire course of experiments.

3. Results and discussions

3.1. Structural properties

Fig. 1 shows XRD patterns of the $Sn_{1-x}In_xO_2$ ($0.0 \leq x \leq 0.12$) films that indicating tetragonal rutile crystal structure ($a = b \neq c$) of SnO_2 without any evidence of secondary phases within the detection limit of the instrument. As a consequence of In-doping, the lattice volume of tetragonal unit cell initially increases up to In-doping concentration around 8 at.% and thereafter decreases gradually as shown in Fig. 1b. Such increase of lattice volume can be explained due to substitution of larger size In^{3+} ions (0.80 Å) replacing Sn^{4+} ions (0.69 Å) in tetragonal SnO_2 unit cell [26]. On higher doping level, Indium atoms might prefer to occupy lattice interstitial sites, thereby resulting a decrease in lattice volume of the cell. In addition, the XRD peaks are also found to broaden significantly after doping. Such broadening may suggest a decrease in crystalline quality of the films. The crystallite sizes (t) are estimated from the Scherrer equation using (110) & (101) diffraction peaks after subtracting the instrumental broadening using LaB_6 standard as shown in Fig. 1c. It has been found the average values of crystallite size initially decreases on increasing In-concentration and then increases slowly on further doping. Surface morphology of the films are identified using FESEM and representative FESEM images for $Sn_{0.92}In_{0.08}O_2$ and undoped SnO_2 are shown in Fig. 2a and b respectively while the inset of the respective figures exhibit the corresponding TEM micrograph. Using TEM micrograph, the average particle size (d) the films are estimated for each film. Fig. 2d shows the particle size distribution for $Sn_{0.92}In_{0.08}O_2$ film and average value of 'd' is found to be ~35.2 nm. Estimated values of average particle size (d) is found to decrease gradually with increase of In-doping concentration as shown in Fig. 2e. The variation of particle size (d) is quite similar to the crystallite size (t) as obtained from earlier XRD analysis (Fig. 1c). Chemical compositions of the films as obtained from EDX associated with TEM are summarized in Table 1 and a representative EDX spectrum for $Sn_{0.92}In_{0.08}O_2$ are shown Fig. 2c.

Chemical composition of the films is also analysed using XPS techniques (Table 1) and are found to be in good agreement with earlier EDX analysis. Fig. 3a shows the core-level XPS spectra for In 3d-obitals that exhibit two distinct peaks at 445.5 and 453.2 eV assigned to In $3d_{5/2}$ and In $3d_{3/2}$ respectively within $Sn_{0.92}In_{0.08}O_2$ film. This confirms that indium ions within SnO_2 lattice are in In^{3+} oxidation state. Core-level XPS spectra for O1s-orbital as shown in Fig. 3b exhibits a strong peak at 530.9 eV confirms the presence of oxygen (O^{2-}) ions [27,28] along with extended tail shouldered at higher binding energy of 532 eV which may be due to structural defects or oxygen deficiency [27,28]. The asymmetric character and broad shoulder towards higher binding energy of Sn 3d core-level XPS spectra, in Fig. 3c, can be well deconvoluted into

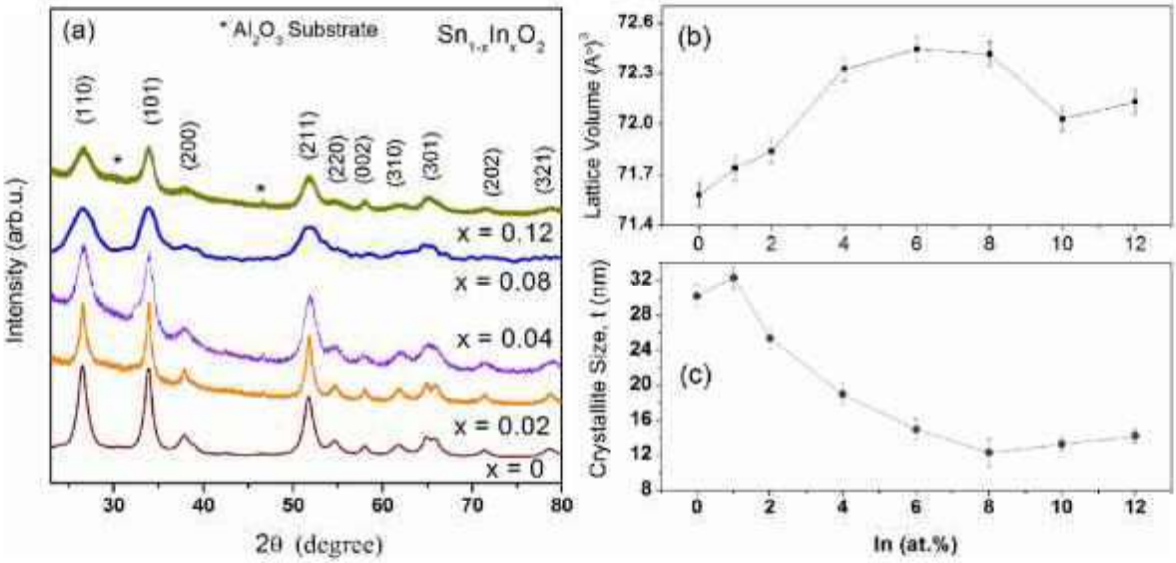

Fig. 1. (a) XRD pattern of $Sn_{1-x}In_xO_2$ thin films prepared under O-rich atmosphere. (b) Variation of the lattice volume and crystallite size of the films with In-doping concentration (at.%).

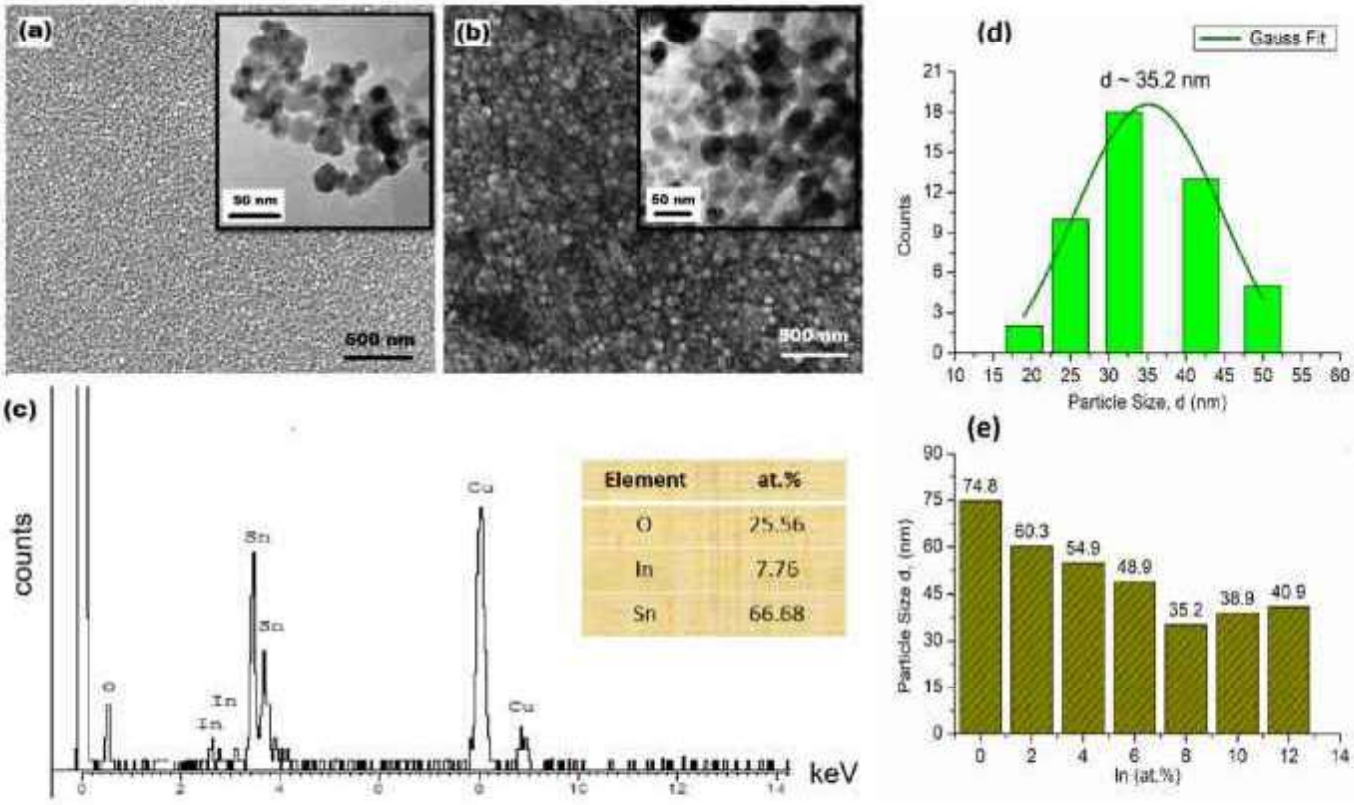

Fig. 2. (a) and (b) FESEM image of $Sn_{0.92}In_{0.08}O_2$ and undoped SnO_2 thin films while the inset shows the corresponding TEM image of the films (c) EDX spectra of $Sn_{0.92}In_{0.08}O_2$ reflecting the chemical composition of the film (d) particle size distribution of $Sn_{0.92}In_{0.08}O_2$ (e) Variation of particle size with In-doping (at.%) estimated from TEM.

two sets of peaks. First set of peaks towards the higher binding energy i. e. 486.8 and 495.3 eV correspond to $3d_{5/2}$ and $3d_{3/2}$ orbitals respectively arises due to Sn^{4+} ions at lattice site [28,29] while the second set of peaks, i.e. 486.1 and 494.6 eV arise due to presence of lower valence Sn or metallic Sn within the lattice [29,30] due to In-doping.

3.2. Magnetic and electrical properties

All the $Sn_{1-x}In_xO_2$ thinfilms films exhibit ferromagnetic behaviour at RT as well as low temperture. Fig. 4a shows the representaive magnetization curve, M (H) as a function of external magnetic field (H) for $Sn_{0.92}In_{0.08}O_2$ thinfilm at 300 K and 5K. Further, it is interesting to note that the undoped SnO_2 film also exhibit weak ferromagnetic behaviour

Table 1
Estimated values of crystallite size (*t*), particle size (*d*) and chemical composition (at.%) for $Sn_{1-x}In_xO_2$ ($0.0 \leq x \leq 0.12$) thin films.

Samples	Average Crystallite size, *t* (nm) from XRD	Composition (at%)						Particle size, *d* (nm) from TEM
		EDX analysis			XPS analysis			
		Sn	O	In	Sn	O	In	
Undoped SnO_2	30.2	70.13	29.87	–	69.98	30.02	–	74.8
$Sn_{0.99}In_{0.01}O_2$	32.3	70.24	29.34	0.42	69.91	29.56	0.53	68.7
$Sn_{0.98}In_{0.02}O_2$	25.4	69.57	29.12	1.31	69.57	29.12	1.20	60.3
$Sn_{0.96}In_{0.04}O_2$	19.0	68.91	27.68	3.41	70.05	27.06	2.89	54.9
$Sn_{0.94}In_{0.06}O_2$	15.0	67.47	27.16	5.37	67.24	27.60	5.16	48.9
$Sn_{0.92}In_{0.08}O_2$	12.3	66.68	25.56	7.76	65.95	26.81	7.24	35.2
$Sn_{0.9}In_{0.1}O_2$	13.9	67.77	23.34	8.89	68.21	23.28	8.51	38.9
$Sn_{0.88}In_{0.12}O_2$	14.2	68.35	21.82	9.83	69.32	24.01	9.67	40.8

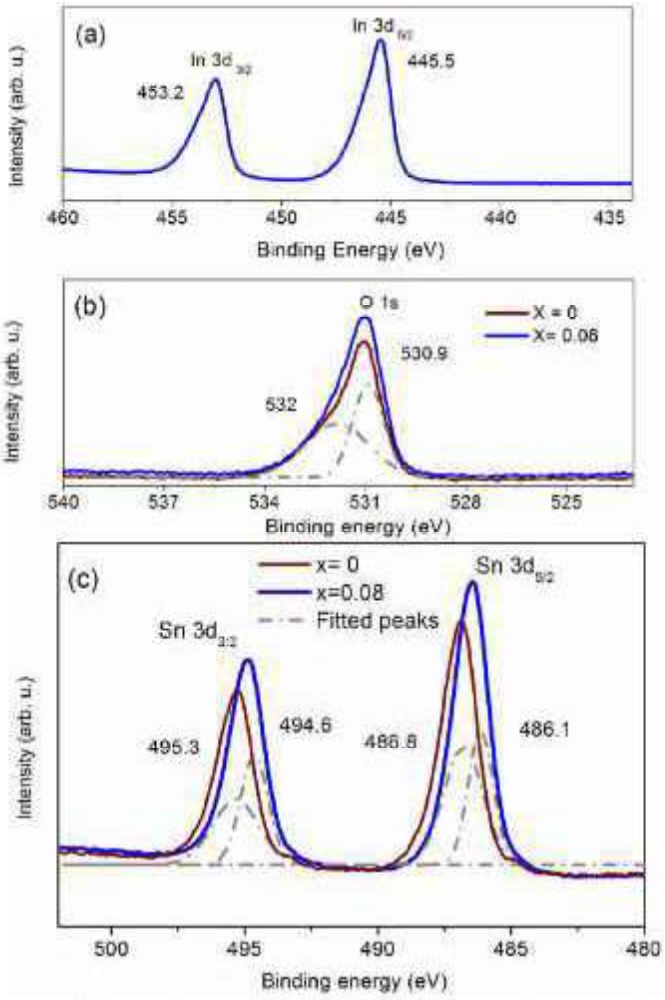

Fig. 3. (a) Core-level XPS spectra for (a) In-*3d* (b) O-*1s* and (c) Sn-*3d* orbitals of undoped SnO_2 and $Sn_{0.92}In_{0.08}O_2$ films.

but the corresponding bulk SnO_2 is diamagnetic as shown in Fig. 4b. In order to eleminate the doubts of any ferromagnetic impurities, magnetic measurement of both sapphhire substrate and In_2O_3 powder are performed. Both exhibit diamagnetic nature as shown in Fig. 4b. Hence it is clear that the FM appeared here in series of SnO_2 thinfilms is quite intrinsic and the magnetic moment is found to enhance significantly after In-doping. It can be seen from Fig. 4c that saturation magnetic moment (M_S) for the $Sn_{1-x}In_xO_2$ thinfilms gradually increases up to a certain In-concentration (~8 at.%) and then decreases on further doping. In order to confirm the ferromagnetic nature of the films, temperature-dependent Zero-field cooled (ZFC) and field-cooled (FC) magnetizaton measuements are also performed and a representative FC-ZFC magnetization curve for $Sn_{0.92}In_{0.08}O_2$ film is shown in Fig. 4d. High temperature magnetization M (T) measurements for $Sn_{0.92}In_{0.08}O_2$ thinfilm as shown in Fig. 4e indicates the existence of the Cuire temperature (T_C) ~ 540 K. It is noticeable that values of estimated T_C for all $Sn_{1-x}In_xO_2$ films are found to be well above RT. On increasing of In-doping concentration, Similar to M_S, T_C of the $Sn_{1-x}In_xO_2$ films also increases initially as depicted in Fig. 4f and then decreases on higher doping level. Hence, it is evident that doping of non-magnetic indium has definite role in inducing RTFM in such low dimension SnO_2 films.

Temperature-dependent resistivity measurements of the $Sn_{1-x}In_xO_2$ films as shown in Fig. 4g confirm the typical semiconducting behaviour of the $Sn_{1-x}In_xO_2$ films. On increasing In-doping concentration (x), resistivity (ρ) of the films are found to enhance gradually up to 8 at.% of In-doping, cosequently carrier density decreases as shown in Fig. 4h. However, the reverse bahaviour are observed when doping conentration exceeds the level of 8 at.%. For lower doping ($x < 0.08$), In^{3+} ions generally substitute the Sn^{4+} ions as evident from earlier XPS and XRD analysis, thereby form acceptor-type In-substitutional defects (In_{Sn}) within lattice. As a consequent, it rises the p-type conductivity of the film. Besides that, stabilization of acceptor-type Sn vacancy (V_{Sn}) defects may also increase p-type conductivity of the film. For higher hoping ($x > 0.08$), the decrease of film resistivity may be due to formation of donor-type Sn interstitial (Sn_i) defects which can actually compensate the acceptor-type In_{Sn} and V_{Sn} defects. Hall-effect measurements reveal n-type conductivity for undoped SnO_2 and also $Sn_{0.98}In_{0.02}O_2$ films. Interestingly, when $x > 0.02$, In-doped SnO_2 films switches to exhibit p-type conductivity rather n-type. It is worthy to note, as soon as the films switches to p-type conductivity, ferromagnetic property of the $Sn_{1-x}In_xO_2$ films has been found to boost signficantly. Therefore, presence of p-type conductivity arrises due to introduction of holes within $Sn_{1-x}In_xO_2$ films might stimulate the ferromagnetic interaction within SnO_2. Fig. 5a and d represent AFM images of $Sn_{0.92}In_{0.08}O_2$ and unoped SnO_2 respectively. The scale provided with the picture indicates that the surface of $Sn_{0.92}In_{0.08}O_2$ more rough compared to the undoped SnO_2 films. The correnspondingMFM images of $Sn_{0.92}In_{0.08}O_2$ films as shown in Fig. 5b and c, clearly indicating some corase grainlike structures, where the bright and dark grains represent the positive and negetive magnetic poles respectively within the material. The high concentration of such bright and darks grains indicates stronger ferromagnetic ordering for the $Sn_{0.92}In_{0.08}O_2$ film as compared to the undoped SnO_2 films (Fig. 5e and f). Similar behaviours are observed for other In-doped SnO_2 films also.

3.3. Photoluminesence spectroscopy studies

In order to understand the origin of such ferromagnetism in $Sn_{1-x}In_xO_2$ thinfilms, it is essential to study the evolution of defects within the material. PL spectroscopy is known to be promising tool to probe the various defects of within nanostructured materials. PL spectra for various $Sn_{1-x}In_xO_2$ films as shown in Fig. 6a, can be deconvoluted into

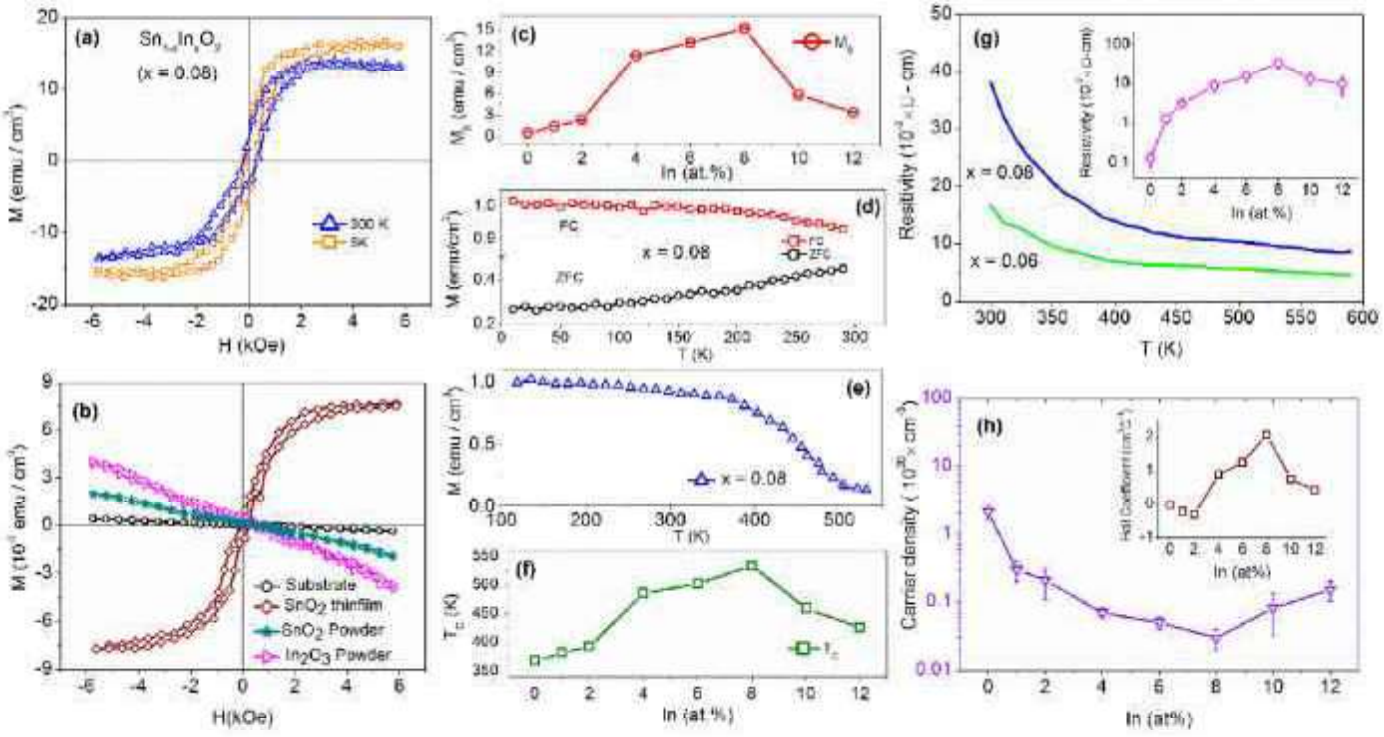

Fig. 4. Magnetization M (H) curve for (a) $Sn_{0.92}In_{0.08}O_2$ thinfilm at 300 K and 5 K (b) SnO_2 thinfilm, bulk SnO_2 powder, In_2O_3 powder along with sapphire substrate. (c) Estimated saturation magnetization (M_S) as function of In-doping concentration (d) Field-cooled (FC) and Zero-field-cooled (ZFC) magnetization curve for $Sn_{0.92}In_{0.08}O_2$ films confirming the intrinsic ferromagnetism of the film. (e) Temperature-dependent magnetization M (T) curve for $Sn_{0.92}In_{0.08}O_2$ thinfilm indicating the existence of Cuire Temperature. (f) Cuire temperature (T_C) for different $Sn_{1-x}In_xO_2$ thinfilms (g) Resitivity as a function of temperature for $Sn_{1-x}In_xO_2$ thinfilms for x = 0.08 and 0.06 shows typical semiconducting behaviour of the films (inset: change in resisitivity as a function of In-doping concentration) and (h) Estimated carrier concentration and Hall coefficient of the different $Sn_{1-x}In_xO_2$ thinfilms.

four different emission bands around wavelength of 366, 385, 460 and 590 nm (Fig. 6b). UV emission around 366 nm generally originates due to the electronic transition close to the band edge thus can be directly proportional to the band gap energy (E_g). As a result of In-doping, the centre of UV emission band shifts towards the higher wavelength indicating a decrease of energy band gap. This decrease in E_g may be due to creation of more In-substitutional (In_{Sn}) acceptor-states within band gap of SnO_2. In addition, the intensity of blue emission band centred around 460 nm is found to enhance gradually up to In-doping of 8 at.% and thereafter decreases on further doping. In order to investigate the origin of blue emission,$Sn_{0.92}In_{0.08}O_2$film are annealed in O_2 atmosphere for 2h and PL spectra of the annealed $Sn_{0.92}In_{0.08}O_2$ film is shown in Fig. 6a (curve f). It is very interesting to note that after annealing the intensity of blue emission band (460 nm) has enhanced significantly while the yellow-orange emission at 590 nm vanishes. After high-temperate annealing in O_2 atmosphere, it is expected that concentration of V_O defects should decrease resulting a significant decrease of yellow-orange emission at 590 nm [31,32]. Thus, it can be understood that yellow-orange emission in PL spectra arises for V_O defects [31,32] within SnO_2 lattice. On the other hand, blue emission at 460 nm can be assigned to V_{Sn} defects. This is because annealing in O_2 are found to be very effective to formation of V_{Sn} defects within SnO_2 [31,33]. Moreover, theoretical analysis by Golovanov et al. [34] also suggested that formation energy of cation vacancy defects within metal oxide decreases through cationic substitution under O-rich atmosphere and thereby favours the stabilization of cation vacancy defects. Thus, here in our case, the cationic substitution using In^{3+} favour the formation of V_{Sn} defects within SnO_2. V_{Sn} defects within SnO_2 create a deep level acceptor-band above the valence band and the electronic transition associated with conduction band and V_{Sn} acceptor band can give rise to blue emission having energy ~2.76 eV [32,33]. Hence, blue emission in SnO_2 carries a signature of formation V_{Sn} defects within lattice. As the intensity of blue emission (Fig. 6d) is found to be strongest for $Sn_{0.92}In_{0.08}O_2$ film, therefore, it possesses highest concentration of V_{Sn} defects among all other samples.

3.4. Raman spectroscopy studies

Raman spectroscopy is another important tool to identify crystal structure and defects within the nanomaterials. In general, SnO_2 has tetragonal rutile unit cell which belongs to D_{4h}^{14} ($P_{42/mnm}$) space group that possesses the following vibrational modes as

$$G(Rutile) = A_{1g} + A_{2g} + A_{2u} + B_{1g} + B_{2g} + 2B_u + E_g + 3E_u$$

It can be seen that E_g, A_{1g}, B_{1g} and B_{2g} are Raman active, E_u and A_{2u} mode are IR active but A_{2g} and B_u are neither Raman active nor infra-red (IR) active [35]. Fig. 7a shows Raman spectra for undoped and $Sn_{1-x}In_xO_2$ thinfilms. Raman spectra of the undoped SnO_2 exhibits four different modes such as Eu LO (354 cm^{-1}), E_g (474 cm^{-1}), A_{1g} (643 cm^{-1}) and A_{2u} (690 cm^{-1}) modes that corresponds to the tetragonal rutile crystal structure of SnO_2 [35,36]. E_g mode at 474 cm^{-1} arises due to vibration of oxygen in Sn–O bond, whereas the A_{1g} mode originates due to the contraction and expansion of Sn–O bond within SnO_2 lattice. Beside that, a weaker A_{2g} mode is also found to appear at 574 cm^{-1} and the intensity found to increase gradually on increasing In-doping concentration. On the other hand, A_{1g} mode becomes flatter and shifted towards the lower wavenumber as shown in Fig. 7b. This occurs due to gradual lowering of crystallite size or grain size after In-doping, (as evident from both XRD and TEM analysis) consequently for enhanced of surface to volume ratio of the films. Thus, on increasing the doping concentration, In-doped SnO_2 films are tend to possess more and more surface defects leading to the local lattice disorder which can change the bond lengths significantly and resulting in reduction of space symmetry D_{4h}^{14} [35] of SnO_2 lattice. In fact, the doping of trivalent In^{3+} ions modify

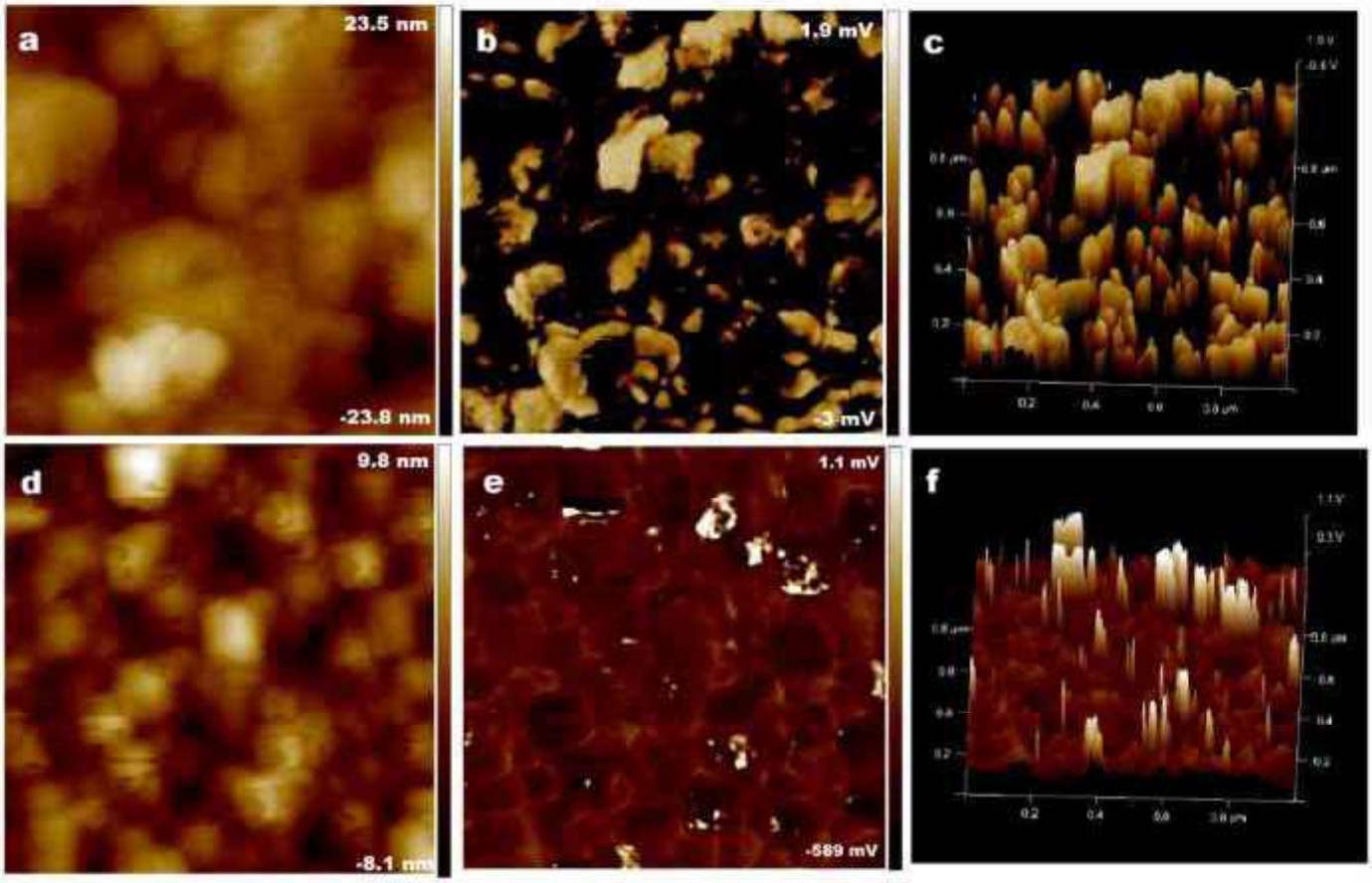

Fig. 5. AFM images for (a) $Sn_{0.92}In_{0.08}O_2$ (d) undoped SnO_2 (Scale bar is provided for understanding of surface topography of the films). The corresponding MFM images (b, c) for $Sn_{0.92}In_{0.08}O_2$ and (e, f) for undoped SnO_2 thin films reavealing the magnetic domain structure.

the local environment surrounding Sn site and can reduce the formation energy of V_{Sn} thus helps to stabilize more V_{Sn} defects [24]. Such serious lattice distortion can transform some Raman inactive modes like A_{2g} and E_u mode into Raman active mode and thus appeared at 574 cm^{-1} and 354 cm^{-1} respectively [37] here in our case. The rise of ratio of intensities A_{2g}/A_{1g} mode, as shown in of Fig. 7c, thus signifies the gradual enhancement of concentration of V_{Sn} defects with increasing In-doping level up to 8 at.% and thereafter diminishes on higher doping level.

3.5. Positron annihilation lifetime spectroscopy studies

PALS is generally known to be very effective to identify the negatively charged cation vacancy defects within the nanomaterials where the positrons can be tarpped for sufficient time. Fig. 8a represents the representative normalised positron lifetime spectra for undoped SnO_2 and $Sn_{0.92}In_{0.08}O_2$ samples. The nature of the spectra depicts an enhancement in the positron lifetimes in $Sn_{0.92}In_{0.08}O_2$ as compared to undoped SnO_2. Using the programme PALSfit [38], three lifetime components such as τ_1, τ_2, τ_3 and their respective relative intensities I_1, I_2 and I_3 are calculated. The shortest lifetime (τ_1) for $Sn_{1-x}In_xO_2$ samples, as shown in Fig. 8b, are found to be slightly greater than the reported positron bulk lifetime of 167 ps in SnO_2 [39]. As the single oxygen vacancy cannot trap positrons, hence, τ_1 might be the average of positron lifetime in bulk and small vacancies like Sn monovacancies (V_{Sn}) or divacancies. On the other hand, the longer lifetime components τ_2 and τ_3 can arise from positron annihilation within the vacancy clusters and annihilation of ortho-positronium atoms in the regions between the crystallites [40]. The variation of longer lifetime components τ_2, τ_3 and their respective intensities I_2 and I_3 are shown in Fig. 8c–f respectively. With increase of doping concentration, the values of positron lifetime components τ_1 and τ_2 gradually increases while τ_3 decreases sharply. The intensity I_2 continues to increase up to In-doping of 8 at. % and afterword decreases that signifies the enhancement of vacancy-clusters. With increase of In-doping initially up to 8 at.%, the formation of Sn monovacancies (V_{Sn}) or Sn vacancy clusters such as $V_{Sn} + In_{Sn}$, $V_{Sn} + O$ etc. effectively leads to the increase positron trapping centres. However, beyond the doping level of 8 at.%, the In^{3+} ions start to occupy the lattice interstitials sites (In_i) which can abruptly block the free diffusion of positrons and thus effectively reduces the positron trapping in defects. Hence, the intensity I_2 suddenly falls and the major contribution to the lifetime τ_2 at this stage arises to those getting annihilated to the crystallite surfaces. However, the other lifetime component τ_3 and its intensity I_3 exhibit systematic variation with In-doping concentration, much significance is not credited as the concerned intensity I_3 is really small (<0.6 %).

The CDBS measurements are performed first by recording the spectra of energies of annihilation gamma rays moving in the opposite directions using high pure germanium detectors. A two-parameter spectrum is thereby generated with the sum and difference of the energies in the X- and Y-axes and the time correlated events in the Z-axis [41]. The distribution of events parallel to the y-axis with sum interval 1022 ± 2.4 keV is a doppler broadened positron annihilation gamma ray spectrum which is free of the detector resolution function and nuclear background effects. Hence, it presents a true reflection of the electron momentum distribution within the material. As the changes in electron momentum distribution are too small to differentiate, the spectra so obtained are generally divided by an identical spectrum obtained for a pure defect free reference sample in order to magnify such small differences. Here, as the reference, we have used single crystalline Al sample with purity 99.999 % and was annealed at 600 °C for 2 h in vacuum before

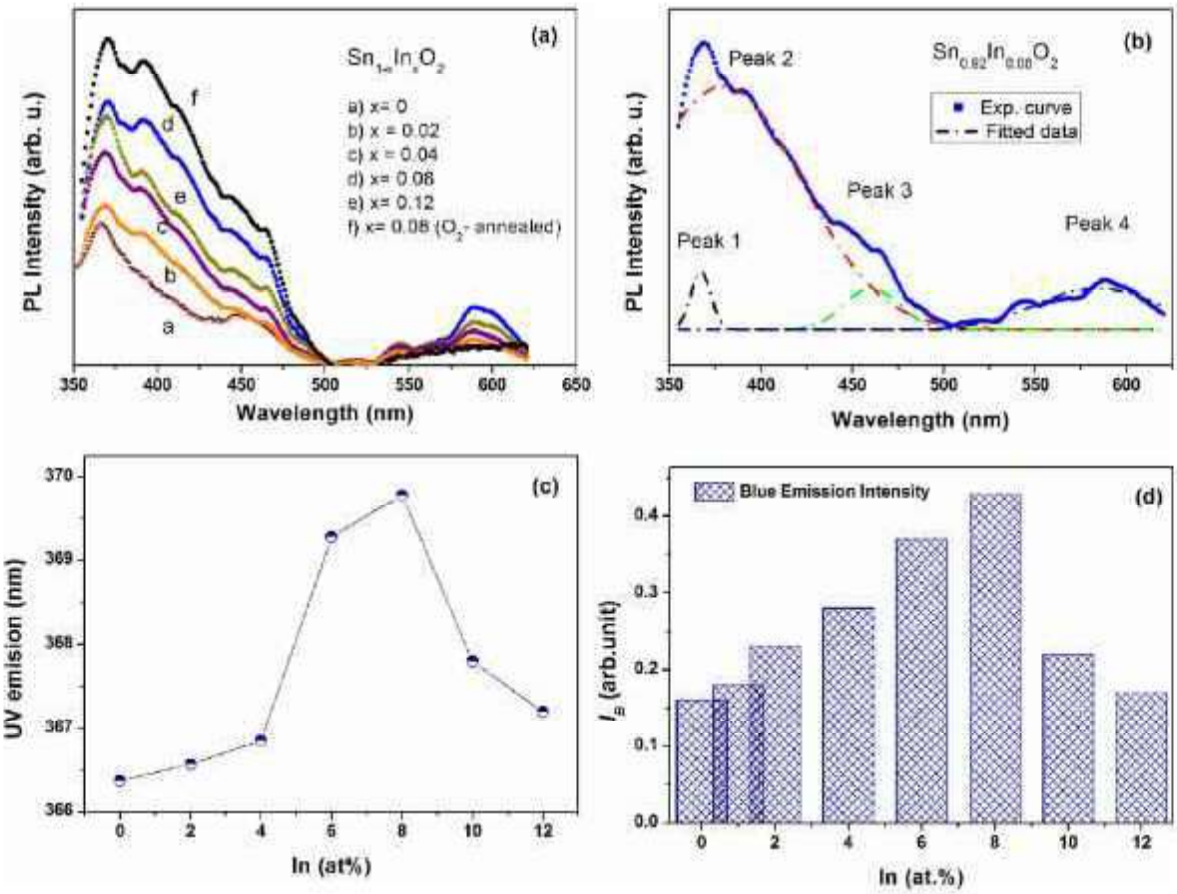

Fig. 6. (a) Room temperature PL spectra of $Sn_{1-x}In_xO_2$ thinfilms.(b) Peak-fittings of PL expermental data (c) Shifting of UV-emission (Peak 1) and (d) relative intensty of blue luminescence (I_B) (Peak-3) with In-doping concentration (at.%).

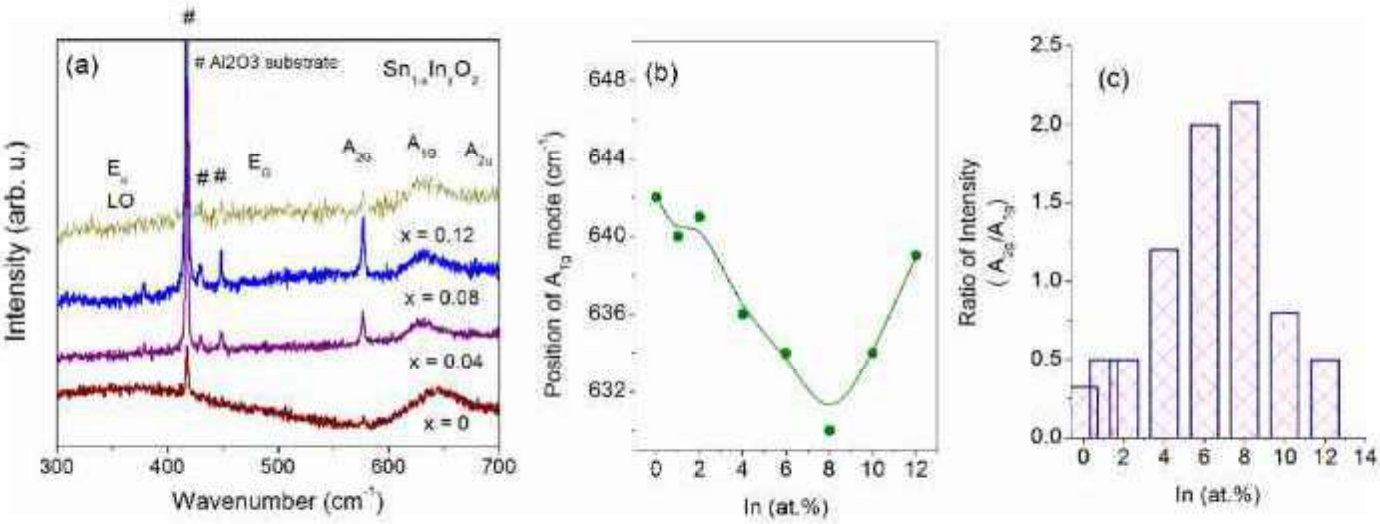

Fig. 7. (a) Raman spectra of $Sn_{1-x}In_xO_2$ thinfilms (b) Shift of Raman A_{1g} mode with In-doping (at.%) and (c) Ratio of intensities of A_{2g}/A_{1g} mode for differernt $Sn_{1-x}In_xO_2$ thinfilms.

performing the measurement. The spectra thus obtained are known as quotient spectra or ratio curves as shown in Fig. 9a. The distinct peak is found to be $p_L = 9.4 \times 10^{-3} m_0c$ where, m_0 being the electron rest-mass of electron and c being velocity of light in free space. This is due to the elemental oxygen environment surrounding the cation vacancies where the positrons gets strongly trapped. A less prominent peak at $p_L = (31–34) \times 10^{-3} m_0c$ whose amplitude is found to increase and the position of peak also be shifted towards higher momentum with the increase of In-doping level. It is understandable as due to increasing number of In^{3+} ions whereas a definite shift of the peak towards higher electron moments that indicates that excess In^{3+} ions segregating over defects and surfaces and positrons getting increased proximity to interact and get annihilated with the electrons of Indium ions.

S and W-parameters are the two very important line-shape

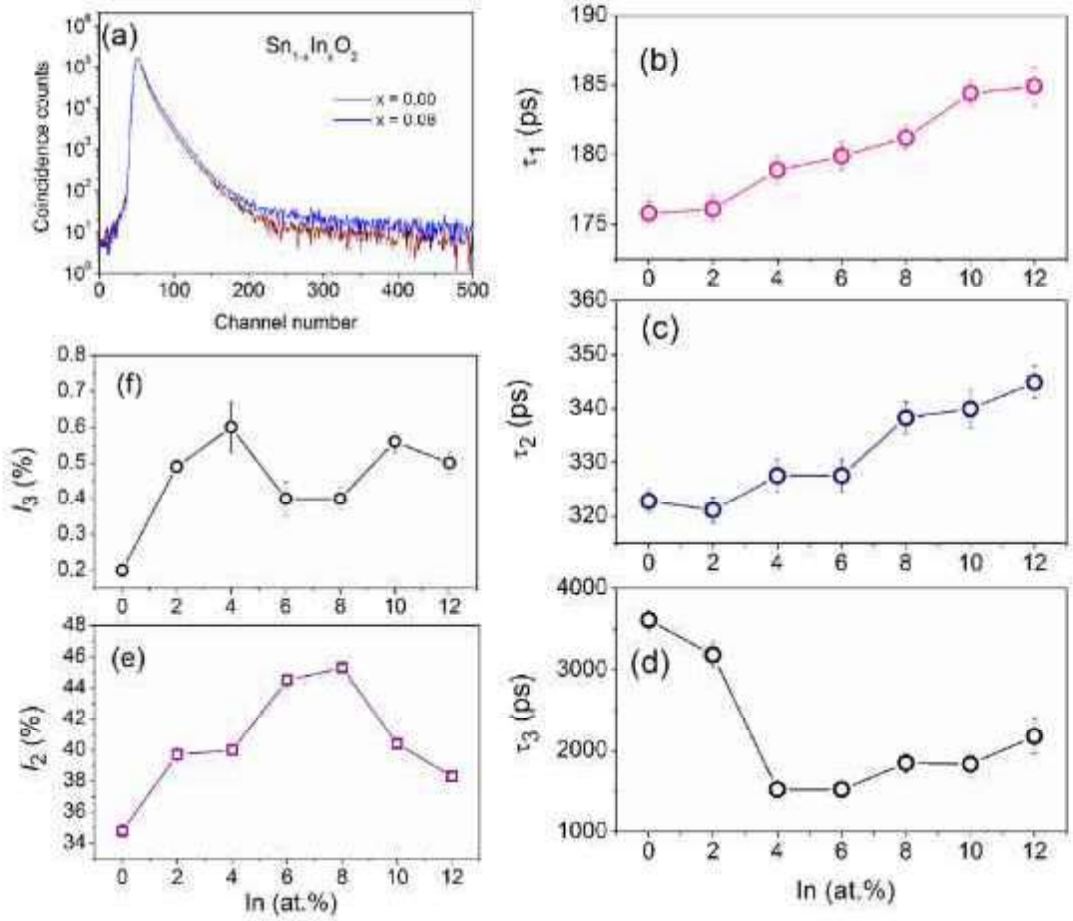

Fig. 8. (a) Peak normalised positron lifetime spectra of undoped SnO_2 and $Sn_{0.92}In_{0.8}O_2$ thinfilm. (b–f) Variation of positron lifetimes τ_1 τ_2 and τ_3 and intensities I_2 and I_3 as funcion of In-doping concentration.

parameters for better understanding of the evolution of defects. *S* and *W*-parametershave been derived from the projected one-dimensional CDB spectra according to the relations

$$S = \frac{\sum_{j=-2}^{2} N_j(\Delta E)}{\sum_{j=-50}^{50} N_j(\Delta E)}$$

and

$$W = \frac{\sum_{j=-12}^{-4} N_j(\Delta E) + \sum_{j=4}^{12} N_j(\Delta E)}{\sum_{j=-50}^{50} N_j(\Delta E)}$$

where N_j (ΔE) is number of counts and j = 0 corresponds to $\Delta E = 0$ and all channels were calibrated for 400 eV. *S*-parameter represents the normalised counts very near to electron rest-mass energy (511 ± 0.8 keV), thus it indicates the fraction of positrons are annihilated with the low momentum electrons i.e. in vacancy sites or voids within the sample. On the other hand, *W*- parameters represents the fraction of positrons are annihilated with high mementum electrons. The relative value of these fractions (*S* and *W*) provides the characteristics of the defects. A straight-line behaviour (Fig. 9c) indicates that there are probably two major positron annihilation sites as bulk and vacancy-type defects. Because of Coulomb's repulsion, positrons cannot get trapped into single oxygen vacancies (V_O), but it can be trapped within negatively charged V_{Sn} defects within $Sn_{1-x}In_xO_2$. Therefore, the increase of *S* -parameter as shown in Fig. 9b, generally indicates higher annihilation probability of positrons with the lower momentum valence electrons which occurs during increase of V_{Sn} vacancy concentrations in the material. Therefore, $Sn_{0.92}In_{0.08}O_2$ film possesses the highest concentration of V_{Sn} defects among all other In-doped films. Beyond doping concentration of 8 at.%, the calculated values of *S*-parameter found to decrease significantly due to decrease of V_{Sn} defect concentration within the $Sn_{1-x}In_xO_2$ films.

3.6. Origin of ferromagnetism within the In-doped SnO_2 films

Correlating all earlier experimental results, it can be understood that the cationic substitution of non-magnetic indium has significant role to stabilize V_{Sn} defects within SnO_2 lattice. In addition, In_{Sn} defects also introduce localized holes that help to promote p-type conductivity within SnO_2. It has been found that under O-rich condition, V_{Sn} defects are the predominant vacancy-type defects which certainly have significant role on determining the magnetic properties of $Sn_{1-x}In_xO_2$ films. Earlier, theoritical literaures [22,23] have suggested that V_{Sn} is a magnetic defect and it's magnetic moment arrises from the spin-polarized 2p-electrons of oxygen ions adjunct to the vavcancy site. With the increase of In-doping concentration in SnO_2, it has been found that concentration of V_{Sn} defects also increases, consequently, the inter-vacancy distance reduces significantly. When concentration of V_{Sn} vacancy exceeds a threshold value, Ruderman-Kittel-Kasuya-Yosida (RKKY)-type ferromagnetic iteraction between of the nearby V_{Sn} defects can be meadiated through the localised holes arrise due to In_{Sn} defects. The strength of such ferromagnetic interaction depends mainly on two factors, one is the concentration of V_{Sn} defects and other is the density of

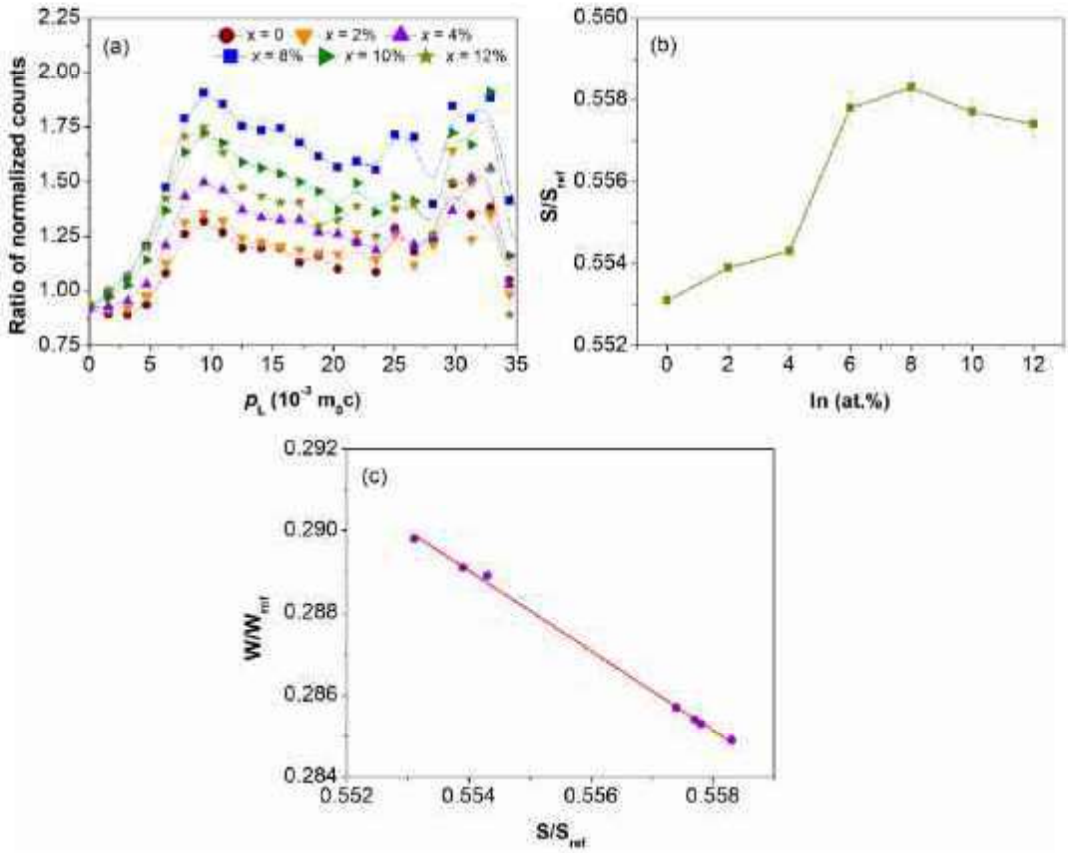

Fig. 9. (a) The quotient spectra obtained from the CDB spectra of the $Sn_{1-x}In_xO_2$ thinfilms with respect to the single crystalline Aluminum (Al) sample. Variation of (b) '*S*'-parameter and (c) *W*-parameter vs *S* -parameter for different $Sn_{1-x}In_xO_2$ films.

chrage carriers (i.e. holes) within SnO_2 film. As earlier experimental analysis revealed that both the concentration of V_{Sn} defects and holes increases gradually with increasing In-content in SnO_2. As a result ferromagnetic interaction between nearby V_{Sn} defects becomes stronger, leading to the enhancement of M_S as well as T_C of $Sn_{1-x}In_xO_2$ films. However, when doping exceeds a certain level, stabilization of different interstitial defects such as In_i and Sn_i defects effectively starts to compensate the acceptor-type In_{Sn} defects. Thus the effective density of holes within the films reduces and consequently, the strength of ferrmagnetic interaction decreases. Thus it can be understood that more In-doping may not be helpful to trigger stronger ferromagnetic interaction rather an optimum In-concentration (~8 at.% here) is essential to achieve large ferromagnetic moment as well as high Cuire temperature. Hence our study demonstrates that proper defect-engineerings are always very effective to stabilize V_{Sn} defects induced hole-mediated ferromagnetism exceeding a threshold vacancy concentration in In-doped SnO_2 films which can serve to goal of spintronics in future.

4. Conclusions

The study successfully demonstrates the impact of non-magnetic Indium substitution on evolution of structural defects, correlated ferromagnetic and electrical properties of $Sn_{1-x}In_xO_2$ ($0 \leq x \leq 0.12$) thinfilms prepared by PLD technique. Under oxygen-rich atmosphere, the substitutions of In^{3+} ions at Sn sites are found to become very effective to stabilize of considerable amount of V_{Sn} defects within SnO_2 thinfilm. Evidnece of the formation of V_{Sn} defects are confirmed from various spectroscopic techniques such as XPS, PL, PALS and Raman spectroscopy. For low doping, the substituition of In^{3+} repacing Sn^{4+} ions creates aceptor-type In_{Sn} defects band within energy band-gap of SnO_2 that introduces holes into the system. It has been found as soon as the doped SnO_2 film switches from n-type to p-type behaviour (i.e. beyond 2 at.%), ferromagnetic properties of the film intensified significantly, resulting large magnetic moment (~15.21 emu/cc) as well as higher Cuire Temperature (~540K). As origin of such enahanced FM in $Sn_{1-x}In_xO_2$ film, we attribute to RKKY-type V_{Sn} -induced hole-mediated FM interaction where the magnetic moment of V_{Sn} defects arrises due to the spin-polarization of 2p-electrons of oxygen ions near to the vacancy site. With the increase of In-doping level, the strength of FM continues to enhance and becomes maximum at nominal In-doping level of 8 at.%. For higher doping, con the stabilization of donor-type defects such as In_i and Sn_i defects starts to compensate the acceptor-type In_{Sn} defects, thereby diminishing the effective hole density and consequently the strength of FM in $Sn_{1-x}In_xO_2$ films. Therefore, such V_{Sn} -induced hole-mediated RTFM in SnO_2-based oxides materials can open up new opportunities in the field of DMS and spintronics in future.

CRediT authorship contribution statement

Shyamsundar Ghosh: Writing – review & editing, Writing – original draft, Methodology, Investigation, Data curation, Conceptualization.

Declaration of competing interest

The authors declare that they have no known competing financial interests or personal relationships that could have appeared to influence the work reported in this paper.

Data availability

Data will be made available on request.

Acknowledgement

Authous would like to express sincere gratitude to Prof. Kalyan Mandal, SNBNCBS, Kolkata, India for providing the access of some laboratory facilities during the work. Authors are also thankful to Prof. Gautam Dev Mukherjee, IISER-Kolkata, India for micro-Raman facility and necessary fruitful suggestions. Authors are also very much grateful to Prof. P.M.G Nambissan, SINP, Kolkata, India for providing PALS facility. Electrical measurements using Hall effect & Four-probe resistivity set-up are performed at the Advanced Laboratory, Departement of Physics, Bejoy Narayan Mahavidyalaya, Hooghly, India.

References

[1] P.D. Esquinazi, W. Hergert, M. Stiller, L. Botsch, H. Ohldag, D. Spemann, M. Hoffmann, W.A. Adeagbo, A. Chassé, S.K. Nayak, H.B. Hamed, Phys. Status Solidi B 257 (2020) 1900623.
[2] A. Zunger, S. Lany, H. Raebiger, Physics 3 (2010) 53.
[3] S.A. Wolf, D.D. Awschalom, R.A. Buhrman, J.M. Daughton, S. Von Molnar, M. L. Roukes, A.Y. Chtchelkanova, D.M. Treger, Spintronics: a spin-based electronics vision for the future, Science 294 (2011) 1488–1495.
[4] T. Dietl, A ten-year perspective on dilute magnetic semiconductors and oxides, Nat. Mater. 9 (2010) 965.
[5] S. Ghosh, G.G. Khan, K. Mandal, Defect-driven magnetism in luminescent n/p-Type pristine and Gd-substituted SnO2 nanocrystalline thin films, ACS Appl. Mater. Interfaces 4 (2012) 2048.
[6] S.B. Ogale, R.J. Choudhary, J.P. Buban, S.E. Lofland, S.R. Shinde, S.N. Kale, V. N. Kulkarni, J. Higgins, C. Lanci, J.R. Simpson, N.D. Browning, S. Das Sarma, H. D. Drew, R.L. Greene, T. Venkatesan, Phys. Rev. Lett. 91 (2003) 077205.
[7] A. Barla, G. Schmerber, E. Beaurepaire, A. Dinia, H. Bieber, S. Colis, F. Scheurer, J. P. Kappler, P. Imperia, F. Nolting, F. Wilhelm, A. Rogalev, D. Müller, J.J. Grob, Phys. Rev. B 76 (2007) 125201.
[8] S. Ghosh, D. De Munshi, K. Mandal, J. Appl. Phys. 107 (2010) 123919.
[9] J.M.D. Coey, P. Stamenov, R.D. Gunning, M. Venkatesan, K. Paul, Ferromagnetism in defect-ridden oxides and related materials, New J. Phys. 12 (2010) 053025.
[10] J.B. Yi, C.C. Lim, G.Z. Xing, H.M. Fan, L.H. Van, S.L. Huang, K.S. Yang, X.L. Huang, X.B. Qin, B.Y. Wang, T. Wu, L. Wang, H.T. Zhang, X.Y. Gao, T. Liu, A.T.S. Wee, Y. P. Feng, J. Ding, FM in dilute magnetic semiconductors through defect engineering: Li-doped ZnO, Phys. Rev. Lett. 104 (2010) 137201.
[11] S. Ghosh, G.G. Khan, B. Das, K. Mandal, Vacancy-induced intrinsic d^0 FM and photoluminescence in potassium doped ZnO nanowires, J. Appl. Phys. 109 (2011) 123927.
[12] J.M.D. Coey, M. Venkatesan, C.B. Fitzgerald, Nat. Mater. 4 (2005) 173.
[13] R. Podila, W. Queen, A. Nath, J.T. Arantes, A.L. Schoenhalz, A. Fazzio, G. M. Dalpian, J. He, S.J. Hwu, M.J. Skove, A.M. Rao, Nano Lett. 10 (2010) 1383.
[14] I.S. Elfimov, S. Yunoki, G.A. Sawatzky, Possible path to a new class of ferromagnetic and half-metallic ferromagnetic materials, Phys. Rev. Lett. 89 (2002) 216403.
[15] H. Peng, H.J. Xiang, Su-H Wei, S.S. Li, J.B. Xiaand, J. Li, Phys. Rev. Lett. 102 (2009) 017201.
[16] Q. Wang, Q. Sun, G. Chen, Y. Kawazoe, P. Jena, Phys. Rev. B 77 (2008) 205411.
[17] P. Li, Y. Lan, Q. Zhang, Z. Zhao, T. Pullerits, K. Zheng, Y. Zhou, J. Phys. Chem. C 120 (2016) 9253–9262.
[18] Nguyen Hoa Hong, Nathalie Poirot, Joe Sakai, Ferromagnetism observed in pristine SnO2 thin films, Phys. Rev. B 77 (2008) 033205.
[19] G.S. Chang, J. Forrest, E.Z. Kurmaev, A.N. Morozovska, M.D. Glinchuk, J. A. McLeod, A. Moewes, T.P. Surkova, Nguyen Hoa Hong, Oxygen-vacancy-induced ferromagnetism in undoped SnO2 thin films, Phys. Rev. B 85 (2012) 165319.
[20] K. Thiyagarajan, K. Sivakumar, Oxygen vacancy-induced room temperature ferromagnetism in graphene-SnO_2 nanocomposites, J. Mater. Sci. 52 (2017) pages5084–5096.
[21] A. Ahmed, M. Nasir, M. Hashim, P. Tripathi, B.S. Choi, Improved room-temperature ferromagnetism in Nd-doped SnO2 nanostructures through defect engineering, J. Phys. Chem. C 125 (40) (2021) 22175–22187.
[22] H. Wang, Y. Yan, K. Li, X. Du, Z. Lan, H. Jin, Role of intrinsic defects in ferromagnetism of SnO2: first-principles calculations, Phys. Status Solidi B 247 (2) (2010) 444–446.
[23] G. Rahman, V.M. García-Suárez, S.C. Hong, Vacancy-induced magnetism in SnO2: a density functional study, Phys. Rev. B 78 (2008) 184404.
[24] A. Janotti, C.G. Van de Walle, Native point defects in ZnO, Phys. Rev. B 76 (2007) 165202.
[25] G. Bouzerar, T. Ziman, Phys. Rev. Lett. 96 (2006) 207602.
[26] R.S. Zeferino, U. Pal, M.B. De Anda Reues, B.R. Rosas, Advances in Nano Research 7 (2019) 13–24.
[27] D. Maestre, A. Cremades, J. Piqueras, L. Gregoratti, Thermal growth and structural and optical characterization of indium tin oxide nanopyramids, nanoislands, and cubes, J. Appl. Phys. 103 (2008) 093531.
[28] S.Y. Li, C.Y. Lee, P. Lin, T.Y. Tseng, Low temperature synthesized Sn doped indium oxide nanowires, Nanotechnology 16 (2005) 451–457.
[29] J. Ba, D.F. Rohlfing, A. Feldhoff, T. Brezesinski, I. Djerdj, M. Wark, M. Niederberger, Nonaqueous synthesis of uniform indium tin oxide nanocrystals and their electrical conductivity in dependence of the tin oxide concentration, Chem. Mater. 18 (12) (2006) 2848–2854.
[30] B.V. Crist, Handbooks of Monochromatic XPS Spectra, XPS International, 1997.
[31] J.H. He, T.H. Wu, C.L. Hsin, K.M. Li, L.J. Chen, Y.L. Chueh, L.J. Chou, Z.L. Wang, Beaklike SnO_2 Nanorods with strong photoluminescence and field-emission properties, Small 2 (2006) 116–120.
[32] A. Kar, M.A. Stroscio, M. Meyyappan, D.J. Gosztola, G. P Wiederrecht, M. Dutta, Tailoring the surface properties and carrier dynamics in SnO_2 nanowires, Nanotechnology 22 (2011) 285709.
[33] X. Xiang, X.T. Zu, S. Zhu, L.M. Wang, V. Shutthanandan, P. Nachimuthu, Y. Zhang, Photoluminescence of SnO_2 nanoparticles embedded in Al_2O_3, J. Phys. D Appl. Phys. 41 (2008) 225102.
[34] V. Golovanov, V. Golovanova, M. Kuisma, T.T. Rantala, Electron spin resonance parameters of cation vacancies in tin dioxide doped with fluorine and hydrogen, J. Appl. Phys. 114 (2013) 143907.
[35] L.Z. Liu, T.H. Li, X.L. Wu, J.C. Shen, P.K. Chu, Optical identification of oxygen vacancy types in SnO_2nanocrystals, J. Raman Spectrosc. 43 (2012) 1423.
[36] S.H. Sun, G.W. Meng, G.X. Zhang, T. Gao, B.Y. Geng, L.D. Zhang, J. Zuo, Raman scattering study of rutile SnO_2nanobelts synthesized by thermal evaporation of Sn powders, Chem. Phys. Lett. 376 (2003) 103.
[37] L.Z. Liu, X.L. Wu, F. Gao, J.C. Shen, T.H. Li, P.K. Chu, Determination of surface oxygen vacancy position in SnO_2nanocrystals by Raman spectroscopy, Solid State Commun. 151 (2011) 811.
[38] J.V. Olsen, P. Kirkegaard, N.J. Pedersen, M. Eldrup PALSfit, A new program for the evaluation of positron lifetime spectra, Phys. Status Solidi C4 (2007) 4004–4006.
[39] C.H. Shek, J.K.L. Lai, G.M. Lin, J. Phys. Chem.Solids 60 (1999) 189.
[40] R. Krause-Rehberg, H.S. Leipner (Eds.), Positron Annihilation inSemiconductors Defect Studies, Springer, Berlin, 1999, pp. 1–126.
[41] P. Asoka-Kumar, M. Alatalo, V.J. Ghosh, A.C. Kruseman, B. Nielsen, K.G. Lynn, Phys. Rev. Lett. 77 (1996) 2097–2100.

Groundwater for Sustainable Development 23 (2023) 101036

Contents lists available at ScienceDirect

Groundwater for Sustainable Development

journal homepage: www.elsevier.com/locate/gsd

Research paper

Microplastics in groundwater: An overview of source, distribution, mobility constraints and potential health impacts during the anthropocene

Uttiya Dey [a,***], Deep Raj [a,**], Mijanur Mondal [a], Palas Roy [b], Abhijit Mukherjee [c,d], Naba Kmar Mondal [e], Kousik Das [a,f,*]

[a] Department of Environmental Science and Engineering, SRM University-AP, Amravati, Andhra Pradesh, India
[b] Bejoy Narayan Mahavidyalaya, Itachuna, West Bengal, India
[c] Department of Geology and Geophysics, Indian Institute of Technology Kharagpur, India
[d] School of Environmental Science and Engineering, Indian Institute of Technology Kharagpur, India
[e] Department of Environmental Science, The University of Burdwan, West Bengal, India
[f] Centre for Geospatial Technology, SRM University-AP, Amravati, Andhra Pradesh, India

HIGHLIGHTS

- Source and migration controlling factors of groundwater microplastics are studied.
- Microplastic contamination pattern is different for inland and coastal aquifers.
- Major sources include run off, agriculture, industrial effluent and landfill site.
- Aquifer physicochemical properties and MP characteristics influence the migration.
- Climate change is another controlling factor of microplastic formation and movement.

GRAPHICAL ABSTRACT

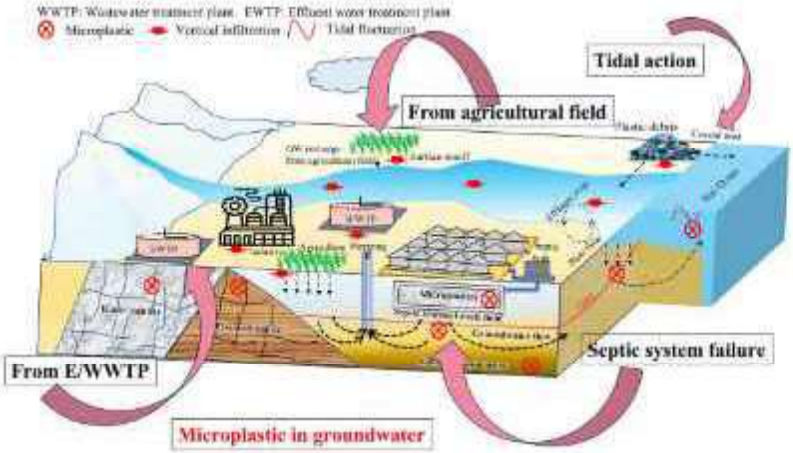

ARTICLE INFO

Keywords:
Groundwater
Microplastics
Human health
Food chain
Bioaccumulation

ABSTRACT

Microplastics (MPs) have already been detected in various environmental matrices like soil, sediment, and surface water, and recently in groundwater also. The occurrence of MPs in groundwater depends up on the transportation through recharge and may controlled by source and local hydrogeology, and partly on the process of surface water-groundwater interaction (SW-GW). Based on the available studies, we intended to establish a hypothetical overview on the source and process-dependent occurrence of MPs in groundwater across terrestrial and coastal aquifers. Groundwater recharge from agricultural stagnant water, losing streams near dumping sites

* Corresponding author. Department of Environmental Science and Engineering, SRM University-AP, Amravati, Andhra Pradesh, India.
** Corresponding author.
*** Corresponding author.
E-mail addresses: uttiya.1988@gmail.com (U. Dey), deepraj2587@gmail.com (D. Raj), kousik.envs@gmail.com (K. Das).

https://doi.org/10.1016/j.gsd.2023.101036
Received 29 August 2023; Received in revised form 3 November 2023; Accepted 3 November 2023
Available online 5 November 2023

Solid State Communications 371 (2023) 115267

Contents lists available at ScienceDirect

Solid State Communications

journal homepage: www.elsevier.com/locate/ssc

Surface-disorder and cationic-site defect-induced ferromagnetism and correlated Raman vibrational modes in $Sn_{0.9}$ $In_{0.1}O_2$ nanocrystalline thin-films

Shyamsundar Ghosh

Department of Physics, Bejoy Narayan Mahavidyalaya, The University of Burdwan, P. O., Itachuna, Hooghly, 712 147, India

ARTICLE INFO

Communicated by: Zhao Liuyan

Keywords:
Oxide-nanomaterials and thin films
Defects
Ferromagnetism
Raman vibration modes
Photoluminescence

ABSTRACT

Exploration of magnetism in otherwise nonmagnetic wide-band oxides through defect-engineering has been become a new challenge to achieve the goal of room-temperature ferromagnetic semiconductor for potential applications in spintronics. In this backdrop, we report surface-disorder and cationic-site defect-induced FM in series of $Sn_{0.9}In_{0.1}O_2$ nanocrystalline thin films prepared using pulsed laser deposition different Argon (Ar) pressure. With the increase of deposition pressure, surface morphology of $Sn_{0.9}In_{0.1}O_2$ nanocrystalline thin-films changes as nanoclusters, nanofibres, nanoflakes and nanowires respectively, crystallite size decreases and surface disorder increases gradually. Raman, X-ray photoelectron and Photoluminescence spectroscopic analysis confirm the formation tin-vacancy (V_{Sn}) and associated combinational defects that significantly increase the ferromagnetic signal in In-doped SnO_2 thin-films. The substitution of trivalent In^{3+} in Sn site also cause serious lattice distortion which transform the Raman inactive modes A_{2g} and E_u modes into Raman active modes and thus appeared at 574 cm^{-1} and 354 cm^{-1} respectively. The nanowires of $Sn_{0.9}In_{0.1}O_2$ are found to possess highest concentration of V_{Sn} defects and therefore it exhibits strongest ferromagnetic moment (M_S) ~ 11.1 emu/cm^3 and highest Curie temperature (T_C) ~ 572 K. The gradual decrease in carrier concentration with the increasing deposition pressure suggests stabilization of hole-mediated V_{Sn}-induced room temperature FM in series of In-doped SnO_2 nanocrystalline thin-films.

1. Introduction

Defect-induced ferromagnetism (FM) in low-dimensional (1D/2D) otherwise nonmagnetic wide-band semiconducting oxide nanostructures has been recently drawn prime research attention due to potential applications in spintronics, magneto-optical and magneto-electrical devices [1–3]. During growth of oxide-based 1D or 2D nanotructures or thins-films in diverse atmosphere, many structural defects like cation vacancies, oxygen vacancies (V_O), interstitials and antisite defects and dislocations can stabilize within lattice. Among them, some type of defects can induce local magnetic moment within host semiconductors [4,5]. In fact, there are significant reports on the evidence of room-temperature FM in ZnO and TiO_2 based-oxides associated either with transition-metal doping or oxygen vacancy defects [6–12]. On the other hand, many theoretical studies [13–16] have suggested that the formation of cation-vacancy defects rather than V_O defects in similar oxides can be more effective to stabilize carrier-mediated room-temperature FM. Density functional theory (DFT) by Elfimov et al. [13] and Pemmaraju et al. [14], and later Osorio-Guillen et al. [15] has predicted that wide-band CaO thin-film can behave as pure ferromagnet with 5% Ca vacancies. Later, Zhang et al. [16] has shown experimentally that the Nb incorporation can help to stabilize Ti vacancy defects in pulsed-lased deposited Nb-doped TiO_2 thin film. Although they do not observed FM due to very low concentration of Ti vacancies and free carrier density. After that, Zn-vacancy induced FM is observed in different nonmagnetic element doped ZnO thin films [6,17], ZnO:Li nanorods [18] and also in our previous work on ZnO:K nanowires [9].

In this backdrop, tin dioxide (SnO_2) is an important transparent conducting oxide (TCO) which finds potential applications many field of science such as sensors, solar panel displays and other transparent electronic devices [19–21]. Unlike ZnO or TiO_2, it has been less explored as far as defect-modified magnetic behaviours are concern. DFT calculations by Gul Rahman et al. [22] have explained tin-vancacy (V_{Sn}) with proper defect-enginnering can generate large magnetic moment in SnO_2. They have also suggested that observation of unexpected gaint magnetic moment (7.5 ± 0.5) μ_B/Co in Co-doped SnO_2 films by Ogale et al. [23],

E-mail addresses: sghoshphysics@gmail.com, shyamsundar@bnmv.ac.in.

https://doi.org/10.1016/j.ssc.2023.115267
Received 14 July 2022; Received in revised form 20 June 2023; Accepted 26 June 2023
Available online 5 July 2023
0038-1098/

may be due to formation of V_{Sn} defects in doped SnO_2. However, stabilization of significant cation vacancy defects is quite difficult in such oxides especially in its pristine form rather needs the proper defect-enginnering [15]. Bouzerar et al. [24] have suggested stabilization of such cation vacancies are possible through the cationic substitution of nonmagnetic group-I elements in HfO_2 or ZrO_2. After that experimentally indeed, cation vacancy-induced FM has been reported in Li:ZnO [6], K:ZnO [9] and Ga:TiO_2 thin film [25]. Here, we have fabricated series of Indium (In)-doped SnO_2 nanocrystalline thin-films under Argon atmosphere using PLD technique. Here, a nominal 10 at. % trivalent Indium are used as dopant at tetravalent Sn site in order to introduce significant amount of holes in SnO_2 lattice. The morphology of $Sn_{0.9}In_{0.1}O_2$ nanocrystalline thin films are varied by changing Ar pressure of PLD chamber. The role of cationic-site defects on the ferromagnetic properties of $Sn_{0.9}In_{0.1}O_2$ nanocrystalline thin-films are investigated in details. The study depicts that nanostructure morphology, film-thickness and surface disorder also play crucial role to stabilize and tune carrier-mediated defect-controlled FM in SnO_2 nanocrystalline thin films.

2. Experimental details

2.1. Synthesis and characterization of thin-films

High purity SnO_2 and In_2O_3 powders (99.99%) are mixed properly with appropriate ratio Sn: In = 9:1) and grinded for 1 h in order to prepare a uniform precursor mixture. Then the precursor material is transformed in the form of a pellet of 1 inch diameter and has been sintered at 800 °C in oxygen for 2 h. The pallet is then mounted on the pulsed laser deposition (PLD) chamber for fabrication of In-doped SnO_2 nanocrystalline thin films on c-axis (0001) sapphire (Al_2O_3) substrate. After that, PLD chamber which is evacuated down to atmospheric pressure of 2×10^{-5} mbar and is filled with pure argon (Ar) gas. Now, different In-doped SnO_2 samples are prepared at different Ar pressure such as 0.01 (sample S1), 0.1 (sample S2), 1 (sample S3) and 10 (sample S4) mbar and the pristine SnO_2 film (sample S0) at 10 mbar. The PLD unit is operated with a Kr–F excimer laser with laser power density ~1.41 J/cm^2, the pulse repetition rate of 5 Hz and substrate temperature of 600 °C. All pure and doped SnO_2 films are deposited for 30 min. All the samples are annealed for 10 min in the same atmosphere in deposition chamber and then cooled naturally at room temperature. Afterwards, the sample S4 has been annealed in O_2 at 500 °C for 2 h and named as sample S5. Some details of sample preparation are also summarised in Table 1.

Identification of Phase and structural characterization of the samples are performed using Grazing Incidence X-ray Diffraction (GIXRD, X'Pert Pro, Panalytical) while morphology and growth of the nanostructured films are observed by Field Emission Scanning Electron Microscopy (FESEM, FEI Helios Nanolab-600). Grain size and elemental compositions of the films are analysed using Transmission electron microscopy (TEM) and energy dispersive spectrum (EDS) associated with TEM. X-ray photoelectron spectroscopy (XPS, PHI 5000 Versaprobe II Scanning XPS microprobe, ULVAC-PHI, USA) with a monochromatic Al-K_α radiation is employed to analysis the valence state of the host and doped ions. Magnetic measurements are performed by superconducting quantum interference devices (SQUIDs) both in room temperature and low temperature. In order to understand the dynamics of defects within lattice, Raman spectroscopy measurements are carried out using a micro-Raman spectrometer (LABRAM HR from Horiba Jobin Yvon) and Photoluminescence (PL) spectroscopy using a spectrofluorometer (Horiba Jobin Yvon, Fluorolog-3) a Xe lamp source under the excitation wavelength of 330 nm. Resistivity measurements are carried out using Hall experiment set-up measurements and four-probe method. In order to avoid any magnetic contamination, extreme precautions are adopted in every step of the various experiments including sample fabrication process. Nonmagnetic tweezers, nonmagnetic containers etc. are used to handle the samples during the entire experiments.

3. Result and discussions

The film morphology as observed from FESEM images are shown in Fig. 1(a–d). It is quite interesting that the morphology of the thin films changes as nanocrystals, nanofibres, nanoflakes and nanowires for sample S1, S2, S3 and S4 respectively. The thicknesses of the films are found to be of the order of 183 nm (sample S1), 126 nm (sample S2), 104 nm (sample S3), 87 nm (sample S4) and 94 nm (sample S0). It is quite interesting to observe that as the deposition pressure increases the thickness of film decreases gradually. X-ray diffraction patterns as shown in Fig. 1e indicates the tetragonal rutile crystal structure ($a = b \neq c$) for undoped and In-doped SnO_2 without any evidence secondary phases. It is noticeable that on increasing deposition pressure, the diffraction peaks are found to broaden gradually which indicates the decrease of crystallite sizes of the films. The average crystallite sizes (t) for each film are estimated using Scherrer equation using (110) & (101) diffraction peaks after subtracting the instrumental broadening using LaB_6 standard. It is found that average crystallite size of In-doped SnO_2 films decreases gradually as depicted in Fig. 1f and changes from around 14.1 nm for sample S1 to around 5.4 nm for sample S4. Fig. 2a and c shows the representative TEM images for sample S1 (nanocrystals) and S4 (nanowires) respectively and the corresponding HRTEM images shown in Fig. 2b and d respectively. Average grain size or particle size for each films are estimated by employing TEM (inset of Fig. 2b and d) and are summarised in Table 2. The inset of HRTEM micrographs shows the respective selected area electron diffraction (SAED) pattern which indicates the polycrystalline nature of the films. The grain sizes estimated from TEM are found to be higher from the crystallite size as obtained from XRD which also indicates the polycrystalline nature of the films. Final elemental composition of the samples are analysed by EDX spectra attached to TEM and are summarised in Table 2. Fig. 2e shows a representative EDX spectrum for sample S4 which shows the presence of Sn, In, O and Cu elements. The existence of copper (Cu) in the sample arises due to use of copper grid for TEM characterization.

Fig. 3a shows the field-dependent magnetization M (H) curve for undoped and In-doped SnO_2 thin films after necessary substrate

Table 1
Detailed experimental specifications used for the fabrication of pristine and In-doped SnO_2 thin-films using pulsed lased deposition.

Substrate	PLD Specification			Deposition time (min)	Sample Precursor	Deposited under Ar Pressure (mbar)	Sample ID
	Laser power density (J/cm^2)	Pulse repetition Rate (Hz)	Substrate Temperature (°C)				
Sapphire (Al_2O_3)	1.41	5	600	30	$Sn_{0.9}In_{0.1}O_2$	0.01	S1
						0.1	S2
						1	S3
						10	S4
						Sample S4 annealed in O_2 externally	S5
					SnO_2	10	S0

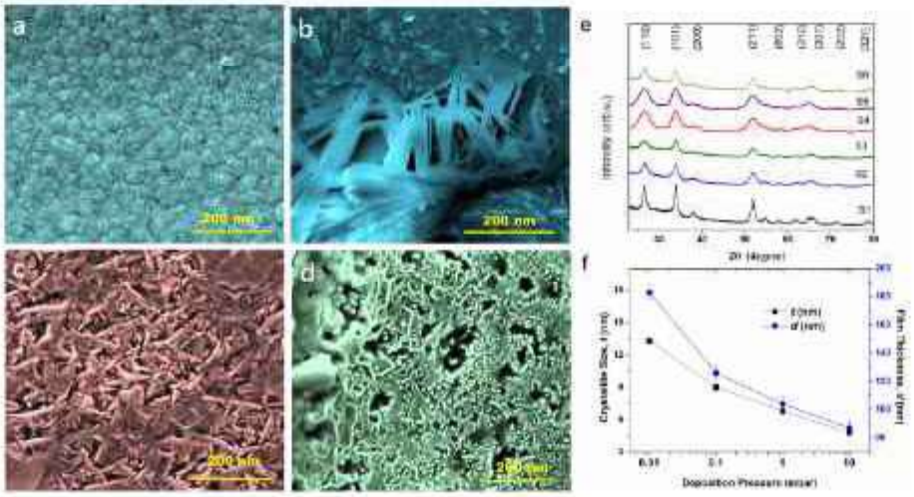

Fig. 1. FESEM micrographs of $Sn_{0.9}$ $In_{0.1}O_2$ thin films deposited under Ar pressure (P_{Ar}) of (a) 0.01, (b) 0.1, (c) 1 and (d) 10 mbar indicating their surface morphologies as nanoclusters, nanofibres, nanoflakes and nanowires respectively. (e) XRD pattern and (f) estimated crystallite sizes and film-thickness of In-doped SnO_2 thin films deposited under different Ar Pressure.

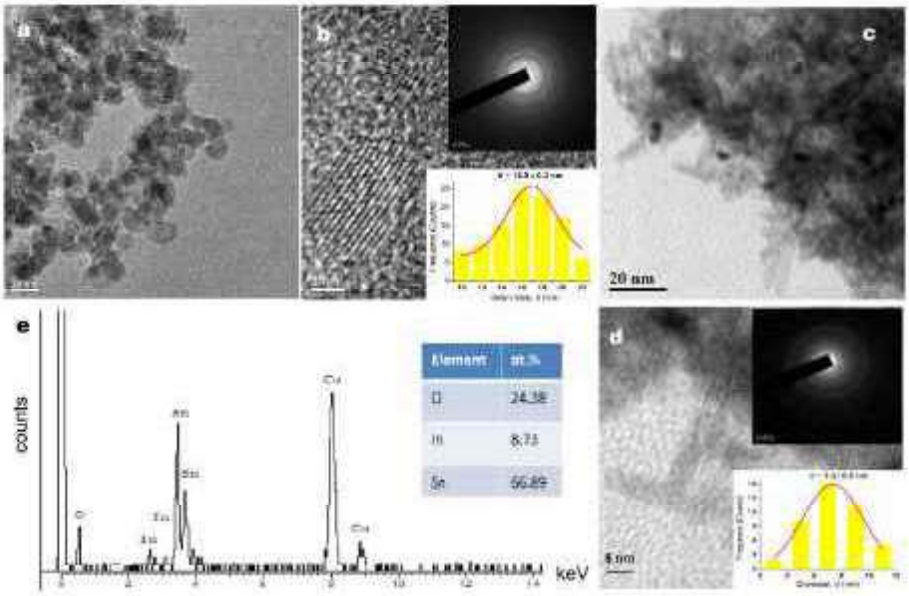

Fig. 2. TEM image (a and c) and corresponding HRTEM images (b and d) of $Sn_{0.9}In_{0.1}O_2$ nanocrystals (sample S1) and nanowires (sample S4) respectively while the insets of b and d show SAED and particle distribution for the corresponding film (e) Representative EDX spectra for $Sn_{0.9}In_{0.1}O_2$ nanowires (sample S4) while the inset shows the corresponding elemental composition of the film.

Table 2
Typical estimated parameters for the pristine and $Sn_{0.96}$ $In_{0.04}O_2$ nanocrystalline thin-films deposited under different Ar pressure.

Sample ID	Morphology	Average Crystallite Size from XRD (nm)	Grain size from TEM	Film thickness (nm)	Elemental Composition (at.%) from EDX			Saturation moment (emu/cm^3)	Curie Temp. (K)	Carrier density n (/cm^3)	Resistivity (Ω-cm)
					O	In	Sn				
S1	Nanocrystals	14.1	16.9	183	22.45	8.31	69.24	3.8	479	9 × 1019	4 × 102
S2	Nanofibres	9.0	15.7	126	23.27	8.93	67.8	7.3	516	5×10^{19}	8.3×10^{2}
S3	Nanoflakes	6.8	10.2	104	22.69	8.65	68.66	8.8	534	8×10^{18}	5.1×10^{4}
S4	Nanowires	4.8	7.3	87	24.38	8.73	66.89	11.04	572	2×10^{18}	1.1×10^{5}
S5	Nanowires	5.4	11.3	91	24.38	8.73	66.89	11.67	576	1.9×10^{18}	1.2×10^{5}
S0	Nanocrystals	28.4	43.2	94	39.21	—	60.79	0.8	405	6×10^{20}	9.1×10^{1}

correction. The magnetization curve of the sapphire substrate is provided at the inset of Fig. 3a which indicates typical diamagnetic nature. It is quite interesting to observe that nanostructured SnO_2 in pristine form exhibits FM at room-temperature and the ferromagnetic moment of SnO_2 is further enhanced (almost 4.75 times) on In-doping for sample S1 deposited under 0.01 mbar Ar pressure. This indicates that doping of

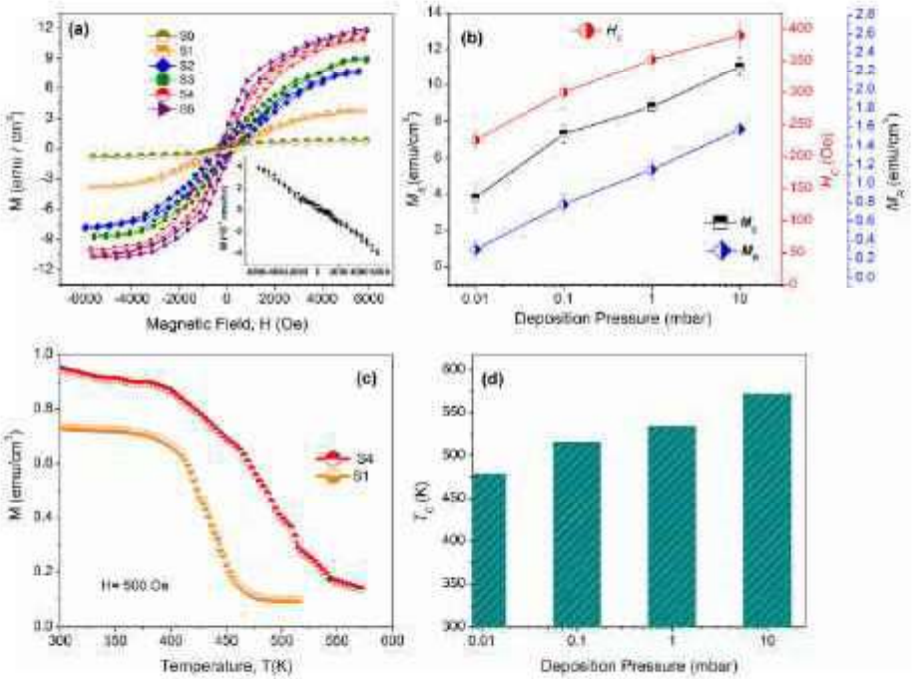

Fig. 3(a). Field-dependent Magnetization, M (H) curve (Inset: for sapphire substrate) (b) Variation of different ferromagnetic parameters of $Sn_{0.9}In_{0.1}O_2$ films with change in deposition pressure. (c) Representative temperature-dependent magnetization, M (T) curve for sample S1 and sample S4. (d) Curie temperature (T_C) estimated for different $Sn_{0.9}In_{0.1}O_2$ nanostructured thin-films.

non-magnetic indium definitely have crucial rule to enhance FM in In-doped SnO_2 films. In addition, as the deposition pressure (Ar) is further increased, morphology of nanostructures changes and the ferromagnetic moment also found to increase gradually. The nanowires of In-doped SnO_2 thin film (sample S4) exhibit the highest saturation magnetization (M_S) as shown in Fig. 3b as compared to other morphologies. Similar to magnetic moment, other ferromagnetic parameters like coercivity (H_C) and remnant magnetization (M_R) also found to follow similar trend as depicted in Fig. 3b. Temperature-dependent magnetization, M (T) curves as shown in Fig. 3c indicates the paramagnetic Curie temperature (T_C) is well beyond the room temperature. Fig. 3d shows the variation of T_C for different the morphologies and In-doped SnO_2 nanowires (sample S4) are found to have highest $T_C \sim 572$ K. Though such unexpected FM was observed in case of SnO_2 nanostructures earlier [30–32], still here the origin seems to be quite different. The undoped SnO_2 thin film (Sample S0), deposited under 10 mbar Ar pressure mbar exhibits relatively poor ferromagnetic behaviour as compared to doped samples which illustrates that the In-doping might have played a crucial role to stabilize and enhance FM in SnO_2. Not only that, the ferromagnetic moment also varies significantly with nanostructure morphology and film thickness and found to be strongest for the In-doped SnO_2 nanowires (sample S4), having the smallest crystallite size. As the crystallite size increases, as a consequent surface to volume ratio should decrease gradually for the other morphologies like Nanoflakes, Nanofibres and Nanocrystals. Such kind of surface modifications can generally affect the presence and dynamics of various defects mainly on the surface of the nanostructures. In addition, ferromagnetic moment of the nanowires (sample S4) are found to be almost unchanged even after annealing in O_2 (sample S5) in 500 °C for 2 h. Fig. 4 shows the representative Zero-field-cooled (ZFC) and field-cooled (FC) curves for sample S1 (nanocrystals) and S4 (nanowires) which again confirm typical ferromagnetic behaviour. Hence in order to understand the origin of FM in the series of In-doped SnO_2 nanostructured thin films, it is very necessary to probe the defects within nanomaterials with proper characterization techniques.

Fig. 5 exhibits the core-level XPS spectra for Sn 3d, O 1s and In 3d orbitals after proper calibration with standard Carbon (C) for undoped

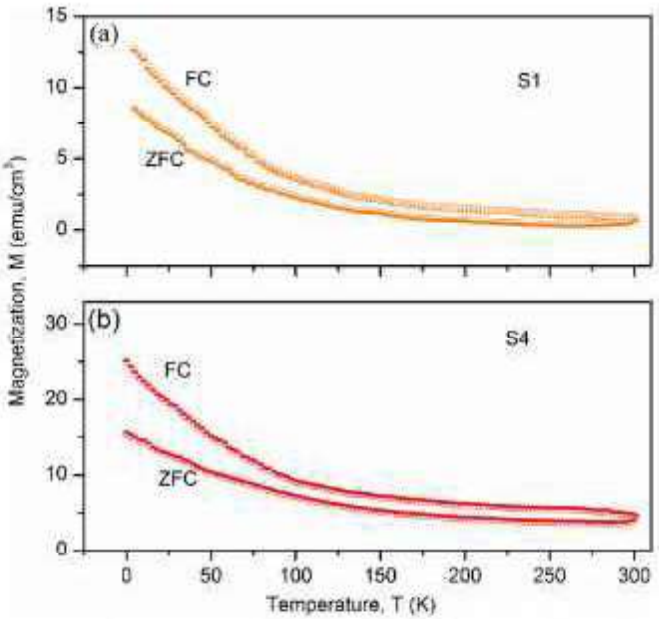

Fig. 4. Zero-Field-Cooled (ZFC) and Field-Cooled (FC) curve with H = 500 Oe for $Sn_{0.9}In_{0.1}O_2$ nanocrystals (sample S1) and nanowires (sample S4).

SnO_2, In-doped SnO_2 samples. XPS spectra for Sn-3d orbitals for bulk Sn and SnO_2 are also provided for reference in Fig. 5a. Analysis of XPS revealed that the presence of 74.2 at. % Sn in bulk SnO_2 while the nanowires (sample S4) of $Sn_{0.9}In_{0.1}O_2$ contains lesser amount of Sn (~67.6 at.%) which might be an indication for formation of V_{Sn} defects. In addition, the peak position for Sn 3d orbital in In-doped SnO_2 thin films are found shift to towards lower binding energy as compared to the undoped SnO_2. In fact the asymmetric nature and broad shoulder towards higher binding energy indicates that Sn 3d core-level can be well deconvoluted into two sets of peaks as evident from Fig. 5b. Peaks

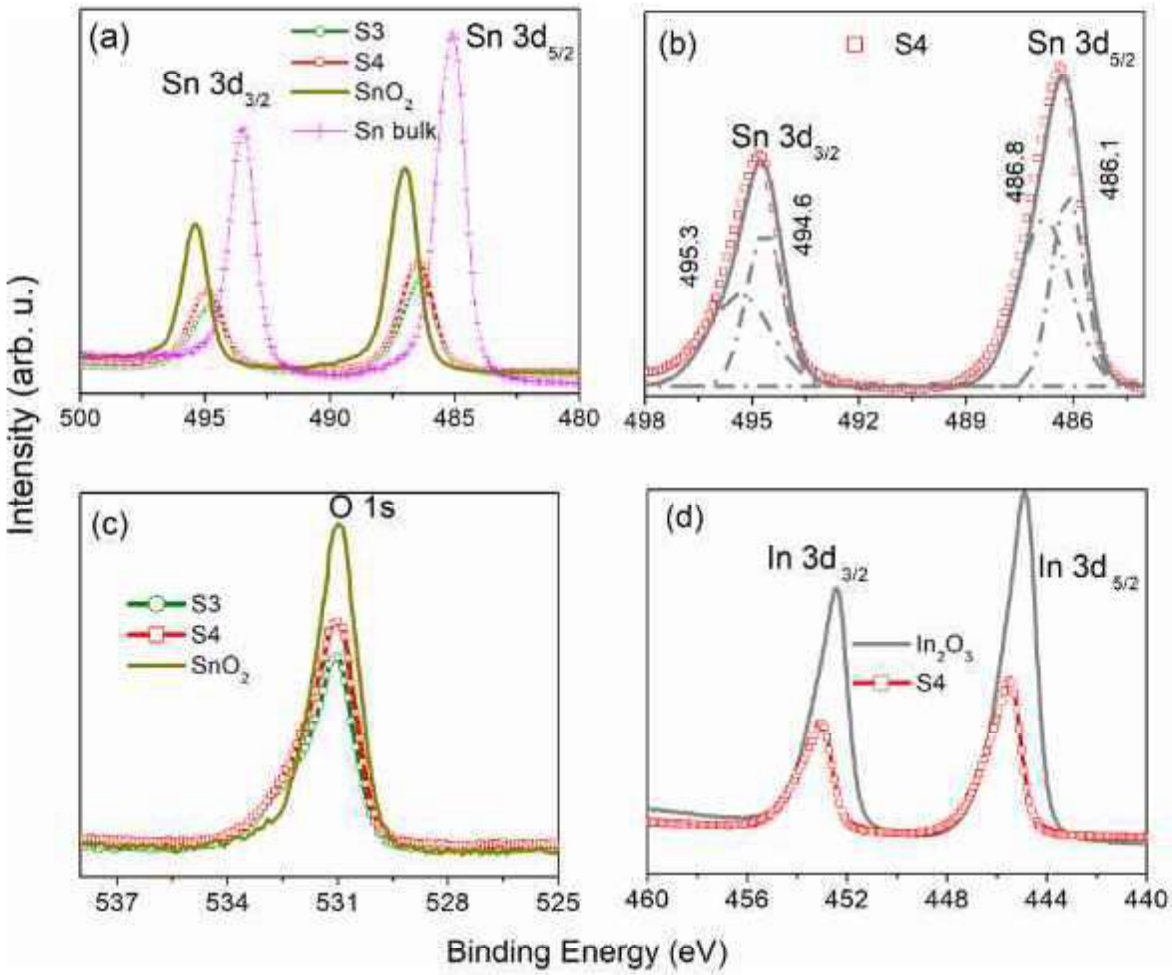

Fig. 5. Core-level XPS spectra of (a) Sn 3d and (c) O 1s orbital for bulk Sn, SnO_2, In-doped SnO_2 nanoflakes (sample S3) and nanowires (sample S4). (b) Deconvolution of Sn-3d XPS spectra (d) representative XPS spectra of In 3d orbitals for $Sn_{0.9}In_{0.1}O_2$ nanowires (sample S4) and In_2O_3.

towards higher binding energy at 486.8 and 495.3 eV correspond to $3d_{5/2}$ and $3d_{3/2}$ orbitals respectively for Sn^{4+} ions at lattice site [26,27]. In the other hand, the peaks with lower binding energy at 486.1 and 494.6 eV arise due to presence of lower valence Sn or metallic Sn within the lattice [26,27] due to In-doping. Fig. 2d shows the core-level XPS spectrum of In 3d orbital within In-doped SnO_2 nanowires (sample S4) which exhibits two distinct peaks at 445.5 and 453.2 eV corresponding to In $3d_{5/2}$ and $3d_{3/2}$ orbitals respectively. In comparison with the pristine In_2O_3, it has been found that peak position for In-3d orbitals in In-doped SnO_2 film are found to be shifted towards higher binding energy due to substitution of In in Sn^{4+} site [26,27]. The O 1s core-level spectrum in Fig. 2c exhibit a strong peak at 530.9 eV confirms the presence oxygen (O^{2-}) ions [28,29] within In-doped SnO_2 lattice.

Raman spectroscopy is one of the effective techniques to probe various crystal defects within such nanomaterials. The tetragonal rutile unit cell of SnO_2 lattice contains two Sn ions and four oxygen ions and belongs to the space group D_{4h}^{14} ($P_{42/mnm}$). Group theory analysis [33] showed that the rutile SnO_2 generally possess 15 vibrational modes

$$G(Rutile) = A_{1g} + A_{2g} + A_{2u} + B_{1g} + B_{2g} + 2B_u + E_g + 3E_u$$

where A_{1g}, B_{1g}, B_{2g} and E_g are Raman active vibrational mode, whereas A_{2u} and E_u mode are IR active and A_{2g} and $2B_u$ modes are neither Raman active nor IR active. Fig. 6a shows the Raman spectra for all the In-doped SnO_2 nanostructured thin-films with along with the substrate as well as the precursor used for sample preparation. In-doped SnO_2 nanocrystals (sample S1) prepared under Ar pressure of 0.01 mbar exhibited E_u LO mode at 354 cm^{-1}, E_g mode at 474 cm^{-1} and A_{1g} mode 643 cm^{-1} and A_{2u} mode at 690 cm^{-1}. The appearance of these peaks indicates the tetragonal rutile crystal structure of SnO_2 which is in agreement with XRD analysis [33,34]. In comparison with Raman spectra of the precursor, an additional mode at around 500 cm^{-1} is found to appear which is due to unreacted In_2O_3 in precursor material [35]. However, this mode remains absent in In-doped SnO_2 films which indicating no unreacted In_2O_3 is present there. Raman E_g mode at 474 cm^{-1} arises due to vibration of oxygen in Sn–O bond, whereas the A_{1g} mode originates due to contraction and expansion of Sn–O bond with lattice. It is quite interesting to observe that as morphology of the In-doped SnO_2 films changes like nanocrystals, nanofibres, nanoflakes and nanowires, a new peak at 574 cm^{-1} is found to appear gradually while the intensity A_{1g} mode decreases (Fig. 6b) continuously. In addition, the Raman A_{1g} mode has been shifted gradually towards the lower wavenumber and also the corresponding full width at half maxima (FWHM) increases gradually, as depicted in Fig. 6c. This can be explained by considering the nano-size effect. As the crystallite size and grain size (as confirmed through XRD and TEM) decreases, as a consequent surface to volume ratio increases, then In-doped SnO_2 nanocrystalline films are tend to possess more and more surface defects like V_{Sn} or local lattice disorder which can change the bond length significantly and thus results the reduction of space symmetry D_{4h}^{14} [33]. In fact the doping of trivalent In^{3+} modifies the local environment surrounding Sn site and can reduce the formation energy of V_{Sn} thus helps to stabilize V_{Sn} defects [24]. Hence, such serious lattice distortion can transform some Raman inactive modes like A_{2g} and E_u mode into Raman active mode and thus appeared at 574 cm^{-1} and 354 cm^{-1} respectively [36] here in our samples. The nanowires of In-doped

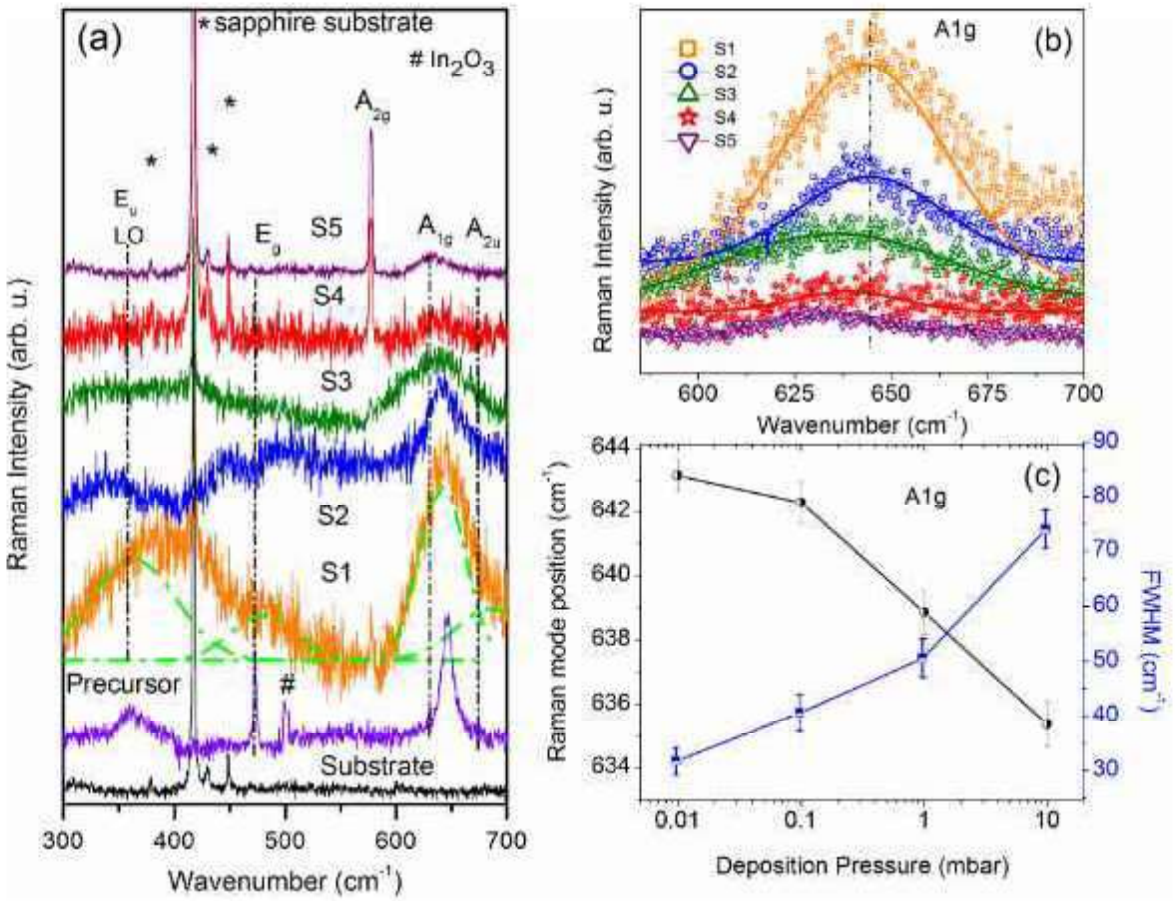

Fig. 6. (a) Raman spectra for various $Sn_{0.96}$ $In_{0.04}O_2$ thin-films, sapphire substrate and the precursor material used for the sample preparation (b) Intensity of Raman A1g mode (c) Variation of peak position and corresponding FWHM of Raman A1g mode for the different $Sn_{0.96}$ $In_{0.04}O_2$ thin-films.

SnO_2 (sample S4) having lowest crystallite size (~5–7 nm) showed the intense A_{2g} mode along with very weak, broader and red-shifted A_{1g} mode and that indicates it possesses highest concentration of V_{Sn} defects. The origin of such Raman A_{2g} mode is further confirmed from the Raman spectra of the In-doped SnO_2 nanowires after annealing in oxygen atmosphere at 500 °C for 2 h. The existence of A_{2g} mode even after the high-temperature annealing in oxygen (for sample S5) indicates the V_{Sn} defects or V_{Sn} associated defect complex are mainly responsible for this mode, rather than oxygen vacancy (V_O) defects that are supposed to decease or even wiped out after such annealing process [37]. On the other hand, A. Janotti and C. G. Van de Walle [37] showed that the formation energy of V_{Sn} defects decrease significantly during annealing in the O-rich condition, therefore stabilization of V_{Sn} defects are most preferable here in the In-doped SnO_2 films.

PL spectroscopy is another promising and widely-used technique to probe various crystalline defects and defect trapping states within the nanomaterials. Fig. 7 shows the room temperature PL spectra of SnO_2 and $Sn_{0.9}In_{0.1}O_2$ nanocrystalline thin films. The undoped SnO_2 thin-film exhibits strong UV emission at 366 nm (peak 1) wavelength associated with the near band edge (NBE) transition from conduction band minimum (CBM) to valence band maximum (VBM) and mid band defect-related blue emission at 460 nm (peak 3) and yellow-orange emission at 590 nm (peak 4). UV-emission peak in $Sn_{0.9}In_{0.1}O_2$ samples are found to shift towards lower wavelength which indicates the increase of band-gap energy. This increase in band gap energy may be associated to decrease of grain size in nanoscale regime as evident from TEM. For $Sn_{0.9}$ $In_{0.1}O_2$ thin films, a distinct peak is found to appear at 385 nm (peak 2) along with other emission bands which are significantly intensified. Indium substitutional defects (In_{Sn}) at Sn site can form a shallow acceptor-type band near to the valance band and the electronic transition between CBM and this acceptor-type defect states can give rise to luminescence at 385 nm (Peak 2). As undoped and In-doped SnO_2 thin-films are deposited under Sn and O-deficient atmosphere, it is quite expected that samples may possess V_{Sn} and V_O defects [40]. V_O defects may exist in different ionized states such as neutral oxygen vacancy (V_O^0), single-ionized oxygen vacancy (V_O^+) and doubly-ionized (V_O^{++}) oxygen vacancy [38]. V_O^0 defect in SnO_2 acts as very shallow donor while single-ionized oxygen vacancy (V_O^+) create a deep level donor bands at ~ 2.1 eV [38]. Hence, the origin of emission peak 4 (~590 nm) here is due the electronic transition from deep level oxygen vacancy (V_O^+) defect states and VBM [38–40] while the blue emission ~ 460 nm (Peak 3) is associated with the existence of V_{Sn} defects. Golovanov et al. [41] have shown that the formation energy of isolated V_{Sn} is quite high in pure SnO_2 but the non-magnetic substitution at cation site, like Indium here in our case, can reduce the formation energy of V_{Sn} defect and thus possible to stabilize considerable V_{Sn} defects [41]. Such V_{Sn} defects can form acceptor states within SnO_2 band-gap and are responsible for the blue-luminescence at 460 nm (~2.76 eV) [40]. It is evident from the PL spectra (Fig. 7a), all the In-doped SnO_2 nanostructured films showed stronger blue-luminescence compared to weak yellow-orange luminescence. It is interesting to notice (for curve f) that yellow-orange luminescence (peak 4) disappears after annealing the sample S4 in oxygen while the blue emission (peak 3) still exists. This certainly confirms that yellow-orange emission (peak 4) is associated with V_O defects which are reduced considerably after annealing in O_2. On the other hand, V_{Sn} defects may still exits even after annealing in O_2 and thus exhibited the blue emission (Peak 3) at 460 nm. The nanowires of In-doped SnO_2 (sample S4) exhibits the strongest blue emission band (curve e) suggesting the presence of maximum concentration of V_{Sn} defects in it.

Fig. 8a shows the temperature-dependent resistivity curves for

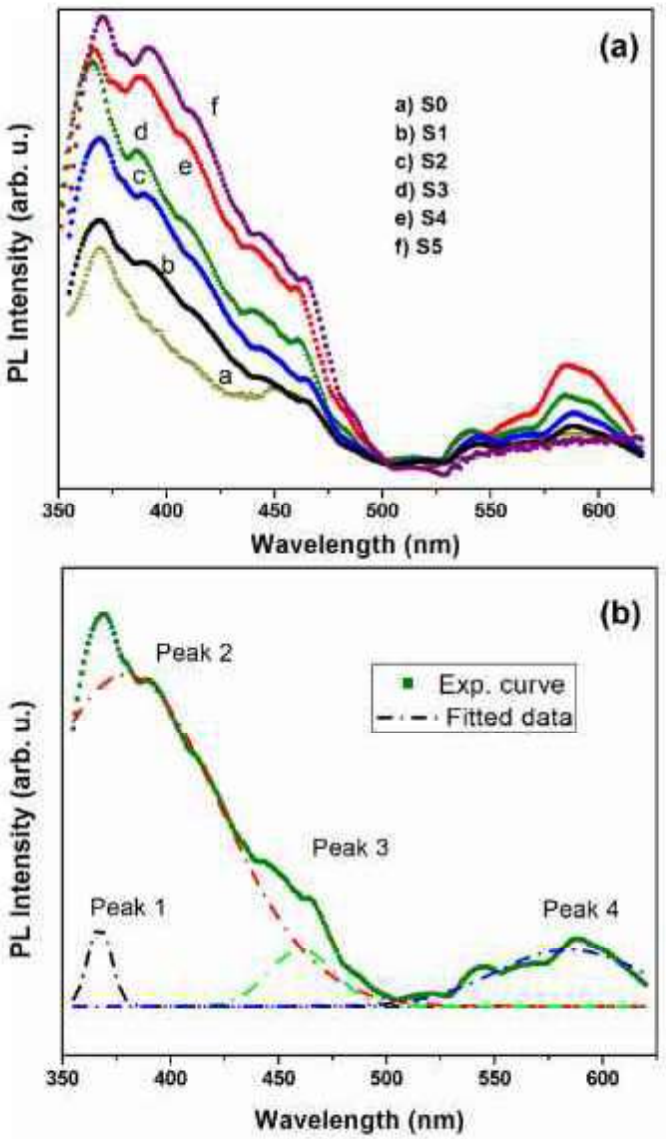

Fig. 7. (a) Photoluminescence spectra of undoped and In-doped SnO_2 nanocrystalline thin-films (b) Representative peak fitting of the experimental data as obtained from PL spectra.

$Sn_{0.9}In_{0.1}O_2$ thin films that indicate typical semiconductor behaviour for all the films. Hall-effect measurement exhibits n-type semiconducting behaviour of pure SnO_2 and $Sn_{0.9}In_{0.1}O_2$ thin-films. The electron carrier concentration (n) of the nanocrystalline thin-films are found to decrease gradually, consequently the resistivity (ρ) increases with increase of deposition pressure as shown in Fig. 8b. The decrease in electron concentration (n) with higher deposition pressure can be explained due to stabilization of more and more acceptor-type defects such as In_{Sn} defects and V_{Zn} defects as evident from the earlier analysis. The increase of resistivity of the films can also be associated with decrease of grain size as conduction interrupts at grain boundaries of different crystallites. Thus nanowires of In-doped SnO_2 (sample S4) having lowest grain size exhibit the highest resistivity ~ 8.3×10^2 Ohm-cm and consequently lowest carrier concentration ~ 2×10^{18} per cm^3 due to stabilization of significant amount of acceptor-type V_{Zn} defects along with In_{Sn} defects.

After correlating the earlier experimental results, here, we demonstrate cation-vacancy defect-induced carrier-mediated room-temperature FM in $Sn_{0.9}In_{0.1}O_2$ nanocrystalline thin films. The substitution of indium replacing Sn atom in SnO_2 lattice can reduce the formation energy of V_{Sn} defects and thus favours to stabilize more V_{Sn} defects in different nanostructure morphologies and also introduces holes in SnO_2 lattice [24]. Theoretical studies [16,22,25] have shown that V_{Sn} defects can introduce a local magnetic moment ~ 4.00 μ_B per defect in SnO_2 and if the concentration of such V_{Sn} defects exceeds the threshold limit, the ferromagnetic interaction between the nearby V_{Sn} defects can be mediated through the localized holes in the lattice. In addition, In_{Sn} defects at Sn site can also introduce local magnetic moment ~ 1μ_B per defect which can further increase the ferromagnetic moment in nanostructured SnO_2 thin films [24]. In the case of nanostructures, the morphology also plays crucial role to stabilize such kind of defects depending on the surface to volume ratio and the grain size associated with that specific morphology. It has been observed as the deposition (Ar) pressure increases, the morphology of nanostructures changes, crystallite size and film thickness decreases, consequently surface disorder of the films increases and thus the samples become prone to possess significant amount of defects or ion vacancies. Earlier spectroscopic evidences also confirm the increase of formation V_{Sn} defects in the $Sn_{0.9}In_{0.1}O_2$ films deposited under increasing Ar pressure, hence resulting stronger ferromagnetic interaction between the magnetic moment of V_{Sn} defects in presence of localised holes arises due to In_{Sn} defects. As the nanowires of $Sn_{0.9}In_{0.1}O_2$ deposited under 10 mbar Ar pressure possess highest concentration of V_{Sn} defects and therefore it exhibits strongest ferromagnetic moment with highest Curie temperature up to 572 K. The persistence of ferromagnetic moment even after annealing in O_2 (i.e. Sample S5) clearly gives the indication that mainly V_{Sn} defects rather V_O defects are responsible for such FM in In-doped SnO_2 films. The gradual decrease in electron concentration (n) with increasing deposition pressure also suggests stabilization of hole-mediated V_{Sn} defect-induced FM in series of In-doped SnO_2 nanocrystalline thin films.

4. Conclusions

$Sn_{0.9}In_{0.1}O_2$ nanostructured thin-films with tunable morphologies such as nanocrystals, nanofibres, nanoflakes and nanowires are fabricated by PLD method using different Ar pressure. The origin of observed room-temperature FM is investigated by employing various spectroscopic techniques which confirm the presence of V_{Sn} defects are responsible for stabilizing FM in $Sn_{0.9}In_{0.1}O_2$ nanostructured thin-films. Oxygen-deficient atmosphere (Ar) and substitution of In^{3+} at Sn site favour to stabilize more V_{Sn} defects within SnO_2 lattice along with a localised hole which helps to mediate the ferromagnetic interaction between the moments of the neighbouring V_{Sn} defects. When $Sn_{0.9}In_{0.1}O_2$ thin-films deposited under higher Ar pressure, the crystallite size and film thickness decrease significantly thereby increases the surface-disorder of the film that also favours the formation of more and more V_{Sn} defects within SnO_2 lattice. Thus, among all the nanostructure morphologies, the nanowires of In-doped SnO_2 thin-films having greater surface-disorder as evident from Raman spectra exhibits strongest ferromagnetic moment (M_S) with Curie temperature (T_C) up to 572 K due to the presence of large concentration of V_{Sn} defects within it. Therefore, triggering the formation of cation vacancy defects through the non-magnetic cationic substitution along with appropriate deposition condition can be very promising to achieve desired room-temperature oxide-based magnetic semiconductor for spintronic and opto-spintronic applications.

Author statement

The author declare that this manuscript (Manuscript Number: SSC-D-22-00532) entitled as "**Surface disorder and cationic-site defect-induced ferromagnetism and correlated Raman vibrational modes in $Sn_{0.9}$ $In_{0.1}O_2$ nanocrystalline thin-films** is original, has not been published before and is not currently being considered for publication elsewhere.

The author confirms sole responsibility for the following: study

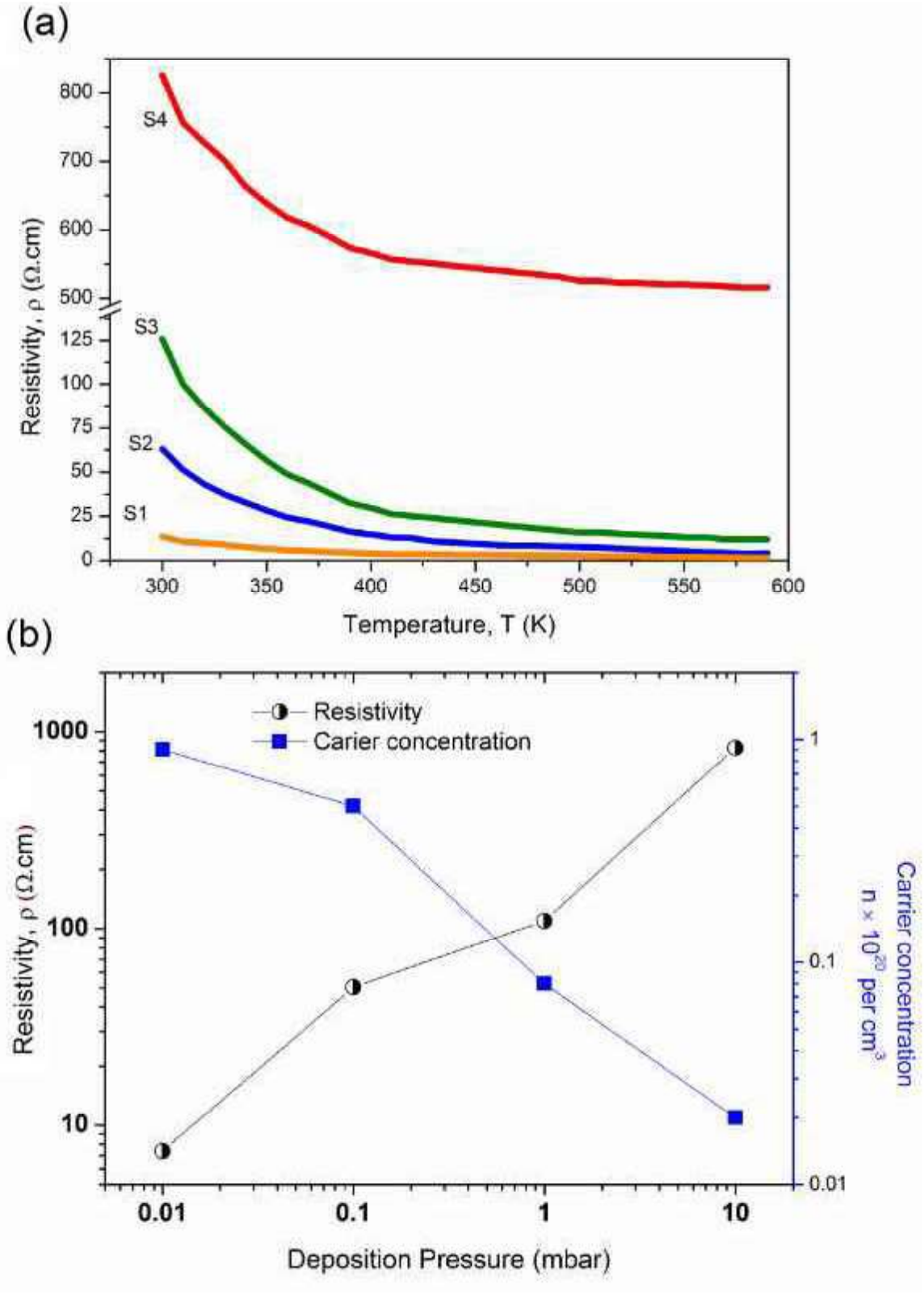

Fig. 8(a). Temperature-dependent electrical resistivity for the different $Sn_{0.96}$ $In_{0.04}O_2$ nanocrystalline thin films and (b) Variation of electrical resistivity and carrier concentration (n) within In-doped SnO_2 with deposition pressure.

conception and design, data collection, analysis and interpretation of results, and manuscript preparation.

Declaration of competing interest

The authors declare that they have no known competing financial interests or personal relationships that could have appeared to influence

the work reported in this paper.

Data availability

Data will be made available on request.

Acknowledgement

Authors would like to acknowledge the support of Prof. K. Mandal, S. N. Bose National Centre for Basic Sciences Kolkata, India for providing sample preparation facility and Prof. P.M.G. Nambisan, Saha Institute of Nuclear Physics, Kolkata, India for fruitful discussions during the course of the work. The author is thankful to Dr. U. Manju, CSIR-Central Glass and Ceramic Research Institute, Kolkata, India for helping in XPS measurements. The author deeply acknowledge Dr. Gautam Dev Mukherjee, Indian Institute of Science Education and Research, Kolkata for providing the micro-Raman spectrometer (LABRAM HR from Horiba Jobin Yvon) facility and other laboratory facilities. The author is also thankful to Dr. B. N. Dev, Indian Institute of Cultivation of Sciences, Jadavpur, Kolkata, India for TEM facilities and fruitful suggestions. Auhors also thankful to Dr. A. Layek, Jadavpur University for his collaborative support during the course of work. Finally, the author acknowledge the support from the advanced laboratory facilities, Department of Physics, B. N. Mahavidyalya, Hooghly specially for the electrical characterization of the samples.

References

[1] S.A. Wolf, D.D. Awschalom, R.A. Buhrman, J.M. Daughton, S. Von Molnar, M. L. Roukes, A.Y. Chtchelkanova, D.M. Treger, Spintronics: a spin-based electronics vision for the future, Science 294 (2011) 1488–1495.

[2] H. Ohno, Making nonmagnetic semiconductors ferromagnetic, Science 281 (1998) 951–956.

[3] M. Stiller, P.D. Esquinazi, Defect-induced magnetism in TiO2: an example of quasi 2D magnetic order with perpendicular anisotropy, Front. Phys. 11 (2023), https://doi.org/10.3389/fphy.2023.1124924.

[4] P.D. Esquinazi, W. Hergert, M. Stiller, L. Bonch, H. Ohldag, D. Spemann, M. Hoffmann, W.A. Adeagbo, A. Ernst, S.K. Nayak, H.B. Hamed, Defect-induced magnetism in nonmagnetic oxides: basic principles, experimental evidence, and possible devices with ZnO and TiO_2, Phys. Status Solidi B 257 (1–29) (2020), 1900623.

[5] A. Zunger, S. Lany, The quest for dilute FM in semiconductors: guides and misguides by theory, Physics 3 (2010) 53.

[6] J.B. Yi, C.C. Lim, G.Z. Xing, H.M. Fan, L.H. Van, S.L. Huang, K.S. Yang, X.L. Huang, X.B. Qin, B.Y. Wang, T. Wu, L. Wang, H.T. Zhang, X.Y. Gao, T. Liu, A.T.S. Wee, Y. P. Feng, J. Ding, FM in dilute magnetic semiconductors through defect engineering: Li-doped ZnO, Phys. Rev. Lett. 104 (2010), 137201.

[7] Q. Wang, Q. Sun, G. Chen, Y. Kawazoe, P. Jena, Vacancy-induced magnetism in ZnO thin films and nanowires, Phys. Rev. B Condens. Matter 77 (2008), 205411.

[8] J.P. Singh, R.H. Chae, d^0 ferromagnetism of magnesium oxide, Condens. Matter 2 (2017) 36.

[9] S. Ghosh, G.G. Khan, B. Das, K. Mandal, Vacancy-induced intrinsic d^0 FM and photoluminescence in potassium doped ZnO nanowires, J. Appl. Phys. 109 (2011), 123927.

[10] A.D. Rata, J. Herrero-Martin, I.V. Maznichenko, F.M. Chiabrera, R.T. Dahm, S. Ostanin, D. Lee, B. Jalan, P. Buczek, I. Mertig, A. Ernst, A.M. Ionescu, K. Dörr, N. Pryds, D.-S. Park, Defect-induced magnetism in homoepitaxial $SrTiO_3$, APL Mater. 10 (2022), 091108.

[11] R. Podila, W. Queen, A. Nath, J.T. Arantes, A.L. Schoenhals, A. Pareio, G. M. Dalpian, J. He, S.J. Hwu, M.J. Skove, A.M. Rao, Origin of FM ordering in pristine micro- and nanostructured ZnO, Nano Lett. 10 (2010) 1383–1386.

[12] S. Ghosh, P.M.G. Nambissan, Evidence of oxygen and Ti vacancy induced FM in post-annealed undoped anatase TiO_2 nanocrystals: a spectroscopic analysis, J. Solid State Chem. 275 (2019) 174–180.

[13] I.S. Elfimov, S. Yunoki, G.A. Sawatzky, Possible path to a new class of ferromagnetic and half-metallic ferromagnetic materials, Phys. Rev. Lett. 89 (2002), 216403.

[14] C.D. Pemmaraju, S. Sanvito, FM driven by intrinsic point defects in HfO_2, Phys. Rev. Lett. 94 (2005), 217205.

[15] J. Osorio-Guillen, S. Lany, A. Zunger, Atomic control of conductivity versus FM in wide-gap oxides via selective doping: V, Nb, Ta in anatase TiO_2, Phys. Rev. Lett. 100 (2008), 036601.

[16] S. Zhang, S.B. Ogale, W. Yu, X. Gao, T. Liu, S. Ghosh, G.P. Das, A.T.S. Wee, R. L. Greene, T. Venkatesan, Electronic manifestation of cation-vacancy-induced magnetic moments in a transparent oxide semiconductor: anatase Nb:TiO2, Adv. Mater. 21 (2009) 2282–2287.

[17] N. Ali, A.R. Vijaya, Z.A. Khan, K. Tarafder, A. Kumar, M.K. Wadhwa, B. Singh, S. Ghosh, Sci. Rep. 9 (2019), 20039, https://doi.org/10.1038/s41598-019-56568-8.

[18] S. Chawla, K. Jayanthi, R.E. Kumala, Room-temperature FM in Li-doped p-type luminescent ZnO nanorods, Phys. Rev. B 79 (2009), 125204.

[19] J. Sun, Q. Tang, A. Lu, X. Jiang, Q. Wan, Individual SnO_2 nanowire transistors fabricated by the gold microwire mask method, Nanotechnology 20 (2009), 255202.

[20] J. Hu, Y. Bando, Q. Liu, D. Golberg, Laser-ablation growth and optical properties of wide and long single-crystal SnO_2 ribbons, Adv. Funct. Mater. 13 (2003) 493.

[21] X.Y. Xue, Y.J. Chen, Y.G. Liu, S.L. Shi, Y.G. Wang, T.H. Wang, Synthesis and ethanol sensing properties of indium-doped tin oxide nanowires Appl. Phys. Lett. 88 (2006), 201907.

[22] Gul Rahman, M. Victor, Garcia-nuñez and soon Cheol Hong, vacancy-induced magnetism in SnO2: a density functional study, Phys. Rev. B 78 (2008), 184404.

[23] S.B. Ogale, R.J. Choudhary, J.P. Buban, S.E. Lofland, S.R. Shinde, S.N. Kale, V. N. Kulkarni, J. Higgins, C. Lanci, J.R. Simpson, N.D. Browning, S. Das Sarma, H. D. Drew, R.L. Greene, T. Venkatesan, High temperature FM with a giant magnetic moment in transparent Co-doped $SnO_{2-\delta}$, Phys. Rev. Lett. 91 (2003), 077205.

[24] G. Bouzerar, T. Ziman, Model for vacancy-induced d^0 FM in oxide compounds, Phys. Rev. Lett. 96 (2006), 207602.

[25] N.N. Bao, J.B. Yi, H.M. Fan, X.B. Qin, P. Zhang, B.Y. Wang, J. Ding, S. Lib, Vacancy-induced room-temperature FM in Ga-TiO_2, Scripta Mater. 66 (2012) 821–824.

[26] J. Ba, D.F. Rohlfing, A. Feldhoff, T. Brezesinski, I. Djerdj, M. Wark, M. Niederberger, Nonaqueous synthesis of uniform indium tin oxide nanocrystals and their electrical conductivity in dependence of the tin oxide concentration, Chem. Mater. 18 (12) (2006) 2848–2854.

[27] B.V. Crist, Handbooks of Monochromatic XPS Spectra, XPS International, 1997.

[28] D. Maestre, A. Cremades, J. Piqueras, L. Gregoratti, Thermal growth and structural and optical characterization of indium tin oxide nanopyramids, nanoislands, and tubes, J. Appl. Phys. 103 (2008), 093531.

[29] S.Y. Li, C.Y. Lee, P. Lin, T.Y. Tseng, Low temperature synthesized Sn doped indium oxide nanowires, Nanotechnology 16 (2005) 451–457.

[30] S. Ghosh, G.G. Khan, K. Mandal, Defect-driven magnetism in luminescent n/p-Type pristine and Gd-substituted SnO2 nanocrystalline thin films, ACS Appl. Mater. Interfaces 4 (2012) 2048.

[31] S. Ghosh, B.N. Dev, Probing of O2 vacancy defects and correlated magnetic, electrical and photoresponse properties in indium-tin oxide nanostructures by spectroscopic techniques, Appl. Surf. Sci. 439 (2018) 891–899.

[32] G.G. Khan, S. Ghosh, K. Mandal, Origin of room temperature d^0 FM and characteristic photoluminescence in pristine SnO_2 nanowires: a correlation, J. Solid State Chem. 196 (2012) 276.

[33] L.Z. Liu, T.H. Li, X.L. Wu, J.C. Shen, P.K. Chu, Optical identification of oxygen vacancy types in SnO_2 nanocrystals, J. Raman Spectrosc. 43 (2012) 1423.

[34] S.H. Sun, G.W. Meng, G.X. Zhang, T. Gao, B.Y. Geng, L.D. Zhang, J. Zuo, Raman scattering study of rutile SnO_2 nanobelts synthesized by thermal evaporation of Sn powders, Chem. Phys. Lett. 376 (2003) 103.

[35] J. Gan, X. Lu, J. Wu, S. Xie, T. Zhai, M. Yu, Z. Zhang, Y. Mao, S.C.I. Wang, Y. Shen, Y. Tong, Oxygen vacancies promoting photoelectrochemical performance of In_2O_3 nanocubes, Sci. Rep. 3 (2013) 1021.

[36] L.Z. Liu, X.L. Wu, F. Gao, J.C. Shen, T.H. Li, P.K. Chu, Determination of surface oxygen vacancy position in SnO_2 nanocrystals by Raman spectroscopy, Solid State Commun. 151 (2011) 811.

[37] A. Janotti, C.G. Van de Walle, Fundamentals of zinc oxide as a semiconductor, Rep. Prog. Phys. 72 (2009), 126501.

[38] A. Far, M.A. Stroscio, M. Meyyappan, D.J. Goorsky, G. P Wiederrecht, M. Dutta, Tailoring the surface properties and carrier dynamics in SnO_2 nanowires, Nanotechnology 22 (2011), 285709.

[39] X. Xiang, X. T Zu, S. Zhu, L.M. Wang, V. Shutthanandan, P. Nachimuthu, Y. Zhang, Photoluminescence of SnO_2 nanoparticles embedded in Al_2O_3, J. Phys. D Appl. Phys. 41 (2008), 225102.

[40] J.H. He, T.H. Wu, C.L. Hsin, K.M. Li, L.J. Chen, Y.L. Chueh, L.J. Chou, Z.L. Wang, Beaklike SnO_2 nanorods with strong photoluminescent and field-emission properties, Small 2 (2006) 116–120.

[41] V. Golovanov, V. Golovanova, M. Kuisma, T. T. Rantala Electron spin resonance parameters of cation vacancies in tin dioxide doped with fluorine and hydrogen, J. Appl. Phys. 114 (2013), 143907.

Original Article

Revision of *Schizomeris* (*Chlorophyta*) with Special Reference to its Sexual Reproduction

Malay Ghosh, Asit Baran De[1]

Department of Botany, Bejoy Narayan Mahavidyalaya, Hooghly, [1]Department of Microbiology, University of Burdwan, Bardhaman, West Bengal, India

Abstract

Objective: Detail microscopic study of morphology and reproduction of *Schizomeris leibleinii* Kützing. **Materials and Methods:** Filaments of this green algae was collected periodically from the underside of the leaves of some living *Nymphaea stellata* Willdenow plants growing in a tank and were preserved in 4% formaldehyde along with a portion of the substrate. Zoospores and gamete formation could be readily induced when the freshly collected specimens were cultured *in vitro* in sterilized water of the natural habitat. **Results:** Many new findings have been revealed, such as the occasional development of branch functioning as accessory holdfast with a lobed lower portion, vegetative reproduction by degeneration of one or more intercalary cells in the region of constriction breaking the filament into two fragments, and isogamous sexual reproduction, which takes place by fusion of nonmotile gametes within the gametangium. Formation of new filament parthenogenetically by germination of unfused isogametes has been reported. **Conclusion:** *S. leibleinii* is homothallic and its life cycle is haplontic.

Keywords: Aflagellate isogametes, isogamy, *Schizomeris leibleinii* Kützing

Introduction

We collected a filamentous alga from Burdwan, West Bengal, India in 2019–2020. It was identified as *Schizomeris leibleinii* Kützing. This alga was recorded for the first time in India from the state of Punjab, growing on the stem of water plants in a tank at Bodal, district Hosiarpur.[1] Later, it has been recorded from nine more states of India.[2,3] Besides India, *Schizomeris* has been recorded from Myanmar,[4] New Zealand,[5] Pakistan,[6] Portugal,[7] Brazil, England, Germany, South Africa, USA,[8] Iran,[9] etc. Thus, *Schizomeris* exhibits both tropical and temperate distribution.

S. leibleinii was described by Kützing.[10] Later Fritsch and Rich[11] described a second species *Schizomeris irregularis* F.E.Fritsch and M.F. Rich. In addition, *Uronema indicum* S.L. Ghose, described from Lahore, Pakistan, as a new species of the genus *Uronema* Lagerheim,[6] was transferred to the genus *Schizomeris* Kützing by Fritsch and Rich[11] as *Schizomeris indicum* (Ghose) Fritsch and Rich. Hence, three species of the genus *Schizomeris* were recorded worldwide. However, recent molecular analyses of collections from widespread locations have revealed that *S. indicum* and *S. irregularis* are actually synonyms of *S. leibleinii*, and *Schizomeris* is, therefore, a monotypic genus[12] in the family Schizomeridaceae (Chaetophorales, Chlorophyta).

We have studied in detail the specimens collected by us from India and compared them with all the published descriptions, and many new findings have been revealed that were not reported before. Besides, in the present investigation, we have revealed the process of sexual reproduction based on the present Indian collections. It may be mentioned here that although the sexual reproduction and life cycle of *S. leibleinii* were reported[13] more than 80 years ago, those have not been mentioned in any subsequent literature; instead, its sexual

Received: 27-Feb-2023 **Revised:** 26-Jul-2023
Accepted: 05-Feb-2024 **Published:** 20-Jun-2024

Access this article online

Quick Response Code:

Website: http://www.jmau.org/

DOI: 10.4103/jmau.jmau_21_23

Address for correspondence: Dr. Malay Ghosh, Department of Botany, Bejoy Narayan Mahavidyalaya, Itachuna, Hooghly - 712 147, West Bengal, India.
E-mail: drmalayghoshbnmv@gmail.com

How to cite this article: Ghosh M, De AB. Revision of *Schizomeris* (*Chlorophyta*) with special reference to its sexual reproduction. J Microsc Ultrastruct 0;0:0.

FISHERIES & AQUATIC LIFE (2023) 31: 147 – 155
Archives of Polish Fisheries
DOI 10.2478/aopf-2023-0015

sciendo

RESEARCH ARTICLE

Histology and histochemistry of the stomach of an Asian schilbeid, *Clupisoma garua* (Hamilton)

Saroj Kumar Ghosh

Received – 13 March 2023/Accepted – 11 September 2023. Published online: 30 September 2023;
Citation: Ghosh, S. K. (2023). Histology and histochemistry of the stomach of an Asian schilbeid, *Clupisoma garua* (Hamilton). Fisheries & Aquatic Life 31, 147-155.

Abstract. The cellular peculiarities and histochemical nature of the stomach in the freshwater catfish *Clupisoma garua* (Hamilton) were explored with light microscopic analysis. The pouch shaped muscular stomach was distinguished into the anterior cardiac and posterior pyloric regions. Histologically, the wall of stomach consisted of four distinct layers of the mucosa, submucosa, muscularis, and very thin serosa. The mucosa contained two kinds of epithelia: the superficial epithelium lined with columnar epithelial cells and the glandular epithelium crowded with numerous gastric glands that open through gastric pits. The vascularized submucosa was made up of loose connective tissues that extended into the mucosa forming lamina propria. The well-developed muscular layer was composed of an inner thick layer of circular muscle and an outer layer of longitudinal muscle bands. The detection and localization of mucopolysaccharides, glycogen, protein, and tryptophan in the various cells bounded in the stomach were described with the feeding behavior of the fish concerned.

Keywords: Garua bacheha, stomach, histomicroscopy, histochemistry

S. K. Ghosh [✉]
Department of Zoology, Bejoy Narayan Mahavidyalaya, Itachuna, Hooghly – 712 147, West Bengal, India

Introduction

The structure of the digestive tract, particularly the stomach varies among fishes and is usually adapted to food and feeding habits. Morphological structures and the shape of the stomach are variable in the different species of fishes and are related to capacity in the body cavity (Pandey and Shukla 2019). The stomach is not differentiated externally from the esophagus but can be compared morphologically by dissimilarities in the mucosal lining, which is thin in the esophagus but sturdy and wavy in the stomach. The structural organization and function of the stomach in fishes has been reported upon earlier (Saadatfar et al. 2010, Naguib et al. 2011, Musa et al. 2013, Ghosh and Chakrabarti 2015, Moawad et al. 2017, De Felice et al. 2021). The gross anatomy and size of the stomach differs markedly among fishes in relation to the nature of the food they consume. The stomach is usually large and pouch-like with thick walls in predatory carnivorous fishes like *Wallago attu* (Bloch & Schneider), *Sperata aor* (Hamilton), and *Chitala chitala* (Hamilton) that feed on large prey (Khanna 2019). The stomachs of omnivorous and planktivorous fishes are shorter than those of carnivores. In *Tenualosa ilisha* (Hamilton), *Gudusia chapra* (Hamilton), and mullets the stomach is

smaller in size but highly stiffened into a gizzard-like structure to triturate food items (Khayyami et al. 2015). Not all teleosts have a true stomach, and it is absent in several fishes. Among cyprinids, the anterior portion of the intestine just behind the esophagus is modified into a sac-like structure, and this intestinal bulb serves for the temporary storage of food (Hofer 2006). The stomach is lacking in *Hippocampus*, *Scomberesox* and *Xenentodon cancila* (Hamilton) (Fänge and Grove 1979). Lacunae still exist in some aspects of studies relating to structural adaptations of the stomach in Indian teleost fishes correlated with feeding habits. With this view, the important food fish *Clupisoma garua* (Hamilton) was selected for the present study.

C. garua (Siluriformes, Ailiidae) is a demersal, predaceous river catfish that feeds on mollusks, aquatic insects, crustaceans, small fishes, and decaying algal matter (Gupta and Banerjee 2016, Bhakta and Sonia 2020). An attempt was in the present investigation to describe the microstructure and function of the stomach of *C. garua* by applying histological and histochemical techniques. This microscopic survey of the stomach will provide information about the detailed composition and chemical nature of various cells in relation to digestion.

Materials and methods

Sample collection

Sexually mature specimens of *C. garua* (ranging from 10.56 to 21.42 cm standard length) were procured live from the Bhagirathi-Hooghly River near areas surrounding Kalyani in West Bengal using traditional fishing gear. They were identified following a key to the classification of fishes by Jayaram (2010). The specimens were anesthetized deeply with Benzocaine (4 mg l^{-1}), and the abdominal cavity of the fish was opened with scissors. The stomach part was removed, cut into small samples and processed with the relevant techniques.

Histological analysis

Small pieces of stomach were immediately fixed in aqueous Bouin's solution for 24 h. After fixation, the samples were washed well in 70% ethanol, dehydrated through graded series of (50–100%) ethanol, and cleared with xylene. The tissues were infiltrated with paraffin wax at 56–58°C for 1.5 h, and embedded in paraffin blocks. Serial sections were cut at 4 µm thickness using a rotary microtome (Weswox MT-1090A) and stained with Delafield's Haematoxylin-Phloxin (HP), Delafield's Haematoxylin-Eosin (HE) (Fischer et al. 2008), and Mallory's Triple (MT) stain (Mallory 1936) for light microscopic observation.

Histochemical analysis

Small fragments of stomach were kept in 10% neutral formalin for 18 h. After the routine procedure, the tissues were embedded in paraffin wax at 52–54°C and sectioned at an 8 µm thickness. The paraffin sections were subjected to the following histochemical investigations: periodic acid–Schiff's (PAS) reaction in combination with Alcian Blue (AB) (PAS-AB) for the detection of neutral and acid mucins (Yamabayashi 1987); Best's Carmine (BC) method for the detection of glycogen (Horobin and Murgatroyd 1971); the Mercuric Bromophenol Blue (MBB) method for detecting basic protein (Mazia et al. 1953); and the Dimethylaminobenzaldehyde (DMAB)-nitrite method for tryptophan (Adams 1957). The stained slides were examined and photographed using an Olympus-Tokyo PM-6 compound microscope at different magnifications.

Results

Histology

The stomach of *C. garua* was a pouch-shaped muscular structure with cardiac and pyloric regions. The wall of the stomach was comprised of four basic

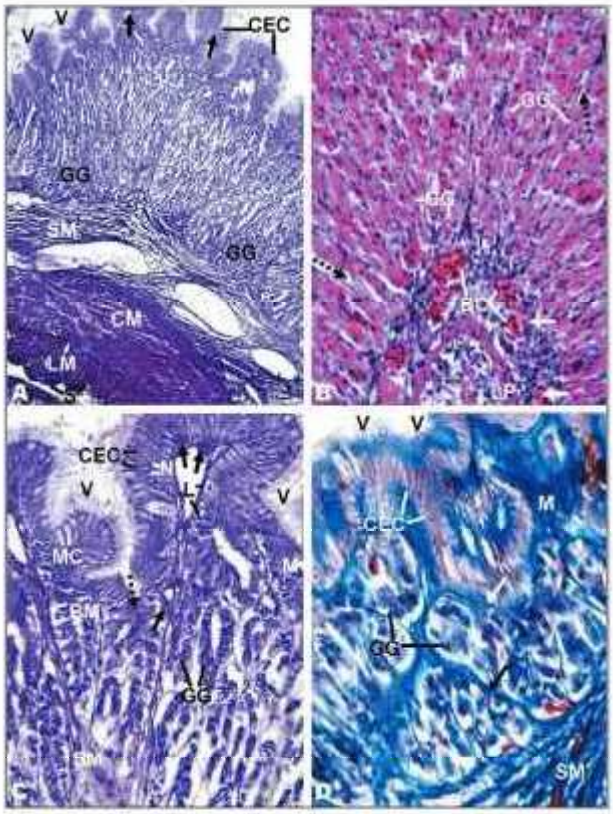

Figure 1. Microphotographs of the transverse sections through the stomach of *C. garua* showing cellular architecture stained with Delafield's Haematoxylin-Phloxin (HP), Delafield's Haematoxylin-Eosin (HE) and Mallory's triple (MT) stain. **(A)** The cardiac stomach shows mucosa (M) with numerous folds (solid arrows) provided with columnar epithelial cells (CEC) and gastric glands (GG), submucosa (SM), thicker circular muscle layer (CM), thinner longitudinal muscle layer (LM) and thin serosa (S). Solid arrows indicate thin top plate over CEC (HP × 4X). **(B)** Mucosa (M) shows clusters of tubular GG and submucosa with blood capillaries (BC) and eosinophilic granular cells (solid arrows) forming lamina propria (LP). Broken arrow marks the opening of GG to the gastric pit (HE × 15X). **(C)** Mucosa (M) containing CEC with prominent nuclei (N) and basal gastric glands (GG) distinguished from the submucosa (SM) by the basement membrane (BM). Note the presence of scattered mucous cells (MC) and lymphocytes (L) in mucosa and eosinophilic granular cells (solid arrows) in SM. Arrow heads specify mucus film over the apical surface of CEC and broken arrow marks the gastric pit (HP × 40X). **(D)** Magnified mucosa (M) exhibits compactly arranged CEC and GG bounded by connective tissue septa (solid arrows) arising from submucosa (SM). Arrow heads indicate mucin film over mucosal surface (MT × 45X).

histological layers: mucosa, submucosa, muscularis, and serosa (Fig. 1A). The mucosa was usually simpler than that in higher vertebrates and expanded by thick longitudinal folds, the rugae, the surface of which were carpeted with tiny depressions, the gastric pits. The cardiac stomach consisted of two types of epithelia: luminal epithelium with a monolayer of simple columnar epithelial cells and the glandular epithelium containing numerous gastric glands (Figs. 1C and D). The columnar epithelial cells were tall and elliptical in shape and tapered at the base. They had centrally or basally placed oval nuclei and their apical lining contained a prominent top plate of mucus. Mucous cells were scattered on the superficial epithelium (Fig. 1C). The glandular epithelium was packed with a cluster of gastric glands that were rounded or tubular in shape and present at the basal portion of the mucosa (Figs. 1B, C, and D). The gastric glands were composed of rhomboidal shaped granular cells with middling rounded nuclei distributed around a lumen. They usually opened into the lumen of the stomach trough the gastric pits (Figs. 1B and C). The gastric glands were firmly bordered by thin strips of connective tissues of lamina propria (Fig. 1D). Few lymphocytes were distinguished in the deeper layer of mucosa by their darkly staining conspicuous nuclei (Fig. 1C). There were no gastric glands in the pyloric stomach.

The submucosa was separated from mucosa by a basement membrane (Fig. 1C) made up of collagenous fibers, connective tissues, nerve fibers, and blood capillaries that protruded into the mucosal foldings forming lamina propria. (Fig. 1B). A few eosinophilic granular cells were also observed in the submucosa (Figs. 1B and C), which was thick in the pyloric stomach. The muscularis layer of the cardiac stomach was thinner than that in the pyloric stomach. It contained an interior circular and outward longitudinal muscular layer (Fig. 1A). The former layer was thicker than the latter. The outermost serosa layer was exceedingly thin and rarely impaled by blood vessels.

Histochemistry

Mucopolysaccharides

Combined periodic acid–Schiff's reaction and Alcian Blue (PAS-AB) showed a purple-bluish color of

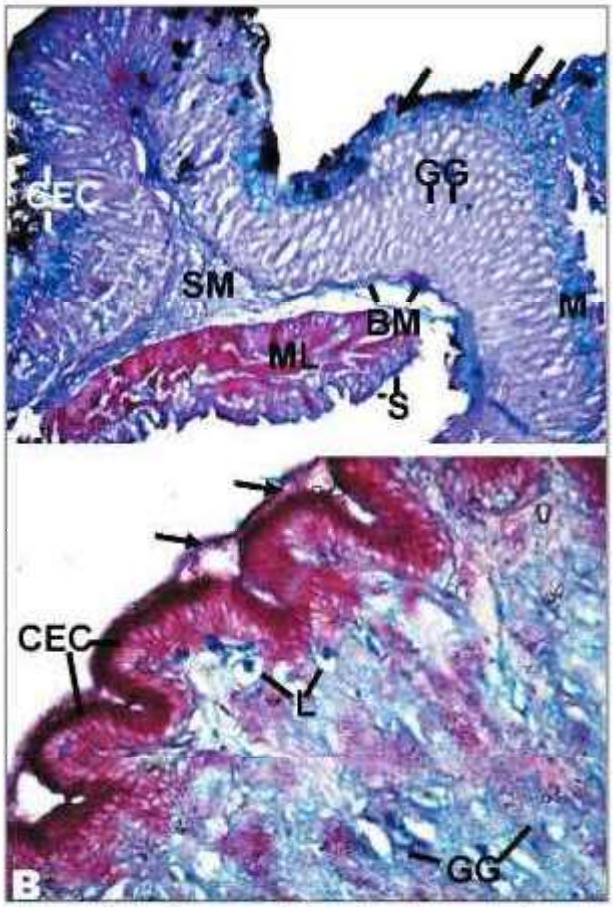

Figure 2. Photomicroscopy of the section of stomach displaying periodic acid–Schiff's (PAS) reaction conjointly with Alcian Blue (AB). **(A)** Localization of neutral mucopolysaccharide in the columnar epithelial cells (CEC) and both acid and neutral mucopolysaccharides in gastric glands (GG) of mucosa (M). Gastric pits (arrows) show bright blue color from the accumulation of acid mucopolysaccharides. The basement membrane (BM), submucosa (SM), muscularis (ML), and serosa (S) layers exhibit positive response (PAS-AB × 10X). **(B)** Intense PAS reaction in CEC along with luminal border of the mucosa (arrows). Note positive reaction in lymphocytes (L) and GG (PAS- AB × 40X).

varied magnitude conforming to the neutral and acid mucopolysaccharides of the different layers coating the stomach. The columnar epithelial cells of gastric mucosa were a bright purple color from PAS, while the gastric glands of glandular epithelium were a purple-bluish color because of the localization of both neutral and acid mucopolysaccharides (Figs. 2A and B). The gastric pits contained acid mucopolysaccharides. The secreted luminal mucin over the apical portion of the columnar epithelial cells were an intense purple color marking the presence of ample neutral mucin (Fig. 2B). The basement membrane between the mucosa and submucosa together with fibrous connective tissues exhibited a distinctive bluish-purple color. The lymphocytes of the mucosa and the muscularis and serosa layer expressed positive reactions with this combined test (Fig. 2A).

Glycogen

The results of Best's carmine test showed a deep red color in the columnar epithelial cells together with the gastric glands of the mucosa because of the marked amount of glycogen (Figs. 3A and B). The blood capillaries in the submucosa contained different shades of staining deposition of glycogen but the connective tissues exhibited a weak reaction. The subtle reaction of glycogen was discernible in the muscularis and serosa layer (Fig. 3A).

Protein

The mercuric bromophenol blue reaction revealed a dark blue color of diversified magnitudes in harmony with the localization of basic protein in various regions of the stomach. Mucous cells and columnar epithelial cells with coarse granules in the apical mucosa showed strong reactivity (Figs 4A and B). Gastric glands exhibited their protein inclusions as darkly stained fine grains dissipated homogeneously in the cytoplasm. The blood capillaries and connective tissues in the submucosa showed a positive reaction (Fig. 4A). The muscularis layer showed an intense reaction.

Tryptophan

The mucosa layer of stomach displayed a deep blue color considered a positive reaction for tryptophan (Fig. 5A). The zymogen granules of the gastric glands in the glandular epithelium showed the maximum intensity of the tryptophan reaction (Fig. 5B). The columnar epithelium cells of the superficial mucosa also furnished positive reactions for tryptophan though comparatively less than that of the gastric glands. The submucosa, the muscularis layer, and

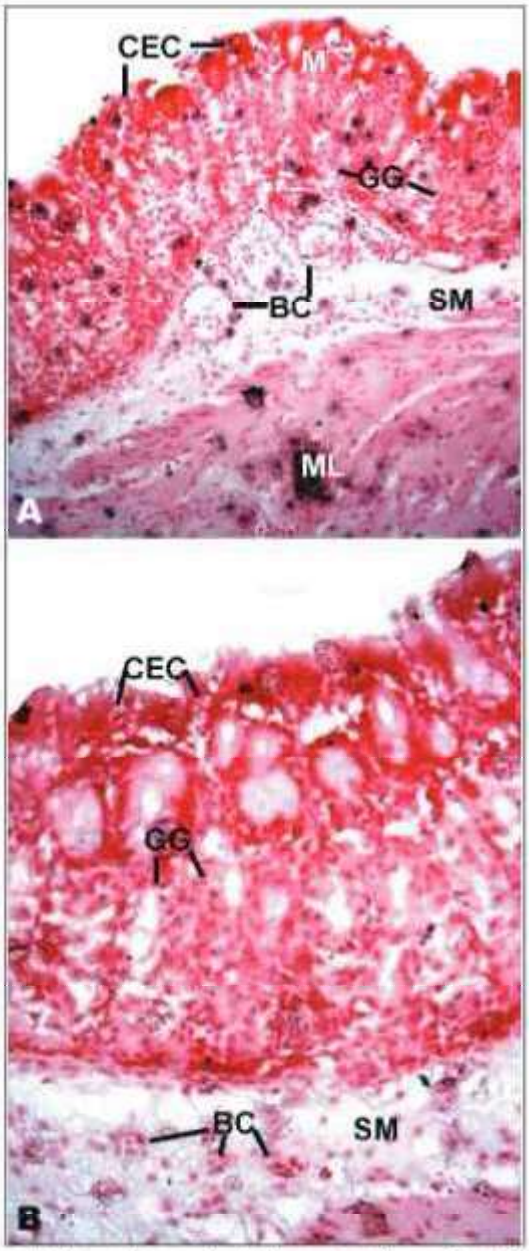

Figure 3. Microphotographs of the section of stomach exhibiting Best's Carmine (BC) reaction for the detection of glycogen. **(A)** Showing glycogen content in the columnar epithelial cells (CEC) and gastric glands (GG) of mucosa (M). Note moderate reaction in blood capillaries (BC) of submucosa (SM) and muscularis layer (ML) (BC × 10X). **(B)** Intense localization of glycogen in CEC and GG of mucosa. BC in SM display a moderate reaction (BC × 40X).

the serosa were colorless and exhibited negative responses to this test (Fig. 5A).

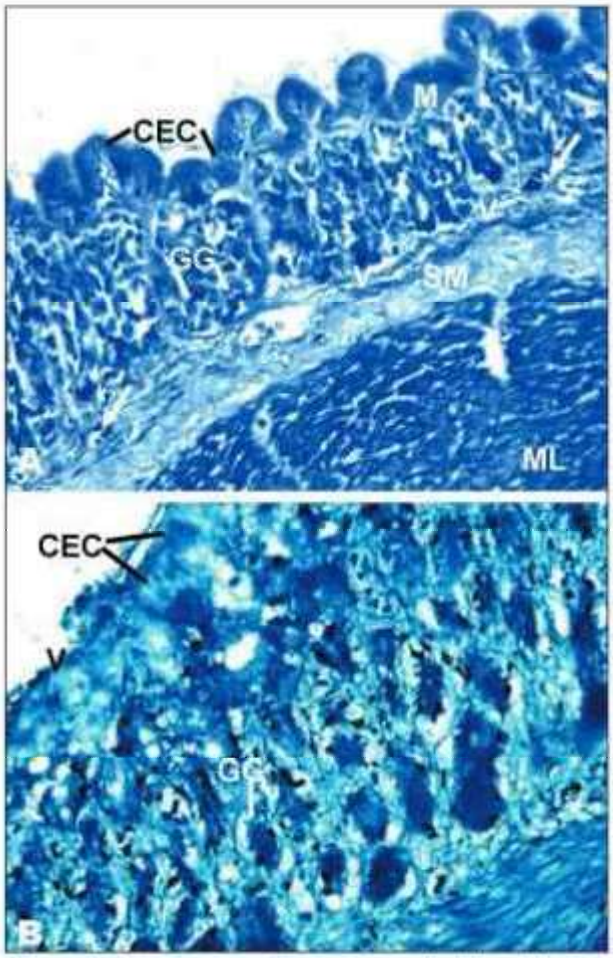

Figure 4. Transverse sections of stomach show Mercuric Bromophenol Blue (MBB) reaction. **(A)** Localization of protein in columnar epithelial cells (CEC) and gastric glands (GG) of mucosa (M). Note the positive reaction in the muscularis layer (ML), connective tissues (arrow heads), and blood capillaries (solid arrows) of the submucosa (SM) (MBB × 10X). **(B)** Inclusion of protein in CEC, GG, and mucous cell of the mucosa layer (MBB × 40X).

Discussion

The digestive system of teleosts exhibits much variation in structure and function and is adapted for particular foods. The anatomy of the stomach is distinctly variable in size and organization in relation to the quantity of food consumed by the species (Ostrander 2000). In *C. garua*, the stomach was pouch-like and thick walled since the fish is predatory in nature. The walls of the stomach were usually

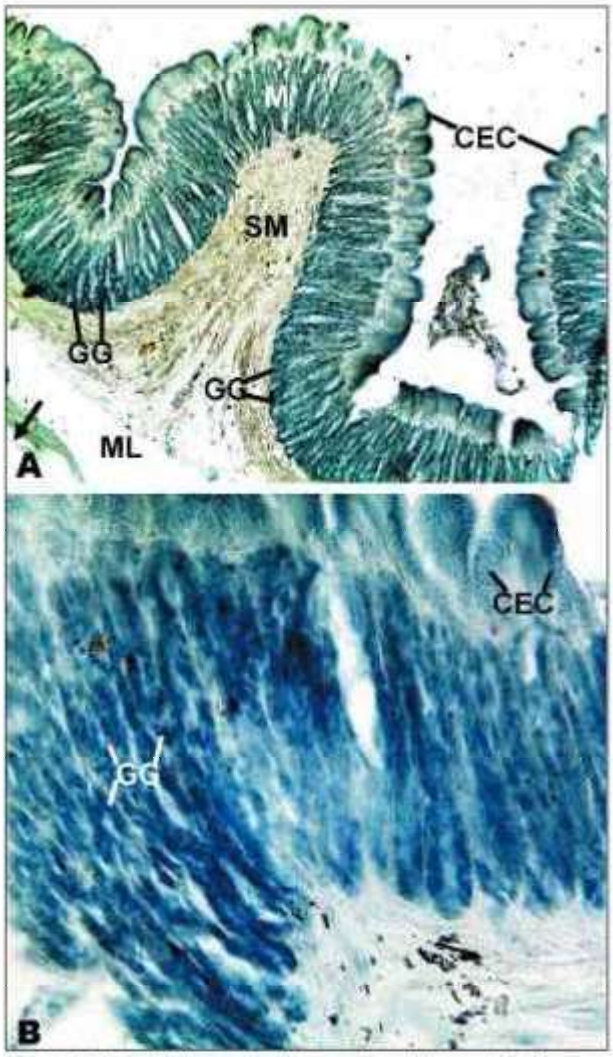

Figure 5. Microphotographs of the section of stomach in *C. garua* showing the localization of trypotophan (DMAB). (A) Mucosa (M) with columnar epithelial cells (CEC) and gastric glands (GG) show a positive tryptophan reaction. The submucosa (SM), mucularis (ML), and serosa (S) display negative reactions (DMAB × 10X). (B) Strong intensity of tryptophan reaction in GG and CEC. (DMAB × 40X).

folded and can expand. Histologically, the stomach of *C. garua* had four layers and is related to other teleost fishes (Arellano et al. 2001, Khayyami et al. 2015). The cardiac stomach was formed by two types of epithelia – surface epithelium and glandular epithelium. The surface epithelium was composed of columnar epithelial cells with a notable top plate of mucin and scanty mucous cells. Barrington (1957) reported that the columnar epithelial cells of the superficial epithelium secreted gastric mucin that protected the stomach surface from mechanical damage. The columnar epithelial cells of the superficial epithelium are described as absorptive in function by some researchers (Grau et al. 1992, Arellano et al. 2001). From the present study, it can be assumed that columnar epithelial cells of the mucosa served a dual purpose of the secretion of mucus and the absorption of digested food stuffs. Very few mucous cells were observed in the gastric mucosa of *C. garua*. Their lubricant secretions safeguard the gastric epithelium from the chemical and physical destruction that could occur (Mescher 2016). The lymphocytes in the mucosa layer of the stomach might have been engaged in protecting the fish against various pathogens (Park and Kim 2001, Moawad et al. 2017).

The gastric glands of the cardiac stomach were primitive in nature and not distinguished into oxyntic and peptic types. They opened into the lumen through the gastric pits and secreted pepsinogen and hydrochloric acid. The gastric histology of teleosts is usually simpler than higher vertebrates as the gastric glands bear a single type of cell that secretes both pepsinogen and hydrochloric acid (Rebolledo and Vial 1979, Albrecht et al. 2001). *C. garua*, a carnivorous catfish, needs the active secretion of digestive enzymes to adequately digest its proteinaceous foods, and, accordingly, profuse bunched gastric glands developed. The proteolytic enzyme pepsin originated in the gastric juice that was secreted by the granular cells of the gastric glands.

The presence of collagenous fibers and connective tissues in the lamina propria of the stomach might provide a protective, stiffened coat in addition to keeping the gastric gland in the perfect location (Albrecht et al. 2001). The muscular layer of the stomach was comparatively thick and formed by the usual inner wide circular layer and outer longitudinal layer of muscle fibers connected with the thin serosa. This organization of muscle layers probably helped to keep the enlargement of the wall of cardiac stomach within bounds. The greater development of the circular muscle layer presumably assisted in decisive contractions for comminuting semi-digested

foods. Murray et al. (1994) and Khayyami et al. (2015) also report similar features.

PAS reactions in the columnar epithelial cells along with the apical border were indicated by the purple color from the presence of neutral mucin, whereas the bluish-purple color of the gastric glands illustrated the subsistence of both acid and neutral mucins. The mucoid nature of the gastric epithelium is reported by several researchers in many teleosts (Murray et al. 1994, Scocco et al. 1996, Raji and Norouzi 2010, Okuthe and Bhomela 2020). The apical border of the columnar epithelium produced a strong PAS reaction because of the presence of mucous cells. The surface epithelium possibly secreted mucus for the lubrication and propulsion of food stuffs toward the pyloric portion and also to neutralize the acid secreted by the gastric glands. The mucin secreted also shielded the gastric epithelium from mechanical abrasion and stoped autodigestion (Petrinec et al. 2005).

The Best's carmine response in the columnar epithelial cells of the stomach was conceivably associated with the synthesis of neutral mucin that needed energy, and the deposited glycogen provided it. The glycogen reaction in the gastric glands of *C. garua* was concomitant with the synthesis of zymogen granules and ergastic matters for the secretion of pepsinogen and HCl. Anwar and Mahmoud (1975) report the presence of ailing glycogen content in different layers of the intestines of Egyptian lizards used as an inception of energy but not accumulated.

The presence of basic protein in the mucosa, submucosa, and muscularis layers of the stomach is required for various metabolic and physiological activities. Arellano et al. (2001) report there are proteins rich in lysine, arginine, cysteine, and cystine in the columnar epithelial cells, gastric glands, lamina propria, and muscular layers of the stomach of *Solea senegalensis* Kaup. The gastric glands of the mucosa layer were firmly positive to mercury-bromophenol blue staining because of the existence of enzymatic precursors like pepsinogen or other gastrointestinal enzymes (Gutiérrez et al. 1986, Gisbert et al. 1999). The existence of a diversified proportion of protein and tryptophan in the columnar epithelial cells of *C. garua* might have been related to the metabolic processes of the cell. The presence of tryptophan residues in the gastric glands stemmed from the condensation of quantities of zymogen as a harbinger of pepsinogen. Medeiros et al. (1970) recorded the amino acids tryptophan, tyrosine, and arginine in the glandular cells of the stomach in *Pimelodus maculatus* Lacepčde for the synthesis of pepsinogen by the gastric glands.

In conclusion, the stomach of *C. garua* had a variety of cells that performed specific specialized functions. The glandular epithelium was characterized by hydrochloric acid and pepsin producing gastric glands, the principal site for gastric digestion. The present study provides information about the cellular features of the stomach that will help to further elucidate the nutritional physiology of this fish species.

Acknowledgments. The author is thankful to Dr. Goutam Bit, Principal of Bejoy Narayan Mahavidyalaya, Itachuna, Hooghly for providing the necessary laboratory facilities.

ORCID iD

Saroj Kumar Ghosh https://orcid.org/0000-0003-3973-8013

References

Adams, C. W. M. (1957). A p-Dimethylaminobenzaldehyde nitrate method for the histochemical demonstration of tryptophan and related compounds. Journal of Clinical Pathology, 10(1), 56-62.

Albrecht, M. P., Ferreira, M. F. N., Caramaschi, E. P. (2001). Anatomical features and histology of the digestive tract of two related neotropical omnivorous fishes (Characiformes; Anostomidae). Journal of Fish Biology, 58(2), 419-430.

Anwar, I. M., Mahmoud, B. I. (1975). Histological and histochemical studies on the intestine of the Egyptian lizards, *Mabuya quinquetaeniata* and *Chalcides ocellatus*. Bulletin of the Faculty of Science, 4, 101-108.

Arellano, J. M., Storch, V., Sarasquete, C. (2001). Histological and histochemical observations in the stomach of the Senegal sole, *Solea senegalensis*. Histology and Histopathology, 16(2), 511-521.

Barrington, E. J. W. (1957). The alimentary canal and digestion. In: The physiology of fishes (Ed.) M. E. Brown. Academic Press, London: 109-161.

Bhakta, D., Sonia, (2020). Review on *Clupisoma garua* (Hamilton, 1822), an inhabitant species in Inland open waters of India. Innovative Farming, 5(1), 25-29.

De Felice, E., Palladino, A., Tardella, F. M., Giaquinto, D., Barone, C. M. A., Crasto, A., Scocco, P. (2021). A morphological, glycohistochemical and ultrastructural study on the stomach of adult Rainbow trout *Oncorhynchus mykiss*. The European Zoological Journal, 88(1), 269-278.

Fänge, R., Grove, D. (1979). Digestion. In: Fish physiology (Ed.) W. S. Hoar, D. S. Randall, J. R. Brett, Academic Press, London: 162-241.

Fischer, A. H., Jacobson, K. A., Rose, J., Zeller, R. (2008). Hematoxylin and eosin staining of tissue and cell sections. Cold Spring Harbor Protocols, 3, 1-3.

Ghosh, S. K., Chakrabarti, P. (2015). Histological, surface ultrastructural, and histochemical study of the stomach of red piranha, *Pygocentrus nattereri* (Kner). Archives of Polish Fisheries, 23(4), 205-215.

Gisbert, E., Sarasquete, M. C., Williot, P., Castelló-Orvay, F. (1999). Histochemistry of the development of the digestive system of Siberian sturgeon during early ontogeny. Journal of Fish Biology, 55(3), 596-616.

Grau, A., Crespo, S., Sarasquete, M. C., Gonzalez de Canales, M. L. (1992). The digestive tract of the amberjack *Seriola dumerili*, Risso: a light and scanning electron microscope study. Journal of Fish Biology, 41(2), 287-303.

Gupta, P., Banerjee, S. (2016). A note on *Clupisoma garua* (Hamilton, 1822), a freshwater catfish of Indian subcontinent (Teleostei: Siluriformes). Iranian Journal of Ichthyology, 3(2), 150-154.

Gutiérrez, M., Sarasquete, C., González de Canales, M. L. (1986). Distribución histoquímica de carbohidratos y proteínas en estómago e intestino de *Anguilla anguilla* L., 1758 (Osteichthyes, Anguillidae). de las Salinas de Cádiz. Investigacao Pesquera, 50(4), 553-564

Hofer, R. (2006). Morphological adaptations of the digestive tract of tropical cyprinids and cichlids to diet. Journal of Fish Biology, 33(3), 399-408.

Horobin R. W., Murgatroyd, L. B. (1971). The staining of glycogen with Best's carmine and similar hydrogen bonding dyes. A mechanistic study. Journal of Histochemistry, 3(1), 1-9.

Jayaram, K. C. (2010). The freshwater fishes of the Indian region. Narendra Publishing House, Delhi: 616 pp.

Khanna, S. S. (2019). An introduction to fishes. Surject Publications, Delhi: 648 pp.

Khayyami, H., Zolgharnein, H., Salamat, N., Movahedinia, A. (2015). Anatomy and histology of the stomach and pyloric caeca in Mugilidae, *Liza klunzingeri* (Day, 1888), from northeastern Persian Gulf. Journal of Entomology and Zoology Studies, 3(6), 401-404.

Mallory, F. B. (1936). The aniline blue collagen stain. Stain Technology, 11(3), 101-102.

Mazia, D., Brewer, P. A., Alfert, M. (1953). The cytochemical staining and measurement of protein with mercuric bromphenol blue. The Biological Bulletin, 104(1), 57.

Medeiros, L. O., Ferris, S., Godinha, H., Medeiros, L. F. (1970). Proteins and polysaccharides of the club shaped cells in the lining epithelium of fish (*Pimelodus maculates*) digestive tract: histochemical study. Annales d'Histochimie, 15(3), 181-186.

Mescher, A. L. (2016). Junqueira's Basic histology text and atlas. McGraw-Hill Education, New York. 560 pp.

Moawad, U. K., Awaad, A. S., Mohamed, G. T. (2017). Histomorphological, histochemical, and ultrastructural studies on the stomach of the adult African catfish (*Clarias gariepinus*). Journal of Microscopy and Ultrastructure, 5(3), 155-166.

Murray, H. M., Wright, G. M., Goff, G. P. (1994). A comparative histology and histochemical study of the stomach from three species of pleuronectid, the Atlantic halibut, *Hippoglossus hippoglossus*, the yellow tail flounder, *Pleuronectes ferruginea*, and the winter flounder, *Pleuronectes americanus*. Canadian Journal of Zoology, 72(7), 1199-1210.

Musa, M., Yanuhar, U., Susilo, E., Soemarno. (2013). Stomach histological decay of milkfish, *Chanos Chanos* (Forsskål, 1775): ontogeny, environmental stress, shifting food composition, and disease infection. Journal of Natural Sciences Research, 3, 194-200.

Naguib, S. A. A., El-Shabaka, H. A., Ashour, F. (2011). Comparative histological and ultrastructural studies on the stomach of *Schilbe mystus* and the intestinal swelling of *Labeo niloticus*. Journal of American Science, 7(8), 251-263.

Okuthe, G. E., Bhomela, B. (2020). Morphology, histology and histochemistry of the digestive tract of the Banded tilapia, *Tilapia sparrmanii* (Perciformes: Cichlidae). Zoologia, 37, 1-14

Ostrander, G. K. (2000). The laboratory fish. Academic Press, California, 678 pp.

Pandey, K., Shukla, J. P. (2019). Fish and Fisheries. Rastogi Publications, Meerut: 588 pp.

Park, J. Y., Kim, I. S. (2001). Histology and mucin histochemistry of the gastrointestinal tract of the mud loach, in relation to respiration. Journal of Fish Biology, 58(3), 861-872.

Petrinec, Z., Nejedli, S., Kuir, S., Opačak, A. (2005). Mucosubstances of the digestive tract mucosa in northern pike (*Esox lucius* L.) and European catfish (*Silurus glanis* L.). Veterinarski Arhiv, 75(4), 317-327.

Raji, A. R., Norouzi, E. (2010). Histological and histochemical study on the alimentary canal in walking catfish (*Clarias batrachus*) and Piranha (*Serrasalmus nattereri*). Iranian Journal of Veterinary Research, 11(3), 255-261.

Rebolledo, I. M., Vial, J. D. (1979). Fine structure of the oxynticopeptic cells in the gastric glands of an

elasmobranch dpecies (*Halaerurus chilensis*). The Anatomical Record, 193(4), 805-822.

Saadatfar, Z., Shahsavani, D., Khoshnegah, S. (2010). Development of stomach in Sturgeon (*Acipenser persicus*). Journal of Applied Animal Research, 37(2), 153-156.

Scocco, P., Ceccarelli, P., Menghi, G. (1996). Glycohistochemistry of the *Tilapia* spp. Stomach. Journal of Fish Biology, 49(4), 584-593.

Yamabayashi, S. (1987). Periodic acid-Schiff-Alcian Blue: A method for the differential staining of glycoproteins. The Histochemical Journal, 19(10-11), 565-571.

Int. J. Aquat. Biol. (2023) 11(5): 406-416
ISSN: 2322-5270; P-ISSN: 2383-0956
Journal homepage: www.ij-aquatichiology.com

Original Article

The histochemistry of the saccus vasculosus in red-bellied Piranha, *Pygocentrus nattereri* Kner, 1858

Saroj Kumar Ghosh[*1]

[1]Fisheries Laboratory, Department of Zoology, Bejoy Narayan Mahavidyalaya, Itachuna, Hooghly-712 147, West Bengal, India.

Abstract: The presence of mucopolysaccharides, glycogen, protein, and lipid component in the cellular constituents of saccus vasculosus of *Pygocentrus nattereri* Kner, 1858 were demonstrated histochemically using light microscopy. The saccus vasculosus was richly vascularized and comprised of a number of loculi enclosed by blood sinusoids. The loculi contained predominant coronet cells and supporting cells. Plenty of secretory materials were observed in the lumen. Periodic acid Schiff's reaction in combination with Alcian blue for mucopolysaccharides was positive for the apical protuberances of coronet cells and secretory matters in the lumen. Significant amounts of glycogen and protein were localized in coronet cells and blood cells. The coronet cells along with luminar protrusion contained an appreciable amount of DNA and RNA. Lipid is notably detected through Sudan black reaction in globular protrusion of coronet cells. The silver reaction was employed to investigate the presence and distribution of neurons within the epithelial lining as well as other regions of the saccus vasculosus. These histochemical tests revealed that the saccus vasculosus served dually as both a secretory and sensory organ.

Article history:
Received 25 September 2023
Accepted 24 October 2023
Available online 25 October 2023

Keywords:
Red piranha
Saccus vasculosus
Chemical nature
Secretory
Sensory

Introduction

The saccus vasculosus, a reddish sac-like structure situated on the ventral wall of the diencephalon in teleosts, is positioned immediately behind the pituitary gland. The size of this specialized ependymal organ varies considerably among various species of chondrichthyes and osteichthyes, ranging from well-developed structures to rudimentary forms, and in some species, it may be absent (Lanzing, 1970). The structure and function of saccus vasculosus in fishes have been described by many workers (Yáñez, 1997; Sueiro et al., 2007; Nakane et al., 2013; Ghosh and Chakrabarti, 2014; Maeda, 2015; Chakrabarti and Khatun, 2017). The epithelial lining of the saccus vasculosus exhibits diverse characteristics, presenting as either a single-layered or multi-layered structure. Within this lining, two distinct cell types coexist: the distinctive coronet cells, also known as crown cells, and the supporting cells which are referred to as glial cells. Anatomically, the saccus vasculosus reveals a close and intricate relationship between neural tissue and blood vessels (Cid et al., 2015).

A review of the literature reveals that there is a considerable difference of opinion regarding the function of saccus vasculosus. A comprehensive review of the literature underscores the substantial variance in viewpoints concerning the function of the saccus vasculosus. Certain researchers have proposed that the saccus vasculosus primarily serves a secretory function (Galer and Billenstien, 1972; Bhatnagar et al., 1978; Saksena, 1989; Gupta, 2007); others have mentioned that saccus vasculosus may be involved in the transport of low molecular substances (Jansen, 1975; Joy and Sathyanesan, 1979). However, recent studies have shed new light on this matter, suggesting that the coronet cells, connected to liquor-contacting neurons, are predominantly sensory in nature (Ryohi and Keiji, 2001; Chakrabarti and Ghosh, 2009; Rodriguez-Moldes and Anadón, 2010; Nakane et al., 2013; Khatun and Chakarabarti, 2016).

In the present investigation, an attempt has been made to elucidate the chemical composition and

*Correspondence: Saroj Kumar Ghosh
E-mail: saroj.fisherylab@gmail.com

DOI: https://doi.org/10.22034/ijab.v11i5.2040

functional significance of the saccus vasculosus to understand the potential physiological roles of the cells involved. Taking this perspective, carnivorous redbelly pirhana, *Pygocentrus nattereri* (Characiformes: Serrasalmidae: Serrasalminae) has been chosen for this study.

Materials and Methods

Specimen collection: Adult specimens of *P. nattereri* (42±2.06 cm in total length; n = 12) were collected from the freshwater ponds of Itachuna (23.029°N, 88.176°E), Hooghly district of West Bengal. The fish were euthanized with an overdose of tricaine methanesulfonate (MS 222; Sigma-Aldrich Chemical). The brain together with saccus vasculosus was disclosed from the head's ventral side and fixed *in situ* with 10% neutral formalin.

Histochemical analysis: The saccus vasculosus along with the base of the brain was cautiously detached from the cranium and submerged in 10% neutral formalin for 18-20 h. The fixed tissues were washed thoroughly in 70% ethanol and dehydrated in an ascending series of ethanol. The tissues were cleared in benzene and embedded in paraffin wax of 52-54°C (CDH Fine Chemical).

Serial sections of 8-10 µm thickness was cut using a rotary microtome (Weswox MT-1090A) and prepared for the histochemical tests to examine the chemical nature of cells lining the saccus vasculosus at the light microscopical level. The histochemical tests include (1) Periodic Acid Schiff's (PAS) reaction in combination with Alcian Blue (AB) (PAS-AB) for the detection of neutral and acid mucins (Yamabayashi, 1987), (2) Best's Carmine (BC) reaction for the detection of glycogen (Horobin and Murgatroyd, 1971), (3) Mercuric Bromphenol Blue (MBB) method for the detection of basic protein (Mazia et al., 1953), (4) Methyl Green Pyronin Y (MGP) method for the detection of nucleic acid (Unna, 1902), (5) Sudan Black B (SB) method for the detection of bound lipid (Berenbaum, 1958), and (6) Silver Impregnation (SI) method for the detection of neurons (Marsland et al., 1954). All the slides were examined and microphotographed using a Leica EC3 light microscope at different magnifications.

Results

In *P. nattereri*, the saccus vasculosus is well-developed and highly vascularized, located on the ventral side of the diencephalon, near the third ventricle of the brain (Fig. 2A). It is composed of an enormous number of loculi having irregular shapes and sizes encircled by blood vessels. The saccus epithelium contains two types of cells: specialized coronet cells and basal supporting cells (Figs. 1B, 2B, 3B, 4B, and 5B). The loculi are either simple or branched patterns and the lumen appears as an intercommunicating arrangement of channels which ramify considerably. The distal branches are linked together to form a collecting channel which opens in the diocoel (Fig. 5A).

Periodic acid Schiff's reaction in combination with Alcian blue: Periodic Acid Schiff's (PAS) reaction in combination with Alcian Blue (AB) (PAS-AB) is used for assessment of high molecular weight glycoproteins, mucins. This combined analysis shows a purple colour as a result of the PAS reaction for neutral mucin and blue colour by cause of AB reaction for acid mucin (Fig. 1A). The cytoplasm of coronet cells lining saccus epithelium impart light purple colour whereas the blood vessels exhibit bluish colour. The apical protrusion and globules of coronet cells are deep bluish-purple colour due to the presence of both acidic and neutral mucopolysaccharides (Fig. 1B). However, the luminal border lined with coronet cells and supporting of saccus vasculosus have PAS positive deposition make a brush border looks. The basement membrane exhibits intense blue colour. PAS-AB positive coagulum is observed in the lumen of the loculi.

Best's carmine reaction: Best's carmine investigation shows different shades of glycogen deposition in the coronet cells according to their physiological activity (Figs. 2A-C). The cytoplasmic content and edged protrusion of coronet cells exhibit abundant glycogen content (Fig. 2B). Supporting cells are packed with little glycogen. The bright red coloured basement membrane and blood sinusoids

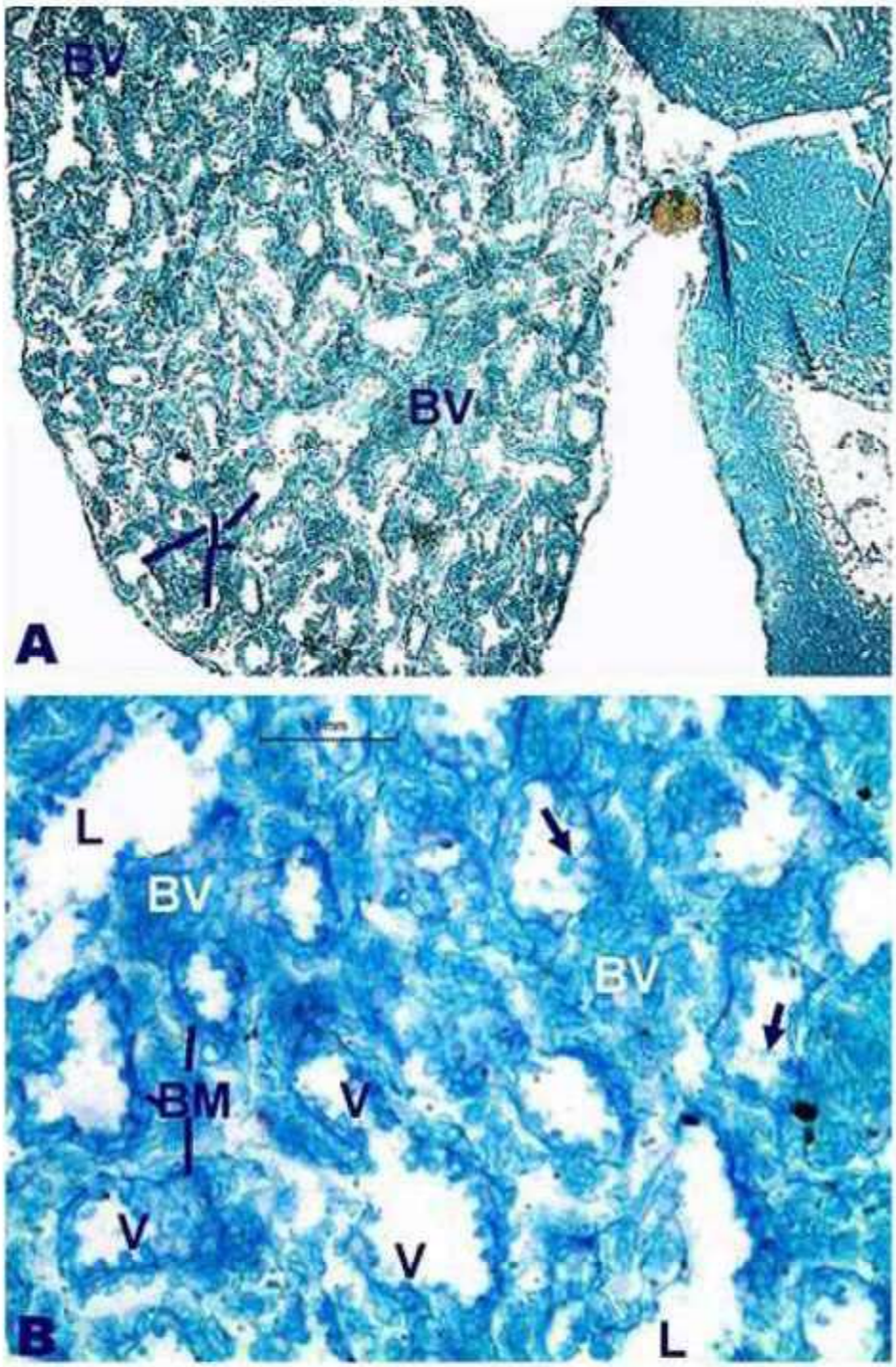

Figure 1. Photomicrographs of the sections of saccus vasculosus of *Pygocentrus nattereri* showing Periodic Acid Schiff's (PAS) reaction in combination with Alcian Blue (AB). **(A)** Coronet cells lining the loculi (L) show purple colour for neutral mucopolysaccharides. Blood vessels (BV) display blue colour because of acidic mucopolysaccharides (10X). **(B)** Apical protrusion of the coronet cells (arrow heads) and basement membrane (BM) exhibit intense purple colour. PAS-AB reaction is also discernible in the BV and coagulum (solid arrows) of the loculi (L) (40X).

surrounding the loculi also display intense carmine stating.

Mercuric bromphenol blue reaction: The saccus vasculosus is deeply stained with acidic mercuric bromphenol blue due to its proteinaceous nature (Fig. 3A). This acidic dye responds to basic groups of protein and furnishes blue colour. The cytoplasm and apical secretion of coronet cells display acute reactions for protein (Figs. 3A-B). A dignified amount of protein is discernible in the blood vessels encircling the loculi. The basal supporting cells and luminal secretion of coronet cells exhibit positive reactions for

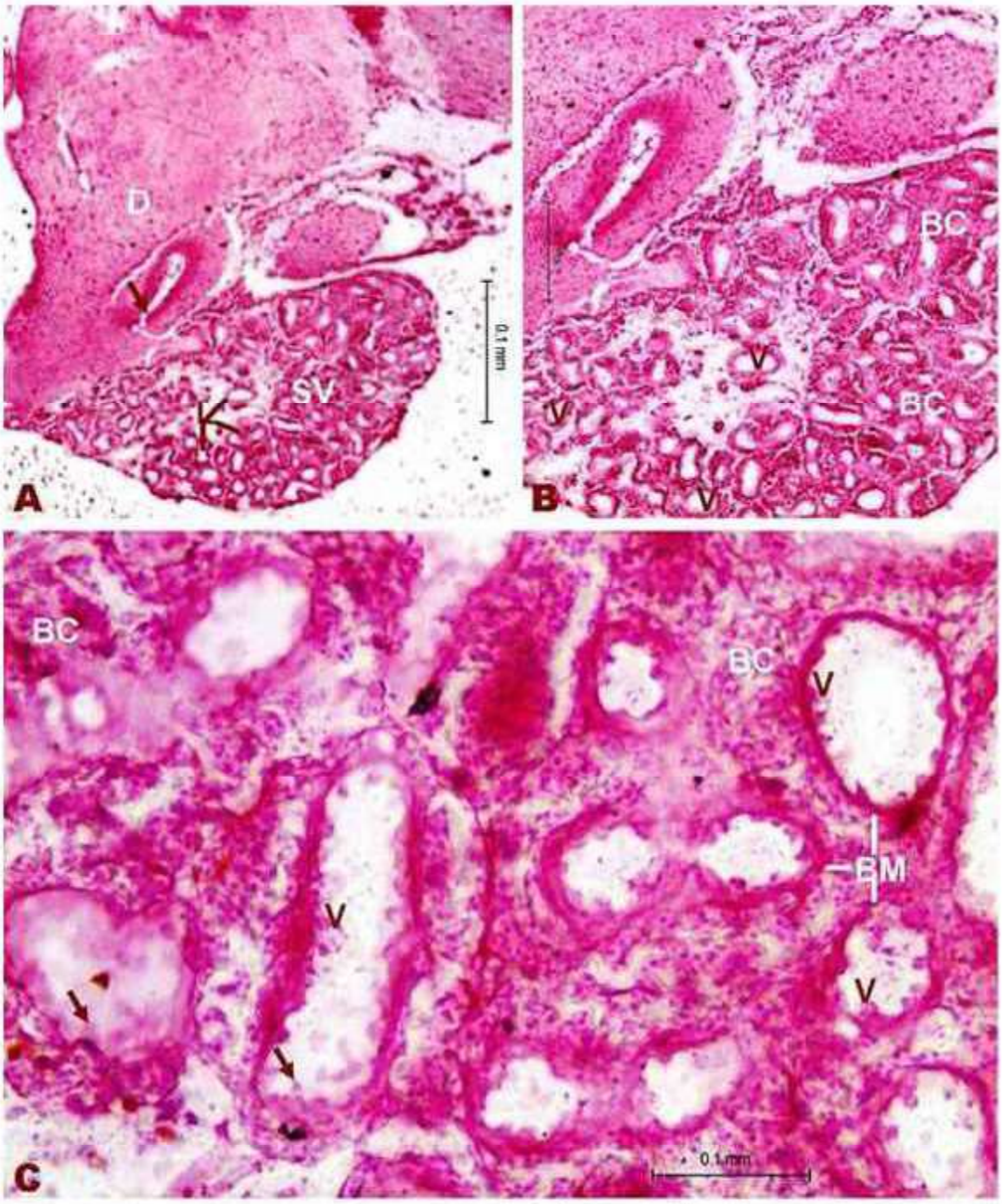

Figure 2. Section of saccus epithelium of *Pygocentrus nattereri* displaying Best's Carmine (BC) reaction. **(A)** Saccus vasculosus (SV) having numerous loculi (L) located on the ventral side of the diencephalon (D), near the third ventricle (arrow) of brain (4X). **(B)** Showing different shades of glycogen in coronet cells (arrow heads) and blood cells (BC) (10X). **(C)** Intense glycogen reaction in the apical protrusion of coronet cells (arrow heads), blood cells (BC) and basement membrane (BM). Note moderate reaction in supporting cells (solid arrows) (40X).

protein.

Methyl green pyronin Y reaction: This classical staining technique employing two basic dyes is used for localization and differentiation of DNA and RNA content in the various cells lining the saccus vasculosus. The combined test affords bluish-green colour for methyl green specifically binds to DNA whereas red colour for pyronin which binds to RNA (Fig. 4A). Strong reaction of DNA is observed in the nucleus of coronet cells while the cytoplasmic content and apical protrusion of coronet cells exhibit purple colour due to appreciable amount of RNA (Fig. 4B). Colloids in the loculi are bluish-purple coloured confirming the mixture of DNA and RNA. The

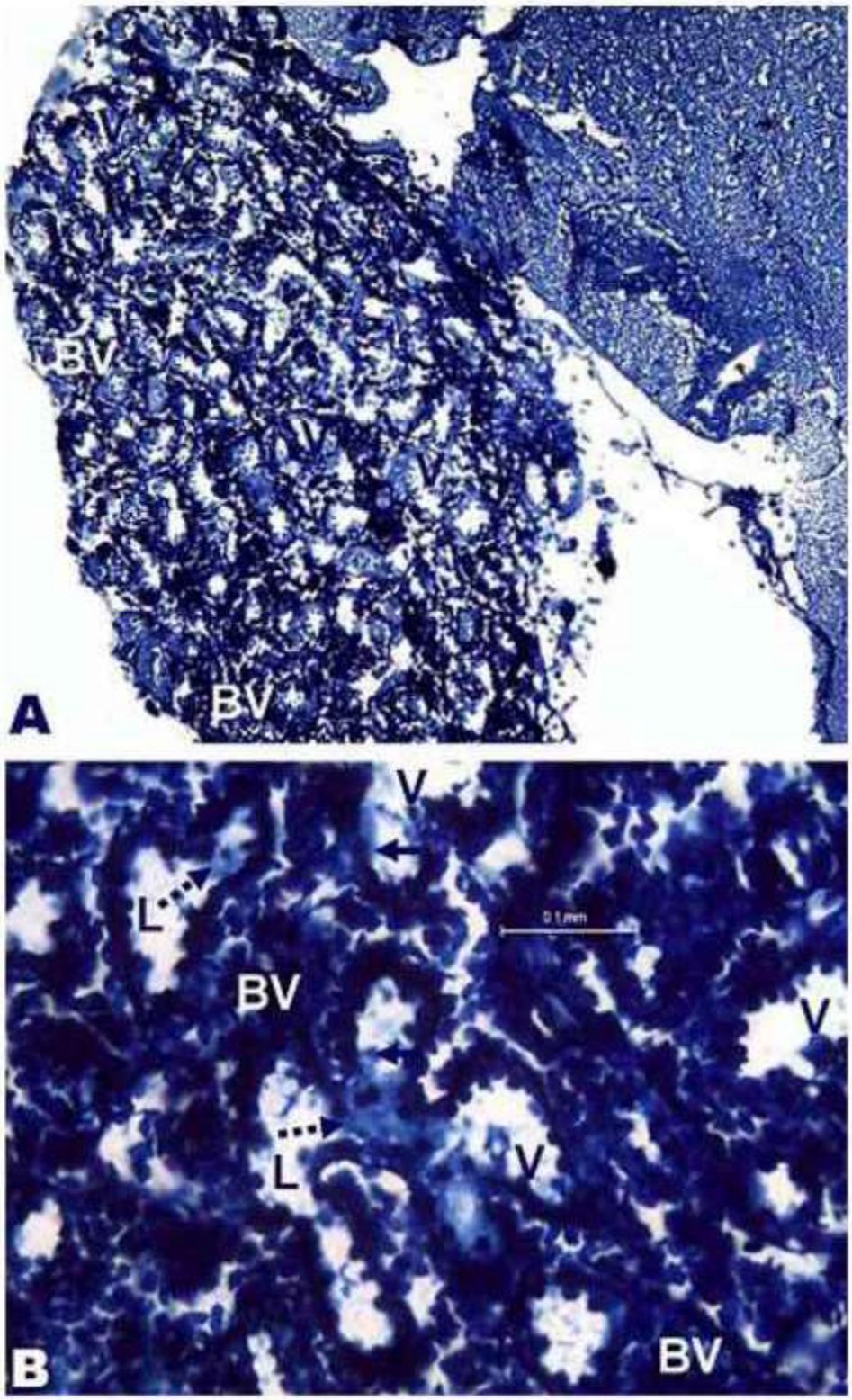

Figure 3. Section of saccus vasculosus of *Pygocentrus nattereri* showing Mercuric Bromphenol Blue reaction. **(A)** Strong protein reaction in coronet cells (arrow heads) and blood vessels (BV) of saccus vasculosus (10X). **(B)** Showing intense protein reaction in the apical processes of coronet cells (arrow heads) and BV encircling the loculi (L). Note positive reaction in supporting cells (solid arrows) and luminal secretions of coronet cells (broken arrows) (40X).

maximum reaction of pyronin for RNA has been noticed in the cytoplasm of blood cells.

Sudan black reaction: Different shades of lipid content are observed in closely arranged coronet cells

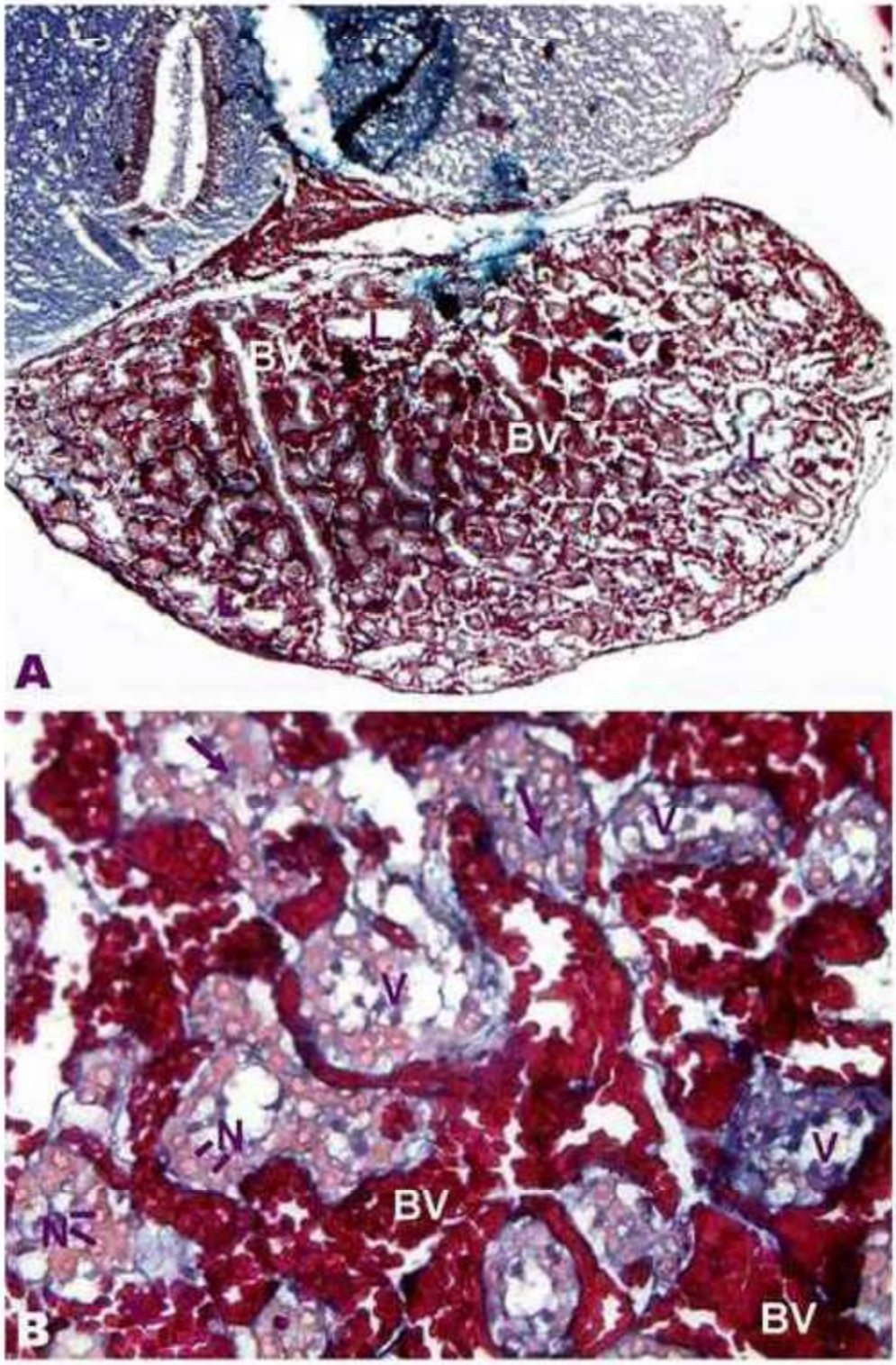

Figure 4. Section of saccus vasculosus of *Pygocentrus nattereri* showing Methyl Green Pyronin Y reaction **(A)** The cellular lining of loculi (L) and blood vessels (BV) of saccus vasculosus show DNA and RNA content (10X). **(B)** Strong methyl green reaction in the nuclei (N) of coronet cells whereas cytoplasmic processes (arrow heads) show pyronin reaction. Note maximum pyronin reaction in BV and luminal secretions (solid arrows) display mixture of DNA and RNA content (40X).

and underlying blood vessels (Fig. 5A). The apical globular protrusion of coronet cells yields an intense reaction of Sudan black. However, the highest lipid reaction is detected in the blood vessels surrounding the loculi (Fig. 5B). Supporting cells are weak in lipid reaction. Varying degrees of sudanophilic droplets in the loculi show lipid in nature.

Silver reaction: The silver reaction is discernible in

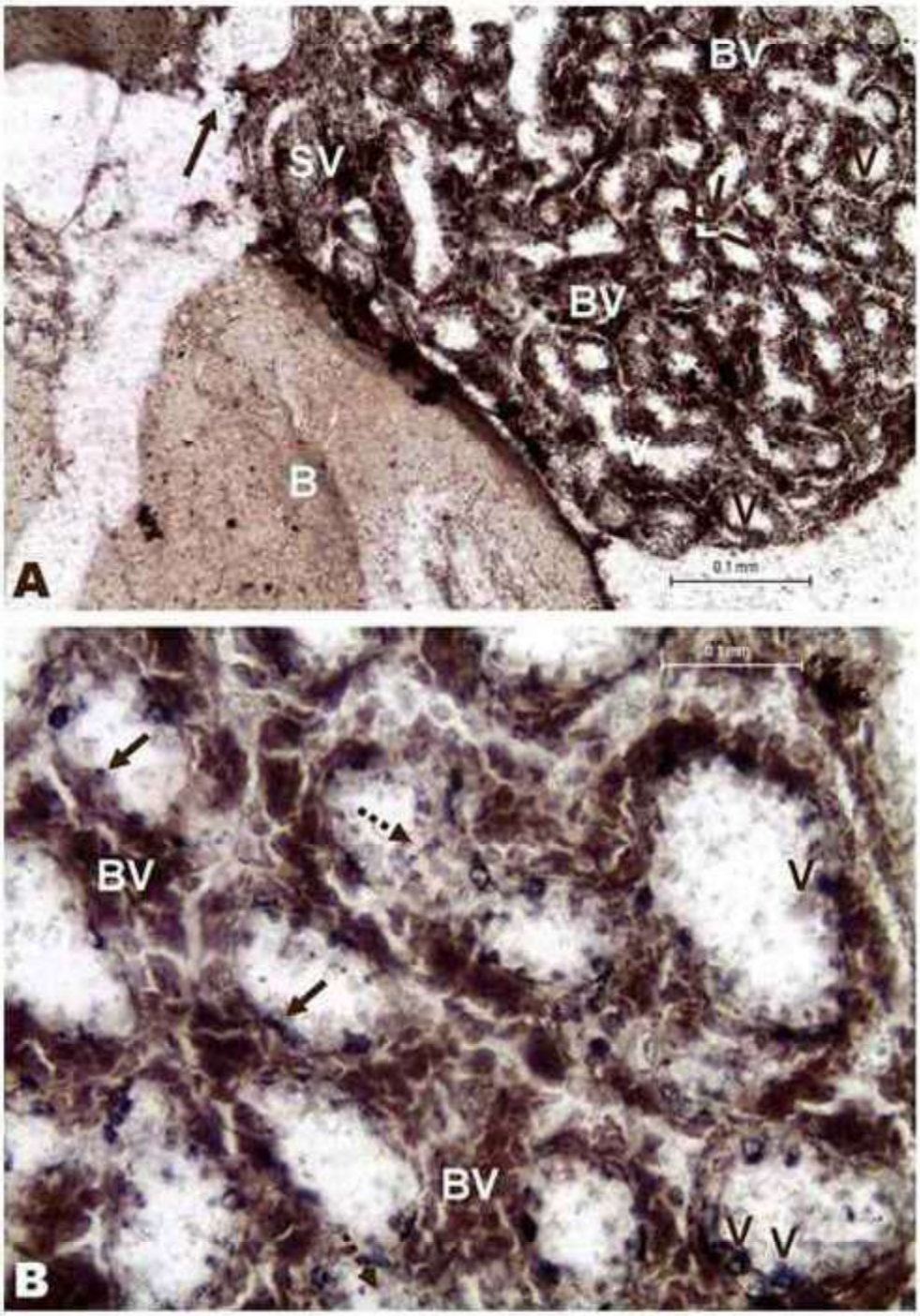

Figure 5. Section of saccus vasculosus of *Pygocentrus nattereri* showing Sudan Black reaction (**A**) Showing sudanophilic materials in coronet cells (arrow heads) of loculi (L) intermingled with blood vessels (BV). Solid arrow marks the connecting channel in between the saccus vasculosus (SV) and diocoel of brain (B) (10X). (**B**) Intense lipid reaction in the apical protrusion (arrow heads) of coronet cells and BV. Note the presence of sudanophilic materials (broken arrows) in L. Solid arrows mark basal cells (40X).

the neural part of saccus vasculosus (Fig. 6A). Enormous silver stain is observed in the ciliary structures on the apical part of coronet cells as well as neurosecretory fibres attached to the basal portion of coronet cells intermingled with blood vessels (Fig. 6B). Some axonic extensions enter and encompass the blood vessels of saccus vasculosus also display positive reaction. Nerve fibres on the outer surface of saccus epithelium are marked with silver stains.

Discussions

The saccus vasculosus is recognized as a

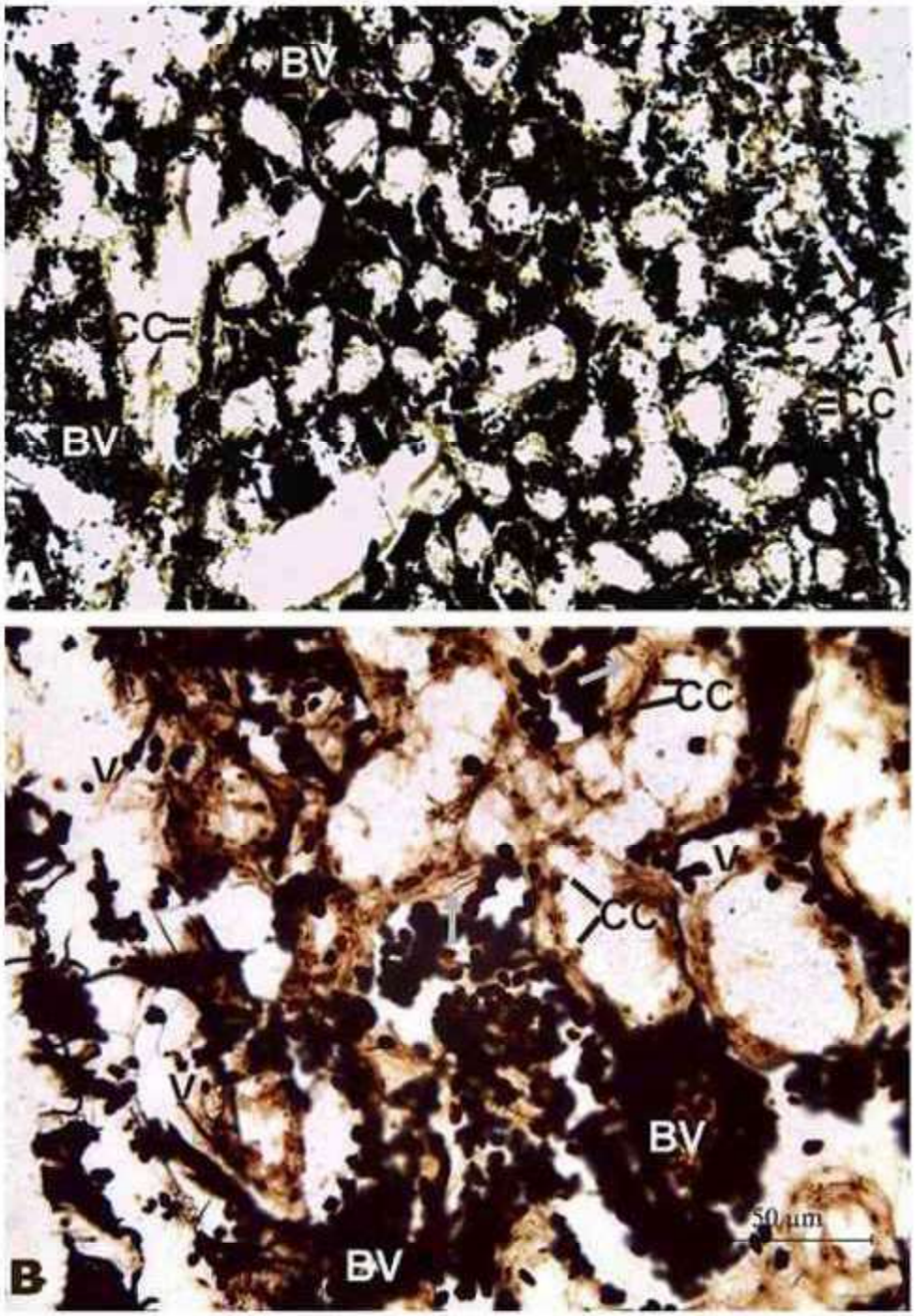

Figure 6. Section of saccus vasculosus of *Pygocentrus nattereri* showing silver reaction (**A**) Showing silver reaction in coronet cells (CC) intermingled with blood vessels (BV). Note intense reaction in nerve fibres (arrows) on outer coating of saccus vasculosus (10X). (**B**) Magnified portion of saccus vasculosus shows silver reaction in the apical ciliary structure (arrow heads) and basal neurosecretory fibres of CC connected with BV. (40X).

circumventricular organ, housing specialized coronet in contact with the venricular cerebrospinal fluid in the absence of a blood-brain barrier (Altner and Zimmerman, 1972). In *P. nattereri*, the well-developed saccus vasculosus is situated on the ventral side of the brain and serves a dual purpose, encompassing both sensory and secretory functions. The saccus vasculosus consists of a vast number of loculi having distinctive cornet cells and supporting cells, which are enveloped by a network of blood sinusoids. The rich vascularization of the saccus vasculosus likely serves to supply nutritive substances

to the various cells lining the epithelium of the saccus. Scharrer (1948) suggested that the blood sinusoids play an important role in the secretion of fluid from the blood stream into the lumen of the saccus vasculosus and they also contribute to adjusting the volume of this fluid. This process helps to equalize differences in intracranial pressure, particularly during vertical movement.

A PAS-positive reaction in the coronet cells signifies the existence of a variety of chemical compounds, including neutral mucopolysaccharides, glycoproteins, mucoproteins, and glycolipids. However, the PAS-AB reaction varies in the different parts of the saccus vasculosus. The apical protrusions of coronet cells and the accumulated material in the loculi lumen are rich in acid and neutral mucopolysaccharides strongly indicating their secretory function. Similar types of findings were also reported in other fishes (Galer and Billenstien, 1972; Bhatnagar et al., 1978; Kulkarni and Sathyanesan, 1982; Ghosh and Chakrabarti, 2014). Lanzing and Lennep (2005) showed the presence of acid mucopolysaccharides in the apical protrusions of coronet cells in teleosts. These mucopolysaccharides are initially stored in globules and subsequently secreted into the brain's ventricle.

The presence of glycogen in the coronet cells of the saccus epithelium in *P. nattereri* likely serves both metabolic and physiological functions. Sundararaj and Prasad (1964) noted that coronet cells exhibit secretory functions and the stored glycogen within their apical protrusions is thought to be released in the form of glucose into the cerebrospinal fluid. Saksena (1989) suggested that the saccus vasculosus serves as a storage site for carbohydrates intended for the brain. Coronet cells are implicated in glycogen metabolism by converting glycogen into acid mucopolysaccharides. Strong glycogen reactions in the blood vessels and basement membrane could generate energy during the transport of various chemicals and the transmission of impulses through the membrane.

The cytoplasmic contents and terminal protrusions of coronet cells are proteinaceous in nature. Protein reaction observed in the coagulum of the lumen strongly implies an extensive secretion of neutral glycoproteins from the coronet cells of the saccus vasculosus. Kulkarni and Sathyanesan (1982) documented an acute protein reaction, further confirming the substantial secretion of glycoproteins from the coronet cells of *Mystus vittatus*. In contrast, the supporting cells present alongside the coronet cells do not exhibit any signs of secretory activity.

The acute response of DNA within the nuclei of coronet cells in the saccus epithelium may be linked to the biochemical differentiation of various stages of coronet cell development. Notably, the cytoplasm of coronet cells displays a strong reaction for RNA, indicating its relatively higher presence. This suggests its essential role in cellular metabolism and the synthesis of proteins which are crucial for augmenting the secretion of products from coronet cells into the lumen. The abundant RNA content in the cytoplasm of coronet cells indicates a significant role in the physiological transformation of electron-dense materials during the formation of secretory products. Bhatnagar et al. (1978) proposed that the RNA and cystine content in the cytoplasm of coronet cells may initiate the production of acid mucopolysaccharides within the coronet cells themselves in the saccus vasculosus of *Cyprinion macrostomus*.

Observations have shown variations of sudanophilic materials among the coronet cells. It is probable that the energy required for the physiological activities and the secretion of the products from the coronet cells primarily originates from the accumulated lipid materials within these cells. Sundararaj and Prasad (1964) documented the localization of phospholipids in the apical protrusions and globules of coronet cells within the saccus vasculosus of *Notopterus chitala*. This observation underscores the potential involvement of the saccus vasculosus in fluid secretion and the extrusion of low molecular weight organic substances into the ventricular system.

The coronet cells in the saccus vasculosus of *P. nattereri* make contact with nerve terminals, indicating a credible sensory role for this neural element. In a study on *Cyprinus carpio*, Ryohi and

Keiji (2001) observed the synaptic vesicles within the terminals on the coronet cells and proposed that the function of these cells in metabolizing cerebrospinal fluid is controlled by cholinergic nerves. Furthermore, Benjamin (1974), in *Gasterosteus aculeatus*, emphasized that the coronet cells are the most prominent feature of the saccus vasculosus and have direct contact with the cerebrospinal fluid. Therefore, it is plausible that coronet cells serve as chemoreceptors and play a role in maintaining the composition of the cerebrospinal fluid.

Acknowledgments

The author is grateful to Dr. Goutam Bit, Principal, Bejoy Narayan Mahavidyalaya, Itachuna, Hooghly-712 147, West Bengal for providing laboratory facilities.

References

Altner H., Zimmermann H. (1972). The saccus vasculosus. In: G.H. Bourne (Ed.). The structure and function of nervous tissue. Academic Press, New York. pp: 293-328.

Benjamin M. (1974). Ultrastructure studies on the coronet cells of the saccus vasculosus of the freshwater stickleback, *Gasterosteus aculeatus*. Zeitschrift fur Zellforschung und Mikroskopische Anatomie, 147: 551-565.

Bernenbaum M.C. (1958). The histochemistry of bound lipids. Quarterly Journal of Microscopical Science, 99: 231-242.

Bhatnagar A.N., Al-Noori S.A., Gorgees N.S. (1978). Studies on the histomorphology and histochemistry of the saccus vasculosus of *Cyprinon macrostomus*. Acta Anatomica, 100: 221-228.

Chakrabarti P., Ghosh S.K. (2009). Histophysiological studies on the saccus vasculosus of *Macrognathus aculeatum* (Bloch). Proceedings of the Zoological Society, 62: 139-142.

Chakrabarti P., Khatun R. (2017). Histophysiological and surface ultrastructural studies of the saccus vasculosus of *Notopterus chitala* (Hamilton). Journal of Microscopy and Ultrastructure, 5: 140-145.

Cid P., Doldán M.J., De Miguel Villegas E. (2015). Morphogenesis of the saccus vasculosus of turbot *Scophthalmus maximus*: assessment of cell proliferation and distribution of parvalbumin and calretinin during ontogeny. Journal of Fish Biology, 87: 17-27.

Galer B.B., Billenstein D.C. (1972). Ultrastructural development of the saccus vasculosus in rainbow trout (*Salmo gairdneri*). Zeitschrift fur Zellforschung und Mikroskopische Anatomie, 128: 162-174.

Ghosh S.K., Chakrabarti P. (2014). Histological and histochemical observations on the saccus vasculosus of freshwater featherback, *Notopterus notopterus* (Pallas, 1769). Entomology and Applied Science Letters, 1: 27-34.

Gupta A. (2007). Studies of saccus vasculosus of *Anabas testudineus* and *Colisa fasciatus* with reference to secretory functions. Journal of Applied Zoological Researches, 18: 64-66.

Horobin R.W., Murgatroyd L.B. (1971). The staining of glycogen with Best's carmine and similar hydrogen bonding dyes. A mechanistic study. Journal of Histochemistry, 3: 1-9.

Jansen W.F. (1975). The saccus vasculosus of the rainbow trout, *Salmo gairdneri* Richardson. Netherlands Journal of Zoology, 25: 309-331.

Joy K.P., Sathyanesan A.G. (1979). A histoenzymological study of the saccus vasculosus of the freshwater teleost, *Clarias batrachus* (L.). Zeitschrift fur Mikroskopisch-Anatomische Forschung, 93: 297-304.

Khatun R., Chakrabarti P. (2016). Histological and surface ultrastructural observations on the saccus vasculosus of *Eutropiichthys vacha*. International Journal of Fisheries and Aquatic Studies, 4: 112-117.

Kulkarni R.S. Sathyanesan A.G. (1982). Histochemical study of the saccus vasculosus of the freshwater teleost, *Mystus vittatus*. Life Science Advances, 3: 257-263.

Lanzing W.J.R. (1970). The development of a saccus vasculosus in *Tilapia mossambica* Peters and other cichlids. Journal of Fish Biology, 2: 249-252.

Maeda R., Shimo T., Nakane Y., Nakao N., Yoshimura T. (2015). Ontogeny of the saccus vasculosus, a seasonal sensor in fish. Endocrinology, 156: 4238-4243.

Marsland T.A., Glees P., Erikson L.B. (1954). Modification of the Glees Silver impregnation for paraffin sections. Journal of Neuropathology and Experimental Neurology, 13: 587-591.

Mazia D., Brewer P.A., Alfert M. (1953). The cytochemical staining and measurement of protein with mercuric bromphenol blue. Biology Bulletin, 104: 57.

Nakane Y., Ikegami K., Iigo M., Ono H., Takeda K., Takahashi D., Uesaka M., Kimijima M., Hashimoto R.,

Arai N., Suga T., Kosuge K., Abe T., Maeda R., Senga T., Amiya N., Azuma T., Amano M., Abe H., Yamamoto N., Yoshimura T. (2013). The saccus vasculosus of fish is a sensor of seasonal changes in day length. Nature Communications, 4: 2108.

Rodriguez-Moldes I., Anadón R. (2010). Ultrastructural study of the evolution of globules in coronet cells of the saccus vasculosus of an elasmobranch (*Scyliorhinus canicula* L.), with some observations on cerebrospinal fluid-contacting neurons. Acta Anatomica, 69: 217-224.

Ryohi F., Keiji K. (2001). An electron microscopic study of the saccus vasculosus in the carp, *Cyprinus carpio*. Medical Bulletin of Fukuoka University, 28: 135-148.

Saksena D.N. (1989). Histophysiology of the saccus vasculosus of the Indian fresh water goby, *Glossogobius giuris* Ham. (Teleostei). Folia Morphologica (Parha), 37: 249-252.

Scharrer E. (1948). The blood vessels of the saccus vasculosus. Anatomical Record, 100: 756.

Sueiro C., Carrera I., Ferreiro S., Molist P., Adrio F., Anadon R., Rodriguez-Moldes I. (2007). New insights on saccus vasculosus evolution: a developmental and immunohistochemical study in elasmobranchs. Brain Behavior and Evolution, 70: 187-204.

Sundararaj B.I., Prasad M.R.N. (1964). The histochemistry of the saccus vasculosus of *Notopterus chitala* (Teleostei). Quarterly Journal of Microscopical Science, 105: 91-98.

Unna P.G. (1902) . Eine modifikation der pappenheimischen färbung auf granuloplasma. Monatshefte für Praktische Dematologie, 35: 76-80.

Yáñez J., Rodríguez M.A., Pérez S., Adrio F., Rodríguez-Moldes I., Manso M.J., Anadón R. (1997). The neuronal system of the saccus vasculosus of trout (*Salmo truttafario* and *Oncorhynchus mykiss*): an immuno-cytochemical and nerve tracing study. Cell and Tissue Research, 288: 497-507.

Yamabayashi S. (1987). Periodic acid-Schiff-Alcian Blue: A method for the differential staining of glycoproteins. The Histochemical Journal, 19: 565-571.

Shodhak (शोधक) **(ISSN: 0302-9832)**
A Journal of Historical Research

JAYANTA MAHAPATRA'S *HUNGER*: A POSTMODERN INDIAN DISCOURSE

Anjan Das
Assistant Professor in English, B.N. Mahavidyalaya, Itachuna, Hooghly, West Bengal
anjanenglis@gmail.com,

Abstract:
An intense attempt of exploration on this paper has chiefly been made into the depiction of socio moral reality in Jayanat Mahapatra's, a wide acclaimed poem **Hunger** written in postmodern Indian context. For a convenient and perceptive discourse, Mahapatra's masterpiece '**Hunger**' has been selected, where the three major characters---poet-speaker, father-fisherman and an adolescent girl of fifteen years, get fully divulged with a piercing message at the end. The term 'hunger' which is basically related with instinctive pursuit of any living being, gets profound discourse from various implications, including physical, cultural, economical, spiritual and social in the context of postmodern Indian scenario. The ethical symbolism and depiction of imagery, its gendered stereotypes are vividly discussed in the relevant means of representation between haves and have-nots, power and powerless etc., and more emphatically analyzed with respect to a larger aspect of socio-moral relations and identities. On literary aspect, the basic concepts of postmodernism are explicated with reference to three characters hailed from two different realms on respective quests of life. Use of graphic narrative is quite obvious on the questions of gender issue in one hand and virginity on the other. A deconstructive endeavour to explore the psycho-analytical constructs of the characters, irrespective of their familial and customary relations, is attempted for discussion on a larger concept of 'obvious truth' over 'obvious lie' in postmodern Indian culture.

Key Words: Social morality, hunger, ethical, familial and customary relations, postmodern, identities.

The post-modernist Jayanta Mahapatra (1928-2023) is one of the luminous poets in the welkin of Indian literature in English, constantly shining on the rich heritage of Indian culture, tradition, myth, folklore, rites etc. by the prolificacy of his poetic inventiveness. While commenting on poetic acumen of Jayanta Mahapatra, specifically in realm of Indo-Anglican poetry, Dr. S. Chellia's thoughtful asseveration 'Modern Indian Poetry in English has, indeed, come its own", is ever striking and evocative. Being a social realist, his poetic cluster is based on 'a true incident' in true sense. Naturally, his masterpiece, *Hunger*, taken from his *tour de force A Rain of Rites*, is a very touchingly poignant and highly moving poem which stands unique in Indian English poetry for the authenticity of experience. A physicist by profession and a poet by vocation, Mahapatra seeks to highlight the ills of society and shameful social reality of the deprivation, humiliation, degradation, and suffering of the poor Indian women. Resembling partly with his another poem *'The Whore House in a Calcutta Street'*, the poem centers on the theme of unwelcome prostitution, the greatest concern of post-modern Indian English poetry.

The term 'postmodernism' as expostulated by the theorist and critic Jean-Francois Lyotard after the end of the Second World War, is in league with the Expressionism where the meaninglessness of human existence is questioned and where the established ideological modes matter the most. As a reaction against the New Criticism, this practice remains challenging in regard to the autonomy of a

Chemical Physics Impact 8 (2024) 100636

Contents lists available at ScienceDirect

Chemical Physics Impact

journal homepage: www.sciencedirect.com/journal/chemical-physics-impact

Review article

A systematic progress in probing the excited state using fluorescence spectroscopy

Brotati Chakraborty [a,*], Samita Basu [b]

[a] Department of Chemistry, Bejoy Narayan Mahavidyalaya, Itachuna, Hooghly, West Bengal PIN 712147, India
[b] Chemical Sciences Division, Saha Institute of Nuclear Physics, 1/AF Bidhannagar, Kolkata 700064, India

ARTICLE INFO

Keywords:
Fluorescence quenching
TRANES
Fluorescence anisotropy
Electron transfer
Proton transfer

ABSTRACT

The mini review focuses on the work carried out in our laboratory over the last two and a half decades to unravel various facets of photoinduced processes, viz. photoinduced electron transfer (PET), excited state proton transfer, energy transfer etc., using fluorescence spectroscopy and imaging. We have demonstrated that PET is manifested by formation of exciplex and that its parent spin state is authenticated by observing steady-state fluorescence in presence of magnetic field, which is quite a non-conventional set-up. It is observed that dielectric constant of the medium governs the magnetic field effect. We have synthesized and explored fluorophores which act as sensors for hydrogen bonds and protic media. Our group has studied the protonation equilibrium of Acridine, which is a good fluorophore in various confined media and observed the perturbation of this equilibrium in presence of DNA bases using steady-state and time-resolved fluorescence techniques. Excimer formation of 9-Aminoacridine Hydrochloride Hydrate (9AA), another strong fluorophore, has been investigated in several solvent matrices and photoinduced interactions of 9AA with amines and viologens are studied. Further, we have utilized fluorescence upconversion technique to segregate direct and diffusion-controlled electron transfer within picosecond-femtosecond time domain. Then attempts have been made to study DNA-ligand and protein-ligand interactions comprehensively, utilizing different techniques of fluorescence spectroscopy. Furthermore, we have synthesized fluorescent carbon dots and have made an endeavor to find their fruitful biological significance. We have also synthesized riboflavin (Rf)-gold nano-assemblies (RfS@AuNPs) by covalently attaching thiolated Rf to gold nanoparticles (AuNPs) and have observed that these RfS@AuNPs accumulate in the nucleus of cancer cells, leading to plasma membrane blebbing and binucleated apoptotic bodies, consistent with activation of apoptosis. Finally, some very recent examples as well as the future prospect of fluorescence spectroscopy have been discussed.

1. Introduction

Fluorescence is one of the spectroscopic phenomena that has versatile applications in photo sciences for its simplicity, high sensitivity and unique specificity for the microenvironment. With the advent of laser, it has become a powerful device to study the structure and dynamics of the chemical reactions involving a wide range of molecules starting from simple organic and inorganic molecules to bio macromolecules or nanocomposites hosted in matters and living systems. Since the number of molecules which possess characteristic fluorescence is quite small, the research on developing new fluorophores is going on to use this technique in the fields of applied chemistry, biochemistry, medical science, etc. The present-day fluorescence microscope with enhanced sensitivity permits detection even at single molecular level which leads to remarkable progress in biotechnology, pharmacy and material science [1,2].

The primary reactions in most of the photochemical and photobiological processes are electron transfer (ET) [3], proton transfer or hydrogen abstraction [4,5] and bond cleavage [6]. The photoinduced electron transfer (PET) between an electron donor (D) and an acceptor (A) leads to the fluorescence quenching of the corresponding excited donor or acceptor. However, the Stern-Volmer analysis cannot be a full-proof evidence of PET *via* evaluation of diffusion-controlled bimolecular quenching constant of the order of $10^9 - 10^{10}$ liter mol $^{-1}$ s $^{-1}$, particularly in solution phase [1,2]. PET is justified only by the formation of fluorescent exciplex, the charge transfer complex formed in the

* Corresponding author at: Department of Chemistry, Bejoy Narayan Mahavidyalaya, Itachuna, Hooghly, West Bengal PIN 712147, India.
E-mail addresses: brotati@bnmv.ac.in, brotati07@gmail.com (B. Chakraborty).

https://doi.org/10.1016/j.chphi.2024.100636
Received 24 December 2023; Received in revised form 11 April 2024; Accepted 10 May 2024
Available online 16 May 2024

excited state or by the detection of radical ions using transient absorption technique [7]. Additionally, the Stokes shift of the exciplex fluorescence with the increase in solvent polarity [8] and the enhancement of the luminescence in presence of an external magnetic field (MF) of the order of 0.01 – 0.02 tesla [9,10] are the reliable observations to justify the phenomenon.

Hydrogen bond plays a pivotal role in the interaction between a hydrogen donor and a hydrogen acceptor to recognize the site-specific phenomenon in molecular level particularly within water, proteins and DNA matrices. If the dipole moment of a fluorophore is quite different in its ground and excited states, then the Franck-Condon excited state of the molecule becomes further stabilized by reorganization of the solvent molecules surrounding it according to their polarity and hydrogen bonding capacity. Owing to this solvation, the fluorescence maximum is red shifted with the increasing polarity and hydrogen bond donor capacity of the solvent. There are some molecules which can donate or accept proton in both the ground and excited states; however, their acidity or basicity constants differ noticably in the respective electronic states. As a result, their proton donating or accepting capacity will change on photoexcitation. The excited state proton transfer (ESPT) can be controlled not only by the pH of the homogeneous aqueous solution but also by the pH at the interface of the heterogeneous micellar media. In some of the cases, where both the hydrogen donor and acceptor molecules are present in the medium, ESPT is facilitated through hydrogen bonding between those two properly oriented molecules. ESPT reaction and dynamics are well studied by probing the fluorescence intensity and lifetime of the deprotonated and protonated molecules with varying pH or increasing concentration of the hydrogen donor/acceptor molecules [4,5].

In this mini review, we revisit the studies that we have been carrying out in our laboratory since almost last two and a half decades using steady-state and time-resolved (within nanosecond and sub-picosecond time regime) fluorescence techniques to explore PET, ESPT and energy transfer involving simple organic molecules, inorganic metal complexes, proteins, DNA and carbon nanodots. We have also made endeavor to utilize fluorophores as hydrogen bonds sensors. Although most of the drug-protein and drug-DNA interactions were carried out *in vitro*, however the fluorescence images of the interaction between the synthesized carbon dots and therapeutically important molecules were taken *in vivo* within HeLa cells using fluorescence microscopes. Amalgamation of our observations would provide adequate guidelines to stimulate predictive insight into biological reactions and throw some light in the unexplored avenues of photoinduced phenomena involving macromolecules bearing biological significance.

2. Experimental techniques

Steady-state fluorescence was recorded by conventional Fluorescence Spectrophotometers. To study the MF effect on exciplex fluorescence, a pair of Helmholtz coil was placed surrounding the sample chamber that can produce variable a.c. MF. A homemade full-wave phase-sensitive detection system was used to improve the signal to noise ratio (1000:1). The time-resolved fluorescence was studied using a fluorescence kinetic spectrometer based on time-correlated-single photon counting technique with picosecond diode laser and MCP-PMT detector and a femtosecond fluorescence upconversion system (FOG-100, CDP Corporation) with a mode-locked Ti-sapphire laser (Mai Tai, Spectra Physics) pumped by a 5 W Millennia (Spectra Physics) to excite the sample using its second harmonic. The microscopic images were collected from a Nikon inverted confocal microscope with an A1R+ confocal scanner head mounted on an Eclipse Ti-E microscope using a 100 × objective.

3. Discussion

3.1. PET manifested by exciplex formation and probed by MF effect

PET reactions between electron rich D and electron deficient A molecules (either of which is in the photoexcited state) lead to the formation of two prime products, viz., contact ion pair (CIP) or exciplex and solvent separated ion pair (SSIP). The solvation is greater in SSIP, whereas electronic coupling is much better in CIP. The interconversion between SSIP and CIP in solution is mainly controlled by the polarity, i.e., dielectric constant (ε) of the medium. With the decrease in ε, which increases the potential energy barrier between SSIP and CIP, the formation of CIP or exciplex formation is favoured and this can be monitored by its broad fluorescence hump that appears in the longer wavelength compared to the fluorophore (either D or A). The fluorescence maximum of exciplex is blue shifted with increasing intensity as ε of the medium decreases [11,12].

The carbazole and its derivatives are well known fluorophores and can act as potential electron D or A depending on the nature of the counter molecules. Aich and Basu have observed the exciplex formation between photo-excited N-ethyl carbazole (ECZ) and 1,4-dicyanobenzene (DCB) which act as D and A respectively and found out the diffusion – controlled bimolecular fluorescence quenching constant from the corresponding Stern-Volmer plots using both steady-state and time-resolved fluorescence techniques [11]. To confirm the formation of radical ion pair (RIP), the steady-state fluorescence experiments are carried out in presence of an external a.c. MF that can be varied within 0.0 – 0.08 tesla corroborated with a phase-locked detection system [11-14]. If the ET occurs with singlet fluorophore, the spin correlation of unpaired electron in the primary RIP encapsulated within a solvent cage is singlet ($D^{\cdot}$● ↑...↓●$A^{\cdot}$). During diffusion inside the cage the inter-radical distance becomes as such where exchange interaction between the radical electrons is negligible and maximum intersystem crossing (ISC) occurs producing corresponding triplet RIP ($D^{\cdot}$● ↑..↑● $A^{\cdot}$) through the hyperfine interactions (HFI) present in the system. In presence of an external MF of the order of HFI the triplet states become non-degenerate (T_0 and $T_{\pm}$) due to Zeeman splitting and ISC would be reduced by almost 2/3, since $S \leftrightarrow T_{\pm}$ is prohibited due to energy difference; hence singlet yield, i.e., exciplex luminescence will increase [9-15]. In this case, the maximum increase in exciplex luminescence at 500 nm is obtained (~ 1.37%) in presence of MF of the order of 0.012 tesla, whereas the fluorescence of ECZ remains unchanged. The polarity, i.e., ε of the medium plays a major role in controlling the optimum separation distance between the radical ions, which generate maximum ISC, hence maximum MF effect. Here, ε value around 9.0 is good enough to have maximum MF effect, whereas the previously studied exciplex systems (Pyrene (Py) – N, N'-dimethylaniline (DMA), etc.) show maximum MF effect within the ε range 14.0 – 18.0 in aprotic solvent [15]. Using Lippert-Mataga plot [11,12] it is found that extent of charge transfer for ECZ-DCB exciplex is 0.15, whereas for Py-DMA it is close to 1.0. Therefore, difference of potential energy between CIP and SSIP is smaller for ECZ-DCB relative to Py-DMA, which facilitates SSIP – CIP interconversion at the lower dielectric. Later, it is found by studying different derivatives of carbazole – DCB systems [16], Py – dimethyl terephthalate systems in comparison with Py-DMA [17] as well as 9-cyanophenanthrene – derivatives of methyl indole systems [18] that not only the extent of charge transfer but also the exciplex energy and the steric bulk of donor and acceptor play the major role in deciding optimum separation distance between the radical ions. Hence, maximum MF effect would be obtained at an optimal ε of the medium. Further, the importance of extent of charge transfer is again established by studying all-*s*-trans-1,6-diphenylhexa-1,3,5-triene (DPH) and DCB exciplex system, where the field effect is maximized at $\varepsilon \sim 10.0$, whereas for DPH-DMA exciplex it is achieved at $\varepsilon = 15$ [19]. DPH is one of the members of the group containing R,ω-diphenyl polyenes. This is one of the popular fluorophores used in the biophysical research. Its

fluorescence polarization property is widely used to measure the internal viscosity of the bilayer membranes. Further, the wavelength dependence of MF effect identifies the formation of 1:1 and 1:2 complexes with increasing concentration of DCB keeping DPH concentration fixed. The unique feature of the complexes is that they show anisotropic MF effect when the excitation light is polarized parallel or perpendicular to the MF [19]. The formation of both 1:1 and 1:2 complex is once more observed with Py - 4,4'bis(dimethylamino)diphenylmethane (DMDPM), where DMDPM contains two potential donor sites [20].

The $B_{1/2}$ value, that is half the field at which the MF effect is saturated, can be mathematically expressed as $[(B_1^2 + B_2^2)/2(B_1 + B_2)]$ according to Weller, hence it becomes an easy tool to measure the HFI present in the total system [21]. However, with increasing concentrations of D the value increases due to hopping of electron from one D to another. Therefore, lifetime of the individual radical ion decreases which broadens the energy of the spin levels and excess field is required to overcome the HFI [12,19].

Similar work on monitoring MF effect on exciplex fluorescence has been carried out by other researchers. Parui et al. have found that at least two types of Py-DMA exciplexes are formed at different locations within the H_2O/AOT/*n*-heptane reverse micelles (RMs) interface [22]. One of the exciplxes is centered at 430 nm while the other at 500 nm. The magnetic field sensitivity of the exciplex centered at 500 nm confirms its location at the mobile zone of the interface of the RM and the dielectric constant of the environment is suitable for observation of MF effect while the one centered at 430 nm possibly resides at the immobile interface. Further, Das et al. have found that two types of Py-DMA exciplexes are formed in non-aqueous AOT RM which reside at different locations [23]. In this case, only the exciplex which emit at longer wavelength are found to be magnetic field sensitive, similar to H_2O/AOT/*n*-heptane RM medium. Larger MF effect and shorter lifetime of the exciplex in non-aqueous RM compared to that of aqueous RM have been justified on the basis of hydrogen bonding and dipolar interaction between the solvent and the polar head group of the RM. Later, Das and Nath have studied Py-DMA exciplex in D_2O/AOT/*n*-heptane RM and found that MF effect on exciplex fluorescence is appreciably larger compared to H_2O/AOT/*n*-heptane RM [24]. In fact, the fluorescence lifetime of the exciplexes have been found to be greater in D_2O/AOT/n-heptane than that in H_2O/AOT/n-heptane medium. These differential behavior in D_2O/AOT/n-heptane RM compared to H_2O/AOT/n-heptane RM is rationalized in the light of stronger hydrogen bond strength in D_2O compared to H_2O. Further, Roy and co-workers have studied MF effect on Py-DMA exciplex fluorescence in THF-DMF binary solvents and have detected the formation of a single type of exciplex at lower value of dielectric constant. However, wavelength-resolved MF effect and lifetime studies have shown the presence of two types of exciplexes at higher value of dielectric constant [25]. Ivanov and co-workers have made theoretical attempts to explore MF effect on exciplex fluorescence using Integral Encounter Theory [26–29].

3.2. Fluorophore acting as a sensor for protic medium

Dibenzo[a,c]phenazine (DBPZ) has a planar and rigid structure containing fused rings which restrict configurational and conformational relaxation processes. However, it allows solvent relaxation process in the excited state. The steady-state and time-resolved fluorescence studies reveal that DBPZ does not show any change in its fluorescence properties with the variation of the polarity of the solvent, if the solvent is aprotic in nature. However, in protic environment its fluorescence peak shifts towards longer wavelength (420 nm and 462 nm in acetonitrile and methanol respectively) and the respective fluorescence quantum yield (0.0089 and 0.0204) as well as lifetime (too small to be measured in acetonitrile and 0.70 ns (98%) and 3.69 (2%) in methanol at 420 nm) increases due to the formation of hydrogen bonded complex with the proton donating solvent. Fig. 1 depicts the steady-state

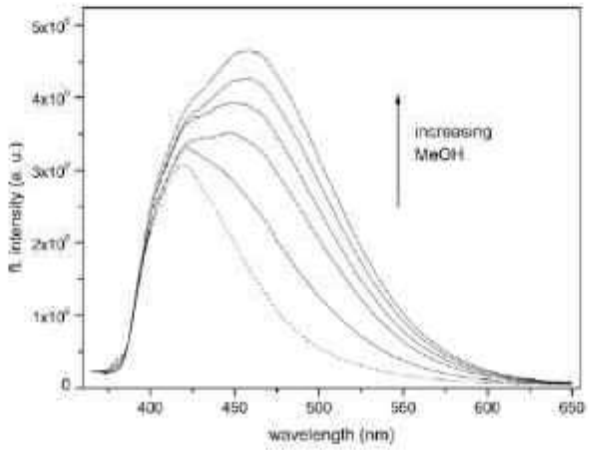

Fig. 1. Steady-state fluorescence spectra of DBPZ (1×10^{-5} M) (λ_{ex} =350 nm) in MeCN with increasing amount of MeOH (v/v): 0% (- - -), 23%, 48%, 58%, 73%, and 100%. [Adapted with permission from Ref. [30]. Copyright 2007 American Chemical Society].

fluorescence spectra of DBPZ in acetonitrile with increasing amount of MeOH. The structure of DBPZ is such that the interaction of the aprotic solvents with the lone pairs of electrons on phenazine nitrogen atoms is inhibited due to the steric hindrance provided by the corresponding proximate hydrogen atoms in its first and eighth positions respectively. Only the protons of the protic solvent even within aprotic environment are able to interact with the lone pair of electrons on nitrogen atoms. This unique feature of DBPZ, which is absent even in its parent molecule, phenazine, is also well supported by the theoretical calculations that confirm the increase of the dipole moment of the molecule in the excited state compared to that in its ground state [30]. DBPZ cannot act as a polarity probe, but can sense solvents with varying hydrogen-bond donor ability.

Ghosh et al. have synthesized different derivatives of 1-keto-1,2,3,4-tetrahydrocabazole (KTC), e.g., 6,7-dimethoxy-9-methyl-2,3,4,9-tetrahydro-1H-carbazol-1-one (DMTCO) [31], 6-hydroxy-1-keto-1,2,3,4-tetrahydrocarbazole [32], 5,6,7,9-tetrahydro-[1,3]dioxolo[4,5-h] carbazol-8-one [33], etc., which are fluorescent in nature. The importance of KTC is that it is one of the significant intermediates for naturally occurring carbazole alkaloids. The fluorescent properties of these derivatives have been studied in different solvents, nonpolar and polar protic as well as aprotic and binary solvent mixtures using steady-state and time-resolved fluorescence. One of the salient features of the experimental observations is that the relative fluorescence quantum yield of the compound is enhanced with increase in polarity of the solvent (0.036 in benzene and 0.129 in acetonitrile for DMTCO [31]). However, the fluorescence maximum is shifted towards longer wavelength more in protic solvent compared to that in a polar aprotic solvent with similar dielectric constant (402 nm in benzene, 415 nm in acetonitrile and 461 nm in methanol for DMTCO[31]). Using Lippert -Mataga analysis it is found that the dipole moment of such derivatives in excited state is much greater than in ground state in polar solvent (5.48 D in aprotic solvent and 7.24 D in protic medium [31]). The wavelength at which fluorescence yield is the highest is graphically correlated with empirical polarity parameter ET (30), H-bond donor acidity α, H-bond acceptor basicity β and polarizability of different solvents to evaluate their specific contributions towards the fluorophore using Kamlet-Taft solvatochromic comparison method. It is found that the photophysics of such compounds is mainly controlled by H-bond donor acidity α, which becomes prominent in protic solvents. Similarly, the fluorescence lifetime of the compound is much longer in protic solvent due to hydrogen bonding than the corresponding aprotic one (0.212 ns in benzene, 1.374 ns in acetonitrile and 3.015 ns in ethanol [31]). Among different protic solvents the fluorescence lifetime becomes maximum in

ethanol. However, with increasing hydrophobic chain length of the alcohols the biexponential fluorescence decay profiles indicate more than one lifetime (0.257 ns and 3.092 ns in hexanol [31]), the shorter one is close to that in aprotic solvent and the longer one supports the protic environment.

Sarangi et al. have synthesized another H-bond sensitive probe, 5-methoxy-1-keto-1,2,3,4-tetrahydro carbazole (MTC) to study its hydrogen bonding ability with heterogeneous AOT/H_2O/n-heptane RMs and binary mixtures of water and acetonitrile as well as water and alcohol using steady-state and time-resolved fluorescence techniques [34]. The fluorescence of MTC is too small to be measured in aprotic solvent with low dielectric like heptane and benzene. However, with polar aprotic solvent like acetonitrile and protic solvents like alcohols and water its fluorescence quantum yield increases. Moreover, the large Stoke's shift observed in protic binary solvent mixtures (407 nm in acetonitrile is shifted towards 460 nm in ethanol and 510 in water) as well as in RMs (407 nm with $w_0 = 1$; 455 nm with $w_0 = 10$) with increasing concentration of water signifies the sensitivity of the molecule towards hydrogen bonding with the solvent. The simultaneous existence of MTC* and corresponding H-bonded MTC* is confirmed from the Time-Resolved Emission Spectra (TRES) and Time-Resolved Area Normalized Emission Spectra (TRANES) analyses. The photophysics of MTC helps to explore the nature of hydrogen bonding inside RMs and clusters formed in binary mixtures with increasing water concentration [34]. Fig. 2 illustrates fluorescence emission decays and TRANES of MTC in 0.1 M AOT/ H_2O/n-heptane RMs.

3.3. Protonation equilibrium of photoexcited acridine (Acr) in reverse micelles/micelles

Acr and its derivatives have considerable pharmaceutical uses and their interactions with DNA have already been extensively studied. Our group was inclined to study the photophysics and photochemistry of Acr and its derivatives using various spectroscopic techniques.

The protonation equilibrium of Acr (Acr↔$AcrH^+$) is studied within AOT/H_2O/n-heptane RMs using steady-state and time-resolved fluorescence techniques [35]. It is found that protonation takes place at the Stern-layer of RMs. With increasing water pool size, the formation of $AcrH^{+*}$ increases with decrease in the concentration of Acr* which prefers to remain in the organic phase. The protonation equilibrium is well supported by TRES and corresponding TRANES analyses (the time of evolution is 0 to 0.5 ns) as shown in Fig. 3. The fluorescence of Acr* at 425 nm is quenched in presence of DMA as shown in Fig. 4A. The linear Stern-Volmer plot (depicted in Fig. 4B) signifies that the phenomenon as purely a diffusion controlled bimolecular quenching. However, with aliphatic triethylamine (TEA), the non-linear Stern-Volmer plot signifies the formation of a water mediated ground state complex between Acr and the aliphatic amine which facilitates ESPT particularly in large-sized RMs [35]. On the other hand, in the SDS micellar medium, ESPT is solely responsible for fluorescence quenching of $AcrH^{+*}$ at 478 nm by TEA within hydrophilic aqueous medium producing linear Stern-Volmer plot, but non-linearity arises when DMA interacts with Acr* undergoing both ET and ESPT with Acr* and $AcrH^{+*}$ at the interface of the micelles [36].

The water-assisted protonation equilibrium between Acr and $AcrH^+$ in excited state is perturbed by pyrimidine DNA bases like Cytosine (C), Uracil (U) and Thymine (T) which has been studied in SDS micellar medium using steady-state and time-resolved fluorescence techniques. All the bases quench the fluorescence intensity and lifetime of $AcrH^{+*}$, however C increases the formation of Acr*. Actually, fluorescence quenching of $AcrH^{+*}$ occurs due to PET from all the bases to the Acr*, however, with C simultaneous occurrence of ESPT from $AcrH^+$ mediated by water molecules causes an increase in relative yield of Acr*. The proton affinity of C (227 kcal/mol) is greater than T (210.5 kcal/mol) and U (208.6 kcal/mol) due to the oxo form of C which is absent in T and U caused by keto-enol tautomerism. The ESPT reduces the ET efficiency of C compared to T and U. Moreover, the rate of ET is greater for T compared to U due to methyl substituent at T that enhances the electron density within pyrimidine ring [37]. Similarly, the extent of ESPT between Adenine and $AcrH^{+*}$ is more compared to that with Adenosine, which highlights the efficiency of 2'-deoxy sugar moiety in regulating the deprotonation kinetics of the bases that increases the stability of DNA under UV radiation [38].

3.4. Study of photophysics of 9-Aminoacridine hydrochloride hydrate (9AA): excimer formation and pet/espt with methyl viologen and amines

9AA is an acridine derivative which is a well-known DNA

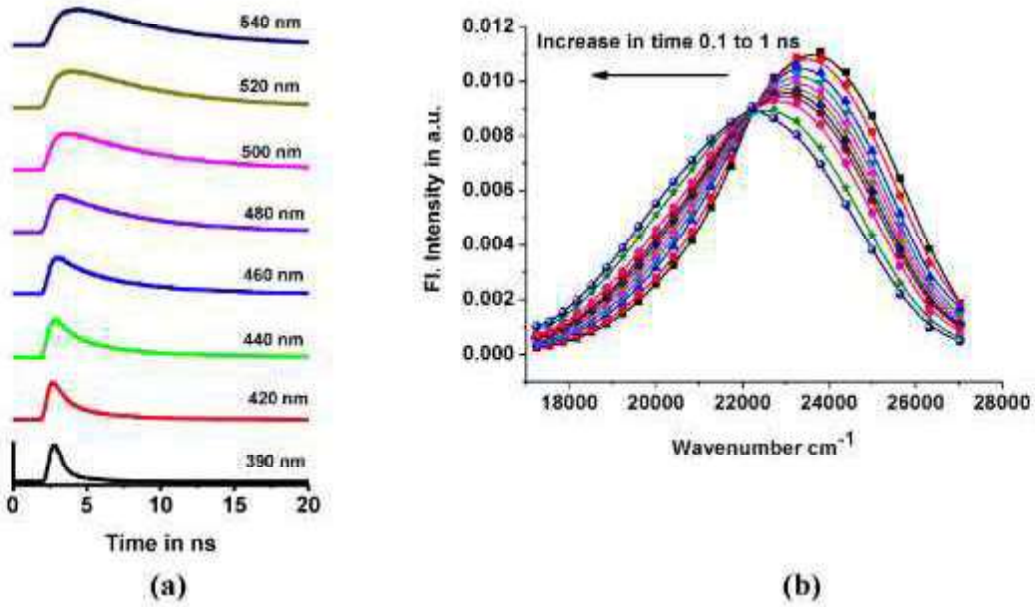

Fig. 2. (a) Fluorescence emission decays of MTC in 0.1 M AOT/ H_2O/n-heptane RMs $w_0 = 6$ at 390, 420, 440, 460, 480, 500, 520, and 540 nm, respectively. (b) TRANES of MTC (10 μM) in 0.1 M AOT/H_2O/n-heptane RMs $w_0 = 6$ between time 0.1 and 1 ns. The arrow indicates an increase in time interval of 0.1 ns. [Adapted with permission from Ref. [34]. Copyright 2013 American Chemical Society].

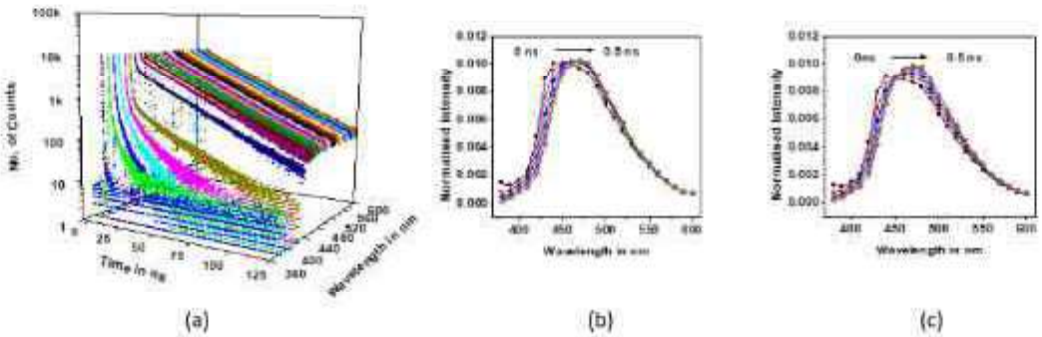

Fig. 3. (a) Fluorescence decays of Acr (0.1 mM) in RMs $w_0 = 5$ at different emission wavelengths with $\lambda_{ex} = 377$ nm. The wavelengths range from 380-600 nm with interval of 10 nm. (b) Peak normalized TRES of Acr (0.1 mM) in RMs with $w_0 = 5$ between time 0 and 0.5 ns. The arrow indicates the increase in time with interval 0.1 ns. (c) TRANES of Acr (0.1 mM) in RMs with $w_0 = 5$ between time 0 and 0.5 ns. The arrow indicates the increase in time with interval 0.1 ns. [Adapted with permission from Ref. [35]. Copyright 2011 American Chemical Society].

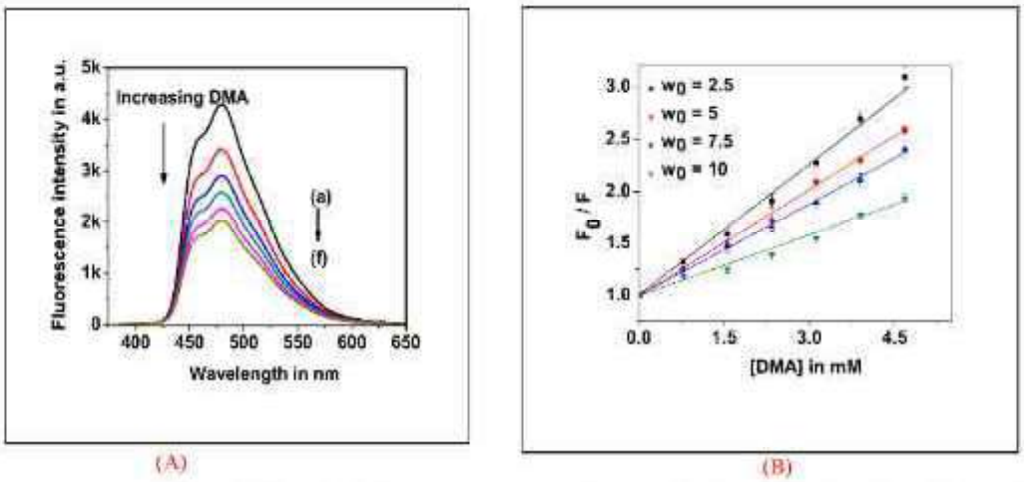

Fig. 4. **(A)** The fluorescence quenching of Acr (0.1 mM) with different concentrations of DMA (a) 0 mM, (b) 0.75 mM, (c) 1.50 mM, (d) 2.25 mM, (e) 3.00 mM, (f) 3.75 mM in RMs with $w_0 = 5$ ($\lambda_{ex} = 356$ nm and $\lambda_{em} = 478$ nm). **(B)** Stern-Volmer plots for RMs with $w_0 = 2.5$ (■), 5 (◆), 7.5 (▲) and 10 (▼) with K_{SV} values 444.7, 344.7, 290.1 and 204.2 M^{-1} respectively. [Adapted with permission from Ref. [35]. Copyright 2011 American Chemical Society].

intercalator. Apart from monomer fluorescence at 460 nm, 9AA shows an excimer fluorescence, which is red shifted with respect to the monomer fluorescence, with increasing concentration in various solvent matrices like water (at 545 nm), CTAB micelle (at 535 nm), Triton- X micelle (at 545 nm), α-cyclodextrin (CD) (at 550 nm), β-CD (at 565 nm) and crown ether (at 545 nm). Fig. 5 shows the fluorescence spectra of 9AA with variation in concentration in CTAB, crown ether, Triton-X, α-cyclodextrin, β-cylcodextrin as well as water depicting the emergence of a new peak owing to the formation of excimer. Fluorescence lifetime study of 9AA in various media also confirms the presence of the excimer species. The TRANES profile of 9AA in CTAB medium between 0 – 20 ns identifies an isoemissive point at 504 nm that indicates the equilibrium between monomer and excimer. Similar TRANES profiles of 9AA are found for aqueous and other confined media. Theoretical studies support the formation of excimer through the hydrogen bond formation among the amino-H and imino-N of the monomers in the photoexcited state [39]. Further, steady-state and time-resolved fluorescence along with flash photolysis technique in conjunction with a MF have shown that 9AA undergoes PET and ESPT with methyl viologen in aqueous medium; however, in CTAB micellar medium only PET predominates [40]. Similar spectroscopic techniques have been used to study the interaction of 9AA with DMA and TEA in homogeneous as well as heterogeneous media [41]. The differential occupational sites of neutral and protonated forms of 9AA and the organic amines in CTAB micelles result in strikingly different observations in comparison to homogeneous medium. Distribution of the neutral and protonated forms of 9AA is facilitated by the difference in pH of the hydrophobic and interfacial areas of CTAB micelle. Different modes of fluorescence quenching of 9AA with DMA and TEA corroborated with absorption studies divulge their difference in the mechanism of interactions. ESPT and PET are prevalent in 9AA-DMA system while in 9AA-TEA system ground-state complex formation, ground- state proton transfer and PET are found to take place.

3.5. Segregating direct and diffusion-controlled electron transfer within femtosecond – picosecond (fs-ps) time regime using time-resolved fluorescence upconversion

The probability of formation of CIP and SSIP through direct or diffusion-controlled PET depends on the polarity, viscosity or heterogeneity of the solvent. Within nanosecond time regime the diffusion-controlled ET prevails over the direct ET. However, in shorter time scale that is within fs-ps time scale, direct ET could be monitored over the diffusion [42]. Proflavin (PF) is another acridine derivative which is a DNA intercalator and a model photosensitizer in photodynamic therapy. Chakraborty et al. have previously studied thoroughly the dynamics of PET with PF-DMA and PF - TEA systems in various solvents having different polarity and viscosity within nanosecond time scale where diffusion is the rate determining step [43,44]. In alcoholic solvents it is found that on gradual addition of DMA the rate constant of PET decreases with increasing chain length of the alcohols. Moreover, the initial addition of TEA increases the fluorescence lifetime of PF from

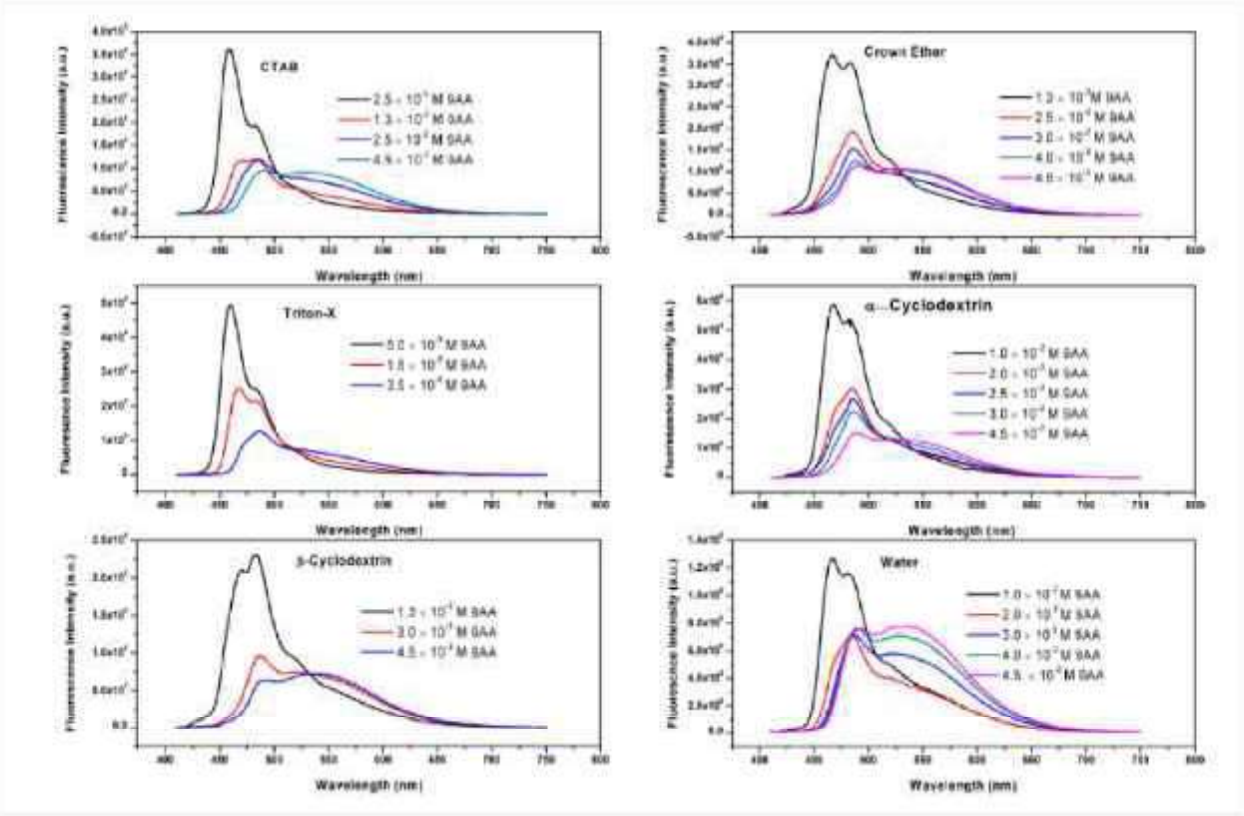

Fig. 5. Fluorescence spectra of 9AA with variation in concentration in CTAB, crown ether, Triton-X, α-cyclodextrin, β-cylcodextrin, and water (λ_{ex} = 400 nm). [Adapted with permission from Ref. [39]. Copyright 2013 American Chemical Society].

4.6 ns to 5 ns in ethanol. The rate constants of PET between PF and DMA and TEA evaluated individually within fs-ps time range show comparable decreasing trend in all the alcohols viz., methanol, ethanol and n-butanol, implying that the rate constants become viscosity independent and that becomes an index of direct ET. To explore the effect of the heterogeneity of the medium on the ET dynamics within fs-ps time scale, anionic SDS and cationic CTAB micelles are chosen as the solvent matrices. On addition of TEA, the shorter fs lifetime of PF decreases instead of increasing due to the formation of ground state complex as observed previously. This indicates the occurrence of direct ET in TEA-bound PF in the hydrophilic region of the micelles. The contradictory result is obtained in case of DMA in SDS micelles containing PF. On addition of initial 6.25 mM of DMA the fs-ps lifetime of PF increases but it decreases again on further addition of DMA. In SDS, PF and DMA are compartmentalised in polar and hydrophobic region respectively that hinders DMA to reduce the lifetime of PF through ET. Moreover, PF is confined within a structured environment formed by DMA with the hydrophobic chains of SDS micelles and that increases its fluorescence lifetime. In cationic CTAB micelles, PF is repelled by the polar head groups of the micelles; therefore, the increase in fs lifetime of PF is observed only with higher concentration of DMA, as shown in Fig. 6. Almost similar observations are obtained with Riboflavin (Rf) and TEA in water [45]. Although the fluorescence of Rf is quenched in presence of TEA, yet its fluorescence lifetimes obtained from the biexponential decays in nanosecond time scale remain almost unchanged indicating the formation of ground state complex. However, within fs-ps time resolution the tri exponential decay profile of Rf generates three lifetimes which decrease with increasing concentration of TEA indicating that within this ultrafast time regime direct ET prevails over diffusion controlled one.

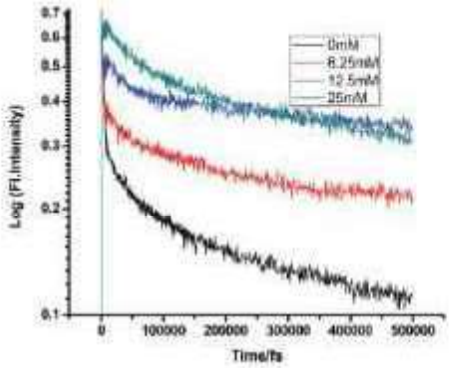

Fig. 6. Femtosecond-resolved fluorescence decay traces of proflavine (0.5 mM) in CTAB (50 mM) with varying concentrations of DMA. [Reproduced from Ref. [42] with permission from the Royal Society of Chemistry].

3.6. Utilization of fluorescence spectroscopy to probe DNA-ligand interaction

DNA-ligand binding is most often monitored by using fluorescence spectroscopy [46–49]. The mode of binding of ligands to DNA can be detected by fluorescence spectroscopy. Fluorescence anisotropy and fluorescence resonance energy transfer yield information regarding the orientation of fluorophoric ligands and their closeness to the DNA base pairs respectively. The multiple applications of transition metal complexes in biology, like in photodynamic therapy, treatment for cancer, DNA foot printing, electron and energy transfer through DNA etc., made the study of their interactions with DNA significant. Koley Seth and co-workers have synthesized methyl group - substituted pyridine (CuL^1 and CuL^3) and pyrrole (CuL^2 and CuL^4) (as shown in Fig. 7) Copper

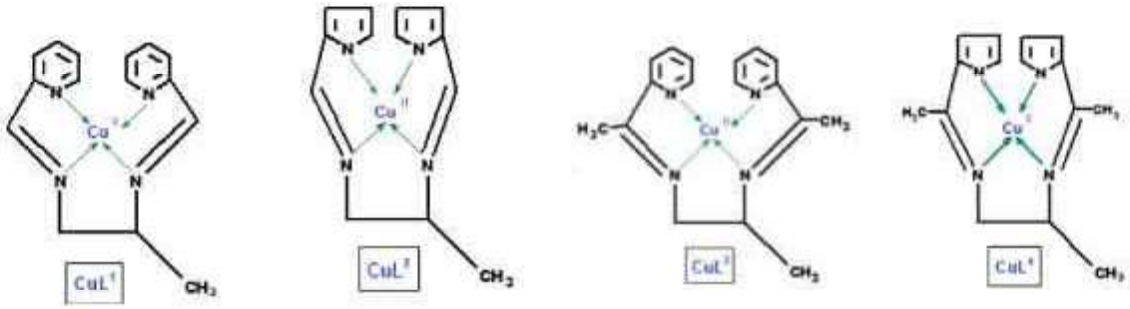

Fig. 7. Structures of CuL^1, CuL^2, CuL^3 and CuL^4.

Schiff-base complexes and have studied their interactions with Calf thymus DNA in tris–HCl/ NaCl buffer solution. In general, the copper complexes are very much useful in DNA binding or cleavage studies. The above-mentioned complexes are almost non-fluorescent. Therefore, their binding properties are well studied using absorption methods. However, Koley Seth et al. have made an attempt to compare the binding constants obtained from absorption studies with those evaluated by an indirect competitive binding method with a standard intercalator, ethidium bromide (EB) using steady-state fluorescence technique. Since EB is a good fluorophore, the fluorescence intensity of EB-bound DNA, which maximizes at 600 nm, quenches with addition of the complexes. The quenching constants are calculated from linear Stern-Volmer plot which helped to calculate the binding constants using double logarithm plot. The binding constant obtained from absorption (K_a: 2.45×10^4) is very close to that obtained from fluorescence (K_f: 2.45×10^4) for CuL^1. However, with addition of methyl group the binding constants calculated from fluorescence quenching become smaller compared to those obtained from absorption for CuL^3 (K_a: 1.69×10^3 and K_f: 1.27×10^3) and CuL^4 (K_a: 8.33×10^4 and K_f: 3.96×10^4). The prominent inconsistency between the binding constants for CuL^4 is due to PET from DNA to the complex, which is favoured by the presence of pyrrole moiety, a competent electron acceptor and the methyl groups which maintain the separation distance between the donor and the acceptor required for an efficient ET through partial intercalation. The occurrence of PET is further confirmed from transient absorption and MF effect studies [50].

Sengupta et al. have monitored the binding of Calf Thymus DNA with Acr as well as some of its derivatives e.g., PF, acridine yellow (AY) and acridine orange (AO) to explore the nature of interaction over intercalation using steady-state and time-resolved fluorescence within ns and fs-ps time regime [51]. Experimental results depict that the fluorescence of Acr is quenched in presence of DNA without any shift in its maximum around 430 nm signifying its total intercalation within DNA (as illustrated in Fig. 8). However, with two other derivatives, AY and PF, the fluorescence maxima are slightly blue shifted (504 nm → 502 nm and 506 nm → 503 nm, respectively) along with regular quenching. Surprisingly, with AO which contains two *N, N* - dimethyl amino groups as substituents, fluorescence intensity increases, instead of quenching, without any shift in the maximum around 505 nm with gradual addition of DNA, which indicates that the nonradiative channels become inactive during interaction. Similar features are reflected in time-resolved studies within nanosecond domain. The fluorescence lifetime of Acr (8.49 ns) does not change with the addition of DNA, whereas in case of AY and PF monoexponential decay profile becomes biexponential. The shorter lifetime (1.3 ns and 0.72 ns for AY and PF respectively) decreases with increasing contribution whereas the longer lifetime (4.85 ns) remains unaltered with decreasing contribution on gradual addition of DNA. These observations signify the occurrence of PET from DNA to Acr derivatives through direct ET within encounter complex and diffusion-controlled ET through the formation of SSIP respectively. In contrast, the lifetime of AO (1.71 ns) is resolved into two components, 1.69 ns and 5.07 ns with initial addition of 8.6 μM DNA, with change in contribution from 100% to 24.15% of the shorter time component and from 16.79% to 75.85% of the longer time component on further addition of DNA (0 – 103.6 μM). The longer component signifies intercalation, however to understand the dynamics of shorter component, the experiments are carried out in fs-ps time regime and it is found that lifetime of this component increases with DNA concentration. It signifies the contribution of ordered water environment surrounding the intercalator near DNA, which increases its radiative lifetime by decreasing non-radiative decays. In case of AO, where *N, N'*- dimethyl amino groups act as potential electron donor like DNA, the role of water dynamics for molecular recognition prevails over ET.

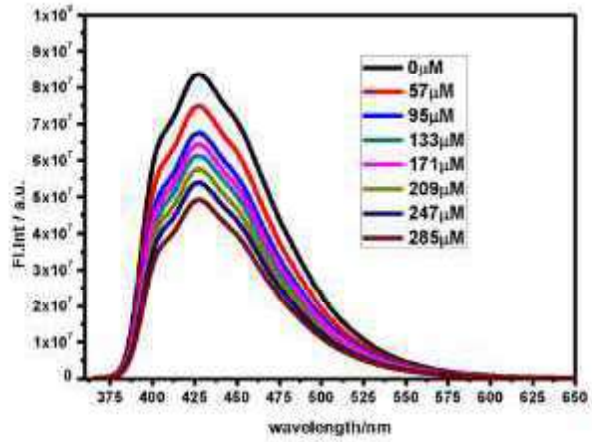

Fig. 8. Fluorescence spectra of acridine (0.01 mM) in absence and presence of varying concentration of CT DNA in tris-buffer (λ_{ex} =343 nm). [Reproduced from Ref. [51] with permission from the Royal Society of Chemistry].

3.7. Utilization of fluorescence spectroscopy to probe protein-ligand interaction

Fluoresce spectroscopy is extensively utilized to study interactions of protein with ligands. Our group has been engaged in comprehensive study of interactions of model proteins, containing trypotophan (Trp) amino acid residues, with various ligands. The advantage of presence of Trp-residue is its intrinsic fluorescence around 350 nm, which is often monitored to investigate the binding of the proteins to ligand molecules. We have made attempts to study the interactions of Human Serum Albumin (HSA), Bovine Serum Albumin (BSA), Hen Egg White Lysozyme (HEWL), Human Hemoglobin A (HbA) and β-Lactoglobulin (βLG) with various small organic molecules as well as metal Schiff base complexes.

HSA and BSA are two popular transport proteins. HSA is the most abundant carrier protein present in human blood which is composed of 585 amino acid residues. Subdomains IIA and IIIA of HSA are known to bind ligands. He and Carter reported that the two halves of HSA form a crevice that houses the sole Trp-residue (Trp 214) of the protein [52]. BSA is made up of three homologous domains (I, II and III) and each domain may be classified into two subdomains, A and B. This protein

contains two Trp-residues (Trp 134, 212), one is located in the hydrophobic binding pocket IIA while the other on the surface of the albumin in domain IB. The prime binding sites of BSA are located in domains IIA and IIIA [53]. HEWL contains six Trp-residues (Trp 28. 62, 63, 108, 111 and 123). Three out of the six Trp-residues are located at the ligand binding sites, two in the hydrophobic matrix box, while one is detached from the others. Trp 62 and 108 primarily contribute to the intrinsic fluorescence of the protein and are housed near the ligand binding site [54]. Tetrameric HbA is the major protein component of erythrocytes and contains six Trp-residues, viz., two Trp α14, two Trp β15 and two Trp β37 [55]. βLG has two Trp-residues in varied microenvironments (Trp 19 and 61) [56].

The binding parameters as well as the thermodynamic parameters in drug-protein interaction are determined by monitoring the quenching of intrinsic fluorescence of the protein in presence of varied concentration of the ligands at various temperatures. Stern-Volmer analysis of the quenching of steady-state and time-resolved fluorescence of the protein is helpful to explore the nature of quenching. Binding constant and number of binding sites are evaluated by using various equations like Scatchard's plot, Hill plot and double logarithm equation as applicable to the system. Further, van't Hoff and Gibb's-Helmholtz equations are used to determine the thermodynamic parameters. In fact, the signs of the thermodynamic parameters help to explore the nature of forces involved in the protein-ligand binding interaction [57]. Table 1 depicts a tabular representation of binding and thermodynamic parameters of various protein-ligand systems studied by our group. The possibility of Förster resonance energy transfer from the photoexcited Trp-moiety of the protein to the ligand molecules is explored in these systems and authenticated by reduction in lifetime of the donor in presence of the acceptor moiety.

Construction of TRES and TRANES for a protein-ligand system is often informative and specifically TRANES can determine the number of emissive species present in the excited state of the system. Interaction of AD with three model proteins are comprehensively explored using TRES/TRANES [58-60]. While studying the interaction of AD with HSA (containing one Trp-residue), a single isoemissive point in the TRANES [60] is observed, indicating the participation of a single Trp-in interaction with AD; whereas, while exploring the interaction of AD with BSA (containing two Trp-residues in varied environments) TRANES contains two isoemissive points emerging at different time intervals (as depicted in Fig. 9) [59], which is attributed to the participation of both the Trp-residues of BSA in interaction with AD. Further, while investigating the interaction of AD with βLG [58], the appearance of a single isoemissive point in the TRANES implies that only one Trp-residues of βLG directly interacts with the acridine derivative, although the protein contains two Trp-residues in varied environments and as concluded from the time-resolved fluorescence study, the interacting Trp-residue is probably Trp-19. Thus, TRANES helps in deciphering the mode of binding of the ligands to the proteins.

Fluorescence anisotropy serves as an index of rigidity of the neighbouring environment of the fluorophore. Steady-state and time-resolved fluorescence anisotropy measurements are carried out to probe the rigidity of the vicinity of the ligand (fluorophore in this case) trapped in the protein pockets. Increase in concentration of HEWL results in increase in steady-state anisotropy of MC 540 because of the formation of protein-ligand complex. Saturation of the anisotropy value is attained after a particular concentration of HEWL which is sufficient to bind almost all MC 540 molecules within its hydrophobic region [66]. Similarly, steady-state anisotropy of MC540 increases steadily in presence of serum albumins [65]. While studying the interaction of AD with three model proteins [58-60] using time-resolved fluorescence anisotropy, for a solution containing only AD the anisotropy decay curve fits to a single exponential function with rotational correlation time of about 0.235 ns. However, in presence of proteins the anisotropy decay curve of AD appears to be bi-exponential with two correlation times – a shorter component and longer component, indicating the occurrence of two dynamic processes in different time scales. An attempt has been made to explain such a behavior using *wobbling-in-cone* model. Fig. 10 shows the time-resolved anisotropy decay curves for a solution containing AD in presence and absence of BSA.

Fluorescence upconversion technique is employed to understand BSA-AD interaction by fluorescence lifetime (in sub-pico second time domain) measurement of AD in absence and presence of the protein [59]. AD shows a double exponential fluorescence decay pattern in sub-picosecond time regime. Upon gradual addition of BSA, this fluorescence decay pattern does not change further, but the lifetime components get reduced, which may possibly be attributed to ET from Trp-residues of BSA to AD, which has further been investigated using laser flash photolysis (LFP) technique.

It is pertinent to mention here, that although the indication of occurrence of photoinduced phenomena like PET, proton transfer or hydrogen abstraction in protein-ligand system has been obtained from fluorescence spectroscopy, but their prevalence is confirmed by LFP technique coupled with a weak MF.

Table 1
Overview of binding and thermodynamic parameters of various protein-ligand systems.

System	K (M^{-1})	ΔG° (kJ mol^{-1})	ΔH° (kJ mol^{-1})	ΔS° ($J\ mol^{-1}\ K^{-1}$)	Ref
AD- βLG	6.17×10^3 at 298 K	−22.04 at 298 K	−151.96	−435.98	[58]
AD-BSA	1.59×10^5 at 299 K	−29.26 at 299 K	−68.79	−132.2	[59]
AD-HSA	3.98×10^5 at 301 K	−30.62 at 301 K	- 87.98	−190.56	[60]
PP-BSA	5.64×10^4 at 298 K	−27.45	−47.90	−69.0	[61]
PP-HSA	3.29×10^5 at 298 K	−37.29 at 298 K	−41.63	−14.54	[62]
AY-HSA	1.88×10^5 at 298 K	−35.92 at 298 K	−33.80	7.11	[62]
9AA-BSA	1.13×10^5 at 298 K	−28.97 at 298 K	−310.42	−944.44	[63]
9AA-HSA	2.82×10^3 at 298 K	−19.63	175.37	654.36	[63]
MC540-HbA	2.89×10^4 at 298 K	−25.46	−77.31	−173.93	[64]
MC540-HSA	5.84×10^4 at 293 K	−25.89 at 293 K	75.00	348.20	[65]
MC540-BSA	4.83×10^4 at 293 K	−26.24 at 293 K	43.90	239.40	[65]
MC540-HEWL (Low conc. of MC540)	1.64×10^4 at 298 K	−9.65 at 298 K	−16.89	24.80	[66]
MC540-HEWL (High conc. of MC540)	1.29×10^4 at 298 K	−17.58 at 298 K	61.38	264.94	[66]
4NQO-HEWL	2.98×10^4 at 298 K	−25.21 at 298 K	−59.27	−113.30	[67]
MQ-HEWL	2.36×10^4 at 298 K	−24.13	12.24	124.12	[68]
NSC-HEWL	7.24×10^4 at 298 K	−28.18 at 298 K	−40.10	−40.16	[69]

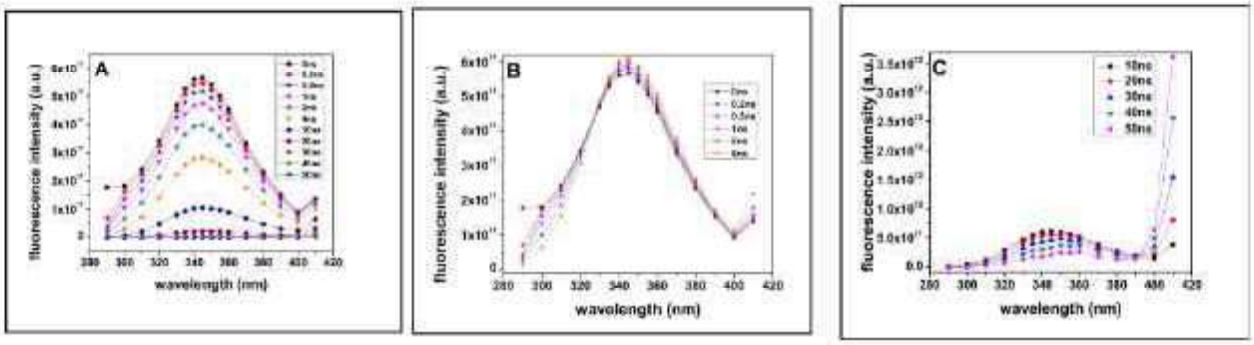

Fig. 9. (A) TRES of AD (12.5 μM) + BSA (5 μM) in phosphate buffer solution between time 0 to 50 ns. (B) TRANES of AD (12.5 μM) + BSA (5 μM) in phosphate buffer solution between time 0 to 4 ns. (C) TRANES of AD (12.5 μM) + BSA (5 μM) in phosphate buffer solution between time 10 to 50 ns. [Reproduced from Ref. [59] with permission from the center National de la Recherche Scientifique (CNRS) and the Royal Society of Chemistry].

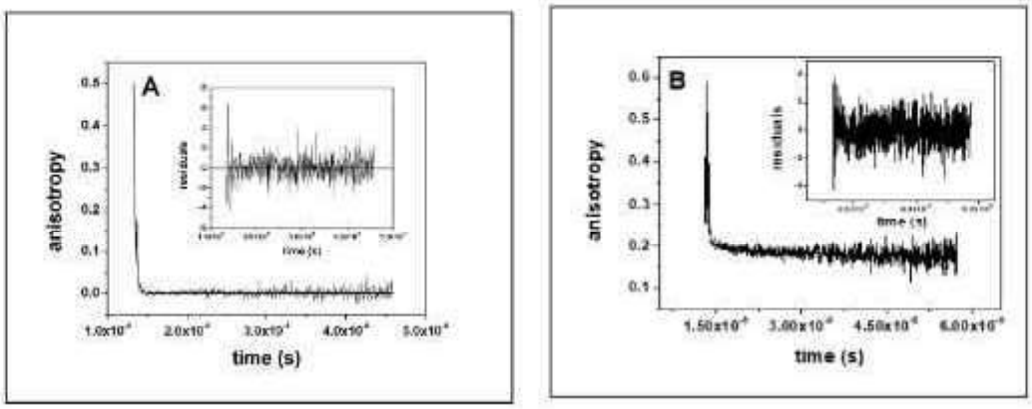

Fig. 10. Time-resolved anisotropy decay curves for (A) a solution of 6 μM AD and (B) a solution containing 6 μM AD + 20 μM BSA; $\lambda_{ex} = 377$ nm and $\lambda_{em} = 420$ nm. [Reproduced from Ref. [59] with permission from the center National de la Recherche Scientifique (CNRS) and the Royal Society of Chemistry].

3.8. Chemically engineered fluorescent dots and their applications in biology

Fluorescent carbon dots (CDs) are known to have a wide range of applications in bioimaging, yet a full understanding of their structures and chemistry remains uncertain because of their complex nano-structured framework. Our group has chemically engineered nontoxic, biocompatible highly fluorescent CDs and addressed their molecular structure and the intrinsic mechanisms governing excitation dependent photoluminescence (PL) [70]. The "excitation-dependent" PL of Ru doped CDs, has been modified by ethylenediamine (EDA), to produce "excitation-independent" highly fluorescent nanodots, Ru:CNDEDAs as illustrated in Fig. 11. It is observed that in the presence of MQ (a model antitumour drug acting as electron acceptor), the PL of Ru:CNDEDAs is quenched remarkably (as depicted in Fig. 12) owing to the formation of a covalent adduct followed by PET [70,71]. Sau et al. have exploited this PET-dependent quenching by developing a chemical sensing platform to quantify toxic and carcinogenic quinone derivatives in live cells, which can be used for drug screening. Experiments in HeLa cells suggest that these photoluminescent CDs are internalized via an endosomal pathway. The Ru:CNDEDAs further exhibit distance-dependent rapid ET with MQ by improving the linker length through chemical engineering with homocystein thiolactone (HCTL) in physiological condition that forms Ru:CNDEDAHCTLs [71]. The energy minimization structure calculations show that the separation distance between donor- acceptor in Ru:CNDEDAs-MQ is 6.5 Å which is lesser than the optimum value for ET [72], whereas in case of Ru:CNDEDAHCTLs-MQ, the distance is improved to 13.2 Å and it is optimal for efficient ET. The occurrence of ET is confirmed by steady-state fluorescence quenching of the CDs in presence of MQ as well as reduction in lifetime of the CDs in presence of the electron acceptor (as shown in Fig. 12). LFP in conjunction with MF authenticates the prevalence of the phenomenon of ET.

Further, Sau and co-workers have synthesized fluorescent polymer-like material (pCD) by using ruthenium doped CDs. The unfamiliar spectral profiles of pCDs with double-humped periodic excitation dependent photoluminescence, and the regular changes in their corresponding average fluorescence lifetime indicate the formation of high energy donor states and low energy aggregated states due to the overlap of molecular orbitals throughout the chemically switchable π-network of CDs on polymerization. To probe the electronic distribution of pCDs, Sau et al. have made attempt to study its occurrence of PET with MQ [73].

Rf (also known as vitamin B2) is widely distributed in human tissues in free or conjugated forms and plays an important role in the redox functions of numerous flavo-enzymes. The Rf receptor is a tumor biomarker, as it is overexpressed in the nucleus of malignant cells found in human breast and prostate cancers. Rf is a DNA intercalator and the fluorescence from its planer isoalloxazin moiety is strongly enhanced upon intercalation. It is proposed that the overexpressed Rf receptors in cancer cells could concentrate Rf in the nucleus, and hence, promote DNA intercalation, leading to DNA strand breaks. To deliver a large number of Rf molecule at a time into nucleus, Sau and coworkers synthesized riboflavin-gold nano-assemblies (RfS@AuNPs) by covalently attaching thiolated Rf to gold nanoparticles (AuNPs) (as illustrated in Fig. 13) [74]. The attached AuNPs promote greater intercalation relative to Rf alone. Sau and coworkers have observed that these RfS@AuNPs accumulate in the nucleus of cancer cells, leading to plasma membrane blebbing and binucleated apoptotic bodies, consistent with activation of apoptosis. These are evident from real time confocal images as depicted in Fig. 14. In addition, RfS@AuNPs increase the concentration of the DNA damage marker γ-H2AX (phosphorylated histone H2AX), which

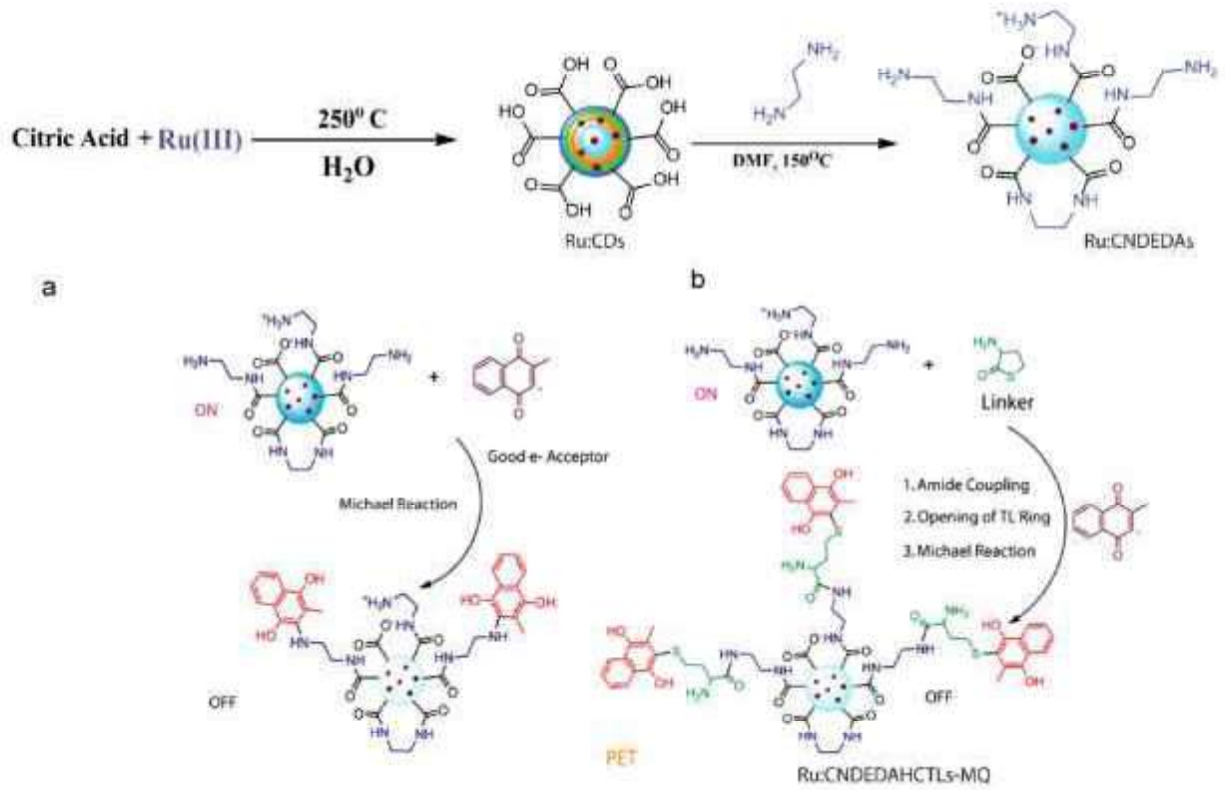

Fig. 11. Synthetic root of **Ru:CNDEDAs** and (a) Plausible ET from **Ru:CNDEDAs** to **MQ** with **Ru:CNDEDAs**. (b).Homocystein-thiolactone assisted plausible distance-dependent ETfrom **Ru:CNDEDAs** to **MQ** and irreversible attachment with **Ru:CNDEDAHCTLs.** The dark red dots, multicolored ball, deep blue balls and faint blue balls represent Ru(III), excitation dependent fluorescent core of **Ru:CDs,** the fluorescent cores and the quenched fluorescent cores of **Ru:CNDEDAs/ Ru:CNDEDAHCTLs** respectively. [Adapted with permission from Ref. [71]. Copyright 2016 American Chemical Society].

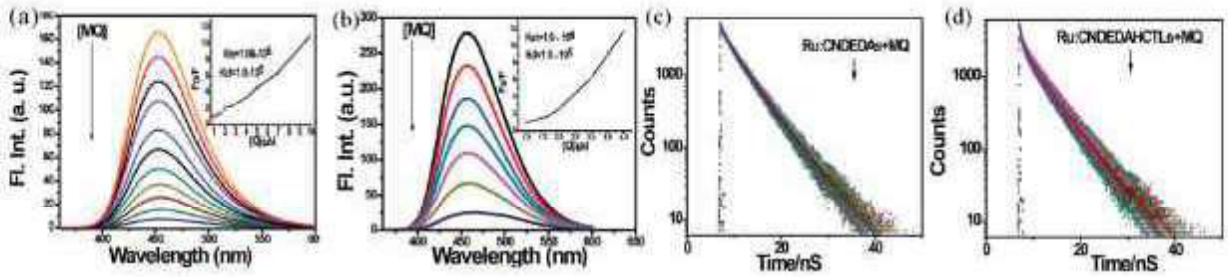

Fig. 12. Steady-state fluorescence spectra of (a) **Ru:CNDEDAs** (b) **Ru:CNDEDAHCTLs** with increasing amount of **MQ** (1-10 μM and 1–4 μM respectively) upon excitation at 350 nm. Insets: corresponding Stern–Volmer plots; Time-resolved fluorescence decay spectra of (c) **Ru:CNDEDAs** (d) **Ru:CNDEDAHCTLs** with increasing concentrations of MQ 1–4μM. (λ_{ex} =375 nm). [Adapted with permission from Ref. [71]. Copyright 2016 American Chemical Society].

forms in response to dsDNA breaks. Microarray gene expression data for RfS@AuNP-treated HeLa cells show significant perturbations to vital biological pathways necessary for cell survival. On integrating these findings, Sau et al. have suggested a mechanism of DNA damage induction followed by apoptosis in the cancer cells upon drug treatment, which might find new applications in tumor diagnosis and cancer therapeutics.

3.9. Some recent examples and future prospects of fluorescence spectroscopy

In the aforementioned sections, we have been focussing on the work carried out in our laboratory over the last two and a half decades. However, many other research groups have been actively engaged in using fluorescence spectroscopy since a long time. In this section we will discuss some recent examples of utilization of fluorescence by other researchers.

Fluorescence upconversion technique is quite popular among photochemists nowadays because it provides an insight into the formative stages of the fluorescent state and these earliest events include vibrational cooling, solvent relaxation, and ultrafast charge transfer etc. In Sections 3.5, 3.6 and 3.7 it has already been discussed that our group has used this technique to segregate direct and diffusion-controlled ET within picosecond-femtosecond time domain and also to study DNA-ligand and protein-ligand interactions. Gustavsson and co-workers have utilized this technique to study the influence of environment on the intramolecular charge transfer process, and the necessity to analyze time-resolved data in detail when solvation and ICT take place at the same time [75]. They have carried out a time-resolved fluorescence study of a triphenylamine–bithiophene–naphthalimide 'push-pull' dye in four solvents of varying polarity by means of this technique. Knutson et al. have studied the ultrafast solvation dynamics of reduced nicotinamide adenine dinucleotide (NADH) free in solution using a femtosecond upconversion spectrofluorometer [76]. NADH in solution

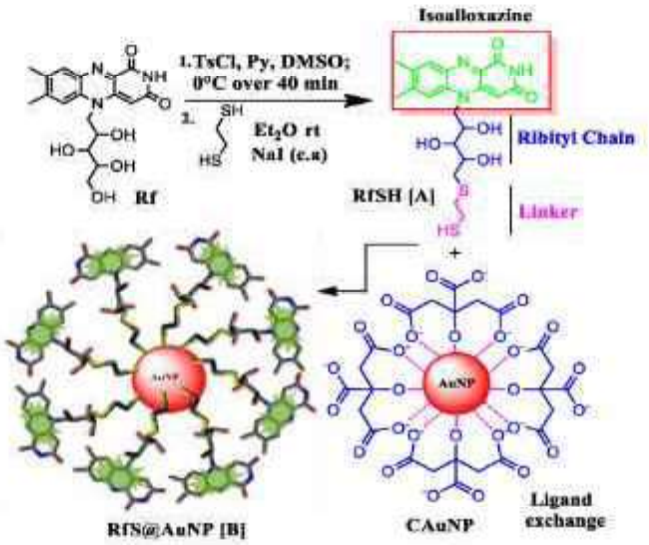

Fig. 13. Synthetic route of **RfS@AuNPs.** [Adapted with permission from Ref. [74]. Copyright 2018 American Chemical Society].

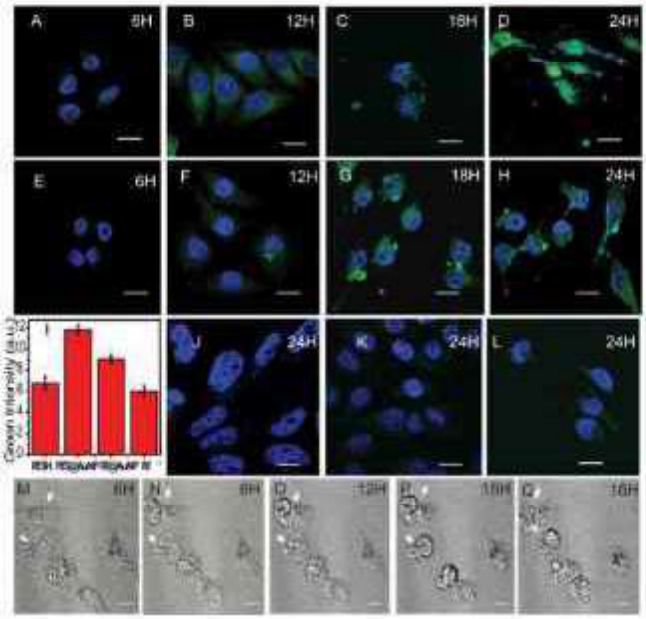

Fig. 14. Real time confocal images of 0.5 nM **RfS@AuNPs** treated HeLa cell captured at (A) 6 H (B) 12 H (C) 18 H (D) 24 H (100X objective; Scale Bar represents 20 μm) and (E) 6 H (F) 12 H (G) 18 H (H) 24 H for **Rf@AuNPs** treated HeLa cells (Scale Bar represents 20 μm) (I) Relative green fluorescence Intensity of **RfSH; Rf@AuNPs; RfS@AuNPs; Rf** fluorescence in the HeLa nucleus after 12H treatment. (J, K, L) Real-time images of cancer cells (HeLa) at maximum time point (24 H) after treatment of (J) **CAuNP** (K) Only **Rf** (L) only **RfSH** (Scale Bar represents 20 μm); Panel: M, N, O, P, Q are the representative time-lapse images of a HeLa cell treated with 0.5 nM **RfS@AuNPs** undergoing membrane blebbing and binucleated (indicated by arrow) cell formation. (The scale bar is 10μm.) [Adapted with permission from Ref. [74]. Copyright 2018 American Chemical Society].

exhibits two types of solvation characteristics. Solvent relaxation for "bulk water" has a lifetime of 1.4 ps and the second solvation process with a lifetime of 27 ps indicates there may be a slower "biological water" behavior of NADH. Hazra et al. have probed excited state double proton transfer dynamics (ESIDPT) of 2,2′-bipyridyl-3,3′-diol molecules in a nontoxic, biocompatible sugar surfactant assembly, octyl-β-D-glucoside (OBG) micelle with the help of fluorescence upconversion technique [77]. The results show that the ESIDPT dynamics in OBG micellar environment takes place in 13 ps time-domain.

In Section 3.6 we have vividly discussed how we have utilized fluorescence to study DNA-ligand interaction. In fact, use of fluorecence upconversion technique has made our study intriguing. It is pertinent to mention that many other scientists resort to fluorescence spectroscopy to explore DNA-ligand interactions. One of the pioneering work by Zewail and co-workers is highly relevant in this context. They have explored the dynamics of hydration at the DNA surface of known local structure and with a ligand positioned in the minor groove with femtosecond resolution [78]. Kundu et al. have investitigated the binding interaction of DSDP, a pyrazole derivative with DNA using steady-state fluorescence quenching, steady-state fluorescence anisotropy and time-resolved decay measurements. In fact, they have used fluorometric competitive displacement assay to confirm that DSDP is a groove binder [79]. Binding of a *β*-carboline analogue AODIQ, a potential nervous system stimulant with DNA has also been explored using various fluorometric measurements [80]. The alteration in the photophysics of the fluorescent molecule has been utilized to study DNA-ligand interaction and the mode of binding in this case has also been found to be groove-binding. Thermodynamic and binding parameters involved in DNA-ligand interaction in both the cases are determined fluorometrically. Paul et al. have found out the intercalative mode of interaction of harmane, a potential cancer cell photosensitizer with DNA. Apart from determining the thermodynamic and binding parameters, they have studied the time-resolved fluorescence anisotropy of the ligand in DNA to explore the modulation of rotational relaxation dynamics of harmane within the biomacromolecule and they have validated their observations in the light of *two-step and wobbling-in-cone* model [81]. Very recently Gupta et al. have tried to explore DNA condensation using chemically diverse condensing agent like protamine, sperminem, cohex and Ni^{2+} using fluorescence spectroscopy. They have attempted to find out the role of ligand binding mode in DNA condensations [82].

Investigation of protein-ligand interaction using model proteins containing Trp-residues have also been reported by a number of other researchers [83-86]. They have mainly utilized the intrinsic fluorescence of Trp-residue, similar to our work, to study the interaction of various ligands with model proteins. Survey of literature shows that binding with proteins devoid of tryptophan residue has also been carried out with fluorescence spectroscopy by a number of researchers. For example, Sahoo et al. studied the binding interaction of diacetylcurcumin with Ribonuclease A, a protein in which tryptophan residue is absent. In this case, intrinsic fluorescence of tyrosine residue is monitored to explore the binding interaction [87]. The flavin enzymes are interesting model systems for involving ultrafast ET reactions taking place in the chromophore's binding pockets. When the photoexcited flavin chromophore is in the oxidized form, it acts as a strong electron acceptor. Thus, if such aromatic residues as tryptophan and/ or tyrosine (which are electron donors) are in the vicinity of the flavin, strong fluorescence quenching via ET takes place on an ultrafast time scale (10^{-14}–10^{-10} s). As discussed in Section 3.7 we have used fluorescence upconversion techique to study protein-ligand interaction in ps-fs time domain. Ultrafast fluorescence upconversion technique has similarly been applied to various 'nonfluorescent' flavoproteins by a number of researchers [88-91].

Survey of literature suggests that fluorescence spectroscopy has also been utilized to study host-guest interactions [92-94], metal ion sensing [95-97] and nanomateials [98-100]. Thus, it is evident from this discussion that fluorescence spectroscopy is used in diverse fields. It has been intensely employed as a powerful spectroscopic tool for quantitative analysis, quality control and characterization in various domains such as inorganic, organic, biological, pharmaceutical and biomedical, food, and environmental analyses It seems that future research in molecular fluorescene will continue to be heavily instrument- or computer-oriented, which may be accompanied by use of several

combinations of chemical methodologies. Thus, information gathered by performing several experiments now can possibly be obtained from a single experiment in the near future.

4. Conclusion

In this mini review we have highlighted our findings accomplished over the last two and a half decades using steady-state and time-resolved (ns-ps-fs time regime) fluorescence techniques. In the beginning we have searched for the novel exciplex systems between electron donors and acceptors which were non-conventional at that time and have also explored the corresponding mechanism that involves the spin dynamics of initially formed RIPs by applying an a.c. MF of the order of 0.1 – 0.2 tesla and a phase sensitive detection system which improves the signal to noise ratio as 1000:1. The exciplex systems which are formed from different derivatives of carbazoles and cyanobenzenes highlight the importance of the correlation among the polarity of the medium, exciplex energy and steric bulk that minimizes the activation barrier between the two primary products, CIP and SSIP and facilitates spin dynamics resulting in an enhancement of exciplex fluorescence. Later, we have extended our work using other exciplex systems like DPH-DCB, Py-DMDPM, etc. We have synthesized some of the derivatives of 1-keto-1,2,3,4-tetrahydrocabazole which show prominent hydrogen bonding ability with protic solvents over the aprotic solvents with similar dielectrics as well as with RMs. These fluorophores resemble our previous system DBPZ except that DBPZ can sense only the polar protic solvents and not the non-polar one. The protonation equilibrium in excited state is well studied with acridine in heterogeneous micellar and reverse micellar media with varied water pool size with increasing proton donor ability. The corresponding TRANES profiles help to assess the time of evolution of the protonation equilibrium. Similarly, the monomer-excimer equilibrium of 9AA in various solvent matrices is established from TRANES. The competition between ESPT and PET is reported between acridine and DMA, TEA and DNA bases as well as between 9AA and methyl viologen and organic amines. The occurrence of PET in homogeneous media is a diffusion-controlled phenomenon as observed with earlier exciplex systems using nanosecond time-resolved fluorescence. However, experiments within ps-fs time-regime help us to identify the direct ET over the diffusion controlled one in heterogeneous SDS and CTAB micellar media with PF and DMA/TEA systems. Similarly, the water dynamics surrounding DNA during interaction with the intercalators becomes significant within ps-fs time domain. The acridine and its derivatives, AY and PF, are well known DNA intercalators. Moreover, these molecules undergo efficient PET with DNA bases. On the contrary, AO does not undergo PET with DNA since it contains electron-rich *N,N'*-dimethylamino groups. Therefore, AO has been proved to be an efficient probe to study the water-dynamics through its encapsulation within the water cage that further increases its lifetime in presence of DNA. We have studied DNA-ligand and protein-ligand interactions comprehensively, by utilizing different techniques of fluorescence spectroscopy. In fact, for proteins containing more than one Trp-residues, TRANES analysis has helped us to explore the number of Trp-residues housed in the model proteins which have directly interacted with the incoming ligands. Furthermore, time-resolved fluorescence anisotropy measurements of the acridine derivatives in presence of various model proteins have yielded interesting observations which have been interpreted in terms of *wobbling-in-cone* model. We have synthesized highly fluorescent excitation-dependent carbon nano dots that become excitation independent on further amination. This Ru:CNDEDA undergoes efficient intramolecular PET with MQ only when the latter is linked with it through a HCTL linker that makes their separation distance greater than 10.0 Å, which is the optimum distance required for an efficient PET as well as magneto dynamics. This system has been used to estimate excess quinone present in the HeLa cells using confocal microscopy. Riboflavin-gold nano-assemblies were synthesized by covalently attaching thiolated Rf to gold nanoparticles and have observed that these RfS@AuNPs accumulate in the nucleus of cancer cells, leading to plasma membrane blebbing and binucleated apoptotic bodies, consistent with activation of apoptosis. Finally, some very recent examples as well as the future prospect of fluorescence spectroscopy have been discussed. It may be mentioned here that although fluorescence is an exhaustive technique which can be used to study systems varying from simple small organic molecules to complicated biological macromolecules, in vitro as well as in vivo, however we have employed LFP in conjunction with MF along with fluorescence spectroscopy to gain a deeper insight. Theoretical calculations have been performed to substantiate our experimental findings. Nevertheless, fluorescence measurement is deepening our understanding of various simple and complex molecular systems and will continue to do so for some more while yet.

Funding statement

There are no funders to report for this submission.

CRediT authorship contribution statement

Brotati Chakraborty: Writing – review & editing, Writing – original draft, Methodology, Conceptualization. **Samita Basu:** Writing – review & editing, Writing – original draft, Supervision, Methodology, Conceptualization.

Declaration of competing interest

The authors declare that they have no known competing financial interests or personal relationships that could have appeared to influence the work reported in this paper.

Data availability

No data was used for the research described in the article.

Acknowledgement

The authors would like to thank Dr. Abhishek Sau, Texas A&M University, USA for his help in preparing the manuscript.

References

[1] B. Valeur, Molecular Fluorescence: Principles and Applications, WILEY-VCH Verlag, Weinheim, 2002.
[2] J.R. Lakowicz, Principles of Fluorescence Spectroscopy, Springer, 2006.
[3] J.R. Bolton, N. Mataga, G.L. Mclendon (Eds.), Electron Transfer in Inorganic, Organic and Biological Systems, American Chemical Society, Washington DC, 1991.
[4] Ke-Li Han, Guang-Jiu Zhao (Eds.), Hydrogen Bonding and Transfer in the Excited State Part I & II, John Wiley and Sons, United Kingdom, 2011.
[5] D. Huppert, E. Kolodney, M. Gutman, E. Nachliel, Effect of water activity on the rate of proton dissociation, J. Am. Chem. Soc. 104 (1982) 6949–6953, https://doi.org/10.1021/ja00389a011.
[6] N.J. Turro, V. Ramamurthy, J.C. Scaiano, Modern Molecular Photochemistry of Organic Molecules, California: University Science Books, 2010.
[7] Orbech N. and Ottolenghi M. 1975 The Exciplex ed. M. Gordon and W. R. Ware (New York: Academic Press).
[8] H. Knibbe, K. Rollig, F.P. Schafer, A. Weller, Charge-Transfer Complex and Solvent-Shared Ion Pair in Fluorescence Quenching, J. Chem. Phys. 47 (1967) 1184–1185, https://doi.org/10.1063/1.1712007.
[9] Salikhov K.M., Molin Y., Sagdeev R.Z. and Buchachenko A.L. 1984 in Spin Polarization and Magnetic Field Effects in Radical Reactions, ed. Yu. N. Molin (Amsterdam: Elsevier).
[10] S. Basu, M. Haldar, M. Chowdhury, Magnetic field effect in chemistry - the Indian Scenario, Proc. Indian Natl. Sci. Acad. 66A (2000) 267–288.
[11] S. Aich, S. Basu, Laser flash photolysis studies and magnetic field effect on a new heteroexcimer between N-ethyl carbazole and 1,4- dicyanobenzene in homogeneous and heterogeneous media, J. Chem. Soc. Faraday Trans. 91 (1995) 1593–1600, https://doi.org/10.1039/FT9959101593.
[12] S. Aich, S. Basu, Magnetic field effect: a tool for identification of spin state in a photoinduced electron-transfer reaction, J. Phys. Chem. A 102 (1998) 722–729, https://doi.org/10.1021/jp972264m.

[13] S. Aich, S. Basu, D.N. Nath, An Improved PSD system to observe magnetic field effect on exciplex luminescence: deviation from previously observed dielectric constant dependence, J. Photochem. Photobiol. A 109 (1997) 95–99, https://doi.org/10.1016/S1010-6030(97)00115-9.
[14] U.E. Steiner, T. Ulrich, Magnetic field effects in chemical kinetics and related phenomena, Chem. Rev. 89 (1989) 51–147, https://doi.org/10.1021/cr00091a003.
[15] K. Bhattacharya, K. Chowdhury, Environmental and magnetic field effects on exciplex and twisted charge transfer emission, Chem. Rev. 93 (1993) 507–535, https://doi.org/10.1021/cr00017a022.
[16] S. Bandyopadhyay, K. Sen, S. Dutta Choudhury, S. Basu, Exciplex Parameters: key Factors in the Dielectric Behaviour of Magnetodynamics, Mol. Phys. 100 (2002) 1079–1084, https://doi.org/10.1080/00268970110109493.
[17] S. Dutta Choudhury, S. Basu, Magnetic field effect on N-ethylcarbazole-dimethylterephthalate and N-ethylcarbazole-1,4-dicyanobenzene: a comparative study focusing on steric effect, Chem. Phys. Lett. 408 (2005) 274–278, https://doi.org/10.1016/j.cplett.2005.04.066.
[18] T. Sengupta, S. Basu, Magnetic field effect on indole exciplexes: a comparative study, Spectrochim. Acta Part A 60 (2004) 1127–1132, https://doi.org/10.1016/j.saa.2003.06.002.
[19] T. Sengupta, S. Aich, S. Basu, Isotropic and Anisotropic Magnetic Field Effect on the Exciplex between All-s-trans-1,6-diphenyl-hexa-1,3,5-triene and 1,4-dicyanobenzene, J. Phys. Chem B. 103 (1999) 3784–3790, https://doi.org/10.1021/jp984095e.
[20] K. Sen, S. Bandyopadhyay, D. Bhattacharya, S. Basu, Dielectric Dependence of Magnetic Field Effect: a tool for Identification of Exciplex and Triplex, J. Phys. Chem. A 105 (2001) 9077–9084, https://doi.org/10.1021/jp011065m.
[21] A. Weller, F. Nolting, H. Staerk, A quantitative interpretation of the magnetic field effect on hyperfine-coupling-induced triplet formation from radical ion pairs, Chem. Phys. Lett. 96 (1983) 24–27, https://doi.org/10.1016/0009-2614(83)80109-2.
[22] P.P. Parui, D.N. Nath, M. Chowdhury, Magnetic field effect on exciplex luminescence: a study of multiple exciplex formation dynamics in biomimicking environment, Chem. Phys. Lett. 404 (2005) 79–84, https://doi.org/10.1016/j.cplett.2005.01.069.
[23] D. Das, D.N. Nath, P.P. Parui, M. Chowdhury, Magnetic field effect on pyrene–DMA exciplex luminescence in non-aqueous AOT reverse micelle, Chem. Phys. Lett. 424 (2006) 300–306, https://doi.org/10.1016/j.cplett.2006.04.076.
[24] D. Das, D.N. Nath, Exciplex luminescence in D_2O solubilized AOT reverse micelle: a magnetic field effect study, Chem. Phys. Lett. 458 (2008) 81–87, https://doi.org/10.1016/j.cplett.2008.04.069.
[25] P. Roy, A.K. Jana, D. Das, D.N. Nath, Study of magnetic field effect on Py-DMA exciplex luminescence in THF–DMF binary solvents: evidence of multiple exciplex formation at higher bulk dielectric constant, Chem. Phys. Lett. 474 (2009) 297–301, https://doi.org/10.1016/j.cplett.2009.04.054.
[26] D.V. Dodin, A.I. Ivanov, A.I. Burshtein, Magnetic field effect in fluorescence of excited fluorophore equilibrated with exciplex that reversibly dissociates into radical-ion pair undergoing the spin conversion, J. Chem. Phys. 137 (2012) 024511, https://doi.org/10.1063/1.4734306 (1–6).
[27] D.V. Dodin, A.I. Ivanov, A.I. Burshtein, Hyperfine interaction mechanism of magnetic field effects in sequential fluorophore and exciplex fluorescence, J. Chem. Phys. 138 (2013) 124102, https://doi.org/10.1063/1.4795576 (1–11).
[28] A.I. Burshtein, A.I. Ivanov, Diffusion affected magnetic field effect in exciplex fluorescence, J. Chem. Phys. 141 (2014) 024508, https://doi.org/10.1063/1.4886509 (1–5).
[29] S.V. Feskov, A.I. Burshtein, A.I. Ivanov, Magnetic Field Effects in Fluorescence of Exciplex and Fluorophore for the Weller Schemes I and II: similarities and Differences, J. Phys. Chem. C 118 (2014) 21365–21376, https://doi.org/10.1021/jp5070643.
[30] D. Dey, A. Bose, D. Bhattacharyya, S. Basu, S.S. Maity, S. Ghosh, Dibenzo[a,c] phenazine: a polarity-insensitive hydrogen bonding probe, J. Phys. Chem. A 111 (2007) 10500–10506, https://doi.org/10.1021/jp073181l.
[31] S. Ghosh, A.K. Mitra, C. Saha, S. Basu, Tuning the solution phase photophysics of two de novo designed hydrogen bond sensitive 9-methyl-2,3,4,9-tetrahydro-1H-carbazol-1-one derivatives, J. Fluoresc. 23 (2013) 1179–1195, https://doi.org/10.1007/s10895-013-1249-z.
[32] A.K. Mitra, S. Ghosh, S. Chakraborty, S. Basu, C. Saha, Synthesis and spectroscopic exploration of carboxylicacid derivatives of 6-hydroxy-1-keto-1,2,3,4-tetrahydrocarbazole: hydrogen bond sensitive fluorescentprobes, J. Lumin. 143 (2013) 693–703, https://doi.org/10.1016/j.jlumin.2013.06.021.
[33] S. Ghosh, A.K. Mitra, S. Basu, S. Chakraborty, C. Saha, 5,6,7,9-Tetrahydro-[1,3] dioxolo[4,5-h]carbazol-8-one: a solvatochromic PET-acceptor fluorescent probe, J. Lumin. 153 (2014) 296–303, https://doi.org/10.1016/j.jlumin.2014.03.046.
[34] M.K. Sarangi, A.K. Mitra, C. Sengupta, S. Ghosh, S. Chakraborty, C. Saha, S. Basu, Hydrogen Bond Sensitive Probe 5-Methoxy-1-keto-1,2,3,4-tetrahydro Carbazole in the Microheterogeneity of Binary Mixtures and Reverse Micelles, J. Phys. Chem. C 117 (2013) 2166–2174, https://doi.org/10.1021/jp310923q.
[35] M.K. Sarangi, D. Dey, S. Basu, Influence of Heterogeneity of Confined Water on Photophysical Behavior of Acridine with Amines: a Time-Resolved Fluorescence and Laser Flash Photolysis Study, J. Phys. Chem. A 115 (2011) 128–135, https://doi.org/10.1021/jp107610k.
[36] M.K. Sarangi, S. Basu, Photophysical behavior of acridine with amines within the micellar microenvironment of SDS: a time-resolved fluorescence and laser flash photolysis study, Phys. Chem. Chem. Phys. 13 (2011) 16821–16830, https://doi.org/10.1039/C1CP20644F.
[37] M.K. Sarangi, A. Mitra, S. Basu, Prototropic Interactions of Pyrimidine Nucleic Acid Bases with Acridine: a Spectroscopic Investigation, J. Phys. Chem. B 116 (2012) 10275–10282, https://doi.org/10.1021/jp305352h.
[38] M.K. Sarangi, D. Bhattacharyya, S. Basu, Influence of 2'deoxy sugar moiety on excited state proton equilibrium of Adenine and Adenosine with Acridine inside SDS micelles; A time-resolved study with quantum-chemical calculations, Chem. Phys. Chem. 13 (2012) 525–534, https://doi.org/10.1002/cphc.201100763.
[39] P. Mitra, B. Chakraborty, D. Bhattacharyya, S. Basu, Excimer of 9-aminocridine hydrochloride hydrate in confined medium: an integrated experimental and theoretical study, J. Phys. Chem. A 117 (2013) 1428–1436, https://doi.org/10.1021/jp3103639.
[40] P. Mitra, B. Chakraborty, S. Basu, Exploring photoinduced electron transfer and excited-state proton transfer reactions involving 9-aminoacridine hydrochloride hydrate and methyl viologen using laser flash photolysis, Chem. Phys. Lett. 610-611 (2014) 108–114, https://doi.org/10.1016/j.cplett.2014.07.004.
[41] P. Mitra, B. Chakraborty, S. Basu, A spectroscopic investigation of the photophysical behaviour of 9-aminoacridine hydrochloride hydrate in presence of organic amines in homogeneous and heterogeneous media, J. Lumin. 149 (2014) 221–230, https://doi.org/10.1016/j.jlumin.2014.01.034.
[42] C. Sengupta, P. Mitra, B. Koley Seth, D. Mandal, S. Basu, Electronic and spatial control over the formation of transient ion pairs during photoinduced electron transfer between proflavine–amine systems in a subpicosecond time regime, RSC Adv 7 (2017) 15149–15157, https://doi.org/10.1039/C6RA26286E.
[43] B. Chakraborty, S. Basu, Study of interaction of proflavin with triethylamine in homogeneous and micellar media: photoinduced electron transfer probed by magnetic field effect, Chem. Phys. Lett. 477 (2009) 382–387, https://doi.org/10.1016/j.cplett.2009.07.015.
[44] B. Chakraborty, S. Basu, Interaction of proflavin with aromatic amines in homogeneous and micellar media: photoinduced electron transfer probed by magnetic field effect, Chem. Phys. Lett. 487 (2010) 51–57, https://doi.org/10.1016/j.cplett.2010.01.013.
[45] C. Sengupta, M.K. Sarangi, A. Sau, D. Mandal, S. Basu, A case study of photo induced electron transfer between Riboflavin and aliphatic amine: deciphering different mechanisms of ET operating from femtosecond to microsecond time domain, J. Photochem. Photobiol. A 296 (2015) 25–34, https://doi.org/10.1016/j.jphotochem.2014.09.010.
[46] E.B. Veale, T. Gunnlaugsson, Synthesis, Photophysical, and DNA Binding Studies of Fluorescent Troger's Base Derived 4-Amino-1,8-naphthalimide Supramolecular Clefts, J. Org. Chem. 75 (2010) 5513–5525, https://doi.org/10.1021/jo1005697.
[47] C.V. Kumar, E.H. Asuncion, DNA Binding Studies and Site Selective Fluorescence Sensitization of an Anthryl Probe, J. Am. Chem. Soc. 115 (1993) 8547–8553, https://doi.org/10.1021/ja00072a004.
[48] S. Bhattacharjee, P.K. Sengupta, S. Bhowmik, Exploring the preferential interaction of quercetin with VEGF promoter G-quadruplex DNA and construction of a pH-dependent DNA-based logic gate, RSC Adv 7 (2017) 37230–37240, https://doi.org/10.1039/C7RA05930B.
[49] S. Sirajuddin, S. Ali, A. Badshah, Drug–DNA interactions and their study by UV–Visible, fluorescence spectroscopies and cyclic voltametry, J. Photochem Photobiol B 124 (2013) 1–19, https://doi.org/10.1016/j.jphotobiol.2013.03.013.
[50] B. Koley Seth, A. Ray, A. Saha, P. Saha, S. Basu, Potency of photoinduced electron transfer and antioxidant efficacy of pyrrole and pyridine based Cu(II)-Schiff complexes while binding with CT-DNA, J. Photochem. Photobiol. B 132 (2014) 72–84, https://doi.org/10.1016/j.jphotobiol.2014.02.007.
[51] C. Sengupta, S. Basu, A spectroscopic study to decipher the mode of interaction of some common acridine derivatives with CT DNA within nanosecond and femtosecond time domains, RSC Adv 5 (2015) 78160–78171, https://doi.org/10.1039/C5RA13035B.
[52] X.M. He, D.C. Carter, Atomic structure and chemistry of human serum albumin, Nature 358 (1992) 209–215, https://doi.org/10.1038/358209a0.
[53] S. Patra, K. Santosh, A. Pabbathi, A. Samanata, Diffusion of organic dyes in bovine serum albumin solution studied by fluorescence correlation spectroscopy, RSC Adv 2 (2012) 6079–6086, https://doi.org/10.1039/C2RA20639A.
[54] K.S. Ghosh, B.K. Sahoo, S. Dasgupta, Spectrophotometric studies on the interaction between (−)-epigallocatechin gallate and lysozyme, Chem. Phys. Lett. 452 (2008) 193–197, https://doi.org/10.1016/j.cplett.2007.12.016.
[55] S. Venkateshrao, P.T. Manoharan, Conformational changes monitored by fluorescence study on reconstituted hemoglobins, Spectrochim. Acta Part A 60 (2004) 2523–2526, https://doi.org/10.1016/j.saa.2003.12.029.
[56] I. Hasni, P. Bourassa, H.A. Tajmir-Riahi, Binding of cationic lipids to milk β-lactoglobulin, J. Phys. Chem. B 115 (2011) 6683–6690, https://doi.org/10.1021/jp200045h.
[57] P.D. Ross, S. Subramanian, Thermodynamics of protein association reactions: forces contributing to stability, Biochemistry 20 (1981) 3096–3102, https://doi.org/10.1021/bi00514a017.
[58] B. Chakraborty, C. Sengupta, U. Pal, S. Basu, Probing the hydrogen bond involving Acridone trapped in a hydrophobic biological nanocavity: integrated spectroscopic and docking analyses, Langmuir 36 (2020) 1241–1251, https://doi.org/10.1021/acs.langmuir.9b03506.
[59] B. Chakraborty, C. Sengupta, U. Pal, Basu S, Acridone in a biological nanocavity: detailed spectroscopic and docking analyses of probing both the tryptophan residues of bovine serum albumin, New J. Chem. 41 (2017) 12520–12534, https://doi.org/10.1039/C7NJ02454A.
[60] B. Chakraborty, P. Mitra, S. Basu, Spectroscopic exploration of drug-protein interaction: a study highlighting the dependence of the magnetic field effect on inter-radical separation distance formed during photoinduced electron transfer, RSC Adv 5 (2015) 61533–61545, https://doi.org/10.1039/C5RA13575C.

[61] B. Chakraborty, S. Basu, Interaction of BSA with proflavin: a spectroscopic approach, J. Lumin. 129 (2009) 34–39, https://doi.org/10.1016/j.jlumin.2008.07.012.
[62] B. Chakraborty, A. Sinha Roy, S. Dasgupta, S. Basu, Magnetic field effect corroborated with docking study to explore photoinduced electron transfer in drug – protein interaction, J. Phys. Chem. A 114 (2010) 13313–13325, https://doi.org/10.1021/jp109604n.
[63] P. Mitra, U. Pal, N.C. Maiti, A. Ghosh, A. Bhunia, S. Basu, Identification of modes of interactions between 9- aminoacridine hydrochloride hydrate and serum proteins by low and high resolution spectroscopy and molecular modelling, RSC Adv 6 (2016) 53454–53468, https://doi.org/10.1039/C6RA04140J.
[64] M. Banerjee, A. Chakrabarti, S. Basu, Interaction between hemoglobin A and merocyanine 540: a spectroscopic investigation supported by docking, Dyes and Pigments 97 (2013) 446e454, https://doi.org/10.1016/j.dyepig.2013.01.005.
[65] M. Banerjee, U. Pal, A. Subudhhi, A. Chakrabarti, S. Basu, Interaction of Merocyanine 540 with serum albumins: photophysical and binding studies, J. Photochem. Photobiol. B 108 (2012) 23–33, https://doi.org/10.1016/j.jphotobiol.2011.12.005.
[66] P. Mitra, M. Banerjee, S. Biswas, S. Basu, Protein interactions of Merocyanine 540: spectroscopic and crystallographic studies with lysozyme as a model protein, J. Photochem. Photobiol. B 121 (2013) 46–56, https://doi.org/10.1016/j.jphotobiol.2013.02.010.
[67] M. Banerjee, S. Maiti, I. Kundu, A. Chakrabarti, S. Basu, Simultaneous occurrence of energy transfer and photoinduced electron transfer in interaction of hen egg white lysozyme with 4-nitroquinoline-1-oxide, Photochem. Photobiol. 86 (2010) 1237–1246, https://doi.org/10.1111/j.1751-1097.2010.00811.x.
[68] S. Banerjee, S. Dutta Choudhury, S. Dasgupta, S. Basu, Photoinduced electron transfer between hen egg white lysozyme and anticancer drug menadione, J. Lumin. 128 (2008) 437–444, https://doi.org/10.1016/j.jlumin.2007.09.020.
[69] B. Koley Seth, A. Ray, S. Biswas, S. Basu, Ni^{II}–Schiff base complex as an enzyme inhibitor of hen egg white lysozyme: a crystallographic and spectroscopic study, Metallomics 6 (2014) 1737–1747, https://doi.org/10.1039/C4MT00096F.
[70] K. Bera, A. Sau, P. Mondal, R. Mukherjee, D. Mookherjee, A. Metya, A.K. Kundu, D. Mandal, B. Satpati, O. Chakrabarti, S. Basu, Metamorphosis of ruthenium-doped carbon dots: in search of the origin of photoluminescence and beyond, Chem. Mater. 28 (2016) 7404–7413, https://doi.org/10.1021/acs.chemmater.6b03068.
[71] A. Sau, K. Bera, P. Mondal, B. Satpati, S. Basu, Distance-dependent electron transfer in chemically engineered carbon dots, J. Phys. Chem. C 120 (2016) 26630–26636, https://doi.org/10.1021/acs.jpcc.6b08146.
[72] M. Kuss-Petermann, O.S. Wenger, Electron transfer rate maxima at large donor-acceptor distances, J. Am. Chem. Soc. 138 (2016) 1349–1356, https://doi.org/10.1021/jacs.5b11953.
[73] A. Sau, K. Bera, U. Pal, A. Maity, P. Mondal, S. Basak, A. Mukherjee, B. Satpati, P. Sen, S. Basu, Design and synthesis of fluorescent carbon-dot polymer and deciphering its electronic structure, J. Phys. Chem. C 122 (2018) 23799–23807, https://doi.org/10.1021/acs.jpcc.8b06322.
[74] A. Sau, S. Sanyal, K. Bera, S. Sen, A.K. Mitra, U. Pal, P.K. Chakraborty, S. Ganguly, B. Satpati, C. Das, S. Basu, DNA damage and apoptosis induction in cancer cells by chemically engineered thiolated riboflavin gold nanoassembly, ACS Appl. Mater. Interfaces 10 (2018) 4582–4589, https://doi.org/10.1021/acsami.7b18837.
[75] V. Maffeis, R. Brisse, V. Labet, B. Jousselme, T. Gustavsson, Femtosecond fluorescence upconversion study of a naphthalimide–bithiophene–triphenylamine push–pull dye in solution, J. Phys. Chem. A 122 (2018) 5533–5544, https://doi.org/10.1021/acs.jpca.8b03177.
[76] S. Cao, H. Li, Y. Liu, M. Zhang, M. Wang, Z. Zhou, J. Chen, S. Zhang, J. Xu, J. R. Knutson, Femtosecond Fluorescence Spectra of NADH in Solution: ultrafast Solvation Dynamics, J. Phys. Chem. B 124 (2020) 771–776, https://doi.org/10.1021/acs.jpcb.9b10656.
[77] S. Satpathy, K. Gavvala, P. Hazra, Fluorescence Up-Conversion Studies of [2,2′-Bipyridyl]-3,3′-diol in Octyl-β-D-glucoside and Other Micellar Aggregates, J. Phys. Chem. A 119 (2015) 12715–12721, https://doi.org/10.1021/acs.jpca.5b09832.
[78] S.K. Pal, L. Zhao, A.H. Zewail, Water at DNA surfaces: ultrafast dynamics in minor groove recognition, Proc. Natl. Acad. Sci. USA 100 (2003) 8113–8118, https://doi.org/10.1073/pnas.1433066100.
[79] P. Kundu, N. Chattopadhyay, Interaction of a bioactive pyrazole derivative with calf thymus DNA: deciphering the mode of binding by multi-spectroscopic and molecular docking investigations, J. Photochem. Photobiol. B 173 (2017) 485–492, https://doi.org/10.1016/j.jphotobiol.2017.06.022.
[80] P. Kundu, S. Ghosh, N. Chattopadhyay, Exploration of the binding interaction of a potential nervous system stimulant with calf-thymus DNA and dissociation of the drug–DNA complex by detergent sequestration, Phys. Chem. Chem. Phys. 17 (2015) 17699–17709, https://doi.org/10.1039/C5CP02101D.
[81] B.K. Paul, N. Guchhait, Exploring the Strength, Mode, Dynamics, and Kinetics of Binding Interaction of a Cationic Biological Photosensitizer with DNA: Implication on Dissociation of the Drug–DNA Complex via Detergent Sequestration, J. Phys. Chem. B 115 (2011) 11938–11949, https://doi.org/10.1021/jp206589e.
[82] S. Gupta, S. Aggarwal, M. Munde, New Insights into the Role of Ligand-Binding Modes in GC-DNA Condensation through Thermodynamic and Spectroscopic Studies, ACS Omega 8 (2023) 4554–4565, https://doi.org/10.1073/pnas.1433066100.
[83] B.K. Paul, N. Ghosh, S. Mukherjee, Binding Interaction of a Prospective Chemotherapeutic Antibacterial Drug with β-Lactoglobulin: results and Challenges, Langmuir 30 (2014) 5921–5929, https://doi.org/10.1021/la501252e.
[84] I. Hasni, P. Bourassa, H.A.T. Riahi, Binding of Cationic Lipids to Milk β-Lactoglobulin, J. Phys. Chem. B 115 (2011) 6683–6690, https://doi.org/10.1021/jp200045h.
[85] B.K. Sahoo, K.S. Ghosh, S. Dasgupta, Investigating the binding of curcumin derivatives to bovine serum albumin, Biophys. Chem. 132 (2008) 81–88, https://doi.org/10.1016/j.bpc.2007.10.007.
[86] V.F. Ximenes, Concomitant binding of two fluorescent probes at site-I of human serum albumin: the protein acting as a scaffold enabling fluorescence resonance energy transfer, J. Photochem. Photobiol. B 234 (2022) 112542, https://doi.org/10.1016/j.jphotobiol.2022.112542.
[87] B.K. Sahoo, K.S. Ghosh, S. Dasgupta, An investigation of the molecular interactions of diacetylcurcumin with ribonuclease A, Protein Pept. Lett. 16 (2009) 1485–1495, https://doi.org/10.2174/092986609789839278.
[88] N. Mataga, H. Chosrowjan, Y. Shibata, F. Tanaka, Ultrafast fluorescence quenching dynamics of flavin chromophores in protein nanospace, J. Phys. Chem. B 102 (1998) 7981–7984, https://doi.org/10.1021/jp982589e.
[89] N. Mataga, H. Chosrowjan, Y. Shibata, F. Tanaka, Y. Nishina, K. Shiga, Dynamics and mechanisms of ultrafast fluorescence quenching reactions of flavin chromophores in protein nanospace, J. Phys. Chem. B 104 (2000) 10667–10677, https://doi.org/10.1021/jp002145y.
[90] D. Zhong, A.H. Zewail, Femtosecond dynamics of a drug-protein complex: daunomycin with Apo riboflavin-binding protein, Proc. Natl. Acad. Sci. USA 98 (2001) 11873–11878, https://doi.org/10.1073/pnas.211440298.
[91] H. Chosrowjan, S. Taniguchi, F. Tanaka, Ultrafast fluorescence upconversion technique and its applications to proteins, FEBS 282 (2015) 3003–3015, https://doi.org/10.1111/febs.13190.
[92] J. Mohanty, A.C. Bhasikuttan, S. Dutta Choudhury, H. Pal, Noncovalent Interaction of 5,10,15,20-Tetrakis(4-N-methylpyridyl)porphyrin with Cucurbit [7]uril: a Supramolecular Architecture, J. Phys. Chem. B 112 (2008) 10782–10785, https://doi.org/10.1021/jp806012x.
[93] S. Dutta Choudhury, J. Mohanty, H.P. Upadhyaya, A.C. Bhasikuttan, H. Pal, Photophysical Studies on the Noncovalent Interaction of Thioflavin T with Cucurbit[n]uril Macrocycles, J. Phys. Chem. B 113 (2009) 1891–1898, https://doi.org/10.1021/jp8103062.
[94] S. Goswami, M. Sarkar, Fluorescence, FTIR and ^{1}H NMR studies of the inclusion complexes of the painkiller lornoxicam with β-, γ-cyclodextrins and their hydroxy propyl derivatives in aqueous solutions at different pHs and in the solid state, New J. Chem. 42 (2018) 15146–15156, https://doi.org/10.1039/C8NJ03093F.
[95] M.K. Goshisht, G.K. Patra, N. Tripathi, Fluorescent Schiff base sensors as a versatile tool for metal ion detection: strategies, mechanistic insights, and applications, Mater. Adv. 3 (2022) 2612–2669, https://doi.org/10.1039/D1MA01175H.
[96] S. Chowdhury, B. Rooj, A. Dutta, U. Mandal, Review on Recent Advances in Metal Ions Sensing Using Different Fluorescent Probes, J. Fluoresc. 28 (2018) 999–1021, https://doi.org/10.1007/s10895-018-2263-y.
[97] P. Razin, V. Manakkadan, V.N.V. Palakkeeshillam, J. Haribabu, C. Echeverria, A. Sreekanth, Simple Fluorescence Sensing Approach for Selective Detection of Fe^{3+} Ions: live-Cell Imaging and Logic Gate Functioning, ACS Omega 37 (2022) 33248–33257, https://doi.org/10.1021/acsomega.2c03716.
[98] K. Halicka, F. Meloni, M. Cook, K. Spychalska, S. Baluta, K. Malecha, M.I. Pilo, J. Cabaj, New Trends in Fluorescent Nanomaterials-Based Bio/Chemical Sensors for Neurohormones Detection-A Review, ACS Omega 7 (2022) 33749–33768, https://doi.org/10.1021/acsomega.2c04134.
[99] A. Sharma, A. Majdinasab, R. Khan, Z. Li, A. Hayat, J.L. Marty, Nanomaterials in fluorescence-based biosensors: defining key roles, Nano-Structures Nano-Objects 27 (2021) 100774, https://doi.org/10.1016/j.nanoso.2021.100774.
[100] O.S. Wolfbeis, An overview of nanoparticles commonly used in fluorescent bioimaging, Chem. Soc. Rev. 44 (2015) 4743–4768, https://doi.org/10.1039/C4CS00392F.

Journal of Photochemistry and Photobiology 21 (2024) 100238

Contents lists available at ScienceDirect

Journal of Photochemistry and Photobiology

journal homepage: www.sciencedirect.com/journal/journal-of-photochemistry-and-photobiology

Advances in exploration of photoinduced electron transfer reactions involving small molecules probed by magnetic field effect

Brotati Chakraborty [a,*], Chaitrali Sengupta [b], Samita Basu [c]

[a] Department of Chemistry, Bejoy Narayan Mahavidyalaya, Itachuna, Hooghly, West Bengal, PIN 712147, India
[b] Department of Chemistry, Indiana University, Bloomington, Indiana 47405, United States
[c] Chemical Sciences Division, Saha Institute of Nuclear Physics, 1/AF Bidhannagar, Kolkata 700064, India

ARTICLE INFO

Keywords:
Photoinduced electron transfer
Laser flash photolysis
Magnetic field effect
Exciplex
Radical ion pairs

ABSTRACT

The review focuses on photoinduced electron transfer (PET) reactions between small molecules and various kinds of chemical and biological systems using a weak external magnetic field (MF). Laser flash photolysis is a competent tool to characterize the intermediates which are formed due to PET. A weak MF, very close to the hyperfine interaction of the system, has the potential to inhibit or enhance reaction channels for singlet and triplet states, which eventually effects the product distribution. At first, well-documented examples of PET involving small molecules like derivatives of phenazines, carbazoles and acridines with classical electron donors in varying homogeneous and heterogeneous media have been discussed and the influence of a weak MF on the dynamics of PET is highlighted. Secondly, utilization of magnetic field effect (MFE) to probe PET in protein pockets has been described. Thirdly, an extensive discussion on PET involving nucleobases, nucleosides, nucleotides and nucleic acids and subsequent MFE on such reactions has been reported. Next, MFE has been exploited to study PET involving nanomaterials. Finally, some very recent studies of MFE have been discussed. Thus, this review is an attempt to unravel various aspects of PET in a large number of systems of varying dimensions by means of several facets of MFE like $B_{1/2}$ parameter, its capability to authenticate the initial spin state and distance dependence property.

Introduction

Photoinduced electron transfer (PET) becomes one of the important avenues for most of the photochemical and photobiological reactions. Literature shows that it plays a pivotal role in determining the fate of many complicated biological phenomena like photosynthesis, respiration, radiation induced DNA damage etc. [1]. However, the occurrence of PET between electron donor and acceptor molecules cannot be assured only from fluorescence quenching studies, where either donor or acceptor is a fluorophore and the other acts as a fluorescence quencher. The identification of the radical ions is the foremost criteria to establish PET and that is possible by means of laser flash photolysis (LFP), a transient absorption technique.

An alternate way to confirm the occurrence of PET is magnetic field effect (MFE) on exciplex luminescence or formation of radical ions [2–5]. Over the past few decades, MFE has been extensively utilized to study primary photochemical processes, viz., the electron transfer (ET), hydrogen atom transfer (HAT) and bond cleavage. However, only a few reports of MFE have been published on the biochemically important processes. PET or H-atom abstraction produces a radical ion pair (RIP) or radical pair (RP) where the conversion between singlet (S) and triplet (T_+, T_0) states takes place by electron-nuclear hyperfine interaction (HFI). If an external magnetic field (MF) has been allied, it removes the degeneracy of the T_+ with S as well as T_0 (as illustrated in Fig. 1) thereby reducing the intersystem crossing (ISC). The overall effect is the increase in the population of the initial spin state.

The RIPs, the primary products of PET, undergo a competitive process of charge recombination to original states or follow charge separated states. In non-polar medium, like cyclohexane, the initial radical ion pair surrounded by solvent molecules is termed as contact ion pair (CIP) or exciplex. On increasing solvent polarity, the formation of solvent separated ion pair (SSIP), where the initially formed radical ions are separated by some intervening solvent molecules inside a common solvent cage, predominates over CIP. The SSIP might be converted to CIP if the intervening solvent molecules are squeezed out and that happens if the dielectric of the medium is reduced. On the other hand, with

* Corresponding author at: Department of Chemistry, Bejoy Narayan Mahavidyalaya, Itachuna, District: Hooghly, West Bengal, PIN 712147, India.
E-mail addresses: brotati@bnmv.ac.in, brotati07@gmail.com (B. Chakraborty).

https://doi.org/10.1016/j.jpap.2024.100238

Available online 30 March 2024

increasing dielectric of the medium SSIP will generate free ions, which are stabilized individually by surrounding solvent molecules [6]. If PET occurs in singlet state the RIPs prefer to undergo back ET with the formation of recombination products rather than free ions. Information about direct ET with the formation of CIPs or SSIPs can be obtained from the fluorescence decay kinetics in the femtosecond time regime, whereas ET as a diffusion-controlled phenomenon can be predicted from bimolecular quenching constant obtained from fluorescence decay kinetics in absence and presence of quencher in the nanosecond time regime. However, if PET occurs in triplet state, the formation of free ions predominates over recombination products. The non-fluorescent radical or radical ion transients can be identified by transient absorption spectroscopy. The formation of geminate RIPs with the identification of its initial spin state can be ascertained from the MFE. The spin correlation of the unpaired electrons of radical ions would be S or T depending on the initial spin state of the excited acceptor or donor, where PET occurs. During diffusion within the solvent cage, the inter-radical distance of SSIP can minimize the exchange interaction energy, which decreases exponentially with the separation distance, and facilitates $S \leftrightarrow T$ interconversion. Here, the extent of ISC depends on the HFI present in the system. The Zeeman splitting of triplet states induced by an external MF of the order of 0.01 – 0.02 T is sufficient to overcome the HFI and reduces the $S \leftrightarrow T$ interconversion. Hence, the singlet yield, i.e., exciplex luminescence or triplet yield, i.e., free ion formation will increase if initial PET occurs in singlet or triplet state respectively. Maximum MFE is obtained when the separation distance between the radical ions of SSIP is sufficient to make exchange interaction energy negligible [7–10]. For homogeneous environment the optimization of the inter-radical separation distance can be achieved simply by controlling dielectric constant or increasing hydrogen bonding ability of the solvent. The change in viscosity or temperature can also serve the purpose. However, the use of organized assemblies, e.g., micelles, reverse micelles and vesicles, which mimic biological cell membrane, is mostly preferred not only for optimization of separation distance just by trapping radical ions in their hydrophobic, hydrophilic or interfacial zones, but also for increasing the lifetimes of the transients from nanosecond to microsecond. Hence, LFP becomes the most convenient tool to study MFE in such heterogeneous environment. In some of the drug-protein or drug-DNA interacting systems, the protein or DNA itself provides the suitable heterogeneous environment. Similarly, nanomaterials comprising of carbon, gold or iron are also able to control the inter-radical distance by encompassing the drug molecules or being linked with them directly or through spacer. The achievement of reaching the targeted distance is further confirmed from one of the features of MFE, i.e., $B_{1/2}$, the field at which half the saturation of MFE is reached. Although $B_{1/2}$ is a measure of HFI present in the system, however, the comparison between its experimental and calculated values highlights the presence of hopping of free electrons from one site to another or existence of super-exchange due to closer proximity of the spin-correlated ions than the optimised one, by increased or reduced experimental values respectively.

In this review, we make an attempt to highlight the above-mentioned salient features of MFE on PET between some of the therapeutically important molecules and fluorophores/proteins/DNA/nanodots in homogeneous and heterogeneous media. It is to be mentioned that most of the systems elaborated in this review are studied in our laboratory.

Experimental

Nanosecond flash photolysis set-up (Applied Photophysics) containing Nd:YAG (Lab series, Model Lab 150, Spectra Physics) laser was utilized for obtaining the transient absorption spectra. The samples were excited at 355 nm (FWHM ≈ 8 ns) laser light and the transients were monitored through absorption of light from a pulsed Xe lamp (250 W). MFE on transient spectra was detected by passing direct current through a pair of electromagnetic coils placed inside the sample chamber. The LFP set-up along with the sample housing is shown in Fig. 2.

Discussion

PET involving small organic molecules in homogeneous and heterogeneous media probed by MFE

Phenazine and its derivatives

Phenazine (PZ) molecules undergo PET both in singlet and triplet states with aromatic amines i.e., *N,N*-diethylaniline (DEA), *N,N*-dimethylaniline (DMA) and 4,4′- bis(dimethylamino)diphenylmethane (DMDPM) [11,12]. The triplet state of PZ is well-studied rather than its singlet state because of its rapid ISC from lowest excited singlet state, ^1B_u ($n\pi^*$) to the corresponding triplet state, ^3B_u ($\pi\pi^*$) [13]. However, Dutta Choudhury and Basu have reported the formation of the fluorescent exciplex through PET between PZ and the aromatic amines in the excited singlet state [14]. A broad hump appears with the maximum (ν_{max}) around 578 nm, 582 nm and 612 nm along with the fluorescence peak of PZ around 452 nm on addition of DMA, DEA and DMDPM respectively in cyclohexane. If the exciplex forms through PET, then its energy ($h\nu_{max} = I - E$ + coulomb attraction energy) should increase with the difference between ionization potential (I) and electron affinity (E) or rather oxidation and reduction potentials of the electron donor and acceptor molecules, which are amines and PZ respectively in this case. The

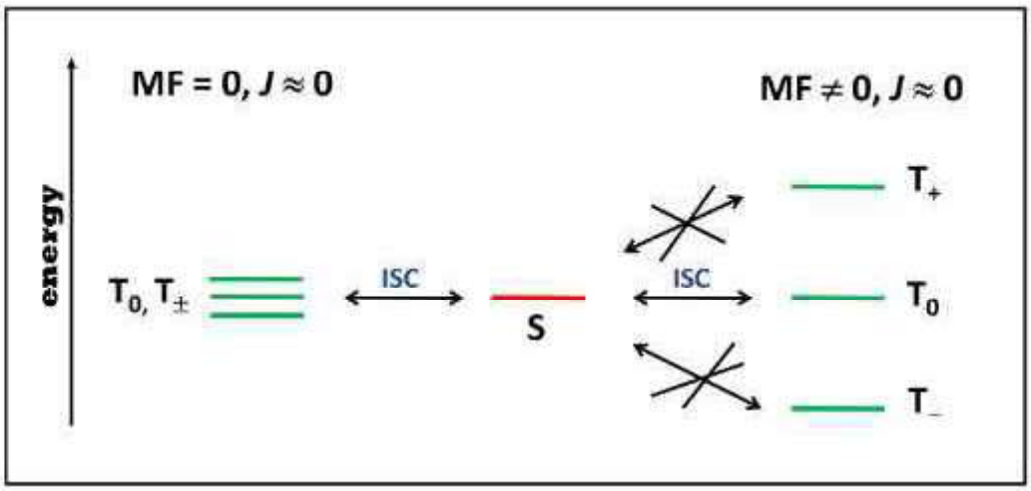

Fig. 1. Energy levels of singlet (S) and triplet (T) states with exchange interaction energy $J \approx 0$ in the absence and presence of MF; an illustration of Zeeman effect.

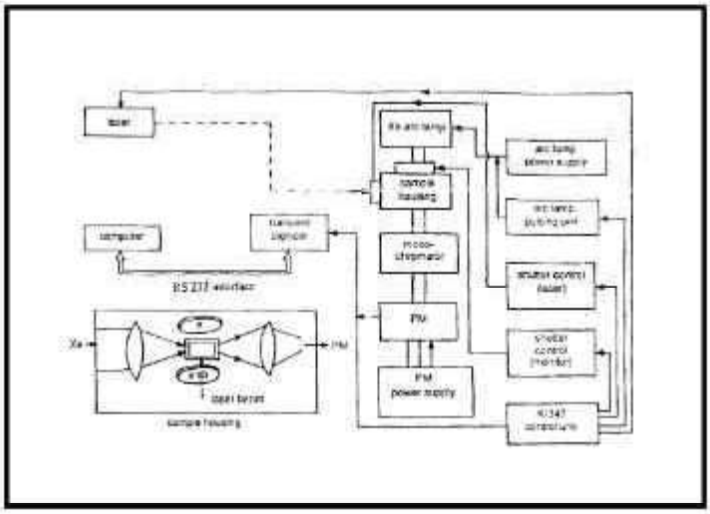

Fig. 2. An illustration of the LFP set-up. Inset shows the sample housing with electromagnets (e). [Reproduced from ref [55] with permission from The Royal Society of Chemistry].

oxidation potentials of DMA and DEA are 0.72 ev and 0.76 eV [15]. Since DMDPM contains two DMA units its oxidation potential should be lower than the single DMA or DEA. Therefore, the observed bathochromic shift of exciplex maximum of PZ-DMA, PZ-DEA and PZ-DMDPM, where PZ is the common electron acceptor, confirms the formation of individual exciplex through PET. LFP experiment in acetonitrile medium identifies the presence of non-fluorescent cationic amine radicals [16]. Interestingly, the transient absorbance of $DMDPM^{+\bullet}$ around 470 nm is much greater than that of $DMA^{+\bullet}$ around 455 nm. Further, the quenching of triplet PZ at 440 nm on addition of DMA and DMDPM shows that both the DMA units of DMDPM participate in the quenching process as a tweezer by caging a single PZ molecule, whereas 1:1 charge transfer occurs with PZ and DMA. Moreover, the absorption maximum of $DMA^{+\bullet}$ is red shifted in moderately polar protic solvent, e.g., butanol and ethanol and the extent of preferential solvation depends on the hydrogen bonding ability of the said solvents. However, cage-like structure of PZ-DMDPM, where charge is distributed among PZ and two DMA units, does not respond to such preferential solvation through hydrogen bonding.

A convenient method of confirming the occurrence of PET is MFE on exciplex luminescence or formation of radical ions [17–25] as discussed in the Introduction. For PZ-amine systems MFE is not observed at all either in cyclohexane or acetonitrile, because both the solvents fail to maintain the optimum separation distance of the radical ions of SSIP which facilitates recombination or free ion formation after spin flipping [16]. Later, Dutta Choudhury and Basu [26] have tried to use different organized assemblies, e.g., micelles, reverse micelles and small unilamellar vesicles (SUVs), where donor and acceptors probably be in different zones, hydrophobic, hydrophilic or interface that qualitatively serves as a linked system to achieve optimum separation distance between the unlinked donor and acceptor [27–31]. Within organized assemblies the formation of radical cations of the amines is detected around 460 - 480 nm using transient absorption technique, i.e., LFP [32–34]. The percentage increase in the yield of $DMA^{+\bullet}$, $DEA^{+\bullet}$ and $DMDPM^{+\bullet}$ in presence of 0.04 T magnetic field is 59, 86 and 12 respectively at 5 μs delay after laser flash when the concentrations of PZ and individual amines are 1×10^{-4} M and 8×10^{-3} M in 10 % SDS micellar medium. The increase of the yield of free ions in presence of MF indicates the occurrence of PET in triplet state in the micellar medium. The biexponential decay rate constants of radical ions in micellar solution can be evaluated from the expression $A(t) = I_f \exp(-k_f t) + I_s \exp(-k_s t)$, where $A(t)$ is the change in absorbance with time and k_f and k_s are the rate constants for the fast and slow components of the decay profiles for caged and escaped radical ions, respectively [35]. In presence of MF, the k_f values decrease, which means the lifetimes of radical ions increase. The effect of application of a weak MF on the transient absorption spectrum of PZ in presence of DMA, DEA, DMDPM and TEA in 10 % SDS micellar medium is depicted in Fig. 3.

If the changes in the absorbance of ions are plotted against applied MF, the $B_{1/2}$ value can be calculated [36–38]. For PZ-DMA, PZ-DEA and PZ-DMDPM the $B_{1/2}$ values are found to be 0.015 T, 0.017 T and 0.29 T respectively. According to the expression obtained from the model of Weller and co-workers based on hyperfine interactions only, the calculated $B_{1/2}$ values for PZ-DMA is 0.005 T. The experimental $B_{1/2}$ value is greater than the calculated one due to shortening of lifetime of radical ions through re-encounter which broadens the energy levels of the spin states [39]. Therefore, excess MF is required to overcome the energy level broadening.

Similar experiments are done using two types of reverse micelles, anionic sodium bis(2-ethylhexyl)sulfosuccinate (AOT) (AOT/heptane) and cationic benzyldimethylhexadecylammonium chloride (BHDC) (water/ BHDC/ benzene). However, the transient absorption peaks of all the radical cations are distinct in AOT, but not in BHDC. The hydrophobic PZ remains in bulk organic solvent or near the tail regions of the micelles, whereas amines are distributed in organic, aqueous and micellar regions. The cationic amines will be stabilized by anionic head groups of AOT, but not by the cationic headgroups of BHDC. As stated earlier, $DMDPM^{+\bullet}$ radical cations are not sensitive towards solvent characteristics due to its large size, here also its transient absorption peaks are prominent both in AOT and BHDC. However, the overall MFE is much smaller in reverse micelles compared to micelles because of the partitioning of the molecules between micellar and organic phases in reverse micelles. The MFE in reverse micelles can be optimised by varying water pool size, $2W_0$ Å, where $W_0 = [H_2O]$ / *[AOT]* [40]. When the value of W_0 is varied from 5, 10, 20 to 40, the maximum MFE is obtained around $W_0 = 10$. This implies that this water pool size provides optimum separation distance between radical ions for spin flipping without losing spin correlation and subsequent free ion formation.

The MFE experiments are carried out in SUVs of *D,L*-dimyristoyl-R-phosphatidylcholine (DMPC) in aqueous solution. Although the transient absorption peaks of cations are distinct, however, the yields are poor owing to lack of caging of the donor and acceptor molecules, since ethanolic solutions of the amines are added to make the SUVs that drives the amines towards aqueous region. However, DMDPM due to its greater hydrophobicity is encapsulated near the hydrophobic zones and shows prominent MFE in spite of its lower concentration compared to DMA and

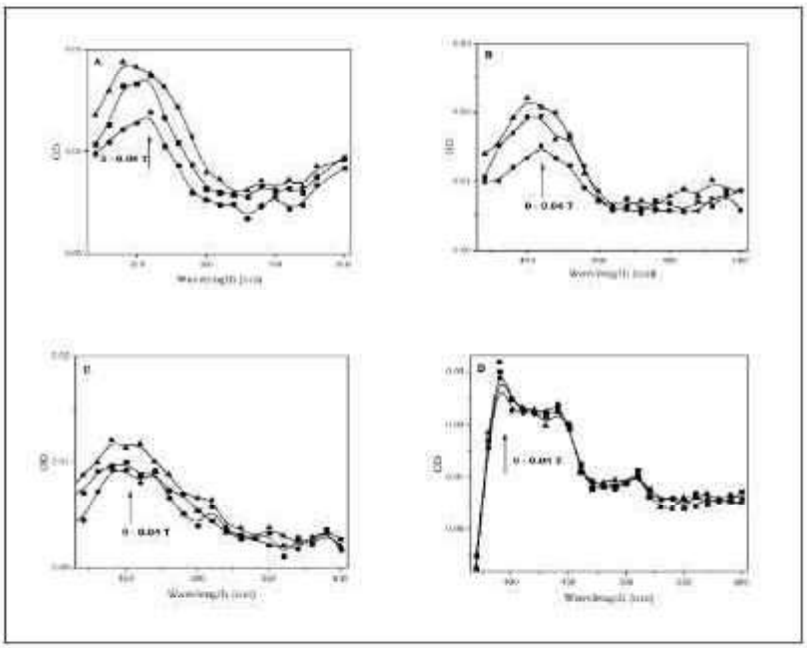

Fig. 3. Effect of an external magnetic field, 0 T (•), 0.02 T (▬), and 0.04 T (▲) on the transient absorption spectra of (A) PZ (1×10^{-4} M)-DMA (8×10^{-3} M), (B) PZ (1×10^{-4} M)-DEA (8×10^{-3} M), (C) PZ (1×10^{-4} M)-DMDPM (8×10^{-3} M), and (D) PZ (1×10^{-4} M)-TEA (8×10^{-3} M) at 0.8 μs after the laser flash in 10 % SDS solution with excitation wavelength 355 nm. [Adapted with permission from Ref. [26] Copyright 2005 American Chemical Society].

DEA.

In general, the organized assemblies are convenient media for gaining aforesaid optimized separation distance between radical ions of SSIPs required for measuring MFE as well as for increasing lifetime of the short-lived transients which are to be measured in the microsecond time scale using this technique. Moreover, organized assemblies, which are structurally quite different from each other, help to identify the micro environment of the donor and acceptor, where they are confined. In SDS micellar media, PZ as well as DMA, DEA and DMDPM remain inside hydrophobic region of micelles, where sufficient space is available for diffusion to make exchange interaction negligible followed by spin-flipping, recombination or free ion formation. In reverse micelles although the molecules are dispersed in organic phase, however the size of the reverse micelles can be modulated by varying W_0 that helps to study distance-dependent MFE. In SUVs, all the molecules remain in the small hydrophobic region, but their number is very few. The importance of structural aspects of different organized assemblies can be indirectly verified by using triethyl amine (TEA), instead of aromatic amines. TEA is quite soluble in water, therefore except SDS micelles, where TEA remain near interface of hydrophobic and aqueous region, other organized assemblies are not suitable to study MFE. In reverse micelles and SUVs, TEA and PZ are confined in totally separate zones, hydrophobic and aqueous, unable to maintain spin-correlation between the geminate radical ions. On the other hand, DMDPM, which is big and well trapped inside hydrophobic regions, exhibit prominent MFE in all these heterogeneous media.

Surprisingly, Dey et al. have later found that one of the derivatives of PZ, dibenzo[a,c]phenazine (DBPZ), shows MFE with DMA, DMDPM and TEA in homogeneous acetonitrile medium in presence of small amount of water, which is really a rare experimental observation [41]. DBPZ in excited state makes charge transfer complex with all the amines showing transient absorption around 460–480 nm for $DMA^{+\bullet}$ and $DMDPM^{+\bullet}$ and around 380 nm for $TEA^{+\bullet}$ [16,42]. Here transient absorption of radical anion, $DBPZ^{\bullet}$ is observed at 560 nm. When the water concentration becomes 0.1 M in acetonitrile, 9.5 %, 15 % and 8.4 % MFE is observed for DBPZ-DMA, DBPZ-DMDPM and DBPZ-TEA systems respectively. With increasing water concentration MFE decreases. Some of the characteristics features of DBPZ are responsible for such unusual observations. DBPZ has planar structure. Moreover, spectroscopic and theoretical studies confirm that it can form hydrogen bond with protic hydrogen bond donating solvents very efficiently [43]. In this case water molecules intervene between radical ions of charge transfer complex and maintain the optimum separation distance between them with proper spin correlation required for MFE through inter-radical hydrogen bond (as shown in Fig. 4). In absence of water molecules, MFE is suppressed due to minimum inter-radical separation and exchange interaction predominates over spin flipping. In presence of excess water, the

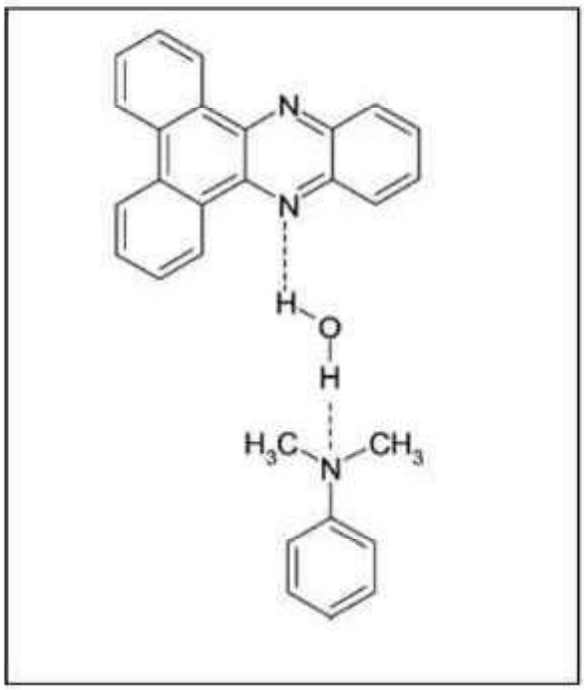

Fig. 4. Water molecules intervene between radical ions of charge transfer complex;the number of water molecules may be more than one. [Adapted with permission from Ref. [41] Copyright 2007 American Chemical Society].

spin correlation is lost in SSIPs and free ions are formed. This phenomenon is well supported by the comparison between experimental and calculated $B_{1/2}$ values for these three systems. The experimental $B_{1/2}$ values for DBPZ-DMA, DBPZ-DMDPM and DBPZ-TEA (shown in Fig. 5) are 0.0081 T, 0.0089 T and 0.0098 T and calculated values are 0.0049 T, 0.0010 T and 0.144 T respectively. Since DMA is smaller in size compared to DMDPM, the re-encounter of $DMA^{+\bullet}$ with neutral DMA which remains in its vicinity shortens its lifetime and broadens the energy levels. Hence, experimental $B_{1/2}$ is greater than the calculated one for DBPZ-DMA. On the other hand, DMDPM due to its large size restricts re-encounter with other approaching DMDPM molecules; therefore, the competition between hyperfine interaction and Zeeman interaction becomes the only operating mechanism which reduces deviation between experimental and calculated $B_{1/2}$ values [44,45]. However, in case of DBPZ-TEA, $TEA^{+\bullet}$ due to its solubility in water is able to approach $DBPZ^{\bullet}$ reducing inter-radical distance that increases exchange interaction. Therefore, inadequate spin flipping makes experimental $B_{1/2}$ lesser than the calculated one. This follows a couple of reports proposed earlier, one by Schulten based on his theoretical studies on sterically rigid intramolecular system and the other by Petrov from his experimental observations of the effect of such exchange narrowing on $B_{1/2}$ [46,47].

Derivatives of carbazole

The formation of exciplex in non-polar medium is very common between aromatic conjugated hydrocarbons, e.g., anthracene (An), pyrene (Py), 9-cyanophenanthrene (CNP), etc., and aromatic amines, DMA and DEA [48–54]. Aich and Basu initiated their studies on identification of exciplex formation through PET by MFE using N-ethyl carbazole (ECZ) and 1,4,5,8,9-pentamethylcarbazole (PMC), which are aromatic conjugated systems containing nitrogen hetero-atom and can act as efficient electron donors in presence of a couple of universal electron acceptors, 1,4-dicyanobenzene (DCB) and 1,2,4,5-tetracyanobenzene (TCNB), on photoexcitation [55–57]. In benzene, the fluorescence peaks of ECZ (350–370 nm) decrease on addition of DCB with bimolecular quenching constant of the order of 10^9 dm^3 mol^{-1} s^{-1} obtained from the Stern-Volmer plot. A broad hump appears with maximum around 450–460 nm with an isoemissive point at 425 nm. Moreover, the maximum of broad band is red-shifted with increasing polarity of the solvent confirming the exciplex formation through PET. Similar behaviour is observed with PMC-DCB, however, here the exciplex is not much prominent like ECZ-DCB. Finally, the exciplex formation through PET with the excited singlet fluorophore (ECZ/PMC) is ascertained by MFE. In presence of MF (0.05 T) the maximum enhancement of exciplex luminescence is obtained about 1.37 % and 0.025 % with $B_{1/2}$ values 0.0032 T and 0.0043 T in THF-DMF mixture with dielectric (ε_{max}) 9.0 and 12.0 for ECZ-DCB and PMC-DCB respectively. Previously for most of the exciplex systems, e.g., Py-DMA, CNP-*trans*-Anethole, etc., maximum MFE was obtained within the range of dielectric constant $14 < \varepsilon_{max} > 18$, where the optimum separation between radical ions of SSIPs is obtained without perturbing the initial singlet correlation and maximum spin flipping followed by recombination occurs to form enhanced CIP/exciplex in presence of MF [19,20,53]. From Lippert-Mataga plot it is observed that with respect to An-DEA, the extent of charge-transfer (δ) is 1.0 and 0.15 for Py-DMA and ECZ-DCB systems respectively [55]. Therefore, with increase in polarity of the solvent, the potential energy barrier between SSIP and CIP reduces much faster facilitating interconversion between SSIP and CIP for ECZ-DCB compared to Py-DMA according to their δ values. Hence, MFE maximizes at lower dielectric for ECZ-DCB than Py-DMA. Similarly, the δ value of PMC-DCB is 0.7 for which ε_{max} is around 12 and that is in between those for ECZ-DCB and Py-DMA [57]. The effect of application of MF on the decay of triplet curves of ECZ in presence of DCB in SDS medium is shown in Fig. 6. Detailed investigation with other derivatives

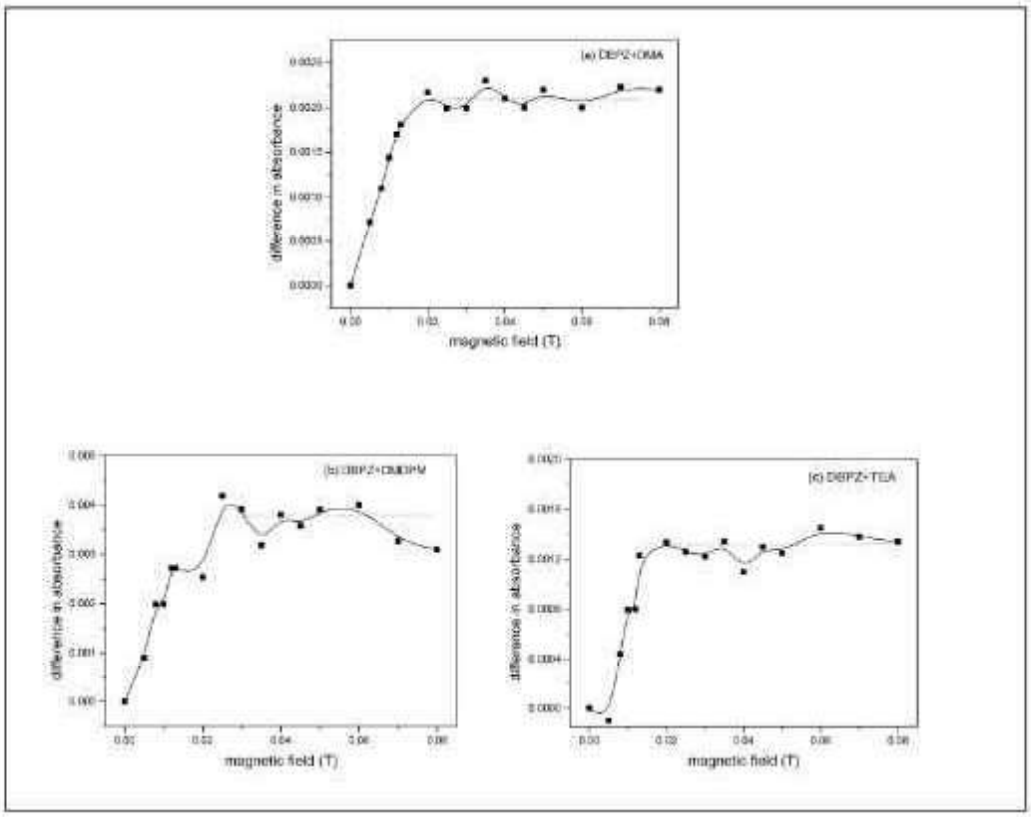

Fig. 5. The difference of absorbance with variation of MF for (a) DBPZ (5×10^{-5} M)-DMA (2.5×10^{-3} M) at 450 nm, (b) DBPZ (5×10^{-5} M)-DMDPM (1.25×10^{-3} M) at 460 nm, and (c) DBPZ (5×10^{-5} M)-TEA (2.5×10^{-3} M) at 420 nm in MeCN/0.1 M H_2O mixture at a delay of 0.6 μs after the laser flash. The dotted lines depict saturation of the MFE. [Adapted with permission from Ref. [41] Copyright 2007 American Chemical Society].

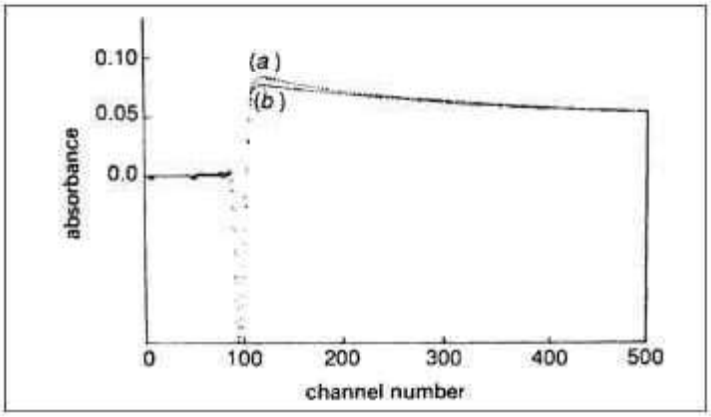

Fig. 6. Decay of triplet curves of ECZ ($1.3 \times$ mol dm^{-3}) and DCB ($2 \times$ mol dm^{-3}) in 10 % SDS micellar medium measured at 430 nm (peak of DCB^{-}) in the (a) absence and (b) presence of a magnetic field of 0.05 T: Each channel represents 8 ns. [Reproduced from ref [55] with permission from The Royal Society of Chemistry].

of carbazole – DCB systems [58,59], Py-DMA in comparison with Py – dimethyl terephthalate [60] as well as CNP – derivatives of methyl indole [61] indicate that ε_{max} depends not only on δ values but also on exciplex energy and steric bulk of donor and acceptor. Later, to study MFE with exciplex systems with one or both the partners fixed on rigid backbone, *N*-vinyl carbazole (VCZ) is grafted on cellulose acetate (CA) using continuous Co-60 γ radiation. The VCZ molecule is attached on CA matrix covalently by opening up its double bond, hence behaves like ECZ [62]. The fluorescence anisotropy measurement supports the restricted rotational motion of grafted VCZ (GVCZ). With GVCZ-DCB system, maximum MFE is obtained at $\varepsilon_{max} = 8.0$ even lower than ECZ-DCB. In GVCZ the carbazole moiety is attached with -O- atom of CA which reduces electron density on the grafted donor moiety and reduces effectively the δ value in GVCZ-DCB complex compared to ECZ-DCB [63].

Instead of DCB when TCNB is used as electron acceptor, exciplex luminescence is not detected at all even in benzene. However, the signature of PET is obtained from the formation of $TCNB^{\bullet}$ radical ions with transient absorption at 430 nm and 465 nm for ECZ-TCNB and PMC-TCNB respectively in 10 % SDS micelles using LFP. Here intersystem crossing rate is very fast due to presence of four -CN groups and it occurs prior to PET with excited singlet fluorophore. The prospect of PET between triplet ECZ or PMC and TCNB is established by MFE where absorbance of $TCNB^{\bullet}$ was enhanced by 0.2 and 0.4 in presence of 0.05 T magnetic field in presence of ECZ and PMC respectively. Moreover, the decay constant of the transient decrease from $2.25 \times 10^4\ s^{-1}$ to $1.25 \times 10^4\ s^{-1}$ and from $1.95 \times 10^4\ s^{-1}$ to $1.31 \times 10^4\ s^{-1}$ for ECZ (5×10^{-5} M) – TCNB (4×10^{-4} M) and PMC (1×10^{-5} M) – TCNB (4×10^{-4} M) in 10 % SDS micellar media respectively. The increase in lifetime of radical ion in presence of MFE confirms the occurrence of PET in triplet state [57].

Acridine and its derivatives

A comprehensive study of the occurrence of PET between acridine (Acr) and its derivatives with small organic molecules in various homogeneous and heterogeneous media (like micelles or reverse micelles) has been carried out by our group. The aforesaid small organic molecules may be classical electron donor like DMA, DMDPM, TEA or acceptor like methylviolgen (MV).

Several previous reports suggest that there exists the following equilibrium [64] in the excited state with varying hydronium ion concentration: $Acr^* + H_3O^{+} \leftrightarrow AcrH^{+}*$. An attempt has been made by Sarangi and co-workers to investigate the behaviour of Acr in AOT/H_2O/n-heptane RMs [65] and it is observed that Acr can detect two different types of water molecules (bound and free) associated with RMs through changes in spectral signatures. The protonated form of Acr chooses to reside near the stern-layer while the deprotonated form has a fondness for the organic phase of RMs. The nature of SV plot obtained for fluorescence quenching of $AcrH^{+}*$ by DMA suggests diffusion controlled bimolecular quenching between the two species. DMA has a tendency to remain in the stern layer of RMs while $AcrH^{+}*$ resides in the stern layer itself, thus facilitating easy access to each other. The advent of characteristic spectral signatures of pertinent radical ion pairs authenticate the occurrence of PET from DMA to $AcrH^{+}*$. Further it is observed that ESPT takes from $^3AcrH^{+}$ to TEA as evident from spectral changes. Unexpectedly, LFP in conjunction with MF helps to prove that latent PET occurs between TEA and $^3AcrH^{+}$ [66]. However, as the pool size of the RMs increases PET is diminished because of increased separation distance between the geminate RPs/RIPs induced by faster water dynamics in larger RMs. In this case the use of MF is highly significant as otherwise the latent PET would have gone unnoticed.

While studying the interaction of proflavin (PF^{+}) with TEA [67], both PET ground state complex formation are detected by Chakraborty and Basu. The nature of the solvent matrix decides the dominant phenomenon in case of PF^{+}-TEA system. In SDS micellar medium, TEA is known to reside in the hydrophilic region near the headgroup and PF^{+} is also present near the negatively charged headgroup owing to its positive charge. Thus, interaction between TEA and PF^{+} in SDS medium is similar to that in homogeneous medium, i.e. they are in close vicinity. However, in CTAB medium PF^{+} is far away from the hydrophilic head group of the micelles due to electrostatic repulsion. Thus, in CTAB medium TEA and PF^{+} are distant from each other. Consequently, in homogeneous and SDS media ground state complex formation dominates over PET which is a distance dependent phenomenon while in CTAB medium, PET is dominant. The occurrence of PET is detected by LFP technique and MFE helps to infer that the PET takes place in the singlet state in SDS medium whereas in CTAB medium the precursors of PET are triplet born. This study shows the importance of solvent matrix in determining the mechanism and spin dynamics of PET reaction. Another study involving the interaction of PF^{+} with DMA and DMDPM highlights the significance of bulk of the electron donor in determining the mechanism and spin dynamics of PET [68]. The occurrence of PET in PF^{+}-DMA and PF^{+}-DMDPM systems are confirmed by detecting $DMA^{\bullet+}$, $DMDPM^{\bullet+}$ and $PF^{\bullet}$ at characteristic wavelengths using LFP technique. DMDPM potentially induces intersystem crossing of proflavin due to its bulk which results in PET in triplet state and on the contrary, in case of PF^{+}-DMA system PET occurs in singlet state as inferred from MFE. In PF^{+}-DMA system, easy access to the close vicinity of the acceptor molecules is possible by the donor molecules through diffusion whereas in PF^{+}-DMDPM system the donor moiety cannot easily reach the acceptor moiety due to its bulk thus maintaining a proper separation distance. Thus, in PF^{+}-DMDPM system, the geminate pairs in SSIPs are stable and

their spins continue to be correlated for a longer time period in comparison to PF^1-DMA system. Subsequently, the transients in case of PF^1-DMA system are obtained significantly around 0.4–0.6 μs while those of PF^1-DMDPM system are found at a longer delay time of 1–1.5 μs. Further, an attempt has been made to decipher PET in PF^1-DMA and PF^1-TEA systems in picosecond-femtosecond time domain using fluorescence upconversion technique [69] by Sengupta et al.. In case of homogeneous alcoholic media, formation of contact ion pair as well as direct ET are the causes of fastest decay components and dielectric constant of the medium governs PET while in heterogeneous micellar media compartmentalization of the donor and acceptor species control the dynamics of PET. Fig. 7 shows femtosecond-resolved fluorescence decay traces of proflavine in presence of TEA in SDS medium.

9-amionoacridine hydrochloride hydrate (9AA) is found to behave both as electron acceptor and electron donor in PET reactions in both homogeneous and heterogeneous media. Initially, the monomer-dimer equilibrium of 9AA in the excited state has been explored by Mitra and co-workers in various solvent matrices using spectroscopic and theoretical techniques [70]. Later, it is found that 9AA can behave as an electron acceptor while reacting with classical electron donor like DMA and TEA in water/acetornitile and CTAB media [71]. In 9AA-DMA system there is simultaneous ESPT and PET while in 9AA-TEA system ground state complexation, ground state proton transfer and PET are prevalent. LFP helps to detect PET as well as ESPT while MFE clearly resolves the two processes since the intermediates of PET are susceptible to MF whereas the products of ESPT are not as they do not involve the formation of spin correlated electron pairs. Interestingly, when 9AA interacts with dimethylviologen (MV^{2+}), which is a popular electron acceptor, PET is found to occur and 9AA plays the role of electron donor [72]. Appearance of transient absorption peaks in the region 390–400 nm and 600–610 nm are the signatures of $MV^{\bullet+}$, which is observed in 9AA-MV^{2+} system, thus confirming the occurrence of PET and MFE has confirmed that PET occurs in the triplet state. The hopping mechanism of ET is established from the disagreement of experimentally observed and calculated values of $B_{1/2}$.

Chakraborty and Basu have detected PET while studying the interaction of DMA, DMDPM, diethylaniline (DEA) and TEA with two other acridine derivatives Acridine Yellow (AY) and Acridone (AD) using LFP in conjunction with MF by detecting the radical ions formed during the ET reaction [73,74]. Although MFE is conventionally observed in organized media like micelles and reverse micelles, as discussed in the aforementioned sections, however in case of AY-amine and AD-amine systems, MFE is obtained in homogeneous medium of ethanol in unlinked donor-acceptor systems. Such an unusual observation of MFE in homogeneous medium has been obtained by Dey et al. previously [41]. In case of AY-amine and AD-amine systems, this observation is attributed to the existence of water molecules as impurities in ethanol medium, which leads to the formation of *in situ* linked donor–acceptor system formation *via* inter-radical ion hydrogen bond. Thus, optimum distance of separation is maintained between the acceptor and donor radical ions so that proper spin-correlation is preserved while the exchange is minimized, thus facilitating significant MFE.

PET involving small organic molecules trapped in protein pockets probed by MFE

ET in proteins has been studied extensively and has drawn the attention of a number of researchers since early days [75–78]. However, small probe molecules when trapped in the nanocavities of proteins can participate in PET with the protein molecules [79,80]. Our group has reported a number of cases of protein-ligand binding [81–92] where BSA, HSA, HEWL and βLG have been used as the protein moiety. The choice of protein molecules is based on the fact that all these model proteins contain one or more tryptophan (Trp) residue which has an intrinsic fluorescence at 350 nm [93] that makes the study of protein-ligand interaction uncomplicated. Apart from having intrinsic fluorescence, Trp residue can also act as a potential electron donor, which has been reported previously [94]. This information compelled us to investigate whether Trp residues in protein molecules can engage itself in PET with small organic molecules trapped in the nano-pockets of proteins. Although steady-state and time-resolved fluorescence techniques have been used to study the protein-ligand binding and to gain an indication regarding the occurrence of PET, we have resorted to LFP technique in conjunction with a weak external MF to authenticate PET and the parental spin-state of the precursors of ET in all these cases.

Interaction of several acridine derivatives (PF^1, AY, AD and 9AA) with BSA, HSA and βLG have been studied. In fact, to ascertain the role of Trp as an electron donor, Seth et al. have studied the interaction of bare Trp with PF^1 [95] in absence of any protein. PET is found to take place from bare Trp to PF^1 in AOT reverse micellar medium. In this case, PET is solely monitored by LFP technique and prominent MFE was observed as optimal separation is maintained in the said solvent matrix between electron donor and acceptor. While studying the interaction of PF^1 and AY with HSA [85], the use of LFP confirmed that occurrence of

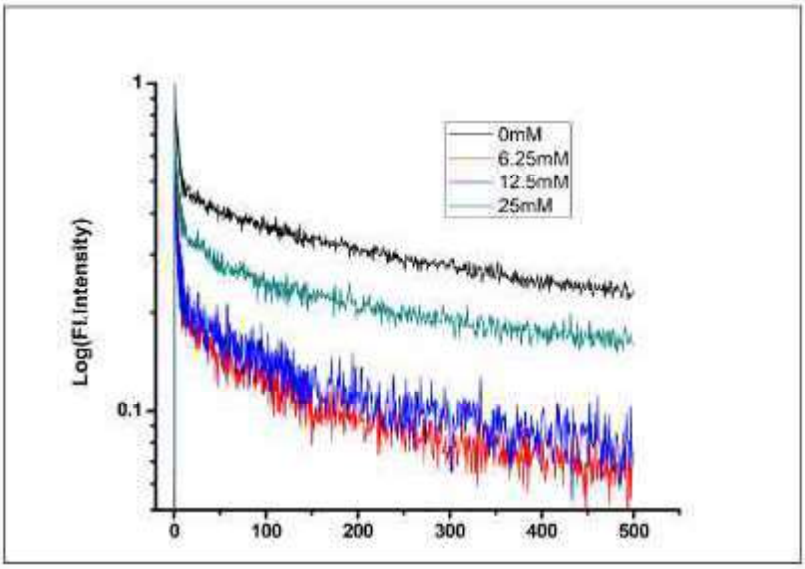

Fig. 7. Femtosecond-resolved fluorescence decay traces of proflavine (0.5 mM) in SDS (100 mM) with varying concentrations of TEA. [Reproduced from ref [69] with permission from The Royal Society of Chemistry].

PET from the sole Trp residue of the protein to PF^{+} as well as AY *via* the appearance of characteristic peaks corresponding to radical ion pairs formed in the due course of PET. Survey of literature suggests that transient absorption peaks of $TrpH^{\bullet+}$ are obtained at 350 nm [91] as well as 560 nm [96] and that of $Trp^{\bullet}$ is at 520 nm [97]. In our earlier works, we have characterized the spectral signatures of the radical ions generated from the two acridine derivatives [67,68,73] to be at 400 nm. Moreover, appreciable MFE is obtained in both AY-HSA and PF^{+}-HSA systems which confirms that the parental spin state of the precursors of PET is triplet. Thus, the integration of all these observations along with fluorescence studies helps to decipher the reaction mechanism as well as to establish the occurrence of PET. Additionally, the stereo-view of the docked conformations illustrates that the separation between the Trp residue in the protein and AY is 1.33 nm while that between Trp and PF^{+} is 1.29 nm, which is responsible for showing MFE as it is known that an optimum spacing of 1.0 to 2.0 nm is required for observing MFE.

Similarly, PET is found to be prevalent in 9AA-HSA and 9AA-BSA systems [86]which has been confirmed by LFP and the fact that the precursors of PET are triplet-born is further proved using a weak MF. The redox potential values of 9AA and Trp moieties are −0.781 V and −1.015 V which validate their roles as electron acceptor and donor respectively.

Interaction of AD has been studied with model proteins BSA, HSA and βLG [81–83] proteins. The uniqueness in the chemical structure of AD is that it contains a keto functional group, which has a potential to denature proteins [98]. Circular dichroism spectroscopy reveals that the secondary structures of all these proteins are appreciably perturbed by AD. A striking difference between the structure of HSA and BSA is that the former contains a single Trp residue (Trp 214) while the latter has two such residues (Trp 212 and Trp 134). Interestingly, Trp 214 of HSA and Trp 212 of BSA are both located within the hydrophobic domain of the respective proteins and they are positioned in a similar environment which is entirely different from the hydrophilic environment of Trp 134 of BSA. PET is monitored using LFP technique in both AD-HSA and AD-BSA systems. Although marked MFE is observed in AD-HSA system but no such effect is detected in AD-BSA system. Such a difference in observation is due to the differential modes of binding of AD with the Trp residues located inside the two different proteins. AD attaches itself

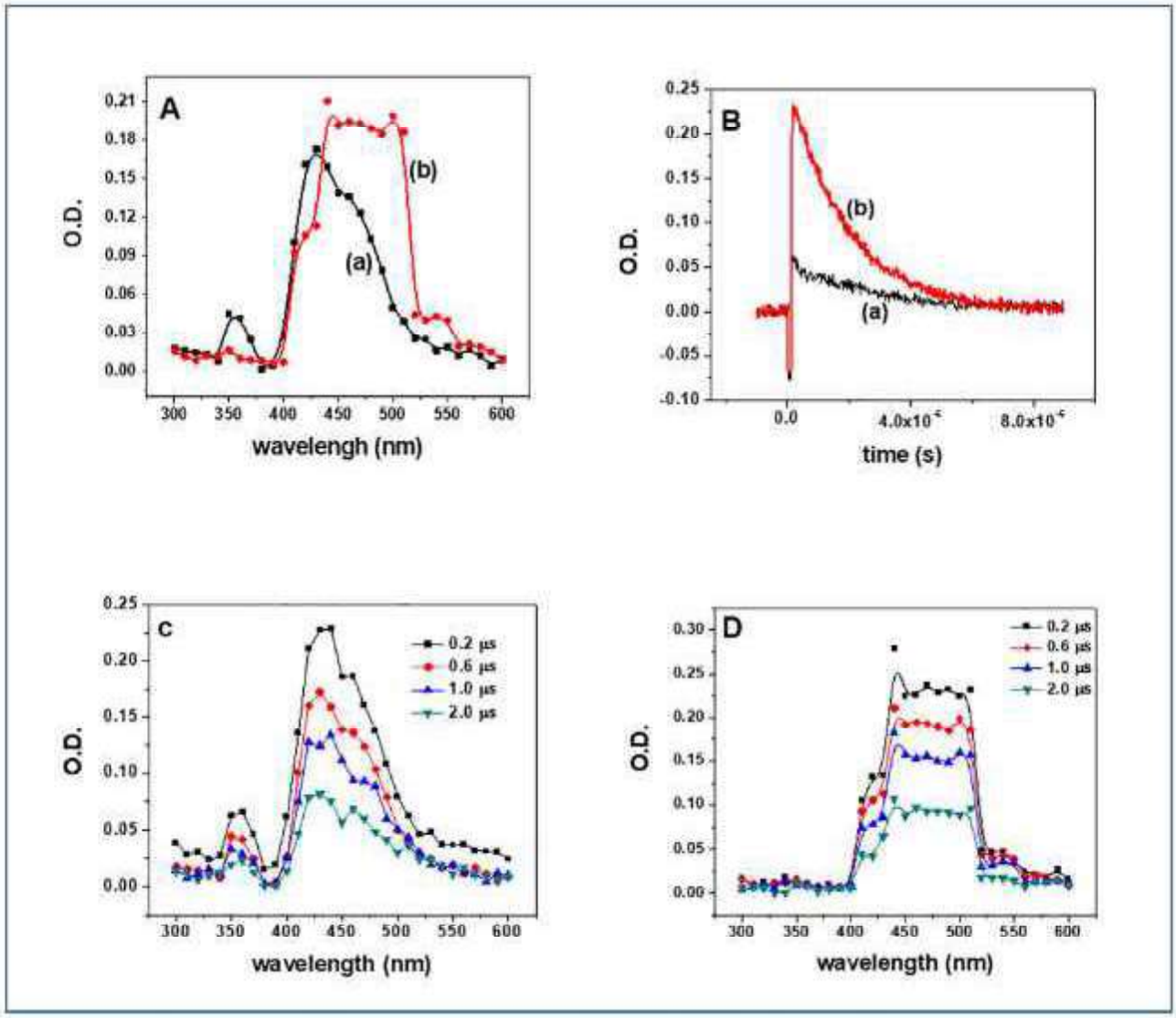

Fig. 8. (A) Transient spectra of (a) 2×10^{-4} (M) AD (■) and (b) 2×10^{-4} (M) AD + 9×10^{-5} (M) HSA (•) in phosphate buffer of pH 7.4 at 0.6 μs after the laser flash at 355 nm. (B) Decay profiles of (a) 2×10^{-4} (M) AD and (b) 2×10^{-4} (M) AD + 9×10^{-5} (M) HSA in phosphate buffer of pH 7.4 at 510 nm after laser flash at 355 nm. (C) Time-resolved transient absorption spectra of 2×10^{-4} (M) AD at 0.2 μs (■), 0.6 μs (•), 1.0 μs (▲) and 2.0 μs (▼) after the laser flash at 355 nm. (D) Time-resolved transient absorption spectra of 2×10^{-4} (M) AD in presence of 9×10^{-5} (M) HSA at 0.2 μs (■), 0.6 μs (•), 1.0 μs (▲) and 2.0 μs (▼) after the laser flash at 355 nm. [Reproduced from Ref. [83] with permission from the Royal Society of Chemistry].

with the sole Trp 214 residue in HSA and is trapped in the cleft of the hydrophobic domain of HSA, strategically maintaining the optimal distance (1.35 nm) from Trp 214 required for observing MFE. On the contrary, in AD-BSA system, AD initially binds to Trp 212 of BSA and later it tries to perturb the rigid structure of the protein to gain access to Trp 134. This proposition is clearly supported by TRANES study. Owing to this dynamic nature of AD within BSA, the optimal distance between the radical ion pairs is not properly retained, which leads to absence of MFE. Fig. 8 shows that application of a weak MF to a solution of 2×10^{-4} (M) AD + 3×10^{-5} (M) HSA results in enhancement in absorbance at 510 and 560 nm which has been attributed to the increased yield of $AD^{\bullet}$ and $TrpH^{\bullet+}$ respectively, thus confirming the occurrence of PET in AD-HSA system. Further, when we have attempted to investigate the interaction of AD with βLG, containing two Trp residues (Trp 19 and Trp 61), it is found that AD exclusively interacts with Trp 19 and hydrogen abstraction supported by hydrogen bonding is prevalent in case of AD-βLG system as evident from LFP study. Moreover, MFE is not observed on the radical pairs which are detected by LFP in this system which is attributed due to the dynamic nature of Trp 19 that undergoes rotation to yield its rotamers and thus geminate pairs is not stable enough to exhibit MFE.

The importance of retention of optimum distance between the radical ions in the geminate cage in MFE involving drug-protein interaction has been highlighted by our group in several other cases. Although PET has been found to take place from HEWL to menadione on photoexcitation, but no MFE is observed possibly because of the close vicinity of the acceptor and donor moieties (0.279 nm) [91], where exchange interaction is not insignificant, thus hindering spin conversion. A similar case of absence of MF effect is also obtained by our group while studying the interaction of 4-nitroquinoline-1-oxide (4NQO) and HEWL as the donor-acceptor separation is about 0.31 nm [90], which inhibits spin conversion enough to show substantial MFE.

Scheme 1 delineates a generalised mechanistic pathway to describe PET between small drug-like molecules and the tryptophan residues in model proteins for drug-protein systems showing MFE.

PET involving small organic molecules and nucleobabses/ nucleosides/ nucleotides/ nucleic acids probed by MFE

DNA molecules are capable of transporting electrons over a long distance and many researchers have extensively studied electron transfer in DNA [99–102]. This has led to the establishment of a number of mechanisms of charge transfer proposed by different researchers. It was proposed that both holes and electrons can migrate through the DNA helix over long distance. Electron hopping mechanisms as well as tunnelling were quite popular among the mechanisms that were attributed to ET in DNA.

In our attempt to study the interaction of small molecules with nucleic acids, initially the interactions of the small molecules with nucleobases, nucleosides and nucleotides have been explored. Sengupta et al. have reported MFE on ET and H-atom abstraction between 2′-deoxyadenosine (ADS) and a quinone drug menadione (MQ), where H atom transfer is competitive with ET [103]. The dependence of the nature of interaction on solvent matrix in MQ-ADS system is detected with the aid of MFE. It is observed that in polar and homogeneous media, ET takes place while H atom transfer is evident only within SDS micelle.

Bose et al. have studied the interaction of MQ and 9,10-anthraquinone (AQ) with the nucleobases (A,T,C,G,U), their nucleosides (dA, dT, dC, dG, dU) and nucleotides (AMP, TMP, CMP, GMP, UMP) in homogeneous organic solvent of acetonitrile (ACN)/ water mixture and heterogeneous SDS micellar medium to explore the competition between ET and hydrogen abstraction (HA) using LFP in conjunction with MF [104–111]. A brief outline of the mode of interaction of the quinones with the bases, nucleotides and nucleosides in different solvent matrix is shown in Table 1 [112]. A few key points of this study are highlighted below:

(i) the nucleotides of all the bases have been found much reluctant to transfer electrons to quinones, which have been attributed

Table 1
An outline of modes of interactions of all the nucleobases, their nucleosides and nucleotides with AQ and MQ in ACN/H_2O and SDS media.

	AQ (ACN/H_2O)	AQ (SDS)	MQ (ACN/H_2O)	MQ (SDS)
A	ET	ET / HA	ET	ET / HA
dA	ET	ET / HA	ET	ET / HA
AMP	HA	HA	HA	HA
T	ET / HA	ET / HA	ET / HA	ET / HA
dT	HA	HA	HA	HA
TMP	HA	HA	HA	HA
C	ET / HA	ET / HA	ET / HA	ET / HA
dC	ET / HA	HA	ET / HA	ET / more HA
CMP	HA	HA	HA	HA
G	HA	ET / HA	HA	HA
dG	ET / HA	ET / HA	ET / HA	ET / HA
GMP	ET / HA	HA	ET / HA	HA
U	ET / some HA	HA	ET / some HA	HA
dU	some HA	HA	some HA	HA
UMP	HA	HA	HA	HA

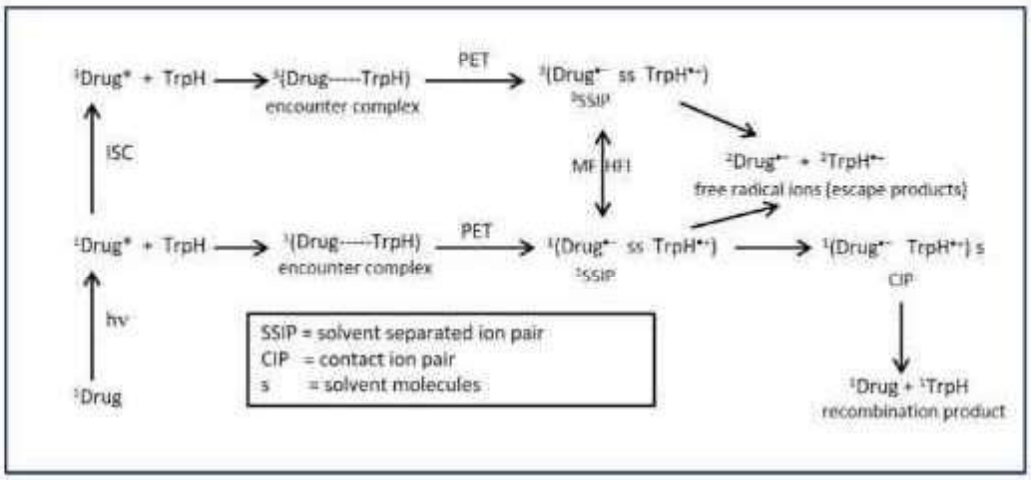

Scheme 1. A generalised reaction pathway to describe PET between small molecules and tryptophan residue of proteins as probed by MFE.

mainly to a semi-circular conformation in homogeneous medium and a rapid spin exchange interaction among the partners of a radical pair in SDS medium

(ii) In case of pyrimidines, the nucleosides have shown a very weak ET than the free bases. It has been attributed to a failure in attaining aromaticity by virtue of keto-enol tautomerism. However, cytidine among the three pyrimidine nucleosides, offers better ET probability which has been attributed to its higher electron density

(iii) In case of purine bases adenine and guanine, the sparing solubility of guanine in the present reaction medium has been found to eclipse ET almost totally from guanine. However, the corresponding nucleosides have undergone both ET and HA. Moreover, a switch over in medium from homogeneous ACN/H_2O to SDS has always favoured HA to be the dominant mode.

Dey et al. have reported ET reactions involving DNA and copper complexes in aqueous medium and heterogeneous reverse micelles [113]. Initially, they have studied the ET reactions taking place between DNA and $[Cu(phen)_2]^{2+}$ [phen = 1,10-phenanthroline] complex on photo-excitation using LFP and MFE. The occurrence of PET from CT-DNA to the photo-excited Cu-complex is rationalized by the formation of a small hump at 370 nm on addition of CT-DNA to the copper-phenanthroline complex. It is well-known that guanine base is the most easily oxidizable component of DNA [114] and thus, the peak at 370 nm may originate from the guanine radical cation. Prominent MFE is found for the triplet born radicals in the interaction of $[Cu(phen)_2]^{2+}$ with DNA even in homogeneous aqueous medium, which is a rare phenomenon (as illustrated in Fig. 9). Although the above-mentioned complex is not covalently linked with DNA, but the copper complex-DNA system behave as a virtually linked system owing to intercalation. The phenomenon of intercalation is facilitated by the electrostatic force of attraction between negatively charged backbone of DNA and positively charged complex as well as hydrophobic interaction between DNA base pairs and phenanthroline ring. It is to be noted that the partial intercalation in the present case helps to maintain the proper distance between the RIPs and consequently leads to observation of substantial MFE.

Among the four amino acids with an aromatic side chain (viz. phenyl alanine, tyrosine, tryptophan, and histidine), phenyl alanine primarily contributes to the stabilization of proteins through hydrophobic interactions, while tryptophan has an electron rich indole ring that has an excellent π electron donating ability. Histidine and tyrosine have efficient metal binding sites. Dey et al. have extended their studies with ternary metal complexes [115] comprising aromatic amino acids, e.g., tyrosine and tryptophan, and a second ligand that contains an aromatic ring, such as 2,2′-bipyridyl or 1,10- phenanthroline, [Cu(phen)(Htyr)] ClO_4 and [Cu(phen)(Htrp)]ClO_4 (Htyr: l- tyrosinato and Htrp: l-tryptophanato) to understand the ET reactions with calf thymus DNA (CT-DNA). It has been observed that in both complexes on photoexcitation intramolecular ET occurred from amino acids to phen. However, in the presence of CT-DNA intermolecular ET occurs between DNA and complexes. Quenching of DNA bound ethidium bromide fluorescence by complexes suggests that the complexes can displace ethidium bromide from DNA backbone. The partial intercalation of the complexes within DNA helps in maintaining the proper inter-radical distance in the radical ion pairs generated through PET, so that spin correlation exists between them and MFE could be observed. When organized assemblies, viz., reverse micelles are used instead of water, as reaction medium, MFE is observed, however it is not very much prominent due to large distance of separation between the radicals of the geminate ion pairs.

Schiff base having N/O/S donor atoms is a popular biologically active ligand owing to its good site-specific and highly sensitive DNA structural probing and cleaving properties. Seth et al. have studied the interaction of pyridine- and pyrrole- substituted Cu-Schiff base complexes having N_4 donor set with CT-DNA in triplet state [116]. The two pyridine-substituted Cu-complexes have very weak characteristic transient absorption peaks, which are not much affected in presence of CT-DNA. On the other hand, the pyrrole-substituted Cu-complexes (A and B as shown in Fig. 10) exhibit prominent characteristic transient absorption peaks and addition of CT-DNA leads to alterations in the spectra along with the formation of isosbestic points that implies the existence of some interactions between the Cu-complex and CT-DNA in the triplet state. In fact, isosbestic points indicate that the presence of equilibrium between the free Cu-complexes and CT-DNA bound Cu-complexes. All the DNA bases are known to be efficient electron donors and guanine is known to be the most potent electron donor among the four bases. The peaks are formed at 370, 420, and 480–500 nm for the formation of DNA radical cations of guanine, adenine, thymine and cytosine respectively. All these peaks are detected when CT-DNA are added to a solution of complex B implying the contribution of all the fours DNA bases as electron donors to the photoexcited copper complex. This is in contrast to our previous report [113] where only guanine acts as the electron donor. However, contribution of guanine as electron donor is more while CT-DNA interacts with complex A. Moreover, the transient absorption spectra of the complexes A and B in

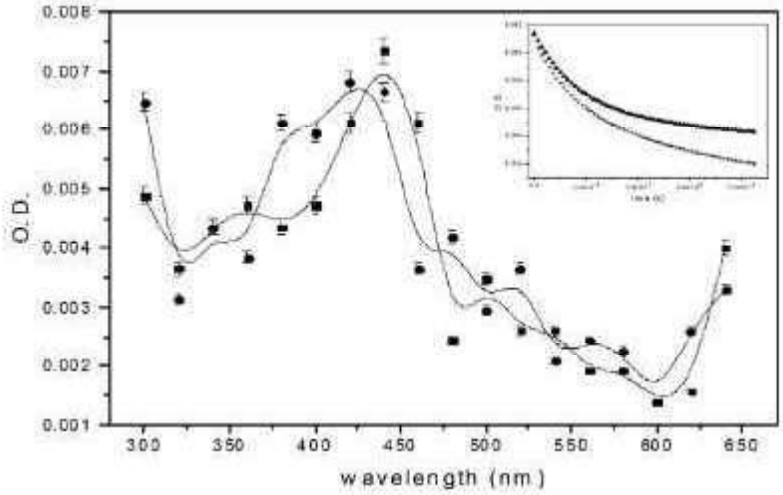

Fig. 9. Transient absorption spectra of the copper complex (40 μM) – DNA (120 μM) in buffer in absence (■) and presence (•) of 0.08 T MF at a delay of 0.6 μs after the laser flash. Inset shows the decay profile of the transient at 380 nm in absence (+) and in presence (▲) of MF. [Adapted with permission from Ref. [113] Copyright 2008 American Chemical Society].

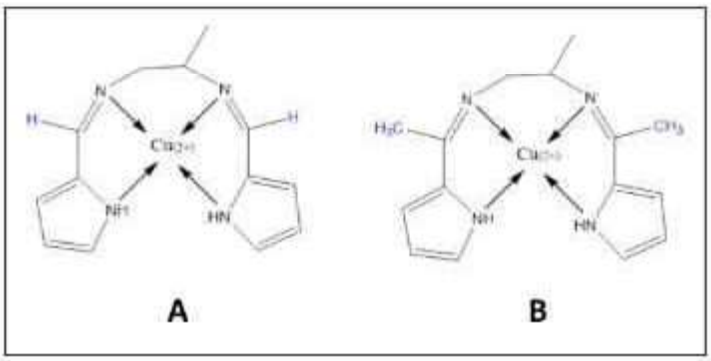

Fig. 10. Structures of complex A and complex B.

presence of CT-DNA show appreciable increase in absorbance at 340, 370 and 550 nm in presence of a weak external MF, implying that PET takes place between the complexes and CT-DNA in the triplet state. Increase in absorbance at 340 and 370 nm can be attributed to the increase in yield of the DNA radical cation while that at 550 nm is due to the increase in yield of Schiff base radical anion in presence of MF. It is to be noted that the extent of PET and MFE is more pronounced in case of system containing complex B in comparison to complex A, which may be due to the structural difference between the two complexes that leads to a variation in the extent of proximity of the complex towards CT-DNA. Methyl substituted complex B is dimensionally larger compared to complex A, which favours intercalation of complex A in the DNA. Further, it is found that complex A has a higher DNA cleavage potential that complex B. Thus, owing to smaller dimension complex A effectively intercalates and comes closer to CT-DNA and also increases the randomness of the system by DNA cleavage. This close vicinity of the complex A and CT-DNA reduces the donor-acceptor distance leading to low MFE. On the contrary, the bulkier structure of complex B creates a steric hindrance and inhibits closer approach of complex B and CT-DNA, which helps in maintaining the optimum donor-acceptor distance between the RIPs, thus exhibiting appreciable MFE.

On comparing the $B_{1/2}$ values of the two copper complexes-DNA systems, it is found that system containing dimensionally smaller complex A has a higher $B_{1/2}$ value compared to that containing complex B. The 'through-space' hole hopping is similar for intrastrand and interstrand DNA bases. However, the superexchange interaction is more dominant for intrastrand base pairs, which decreases the rate of hole hopping on increasing the size of the nucleobases bridge [117]. As mentioned earlier, complex A has a higher DNA cleavage activity compared to complex B. Therefore, in complex B-DNA system, lesser cleavage of DNA strands results in prevalence of both hole-hopping as well as super-exchange, while in complex A-DNA system, hole-hopping is preferred. Lowering in $B_{1/2}$ value in case of complex B-DNA system compared to complex A-DNA system is due to the negative effect induced by superexchange which lowers the effective HFI present in the system. In fact, Schulten suggested that sterically fixed intramolecular system may exhibit the lowering of effective HFI even by 50 % owing to the presence of superexchange compared to intermolecular one [46].

PET involving small organic molecules and nanomaterials probed by MFE

There are several reports on the direct intersections of therapeutically important molecules with different kinds of nano particles. Sengupta et al. have investigated ET between small (3–5 nm) gold nanoparticles (AuNPs) with two acridine derivatives AY and 9AA [118]. It has been observed that 9AA undergoes better extent of ET due to proper orientation to the attachment of AuNPs in both nanosecond and picosecond time regime. Moreover, presence of electron donating methyl ($-CH_3$) and amine ($-NH_2$) functional groups in AY makes it bulky and less feasible to take part in ET reaction with AuNPs.

An interesting observation regarding MFE on the interaction between sanguinarine (Sgr), another important anticancer drug [119], with iron nanoparticle (FeNP) (Fe_3O_4) in acetonitrile medium has reported by Das Chakraborty et al. [120]. A ground state complex is formed between Sgr and FeNP where the quaternary ammonium group of Sgr binds with the free acid group on the surface of FeNP capped with trisodium citrate. LFP identifies the triplet transients of Sgr which rapidly increase in presence of an external MF of the order of 0.08 T. Usually, singlet to triplet electronic state transitions are facilitated by spin-orbit (L-S) coupling which is influenced by an external MF of the order of few tesla [121]. However, here it happens only in presence of very small MF only due to the presence of FeNP. FeNP is a ferrimagnetic material that in presence of MF becomes superparamagnetic where a strong internal magnetization is developed through exchange coupling of electrons and hence singlet to triplet transition of Sgr is increased radically. However, in absence of MF the supermagnetic FeNP cannot hold its magnetization capability. Therefore, such materials are useful for switching ON—OFF of MFE. It is essential to point out that in the presence of diamagnetic AuNP, instead of FeNP, the singlet-triplet transition of Sgr is not affected at all in the presence of low MF. On the other hand, in aqueous medium the intramolecular hydrogen abstraction between the citrate ion and Sgr produces singlet geminate radical pair [(Sgr-H)••(OOC—Cyt)] on the same FeNPs surface which is further stabilized by surrounding water molecules through hydrogen bonding. Obviously, the yield of singlet spin-correlated radical pair increases in presence of MF because of suppression of intersystem crossing. Hence, the absorbance and lifetime of H-abstracted Sgr, $(Sgr\text{-}H)^{\bullet}$ at 410 nm [122] decreases as depicted by flash photolysis decay profiles.

The applications of carbon dots (CD) are popular in different areas of biotechnology as well as in production of light emitting devices [123]. However, their highly complex structure makes them an excitation dependent fluorophore, hinders the progression of the investigation of their physical, chemical, and structural properties using spectroscopy. Sau et al. [124] have successfully prepared an excitation-independent fluorophore, i.e., Ru doped ethylene diamine capped carbon nanodots (Ru:CNDEDAs), which contains free electrons on their surface. To study their competence in PET, MQ is chemically engineered with Ru:CNDEDAs directly and through homocystein thiolactone (HCTL) (Ru:CNDEDAHCTLs) in physiological condition. Both Ru:CNDEDAs and Ru:CNDEDAHCTLs undergoes PET in presence of MQ, however efficiency of ET is greater with Ru:CNDEDAHCTLs rather than Ru:CNDEDAs as found from their fluorescence quenching studies using steady-state and time-resolved techniques. Moreover, formation of free radical ions, [Ru:CNDEDAs$^{\bullet+}$]/ [Ru:CNDEDAHCTLs$^{\bullet+}$] and [MQ$^{\bullet-}$] is more in the HCTL linked system as detected by LFP. The distance between electron donor and acceptor moieties is assessed using energy minimised conformation. It is found that inter-radical ion distance is 0.65 nm and 1.32 nm even when MQ is linked with Ru:CNDEDAs and Ru:CNDEDAHCTLs respectively. The former does not favour an efficient ET because of

predominance of back ET; however, the latter favours ET due to the greater inter-radical ion distance more than 1.0 nm [125]. The results also tally well with the observed MFE. In Ru:CNDEDAHCTLs – MQ system the inter-radical ion separation distance is enough to minimize J and generate maximum spin flipping. In presence of MF (~0.08T) the ion formation increases that also supports the occurrence of PET in triplet states of the corresponding CDs. Here, the experimental $B_{1/2}$ is much higher than the calculated one might be due to electron hopping through conjugated π-electron cloud associated with nitrogen atoms on the Ru:CNDEDAHCTLs surface. The effect of MF on the transient absorption spectra of Ru:CNDEDAHCTLs in the presence of MQ is elucidated in Fig. 11. Similar observations are obtained with a fluorescent polymer-like material (pCD) where ruthenium doped carbon dots (CDs) act as building blocks [126]. The experimental results are further well supported by molecular and computational modelling. The high energy donor states and low energy aggregated states are formed due to the overlap of molecular orbitals throughout the chemically switchable π-network of CDs on polymerization.

It has been already mentioned in the previous section that MQ preferably undergoes ET and HAT with nucleobase adenine (ADN) or nucleoside adenosine in polar acetonitrile and SDS micellar media respectively. Recently, Behera et al. [127] have reported that even when both MQ and ADN are confined within micellar medium, they can undergo ET instead of hydrogen abstraction in presence of FeNP. However, the incorporation of AuNP instead of FeNP within micelles enhances hydrogen abstraction. LFP associated with MF (0.08 T) shows the enhancement of transient absorption and lifetime of MQ $^{\bullet}$ around 380 nm as well as 520 nm and MQH$^{\bullet}$ around 420 nm in presence of FeNP and AuNP supporting PET and hydrogen abstraction between MQ and ADN respectively within 5 % SDS micellar media. Table 2 depicts the change in lifetime of radicals at 380, 420 and 520 nm in absence and presence of MF. The effect of MF on the transient absorption spectra of MQ-ADN, ^{Au}MQ-ADN and ^{Fe}MQ-ADN is shown in Fig. 12. It is hypothesized that the contradictory behaviour of FeNP and AuNP arises due to the preferential absorption of MQ and ADN towards the respective nanoparticles. MQ interacts preferentially with FeNP through oxygen (sp^2 O) atom, therefore ADN donates its lone pair of electrons on -NH_2 spontaneously to MQ. On the contrary, instead of MQ, ADN prefers to be associated with AuNP through its -NH_2 (sp^3 N-atom) group [128] which reduces its ability to donate electron enhancing hydrogen abstraction ability of MQ.

The incorporation of CD, which is anionic in nature, can also modify the reaction pathways. Although the hydrogen abstraction ability of MQ within anionic SDS is not hampered in presence of negatively charged CDs, however, Behera et al. [129] have found out from their LFP and MFE studies that when cationic CTAB micellar medium is used instead of SDS, the formation of MQ$^{\bullet-}$ is enhanced in presence of CDs. As the polar head groups on the surface of CTAB micelles are positively charged, they can attract the negatively charged CDs which leads to boosting of ET between MQ and CDs. The ET product radical MQ$^{\bullet-}$ shows a characteristic signature peak at 360 nm along with a small hump around 470–520 nm. On the other hand, HAT results in formation of a semiquinone MQH$^{\bullet}$ radical, which has absorption at ~360 nm and a small hump at ~410 nm. The effect of MF on the transient absorption spectra of CD in presence of MQ in water, SDS and CTAB are depicted in Fig. 13. Although both HAT and ET between CD amd MQ are plausible for CTAB and SDS micelles in absence of MF, a more preferred ET is observed for CTAB, while an enhancement of HAT in SDS is noted in the presence of MF (Scheme 2).

Some recent examples of MFE on the precursors of PET

Till now, we have been focussing on the work carried out in our laboratory over the last two and a half decades. However, many other research groups have been engaged in studying MFE since a long time. In this section we will discuss some recent examples of MFE studied by other researchers.

Recently, Wakasa et al. have reported low field effect (LFE) on PET reaction between benzophenone (BP) and 1,4-diazabicyclo[2.2.2] octane (DABCO) in an ionic liquid of *N,N,N*-trimethyl-*N*-propylammonium bis(trifluoromethane-sulfonyl)amide (TMPA TFSA). The co-effcient of viscosity of the ionic liquid is varied from 39 cP to 195 cP along with variation in temperature. At a low MF (~2 mT) comparable with the hyperfine coupling in DABCO cation, so-called LFEs, whose effect is opposite to the MFE caused by the hyperfine coupling mechanism, is observed on the yield of the benzophenone anion radical. The magnitude of LFE is found to increase linearly with increase in the lifetime of the radical pair while the MF for LFE maximum is unaltered. However, simple degenerate model is not sufficient to explain this observation [130].

Yamada and co-workers have investigated the photoinduced intramolecular ET reaction and subsequent MFE in ligand complex (RuP–C_{60}) as a semi-rigid linked system in two solvents, viz., toluene and o-dichlorobenzene [131]. The transient absorption spectra indicates that the intramolecular ET reaction is observed only in o-dichlorobenzene. The decay rate constants (k_d) for the biradical is reduced sharply at lower MF ($\leq$ 0.06 T) and rapidly recovered at 0.08 T. The k_d value is observed to decrease gradually above 0.2 T. The MFEs strongly imply the formation of the singlet-born biradical for RuP–C_{60}. The dip in the MFE at 0.06 T has been attributed to the S–T level crossing mechanism. The MFEs above 0.2 T can be elucidated by a spin–spin relaxation mechanism due to the anisotropic Zeeman interaction being related to the exchange interaction.

Kattnig and co-workers have been working with MFE on exciplex-forming systems since a long time [132]. In fact, they have investigated the outcome of preferential solvation in microheterogeneous solvent mixtures on the radical pair dynamics of the system 9, 10-dimethylanthracene (fluorophore)/DMA by using time-resolved

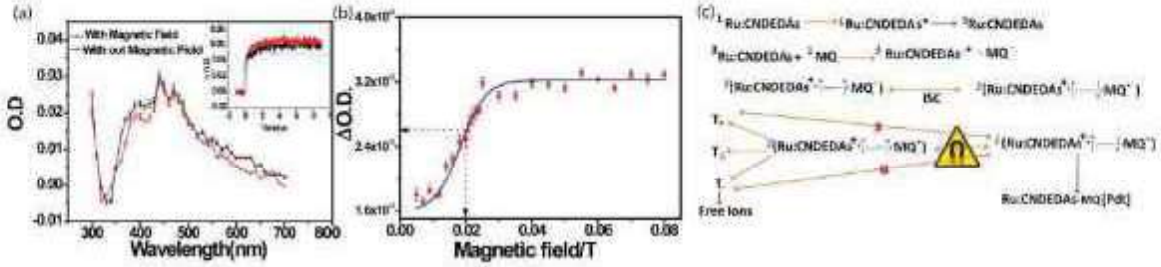

Fig. 11. Transient absorption spectra of (a) **Ru:CNDEDAHCTLs** in the presence of **MQ** in absence (red line) and in presence (black line) of MF (Inset: Growth profile of the transient of **Ru:CNDEDAHCTLs** at 600 nm in absence (black line) and in presence (red line) of MF (0.08 T) in PBS buffer.) (b) The difference of absorbance with variation of MF for **Ru:CQDEDAHCTLs -MQ** (1.5 mM) system monitored at 400 nm. (c) Schematic representation of **Ru:CNDEDAHCTLs**$^{+}$ and **MQ**$^{-}$ radical generation (black vertical arrows represent the spin correlation between the geminate free electrons, either triplet (*3*) or singlet (*1*). [Adapted with permission from Ref. [124] Copyright 2016 American Chemical Society].

Table 2
The lifetime of transient species (τ in μs) obtained at their respective wavelengths has been calculated in the presence and absence of a 0.08T MF. The parenthesis represents the amplitude of the transients obtained from the fitting (equation-2). The experimental error in the above measurements is less than 10 %. [Reprinted with permission from Ref. [127]. Copyright 2020 Springer Nature Limited].

		MQ		MQ-ADN		^{Ac}MQ-ADN		^{Fc}MQ-ADN	
Magnetic field (T)		0	0.08	0	0.08	0	0.08	0	0.08
380 nm	τ_1	1.12	1.61 (70)	1.75 (38)	2.07 (61)	2.11 (74)	2.46 (71)	1.42 (35)	2.14 (47)
	τ_2	–	0.40 (30)	0.20 (62)	0.07 (39)	0.40 (26)	0.40 (29)	0.38 (65)	0.32 (53)
	$<\tau>$	1.12	1.68	1.50	2.02	2.00	2.33	1.07	1.87
420 nm	τ_1	1.50	2.06 (72)	2.20 (55)	2.56 (76)	3.10 (79)	5.75 (20)	3.09	2.15 (51)
	τ_2	–	0.54 (28)	0.08 (45)	0.2 (24)	0.20 (21)	0.15 (80)	–	1.79 (49)
	$<\tau>$	1.50	1.91	2.13	2.50	3.05	5.22	3.09	1.99
520 nm	τ_1	1.33	2.56 (28)	1.83 (16)	3.14 (20)	–	–	2.77 (35)	2.83 (94)
	τ_2	–	0.56 (72)	0.30 (82)	0.70 (80)	–	–	1.43 (65)	1.08 (06)
	$<\tau>$	1.33	1.63	1.17	1.98	–	–	2.11	2.78

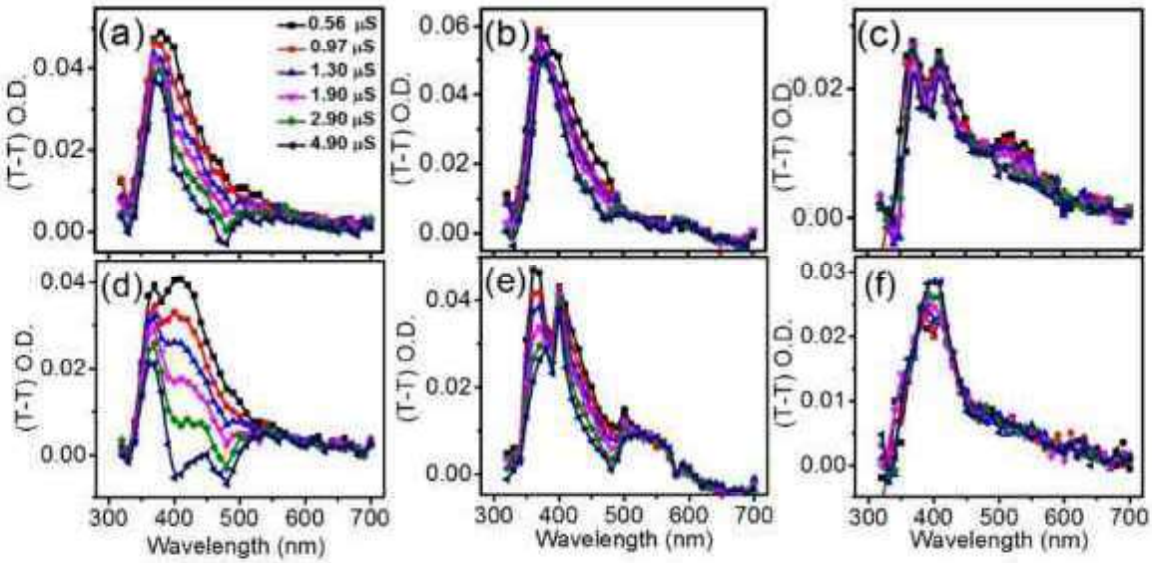

Fig. 12. Transient absorption spectra of (a) MQ-ADN, (b) ^{Ac}MQ-ADN and, (c) ^{Fc}MQ-ADN respectively generated between the pump and probe pulse delay from 0.5-4.9 μs time delay after the laser flash in the absence of MF and their respective spectrum in the presence of MF is shown in (d), (e), (f). [Reprinted with permission from Ref. [127]. Copyright 2020 Springer Nature Limited].

MFE (TR-MFE) measurements, wherein the exciplex emission is noted in the absence and the presence of an external MF using time-correlated single photon counting [133]. It is found that in microheterogeneous environments, the MFE of the exciplex emission occurs on a faster time scale compared to that in iso-dielectric homogeneous solvents. TR-MFE studies show that the quenching reaction directly yielding the radical ion pair is preferred in microheterogeneous environments. The MFE pertinent to this study is a consequence of the radical pair mechanism. Of late they have synthesized a bridged intramolecular exciplex system where the radicals cannot separate freely and interesting MFE is expected to be observed [9]. Such a new class of exciplex-forming donor–acceptor systems is 9-methylanthracene (MAnt)–$(CH_2)_n$–O–CH_2–CH_2–DMA, which feature chain-linked MAnt and DMA, for $n = 6$, 8, 10, and 16. The chain length and solvent polarity dependence of the MFEs is explored in homogenous binary solvent mixtures of propyl acetate and butyronitrile with varying dielectric constants in the range from 6 to 24.7 (at 295 K; $\eta = 0.58$ cP). MFEs are explained in terms of the hyperfine and $S/T_{\pm}$ level crossing mechanisms, in which the MF affects the S–T conversion within the RIP by altering the energy gap of singlet and triplet states. It is observed that the MFEs increase with increasing chain length. MFE is initially found to increase with increasing polarity of the solvent, reaches a maximum at $\varepsilon_s \approx 25$, and finally decreases for larger solvent polarity.

MFE on flavin-based radical pair system is of great interest to a number of researchers, especially because cryptochrome, a blue-light photoreceptor protein, plays a pivotal role in animal magnetoreception [134–136]. Cryptochromes (Crys) are thought to govern avian magnetoreception., which help the migratory birds to detect the direction of Earth's magnetic field for the purpose of navigation. Crys contain a non-covalently bound flavin adenine dinucleotide (FAD) cofactor and a Trp triad which functions as an ET chain. Upon blue-light activation, PET between the FAD cofactor and Trp residues leads to the formation of a spin-correlated radical pair, which is sensitive to external MF. Timmel and co-workers have developed a novel detection scheme for investigating MFEs in flavin-based systems [137]. This technique enables detection of MFE for samples containing flavins and cryptochromes in nanomolar range. This method involves monitoring MF-dependent changes in the prompt fluorescence of a continuously photoexcited system, which is shown to reflect the magnetosensitivity of the radical pair and Timmel et al. have applied this detection method to measure MFE in cryptochrome. Hore and co-workers have designed a series of model proteins called maquettes, which contain a single Trp residue at different distances from a covalently bound flavin [138,139]. It is found that these maquettes exhibit a strong MFE. This work has been done with the intention to understand the biophysical properties required of a protein-based magnetoreceptor. The same group of researchers has observed MFE on PET reactions in purified cryptochrome from *Drosophila melanogaster*. An amalgamation of transient absorption and

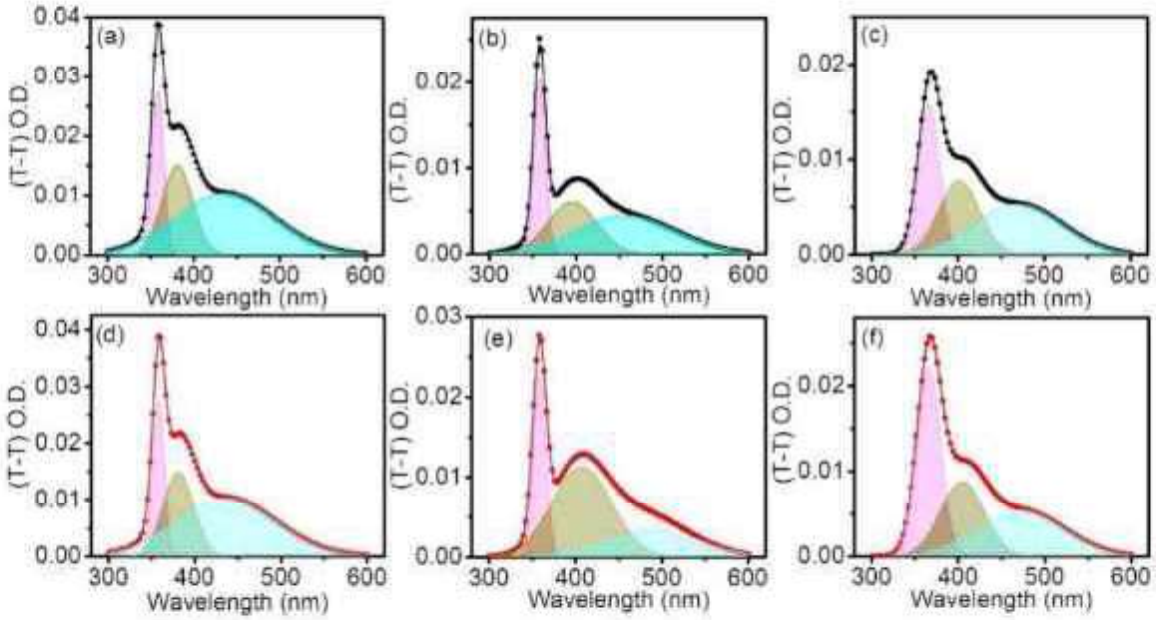

Fig. 13. The de-convolution graph of the TA spectra of CDs in the presence of MQ (1 mM) in (a, d) water, (b, e) SDS, and (c, f) CTAB respectively without (upper panel-a, b, c) and with MF (lower panel- d, e, f). The convoluted spectrum of three independent Gaussian functions is represented in cyan, magenta, and dark yellow colors. [Adapted with permission from Ref. [129] Copyright 2021 American Chemical Society].

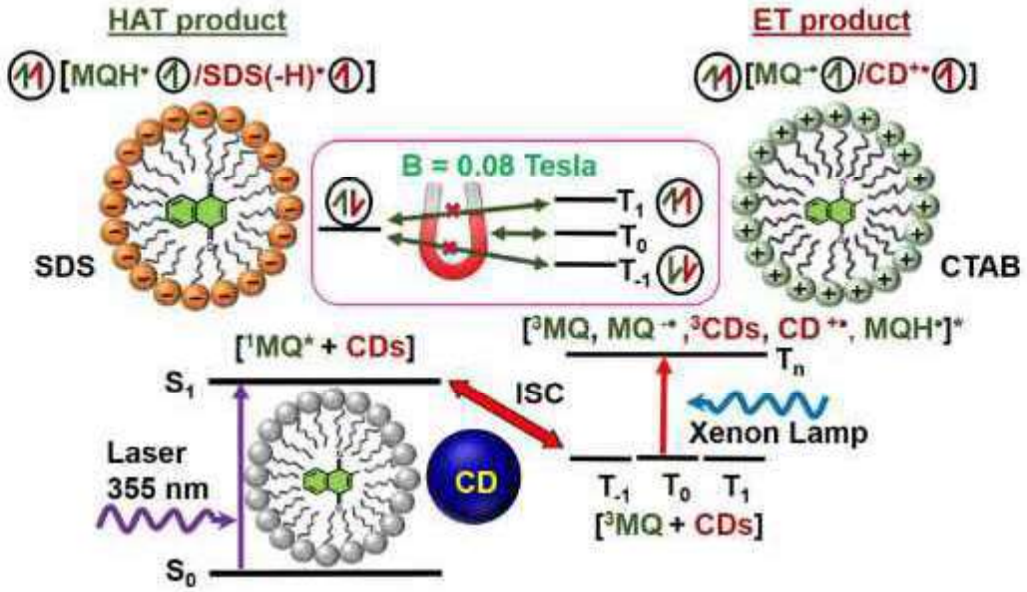

Scheme 2. Probable mechanistic charge transfer pathways and MFE involving MQ and CD in SDS and CTAB micelles. [Adapted with permission from Ref. [129] Copyright 2021 American Chemical Society].

broadband cavity–enhanced absorption spectroscopy have been used to explore MFE in this case and the magnetic sensitivity of *Drosophila* cryptochrome are interpreted in terms of the radical pair mechanism [140]. Although millitesla MFE on purified *Drosophila* cryptochrome has been observed *in vitro*, the magnetic sensitivity of a protein is not a sufficient evidence for magnetic sensing in the whole organism. In fact, very recently Hore et al. have carried out test of 108,609 Drosophila from different strains over a time period of six years and after an extensive statistcal analyses they have concluded that *Drosophila* has no preference for or against a MF and *Drosophila* negative geotaxis is not affected by external MF [141]. It is also found that CRY4 from the night migratory European robin appears to be fit for purpose as a magnetic sensor, and that it is more magnetically sensitive than CRY4 from the non-migratory pigeon and chicken under same conditions *in vitro* [142]. In fact, $B_{1/2}$ values for Cry4a protein from migratory European robin, pigeon and chicken have been measured [143]. $B_{1/2}$ is found to be larger than expected on the basis of hyperfine interactions and it increases with the delay between pump and probe laser pulses. Semiclassical spin dynamics simulations indicate that this behavior can be explained by singlet–triplet dephasing relaxation mechanism.

Conclusion

If a weak MF can alter the reaction channels for S and T spin states of a system then MFE on the product distribution is likely to take place. Although the interaction of a very low MF (< 1 mT) with an electron

spin is less than a millionth of the thermal energy at room temperature (k_BT), it still can have an appreciable effect on the quantum yields of radical pair reactions. In this review article we have focussed on MFE due to hyperfine coupling mechanism as this mechanism is operative at low field, which is relevant to the examples discussed. Here, we have mostly revisited our earlier works related to MFE on PET involving small organic molecules in various homogeneous and micellar solvent matrices, protein pockets, DNA and nanomaterials. In order to broaden the scope othe review we have briefly described some contemporary examples of MFE reported by other research groups. We have made an attempt to showcase the utilization of various aspects MFE ($B_{1/2}$ parameter, its capability to authenticate the initial spin state and distance dependence property) to decipher PET. We hope that future work will involve MFE on PET in relatively more complex molecular and hybrid molecule/nano-particle systems and emphasis is laid on more application-oriented areas.

CRediT authorship contribution statement

Brotati Chakraborty: Conceptualization, Formal analysis, Writing – original draft, Writing – review & editing. **Chaitrali Sengupta:** Writing – original draft. **Samita Basu:** Conceptualization, Funding acquisition, Supervision, Writing – original draft, Writing – review & editing.

Declaration of competing interest

The authors declare that they have no known competing financial interests or personal relationships that could have appeared to influence the work reported in this paper.

Data availability

Data will be made available on request.

Acknowledgements

Funding from MMDDA, CBAUNP and BARD projects of Saha Institute of Nuclear Physics, Department of Atomic Energy, Government of India is greatly acknowledged.

References

[1] Vols. 1-5V. Balzani (Ed.), Electron Transfer in Chemistry, Wiley-VCH Verlag GmbH, Weinheim, Germany, 2001. Vols. 1-5.
[2] M. Murakami, K. Maeda, T. Arai, Dynamics of intramolecular electron transfer reaction of FAD studied by magnetic field effects on transient absorption spectra, J. Phys. Chem. A 109 (2005) 5793–5800, https://doi.org/10.1021/jp0519722.
[3] D. Das, D.N. Nath, P.P. Parui, M. Chowdhury, Magnetic field effect on pyrene–DMA exciplex luminescence in non-aqueous AOT reverse micelle, Chem. Phys. Lett. 424 (2006) 300–306, https://doi.org/10.1016/j.cplett.2006.04.076.
[4] D. Das, D.N. Nath, Exciplex luminescence in D_2O solubilized AOT reverse micelle: a magnetic field effect study, Chem. Phys. Lett. 458 (2008) 81–87, https://doi.org/10.1016/j.cplett.2008.04.069.
[5] D. Das, D.N. Nath, Photoreaction of thioxanthone with indolic and phenolic derivatives of biological relevance: magnetic field effect study, J. Phys. Chem. A 112 (2008) 11619–11626, https://doi.org/10.1021/jp806860z.
[6] D.N. Nath, S. Basu, M. Chowdhury, Effect of variation of dielectric constant on the magnetic field modulation of exciplex luminescence: nontypical behavior of alcohols, J. Chem. Phys. 91 (1989) 5857–5859, https://doi.org/10.1063/1.457540.
[7] P. Roy, A.K. Jana, D. Das, D.N. Nath, Study of magnetic field effect on Py-DMA exciplex luminescence in THF–DMF binary solvents: evidence of multiple exciplex formation at higher bulk dielectric constant, Chem. Phys. Lett. 474 (2009) 297–301, https://doi.org/10.1016/j.cplett.2009.04.084.
[8] S.B. Richert, A. Rosspeintner, S. Landgraf, G. Grampp, E. Vauthey, D.R. Kattnig, Time-resolved magnetic field effects distinguish loose ion pairs from exciplexes, J. Am. Chem. Soc. 135 (2013) 15144–15152, https://doi.org/10.1021/ja407052r.
[9] H.M. Hoang, V.T.B. Pham, G. Grampp, D.R. Kattnig, Magnetic field-sensitive radical pair dynamics in polymethylene ether-bridged donor - acceptor systems, ACS Omega 3 (2018) 10296–10305, https://doi.org/10.1021/acsomega.8b01232.
[10] S.V. Peskov, M.V. Rogozina, A.I. Ivanov, A. Aster, M. Koch, E. Vauthey, Magnetic field effect on ion pair dynamics upon bimolecular photoinduced electron transfer in solution, J. Chem. Phys. 150 (2019) 024501, https://doi.org/10.1063/1.5064902.
[11] Y. Hirata, I. Tanaka, Intersystem crossing to the lowest triplet state of phenazine following singlet excitation with a picosecond pulse, Chem. Phys. Lett. 43 (1976) 568–570, https://doi.org/10.1016/0009-2614(76)80625-2.
[12] V.A. Kuz-min, P.P. Levin, Triplet exciplexes of phenazine with tertiary aromatic amines, Russ. Chem. Bull. 37 (1988) 1098–1101, https://doi.org/10.1007/BF00961908.
[13] R.M. Hochstrasser, C. Marzzacco, Perturbations between electronic states in aromatic and heteroaromatic molecules, J. Chem. Phys. 49 (1968) 971–984, https://doi.org/10.1063/1.1670262.
[14] S. Dutta Choudhury, S. Basu, Singlet state exciplex formation of phenazine with some aromatic amines, Chem. Phys. Lett. 373 (2003) 67–71, https://doi.org/10.1016/S0009-2614(03)00584-0.
[15] S. Nad, H. Pal, Electron transfer from aromatic amines to excited coumarin dyes: fluorescence quenching and picosecond transient absorption studies, J. Phys. Chem. A 104 (2000) 673–680, https://doi.org/10.1021/jp993206z.
[16] S. Dutta Choudhury, S. Basu, Caging of phenazine by 4,4' -bis(dimethylamino) diphenylmethane: a comparative study with phenazine-N,N-dimethylaniline, Chem. Phys. Lett. 383 (2004) 533–536, https://doi.org/10.1016/j.cplett.2003.11.078.
[17] K.M. Salikhov, Y. Molin, R.Z. Sagdeev, A.L. Buchachenko, Spin Polarization and Magnetic Field Effects in Radical Reactions, Elsevier, Amsterdam, 1984.
[18] U.E. Steiner, T. Ulrich, Magnetic field effects in chemical kinetics and related phenomena, Chem. Rev. 89 (1989) 51–147, https://doi.org/10.1021/cr00091a003.
[19] K. Bhattacharya, M. Chowdhury, Environmental and magnetic field effects on exciplex and twisted charge transfer emission, Chem. Rev. 93 (1993) 507–535, https://doi.org/10.1021/cr00017a022.
[20] S. Basu, M. Halder, M. Chowdhury, Magnetic field effect in chemistry - the Indian scenario, Proc. Indian Natl. Sci. Acad. 66A (2000) 267–288.
[21] I.R. Gould, R.H. Young, R.E. Moody, S. Farid, Contact and solvent-separated geminate radical ion pairs in electron-transfer photochemistry, J. Phys. Chem. 95 (1991) 2068–2080, https://doi.org/10.1021/j100158a031.
[22] N.Kh. Petrov, A.I. Shushin, E.I. Frankevich, Solvent effect on magnetic field modulation of exciplex fluorescence in polar solutions, Chem. Phys. Lett. 82 (1981) 339–343, https://doi.org/10.1016/0009-2614(81)85169-X.
[23] A. Bose, D. Dey, S. Basu, Structure-dependent switchover of reaction modes: a laser flash photolysis and magnetic field effect study, J. Photochem. Photobiol. A 186 (2007) 130–134, https://doi.org/10.1016/j.jphotochem.2006.07.021.
[24] E.W. Evans, D.R. Kattnig, K.B. Henbest, P.J. Hore, S.R. Mackenzie, C.R. Timmel, Sub-millitesla magnetic field effects on the recombination reaction of flavin and ascorbic acid radicals, J. Chem. Phys. 145 (2016) 085101, https://doi.org/10.1063/1.4961266.
[25] B. Chakraborty, S. Basu, Revisiting magnetic field effects in homogeneous medium and bio-mimicking environments with emphasis on acridine derivatives, J. Ind. Chem. Soc. 98 (2021) 100057, https://doi.org/10.1016/j.jics.2021.100057.
[26] S.D. Choudhury, S. Basu, Exploring the extent of magnetic field effect on intermolecular photoinduced electron transfer in different organized assemblies, J. Phys. Chem. A 109 (2005) 8113–8120, https://doi.org/10.1021/jp053222y.
[27] T. Ulrich, U.E. Steiner, Magnetic-field-dependent recombination kinetics of geminate radical pairs in reversed micelles of variable size, Chem. Phys. Lett. 112 (1984) 365–370, https://doi.org/10.1016/0009-2614(84)85759-0.
[28] Y. Tanimoto, M. Takayama, M. Itoh, R. Nakagaki, S. Nagakura, Magnetic field effects on the photoinduced electron-transfer reaction of 1-acetonaphthone and diphenylamine in micellar solution, Chem. Phys. Lett. 129 (1986) 414–418, https://doi.org/10.1016/0009-2614(86)80370-0.
[29] D. Baumann, T. Ulrich, U.E. Steiner, Time-resolved investigation of singlet radical pair recombination in water-in-oil microemulsions: magnetic field effects in two time domains, Chem. Phys. Lett. 137 (1987) 113–120, https://doi.org/10.1016/0009-2614(87)80314-7.
[30] A. Uehara, H. Nakamura, S. Usui, T. Matsuo, Magnetic field effects on the decay rates of photogenerated geminate radical pairs in reversed micelles, J. Phys. Chem. 93 (1989) 8197–8203, https://doi.org/10.1021/j100362a012.
[31] P.P. Parui, D.N. Nath, M. Chowdhury, Determination of interfacial dielectric constant of AOT-based reverse micelle by probing magnetic field effect on pyrene–DMA exciplex luminescence, Chem. Phy. Lett. 396 (2004) 329–334, https://doi.org/10.1016/j.cplett.2004.08.052.
[32] T. Ogata, Y. Yamamoto, Y. Wada, K. Murakoshi, M. Kusaba, N. Nakashima, A. Ishida, S. Takamuku, S. Yanagida, Phenazine-photosensitized reduction of CO_2 mediated by a cobalt-cyclam complex through electron and hydrogen transfer, J. Phys. Chem. 99 (1995) 11916–11922, https://doi.org/10.1021/j100031a020.
[33] A. Chowdhury, S. Basu, Interactions between 9,10-anthraquinone and aromatic amines in homogeneous and micellar media: a laser flash photolysis and magnetic field effect study, J. Lumin. 121 (2006) 113–122, https://doi.org/10.1016/j.jlumin.2005.11.001.
[34] H.N. Ghosh, H. Pal, A.V. Sapre, J.P. Mittal, Charge recombination reactions in photoexcited C_{60}-amine complexes studied by picosecond pump probe spectroscopy, J. Am. Chem. Soc. 115 (1993) 11722–11727, https://doi.org/10.1021/ja00078a010.
[35] M. Wakasa, H. Hayashi, Y. Mikami, T. Takeda, Reversion of magnetic field effects observed in the reaction of a triplet-born radical pair consisting of two equivalent

sulfur-centered radicals, J. Phys. Chem. 99 (1995) 13181–13186, https://doi.org/10.1021/j100035a022.
[36] P. Nolting, A. Staerk, A. Weller, Magnetic field effect on the hyperfine-induced triplet formation in systems undergoing donor to radical pair electron transfer, Chem. Phys. Lett. 88 (1982) 523–527, https://doi.org/10.1016/0009-2614(82)85001-X.
[37] S.Y. Wong, P. Benjamin, P.J. Hore, Magnetic field effects on radical pair reactions: estimation of $B_{1/2}$ for flavin-tryptophan radical pairs in cryptochromes, Phys. Chem. Chem. Phys. 25 (2023) 975–982, https://doi.org/10.1039/D2CP03793A.
[38] A. Weller, P. Nolting, H. Staerk, A quantitative interpretation of the magnetic field effect on hyperfine-coupling-induced triplet formation from radical ion pairs, Chem. Phys. Lett. 96 (1983) 24–27, https://doi.org/10.1016/0009-2614(83)80109-2.
[39] H. Staerk, R. Treichel, A. Weller, Life uncertainty broadening in photoinduced electron transfer, Chem. Phys. Lett. 96 (1983) 28–30, https://doi.org/10.1016/0009-2614(83)80110-9.
[40] P.L. Luisi, M. Giomini, M.P. Pileni, B.H. Robinson, Reverse micelles as hosts for proteins and small molecules, Biochim. Biophys. Acta 947 (1988) 209–246, https://doi.org/10.1016/0304-4157(88)90025-1.
[41] D. Dey, A. Bose, M. Chakraborty, S. Basu, Magnetic field effect on photoinduced electron transfer between dibenzo[a,c]phenazine and different amines in acetonitrile-water mixture, J. Phys. Chem. A 111 (2007) 878–884, https://doi.org/10.1021/jp0661802.
[42] T. Shida, W.H. Hamill, Molecular ions in radiation chemistry. I. Formation of aromatic-amine cations in CCl_4 by resonance charge transfer at 77°K, J. Chem. Phys. 44 (1966) 2369–2374, https://doi.org/10.1063/1.1727050.
[43] D. Dey, A. Bose, D. Bhattacharyya, S. Basu, S.S. Maity, S. Ghosh, Dibenzo[a,c] phenazine: a polarity-insensitive hydrogen-bonding probe, J. Phys. Chem. A 111 (2007) 10500–10506, https://doi.org/10.1021/jp0731611.
[44] H.W. Kruger, M.E. Michael-Beyerle, H. Seidlitz, The influence of electron hopping on the recombination dynamics of radical ion pairs in liquid solution, Chem. Phys. Lett. 87 (1982) 79–82, https://doi.org/10.1016/0009-2614(82)83559-6.
[45] K. Sen, S. Bandyopadhyay, D. Bhattacharya, S. Basu, Dielectric dependence of magnetic field effect: a tool for identification of exciplex and triplex, J. Phys. Chem. A 105 (2001) 9077–9084, https://doi.org/10.1021/jp011063m.
[46] K. Schulten, The effect of intramolecular paramagnetic-diamagnetic exchange on the magnetic field effect of radical pair recombination, J. Chem. Phys. 82 (1985) 1312–1316, https://doi.org/10.1063/1.448454.
[47] N.Kh. Petrov, M.V. Alfimov, M.F. Budyka, T.N. Gavrishova, H. Staerk, Intramolecular electron hopping in double carbazole molecules studied by the fluorescence-detected magnetic field effect, Phys. Chem. A 103 (1999) 9601–9604, https://doi.org/10.1021/jp9917796.
[48] H. Beens, H. Knibbe, A. Weller, Dipolar nature of molecular complexes formed in the excited state, J. Chem. Phys. 47 (1967) 1183–1184, https://doi.org/10.1063/1.1712006.
[49] J.B. Birks, Excimers and Exciplexes, Nature 214 (1967) 1187–1190, https://doi.org/10.1038/2141187a0.
[50] T. Forster, Excimers and exciplexes, in: M. Gordon, W.R. Ware (Eds.), The Exciplex, Academic Press, New York, 2009, pp. 1–22.
[51] A. Weller, Singlet- and triplet-state exciplexes, in: M. Gordon, W.R. Ware (Eds.), The Exciplex, Academic Press, New York, 2009, pp. 23–38.
[52] N. Orbech, M. Ottolenghi, Intersystem crossing and ionic recombination processes studied by pulsed laser excitation of charge-transfer systems, in: M. Gordon, W. R. Ware (Eds.), The Exciplex, Academic Press, New York, 2009, pp. 75–111.
[53] S. Basu, D. Nath, M. Chowdhury, Magnetic-field effect on exciplex luminescence. The trans-anethole-9-cyanophenanthrene system, J. Chem. Soc. Faraday Trans. 2 83 (1987) 1325–1333, https://doi.org/10.1039/F29878301325.
[54] M.H. Gehlen, F.C. De Schryver, Fluorescence quenching in micelles in the presence of a probe-quencher ground-state charge-transfer complex, J. Phys. Chem. 97 (1993) 11242–11246, https://doi.org/10.1021/j100145a021.
[55] S. Aich, S. Basu, Laser flash photolysis studies and magnetic field effect on a new heteroexcimer between N-ethylcarbazole and 1,4-dicyanobenzene in homogeneous and heterogeneous media, J. Chem. Soc. Faraday Trans. 91 (1995) 1593–1600, https://doi.org/10.1039/FT9959101593.
[56] S. Aich, S. Basu, D.N. Nath, An improved phase-locked detection system for the observation of the magnetic field effect on exciplex luminescence: deviation from previously observed dielectric constant dependence, J. Photochem. Photobiol. A 109 (1997) 95–99, https://doi.org/10.1016/S1010-6030(97)00115-9.
[57] S. Aich, S. Basu, Magnetic field effect: a tool for identification of spin state in a photoinduced electron-transfer reaction, J. Phys. Chem. A 102 (1998) 722–729, https://doi.org/10.1021/jp972264m.
[58] S. Bandyopadhyay, K. Sen, S. Dutta Choudhury, S. Basu, Exciplex parameters in dielectric behaviour of magnetodynamics, RIKEN Review 44 (2002) 56–58.
[59] S. Bandyopadhyay, K. Sen, S. Dutta Choudhury, S. Basu, Exciplex parameters: key factors in the dielectric behaviour of magnetodynamics, Mol. Phys. 100 (2002) 1079–1084, https://doi.org/10.1080/00268970110109493.
[60] S. Dutta Choudhury, S. Basu, Magnetic field effect on N-ethylcarbazole–dimethylterephthalate and N-ethylcarbazole–1,4-dicyanobenzene: a comparative study focusing on steric effect, Chem. Phys. Lett. 408 (2005) 274–278, https://doi.org/10.1016/j.cplett.2005.04.066.
[61] T. Sengupta, S. Basu, Magnetic field effect on the exciplex between all-s-trans-1,4-diphenylbuta-1,3-diene and 1,4-dicyanobenzene: a comparative study with other α,ω -diphenyl polyenes, Spectrochim. Acta A Mol 57 (2001) 1103–1110, https://doi.org/10.1016/S1386-1425(00)00429-7.
[62] S. Aich, A. Bhattacharyya, S. Basu, Fluorescence polarization of N-vinyl carbazole grafted on cellulose acetate film and its electron transfer reaction with 1,4-dicyanobenzene, Radiat. Phys. Chem. 50 (1997) 347–354, https://doi.org/10.1016/S0969-806X(97)00046-7.
[63] S. Aich, T. Sengupta, A. Bhattacharyya, S. Basu, Magnetic field effect on an exciplex between N-vinyl carbazole grafted on cellulose acetate film and 1,4-dicyanobenzene, J. Polym. Sci. A 37 (1999) 3910–3915, https://doi.org/10.1002/(sici)1099-0518(19991101)37:21%3C3910::aid-pola5%3E3.0.co;2-u.
[64] T. Pedzinski, B. Marciniak, G. Hug, Quenching of the excited singlet state of acridine and 10-methylacridinium cation by thio-organic compounds in aqueous solution, J. Photochem. Photobiol. A 150 (2002) 21–30, https://doi.org/10.1016/S1010-6030(02)00026-X.
[65] M.K. Sarangi, D. Dey, S. Basu, Influence of heterogeneity of confined water on photophysical behavior of acridine with amines: a time-resolved fluorescence and laser flash photolysis study, J. Phys. Chem. A 115 (2011) 128–135, https://doi.org/10.1021/jp107610k.
[66] M.K. Sarangi, S. Basu, Associated electron and proton transfer between Acridine and Triethylamine in AOT reverse micelles probed by laser flash photolysis with magnetic field, Chem. Phys. Lett. 506 (2011) 205–210, https://doi.org/10.1016/j.cplett.2011.03.035.
[67] B. Chakraborty, S. Basu, Study of interaction of proflavin with triethylamine in homogeneous and micellar media: photoinduced electron transfer probed by magnetic field effect, Chem. Phys. Lett. 477 (2009) 382–387, https://doi.org/10.1016/j.cplett.2009.07.018.
[68] B. Chakraborty, S. Basu, Interaction of proflavin with aromatic amines in homogeneous and micellar media: photoinduced electron transfer probed by magnetic field effect, Chem. Phys. Lett. 487 (2010) 51–57, https://doi.org/10.1016/j.cplett.2010.01.013.
[69] C. Sengupta, P. Mitra, B. Koley Seth, D. Mandal, S. Basu, Electronic and spatial control over the formation of transient ion pairs during photoinduced electron transfer between proflavine–amine systems in a subpicosecond time regime, RSC Adv 7 (2017) 15149–15157, https://doi.org/10.1039/C6RA28256E.
[70] P. Mitra, B. Chakraborty, D. Bhattacharyya, S. Basu, Excimer of 9-aminoacridine hydrochloride hydrate in confined medium: an integrated experimental and theoretical study, J. Phys. Chem. A 117 (2013) 1428–1438, https://doi.org/10.1021/jp3103639.
[71] P. Mitra, B. Chakraborty, S. Basu, A spectroscopic investigation of the photophysical behaviour of 9-aminoacridine hydrochloride hydrate in presence of organic amines in homogeneous and heterogeneous media, J. Lumin. 149 (2014) 221–230, https://doi.org/10.1016/j.jlumin.2014.01.034.
[72] P. Mitra, B. Chakraborty, S. Basu, Exploring photoinduced electron transfer and excited-state proton transfer reactions involving 9-aminoacridine hydrochloride hydrate and methyl viologen using laser flash photolysis, Chem. Phys. Lett. 610-611 (2014) 108–114, https://doi.org/10.1016/j.cplett.2014.07.004.
[73] B. Chakraborty, S. Basu, Magnetic field effect on electron transfer reactions of acridine yellow with amines of varied structures in homogeneous medium, Chem. Phys. Lett. 493 (2010) 76–82, https://doi.org/10.1016/j.cplett.2010.05.016.
[74] B. Chakraborty, S. Basu, Magnetic field effect on photoinduced electron transfer reaction associated with hydrogen bond formation in homogeneous medium, Appl. Magn. Reson. 42 (2012) 5–15, https://doi.org/10.1007/s00723-011-0254-0.
[75] R.A. Marcus, N. Sutin, Electron transfers in chemistry and biology, Biochim. Biophys. Acta 811 (1985) 265–322, https://doi.org/10.1016/0304-4173(85)90014-X.
[76] H.B. Gray, J.R. Winkler, Electron transfer in proteins, Annu. Rev. Biochem. 65 (1996) 537–561, https://doi.org/10.1146/annurev.bi.65.070196.002541.
[77] H.B. Gray, J.R. Winkler, Long-range electron transfer, Proc. Natl. Acad. Sci. 102 (2005) 3534–3539, https://doi.org/10.1073/pnas.0408029102.
[78] M. Cordes, B. Giese, Electron transfer in peptides and proteins, Chem. Soc. Rev. 38 (2009) 892–901, https://doi.org/10.1039/B805743P.
[79] R. Boch, N. Mohtat, Y. Lear, J.T. Arnason, T. Durst, J.C. Scaiano, Study of photoinduced energy and electron transfer in α-terthienyl-bovine serum albumin conjugates: a laser flash photolysis study, Photochem. Photobiol. 64 (1996) 92–99, https://doi.org/10.1111/j.1751-1097.1996.tb02426.x.
[80] A.C. Bhasikuttan, A.V. Sapre, L.V. Shastri, Photoinduced electron transfer in crystal violet (CV^+)–bovine serum albumin (BSA) system: evaluation of reaction paths and radical intermediates, J. Photochem. Photobiol. A 150 (2002) 59–66, https://doi.org/10.1016/S1010-6030(02)00098-9.
[81] B. Chakraborty, C. Sengupta, U. Pal, S. Basu, Probing the hydrogen bond involving Acridone trapped in a hydrophobic biological nanocavity: integrated spectroscopic and docking analyses, Langmuir 36 (2020) 1241–1251, https://doi.org/10.1021/acs.langmuir.9b03586.
[82] B. Chakraborty, C. Sengupta, U. Pal, S. Basu, Acridone in a biological nanocavity: detailed spectroscopic and docking analyses of probing both the tryptophan residues of bovine serum albumin, New J. Chem. 41 (2017) 12520–12534, https://doi.org/10.1039/C7NJ02454A.
[83] B. Chakraborty, P. Mitra, S. Basu, Spectroscopic exploration of drug-protein interaction: a study highlighting the dependence of the magnetic field effect on inter-radical separation distance formed during photoinduced electron transfer, RSC Adv 5 (2015) 61533–61545, https://doi.org/10.1039/C5RA13575C.
[84] B. Chakraborty, S. Basu, Interaction of BSA with proflavin: a spectroscopic approach, J. Lumin. 129 (2009) 34–39, https://doi.org/10.1016/j.jlumin.2008.07.012.
[85] B. Chakraborty, A. Sinha Roy, S. Dasgupta, S. Basu, Magnetic field effect corroborated with docking study to explore photoinduced electron transfer in drug – protein interaction, J. Phys. Chem. A 114 (2010) 13313–13325, https://doi.org/10.1021/jp109604s.

[86] P. Mitra, U. Pal, N.C. Maiti, A. Ghosh, A. Bhunia, S. Basu, Identification of modes of interactions between 9- aminoacridine hydrochloride hydrate and serum proteins by low and high resolution spectroscopy and molecular modelling, RSC Adv 6 (2016) 53454–53466, https://doi.org/10.1039/C6RA04140J.
[87] M. Banerjee, A. Chakrabarti, S. Basu, Interaction between hemoglobin A and merocyanine 540: a spectroscopic investigation supported by docking, Dyes and Pigments 97 (2013) 446–454, https://doi.org/10.1016/j.dyepig.2013.01.005.
[88] M. Banerjee, U. Pal, A. Subudhhi, A. Chakrabarti, S. Basu, Interaction of Merocyanine 540 with serum albumins: photophysical and binding studies, J. Photochem. Photobiol. B 108 (2012) 23–33, https://doi.org/10.1016/j.jphotobiol.2011.12.005.
[89] P. Mitra, M. Banerjee, S. Biswas, S. Basu, Protein interactions of Merocyanine 540: spectroscopic and crystallographic studies with lysozyme as a model protein, J. Photochem. Photobiol. B 121 (2013) 46–56, https://doi.org/10.1016/j.jphotobiol.2013.02.010.
[90] M. Banerjee, S. Maiti, I. Kundu, A. Chakrabarti, S. Basu, Simultaneous occurrence of energy transfer and photoinduced electron transfer in interaction of hen egg white lysozyme with 4-nitroquinoline-1-oxide, Photochem. Photobiol. 86 (2010) 1237–1246, https://doi.org/10.1111/j.1751-1097.2010.00811.x.
[91] S. Banerjee, S. Dutta Choudhury, S. Dasgupta, S. Basu, Photoinduced electron transfer between hen egg white lysozyme and anticancer drug menadione, J. Lumin. 128 (2008) 437–444, https://doi.org/10.1016/j.jlumin.2007.09.020.
[92] B. Koley Seth, A. Ray, S. Biswas, S. Basu, Ni^{II}–Schiff base complex as an enzyme inhibitor of hen egg white lysozyme: a crystallographic and spectroscopic study, Metallomics 6 (2014) 1737–1747, https://doi.org/10.1039/C4MT00099F.
[93] S. Patel, A. Datta, Steady state and time-resolved fluorescence investigation of the specific binding of two chlorin derivatives with human serum albumin, J. Phys. Chem. B 111 (2007) 10557–10562, https://doi.org/10.1021/jp072544u.
[94] B. Pullman, A. Pullman, Electron-donor and –acceptor properties of biologically important purines, pyrimidines, pteridines, flavins, and aromatic amino acids, Proc. Natl. Acad. Sci 44 (1958) 1197–1202, https://doi.org/10.1073/pnas.44.12.1197.
[95] B. Koley Seth, A. Sau, U. Pal, S. Basu, B. Chakraborty, Interaction of proflavin with tryptophan in reverse micellar microenvironment of AOT: photoinduced electron transfer probed by magnetic field effect, J. Lumin. 220 (2020) 116953, https://doi.org/10.1016/j.jlumin.2019.116953.
[96] D.V. Bent, E. Hayon, Excited state chemistry of aromatic amino acids and related peptides. III. Tryptophan, J. Am. Chem. Soc. 97 (1975) 2612–2619, https://doi.org/10.1021/ja00843a004.
[97] D. Creed, The photophysics and photochemistry of the near-UV absorbing amino acids-I. Tryptophan and its simple derivatives, Photochem. Photobiol. 39 (1984) 537–562, https://doi.org/10.1111/j.1751-1097.1984.tb03890.x.
[98] T. Asakura, K. Adachi, E. Schwartz, Stabilizing effect of various organic solvents on protein, J. Biol. Chem. 253 (1978) 6423–6425, https://doi.org/10.1016/S0021-9258(19)46949-4.
[99] B. Giese, Long-distance electron transfer through DNA, Annu. Rev. Biochem. 71 (2002) 51–70, https://doi.org/10.1146/annurev.biochem.71.083101.134037.
[100] F. Boussicault, M. Robert, Electron transfer in DNA and DNA-related biological processes. Electrochemical insights, Chem. Rev. 108 (2008) 2622–2645, https://doi.org/10.1021/cr0680787.
[101] B. Giese, J. Amaudrut, A.K. Kohler, M. Spormann, S. Wessely, Direct observation of hole transfer through DNA by hopping between adenine bases and by tunnelling, Nature 412 (2001) 318–320, https://doi.org/10.1038/35085542.
[102] F.D. Lewis, H. Zhu, P. Daublain, T. Fiebig, M. Raytchev, Q. Wang, V. Shafirovich, Crossover from superexchange to hopping as the mechanism for photoinduced charge transfer in DNA hairpin conjugates, J. Am. Chem. Soc. 128 (2006) 791–800, https://doi.org/10.1021/ja0540831.
[103] T. Sengupta, S. Dutta Choudhury, S. Basu, Medium-dependent electron and H atom transfer between 2′-deoxyadenosine and menadione: a magnetic field effect study, J. Am. Chem. Soc. 126 (2004) 10589–10593, https://doi.org/10.1021/ja0490976.
[104] A. Bose, D. Dey, S. Basu, Interactions of guanine and guanosine hydrates with quinones: a laser flash photolysis and magnetic field effect study, J. Phys. Chem. A 112 (2008) 4914–4920, https://doi.org/10.1021/jp711846n.
[105] A. Bose, D. Dey, S. Basu, Laser flash photolysis and magnetic-field-effect studies on interaction of thymine and thymidine with menadione: role of sugar in controlling reaction pattern, Sci. Technol. Adv. Mater 9 (2008) 024205, https://doi.org/10.1088/1468-6996/9/2/024205.
[106] A. Bose, A.K. Sarkar, S. Basu, Interaction of 9,10-anthraquinone with adenine and 2′-deoxyadenosine, Biophys. Chem. 136 (2008) 59–65, https://doi.org/10.1016/j.bpc.2008.04.011.
[107] A. Bose, S. Basu, Laser flash photolysis and magnetic field effect studies on the interaction of uracil and its derivatives with menadione and 9,10-anthraquinone, J. Phys. Chem. A 112 (2008) 12045–12053, https://doi.org/10.1021/jp805632j.
[108] A. Bose, S. Basu, Role of sugar in controlling reaction pattern: a comparative study with adenine and 2′-deoxyadenosine, J. Photochem. Photobiol. A 201 (2009) 197–202, https://doi.org/10.1016/j.jphotochem.2008.10.017.
[109] A. Bose, S. Basu, Medium-dependent interactions of quinones with cytosine and cytidine: a laser flash photolysis study with magnetic field effect, Biophys. Chem. 140 (2009) 62–68, https://doi.org/10.1016/j.bpc.2008.11.010.
[110] A. Bose, A.K. Sarkar, S. Basu, Role of sugar in controlling reaction pathways: a study with thymine and thymidine, J. Lumin. 129 (2009) 1186–1191, https://doi.org/10.1016/j.jlumin.2009.05.019.
[111] A. Bose, S. Basu, Interaction of quinones with three pyrimidine bases: a laser flash photolysis study, J. Lumin. 129 (2009) 1385–1389, https://doi.org/10.1016/j.jlumin.2009.07.007.
[112] B. Chakraborty, A. Bose, S. Basu, Electron transfer and hydrogen abstraction in biologically relevant systems, in: D.V. Stass, V.I. Feldman (Eds.), Selectivity, Control, and Fine Tuning in High-Energy Chemistry, Research Signpost, India, 2011, pp. 93–116.
[113] D. Dey, A. Bose, N. Pramanik, S. Basu, Magnetic field effect on photoinduced electron transfer between $[Cu(phen)_2]^{2+}$ and DNA, J. Phys. Chem. A 112 (2008) 3943–3946, https://doi.org/10.1021/jp711541r.
[114] J. Ma, W. Lin, W. Wang, Z. Han, S. Yao, N. Lin, Triplet state mechanism for electron transfer oxidation of DNA, J. Photochem. Photobiol. B 57 (2000) 76–81, https://doi.org/10.1016/s1011-1344(00)00081-6.
[115] D. Dey, N.R. Pramanik, S. Basu, Exploring the mechanism of electron transfer between DNA and a ternary copper complex, J. Phys. Chem. B 113 (2009) 8689–8694, https://doi.org/10.1021/jp810778h.
[116] B. Koley Seth, A. Ray, A. Saha, P. Saha, S. Basu, Potency of photoinduced electron transfer and antioxidant efficacy of pyrrole and pyridine based Cu(II)-Schiff complexes while binding with CT-DNA, J. Photochem. Photobiol. B 132 (2014) 72–84, https://doi.org/10.1016/j.jphotobiol.2014.02.007.
[117] A.A. Voityuk, J. Jortner, B. Bixon, N. Rosch, Electronic coupling between Watson–Crick pairs for hole transfer and transport in desoxyribonucleic acid, J. Chem. Phys. 114 (2001) 5614–5620, https://doi.org/10.1063/1.1352035.
[118] C. Sengupta, P. Mitra, S. Chatterjee, G. Bhattacharjee, B. Satpati, S. Basu, Photoinduced electronic interactions between acridine derivatives and small gold nanoparticles: a spectroscopic insight, J. Mol. Liq. 272 (2018) 198–208, https://doi.org/10.1016/j.molliq.2018.09.080.
[119] F. Pica, E. Balestrieri, A. Serafino, R. Sorrentino, R. Gaziano, G. Moroni, N. Moroni, G. Palmieri, M. Mattei, E. Garaci, P. Sinibaldi-Vallebona, Antitumor effects of the benzophenanthridine alkaloid sanguinarine in a rat syngeneic model of colorectal cancer, Anticancer Drugs 23 (2012) 32–42, https://doi.org/10.1097/CAD.0b013e32834a0c8e.
[120] S.Das Chakraborty, A. Sau, A. Maity, U. Paul, C. Sengupta, M. Bhattacharya, S. Banik, B. Satpati, S. Basu, D. Senapati, Low magnetic field induced surface enhanced transient spin-trajectory modulation of a prototype anticancer drug sanguinarine on a single domain superparamagnetic nanosurface, J. Phys. Chem. C 122 (2018) 20619–20631, https://doi.org/10.1021/acs.jpcc.8b06129.
[121] S. Zhang, Z. Li, Roles of nonequilibrium conduction electrons on the magnetization dynamics of ferromagnets, Phys. Rev. Lett. 93 (2004) 127204, https://doi.org/10.1103/PhysRevLett.93.127204.
[122] S.Das Chakraborty, A. Sau, D.V. Kuznetsov, A. Banerjee, M. Bardhan, M. Bhattacharya, D. Dasgupta, S. Basu, D. Senapati, Development of a triplet–triplet absorption ruler: DNA-and chromatin-mediated drug molecule release from a nanosurface, J. Phys. Chem. B 120 (2016) 6872–6881, https://doi.org/10.1021/acs.jpcb.6b05278.
[123] K. Bera, A. Sau, P. Mondal, R. Mukherjee, D. Mookherjee, A. Metya, A.K. Kundu, D. Mandal, B. Satpati, O. Chakrabarti, S. Basu, Metamorphosis of ruthenium-doped carbon dots: in search of the origin of photoluminescence and beyond, Chem. Mater. 28 (2016) 7404–7413, https://doi.org/10.1021/acs.chemmater.6b03008.
[124] A. Sau, K. Bera, P. Mondal, B. Satpati, S. Basu, Distance-dependent electron transfer in chemically engineered carbon dots, J. Phys. Chem. C 120 (2016) 26630–26636, https://doi.org/10.1021/acs.jpcc.6b06146.
[125] M. Kuss-Petermann, O.S. Wenger, Electron transfer rate maxima at large donor–acceptor distances, J. Am. Chem. Soc. 138 (2016) 1349–1358, https://doi.org/10.1021/jacs.5b11958.
[126] A. Sau, K. Bera, U. Pal, A. Maity, P. Mondal, S. Basak, A. Mukherjee, B. Satpati, P. Sen, S. Basu, Design and synthesis of fluorescent carbon-dot polymer and deciphering its electronic structure, J. Phys. Chem. C 122 (2018) 23799–23807, https://doi.org/10.1021/acs.jpcc.8b08322.
[127] R.K. Behera, A. Sau, L. Mishra, S. Mondal, K. Bera, S. Kumar, S. Basu, M. K. Sarangi, Metal nanoparticle alters adenine induced charge transfer kinetics of vitamin K3 in magnetic field, Sci. Rep. 10 (2020) 18454, https://doi.org/10.1038/s41598-020-75262-8.
[128] H. Kimura-Suda, D.Y. Petrovykh, M.J. Tarlov, L.J. Whitman, Base-dependent competitive adsorption of single-stranded DNA on gold, J. Am. Chem. Soc. 125 (2003) 9014–9015, https://doi.org/10.1021/ja035756n.
[129] R.K. Behera, L. Mishra, S. Mondal, S. Kumar, A. Panigrahi, S. Singha, S. Basu, M. K. Sarangi, Magnetic field probes the impact of the ionic micellar interface on photoinduced charge-transfer kinetics of carbon dots, J. Phys. Chem. C 125 (2021) 17418–17427, https://doi.org/10.1021/acs.jpcc.1c04342.
[130] N. Harada, T. Matsuo, T. Yago, K. Maeda, M. Wakasa, Low magnetic field effects on a photoinduced electron transfer reaction in an ionic liquid, Chem. Phys. Lett. 773 (2021) 138569, https://doi.org/10.1016/j.cplett.2021.138569.
[131] H. Yonemura, Y. Motoda, S. Yamada, Magnetic field effects on the photoinduced electron-transfer reactions in a ruthenium porphyrin-C_{60} ligand complex, Appl. Magn. Reson. 38 (2010) 217–235, https://doi.org/10.1007/s00723-009-0114-3.
[132] D.R. Kattnig, A. Rosspeintner, G. Grampp, Magnetic field effects on exciplex-forming systems: the effect on the locally excited fluorophore and its dependence on free energy, Phys. Chem. Chem. Phys. 13 (2011) 3446–3460, https://doi.org/10.1039/c0cp01517b.
[133] V.T.B. Pham, H.M. Hoang, G. Grampp, D.R. Kattnig, Effects of preferential solvation revealed by time-resolved magnetic field effects, J. Phys. Chem. B 121 (2017) 2677–2683, https://doi.org/10.1021/acs.jpcb.7b00510.
[134] S.R.T. Neil, J. Li, D.M.W. Sheppard, J. Storey, K. Maeda, K.B. Henbest, P.J. Hore, C.R. Timmel, S.R. Mackenzie, Broadband cavity-enhanced detection of magnetic field effects in chemical models of a cryptochrome magnetoreceptor, J. Phys. Chem. B 118 (2014) 4177–4184.

[135] Z. Zeng, J. Wei, Y. Liu, W. Zhang, T. Mabe, Magnetoreception of photoactivated cryptochrome 1 in electrochemistry and electron transfer, ACS Omega 3 (2018) 4752–4759, https://doi.org/10.1021/acsomega.6b00645.
[136] T. Ritz, S. Adem, K. Schulten, A model for photoreceptor-based magnetoreception in birds, Biophys. J. 78 (2000) 707–718, https://doi.org/10.1016/S0006-3495(00)76629-X.
[137] E.W. Evans, J. Li, J.G. Storey, K. Maeda, K.B. Henbest, C.A. Dodson, P.J. Hore, S. Mackenzie, C.R. Timmel, Sensitive fluorescence-based detection of magnetic field effects in photoreactions of flavins, Phys. Chem. Chem. Phys. 17 (2015) 18456–18463, https://doi.org/10.1039/c5cp00725b.
[138] C. Bialas, L.E. Jarocha, K.B. Henbest, T.M. Zollitsch, G. Kodali, C.R. Timmel, S. R. Mackenzie, P.L. Dutton, C.C. Moser, P.J. Hore, Engineering an artificial flavoprotein magnetosensor, J. Am. Chem. Soc. 138 (2016) 16584–16587, https://doi.org/10.1021/jacs.6b09682.
[139] T.M. Zollitsch, L.E. Jarocha, C. Bialas, K.B. Henbest, G. Kodali, P.L. Dutton, C. C. Moser, C.R. Timmel, P.J. Hore, S.R. Mackenzie, Magnetically sensitive radical photochemistry of non-natural flavoproteins, J. Am. Chem. Soc. 140 (2018) 8705–8713, https://doi.org/10.1021/jacs.8b03104.
[140] D.M.W. Sheppard, J. Li, K.B. Henbest, S.R.T. Neil, K. Maeda, J. Storey, E. Schleiher, T. Biskup, R. Rodriguez, S. Weber, P.J. Hore, C.R. Timmel, S. R. Mackenzie, Millitesla magnetic field effects on the photocycle of an animal cryptochrome, Sci. Rep. 7 (2017) 42228, https://doi.org/10.1038/srep42228.
[141] M. Bassetto, T. Reichl, D. Kobylkov, D.R. Kattnig, M. Winklhofer, P.J. Hore, H. Mouritsen, No evidence for magnetic field effects on the behaviour of *Drosophila*, Nature 620 (2023) 595–599, https://doi.org/10.1038/s41586-023-06397-7.
[142] J. Xu, L.E. Jarocha, T. Zollitsch, M. Konowalczyk, K.B. Henbest, S. Richert, M. J. Golesworthy, J. Schmidt, V. Dejean, D.J.C. Sowood, M. Bassetto, J. Luo, J. R. Walton, J. Fleming, Y. Wei, T.L. Pitcher, G. Moise, M. Herrmann, H. Yin, H. Wu, R. Bartolke, S.J. Kaselhagen, S. Horst, G. Dautaj, P.D.F. Murton, A. S. Gehrckens, Y. Chelliah, J.S. Takahashi, K.-W. Koch, S. Weber, I.A. Solov'yov, C. Xie, S.R. Mackenzie, C.R. Timmel, H. Mouritsen, P.J. Hore, Magnetic sensitivity of cryptochrome 4 from a migratory songbird, Nature 594 (2021) 535–540, https://doi.org/10.1038/s41586-021-03618-9.
[143] M.J. Golesworthy, T. Zollitsch, J. Luo, D. Selby, L.E. Jarocha, K.B. Henbest, O. Paré-Labrosse, R. Bartölke, J. Schmidt, J. Xu, H. Mouritsen, P.J. Hore, C. R. Timmel, S.R. Mackenzie, Singlet–triplet dephasing in radical pairs in avian cryptochromes leads to time-dependent magnetic field effects, J. Chem. Phys. 159 (2023) 105102, https://doi.org/10.1063/5.0166675.

RESEARCH ARTICLE | JANUARY 12 2024

Electromagnetic shielding: Effect of Ni and Li substitution in co substituted Zn-ferrite

Madhumita Dalal

AIP Conf. Proc. 2995, 020048 (2024)
https://doi.org/10.1063/5.0178363

Electromagnetic Shielding: Effect of Ni and Li substitution in Co substituted Zn-ferrite

Madhumita Dalal[a)]

Deptartment of Physics, Bejoy Narayan Mahavidyalaya, Itachuna, Hooghly, Pin – 712147, India

[a)]Corresponding author: dalal.madhumita@gmail.com

Abstract

Ferrites are the most commonly known magnetic materials while multi-walled carbon nanotubes (MWCNTs) are known for superior conducting capability. Nanoparticles of ferrites integrated in MWCNTs exhibit excellent electromagnetic (EM) wave absorption efficiency. Main mechanism involved here is the matching between magnetic and dielectric loss. A thin layer of Ni-Zn-Co ferrite/MWCNT nanocomposite of thickness ~ 1 mm can absorb ~ 99.4 % (−22 dB) of the incident EM wave at a frequency of 15.24 GHz while Li-Zn-Co ferrite/MWCNT nanocomposites exhibits 99.1 % (−20.5 dB) absorption of incident EM wave at 15.27 GHz. These ferrite/MWCNT nanocomposites could be highly beneficial for shielding harmful EM waves at high frequencies.

INTRODUCTION

We are living in a world where smart phone became an inescapable gadget. In earlier years of invention, it was mainly used for communication. But, now a day it serves multitude of utilities which includes education, business, entertainment, bill payment, different kinds of online bookings and many more important works. Before pandemic some of us were aware of various harmful effects of using smart phone and tried to avoid excessive use of it. But in the pandemic situation everything goes online and we started spending most of the hours on smart phone. Now we became habituated in attending online meetings, seminars, conferences, workshops on our smart phone. Even we are consulting our doctors through audio-visual conversation on smart phone. Students are now spending hour after hours on smart phone as it became a teaching-learning gadget in the pandemic situation. Extensive use of smart phone badly affects ones mental health. Not only that, smart phone continuously emits electromagnetic (EM) radiation which has worse impact on our physical health. Frequent use of smart phone may lead to the harmful effects on biological systems like, structural rearrangement of protein due to non-thermal microwave (MW) effects, increase in heart-beat rate, inducing deoxyribo nucleic acid (DNA) strand breaks, weakening of immune responses and the possibility of cancer. EM radiation from smart phone and cell tower not only affects human beings but it also affects the birds, animals, plant and environment. These problems caused by electromagnetic interference (EMI) may be eliminated by MW absorbers having the capability of absorbing unwanted EM signals. Thus, efficient MW shielding materials are very much demanding in present situation to reduce the MW hazards significantly. In this regard the composite state of magnetic nanoparticles and multi wall carbon nanotubes (MWCNTs) are highly suitable for MW absorption. MW absorption efficiencies of two potential candidates namely, Ni-Zn-Co ferrite and Li-Zn-Co ferrite in MWCNT matrix is discussed in this article.

SAMPLE PREPARATION AND CHARACTERIZATION TECHNIQUES

Nanoparticles of $Ni_{0.3}Zn_{0.4}Co_{0.3}Fe_2O_4$ are prepared by co-precipitation method using $NiCl_2{\bullet}6H_2O$, $ZnCl_2$, $CoCl_2{\bullet}6H_2O$ and $FeCl_3$ as precursor materials. The chloride salts are taken in a ratio of 0.3:0.4:0.3:2 and dissolved

66th DAE Solid State Physics Symposium
AIP Conf. Proc. 2995, 020046-1–020046-5; https://doi.org/10.1063/5.0178363
Published by AIP Publishing. 978-0-7354-4764-6/$30.00

in deionized water by ultrasonication. Sodium hydroxide (NaOH) solution is added drop wise to the homogeneous salt solution while ultrasonication is maintained and continued for further two hours. The precipitate is filtered and washed several times to neutralize pH and also to remove unwanted ions. Finally the product is dried, powdered and annealed at 600 °C. The nanoparticles (designated as NZCF) prepared in this way are integrated in MWCNT matrix in a ratio of 9:1 by means of ultrasonication where xylene is used as mediator. The powdered product is designated as NZCF/MWCNT.

Nanoparticles of $Li_{0.3}Zn_{0.3}Co_{0.1}Fe_{2.3}O_4$ are prepared by sol-gel method using $LiNO_3$, $Zn(NO_3)_2{\bullet}6H_2O$, $Co(NO_3)_2{\bullet}6H_2O$ and $Fe(NO_3)_3{\bullet}9H_2O$ as precursor materials. The nitrate salts are taken in a ratio of 0.3:0.2:0.1:2.3 and dissolved in deionized water by magnetic stirring. Equimolar citric acid is dissolved in deionized water separately and the aqueous citric acid solution is added drop wise to the aqueous nitrates solution under magnetic stirring. As soon as a gel is formed it is shifted to an oven at 200 °C. Finally the product is powdered and annealed at 500 °C. The nanoparticles (designated as LZCF) prepared in this way are integrated in MWCNT matrix in the previous manner and designated as LZCF/MWCNT.

X-ray diffraction (XRD) patterns of the samples are recorded by means of a powder X-ray diffractometer, Model BRUKER D8 Advance with da Vinchi, using Cu Kα radiation (λ=1.5405). High resolution transmission electron microscopy (HRTEM) micrographs are recorded using JEOL JEM 2100 HRTEM operating at 200 kV. Scanning electron microscopy (SEM) micrograph is recorded using ZEISS SUPRA40 field emission gun SEM. Scattering parameters, S11 and S21, of the EM waves in X- and K_u-bands of microwave region were measured using an Agilent E8363B vector network analyzer.

RESULTS AND DISCUSSION

XRD pattern (Fig. 1a) confirms pure phase formation of NZCF nanoparticles with an average crystallite size, $\langle d_{cryst} \rangle$ of ~ 17 nm [1]. A pure cubic $Fd\bar{3}m$ phase (Fig. 1b) is confirmed in LZCF nanoparticles also with $\langle d_{cryst} \rangle$ ~ 19 nm [2]. Absence of any extra peak rules out the formation of impurities in the prepared samples. The XRD patterns are fitted using Rietveld method and several structural parameters are derived from fitting. The lattice parameters obtained from the fitting for the two samples are 8.382 and 8.370 Å, respectively. Both the samples may be considered not to have any kind of defects as the r.m.s lattice strains derived for the two samples are very small which are about 2.37×10^{-3} and 0.16×10^{-3}, respectively.

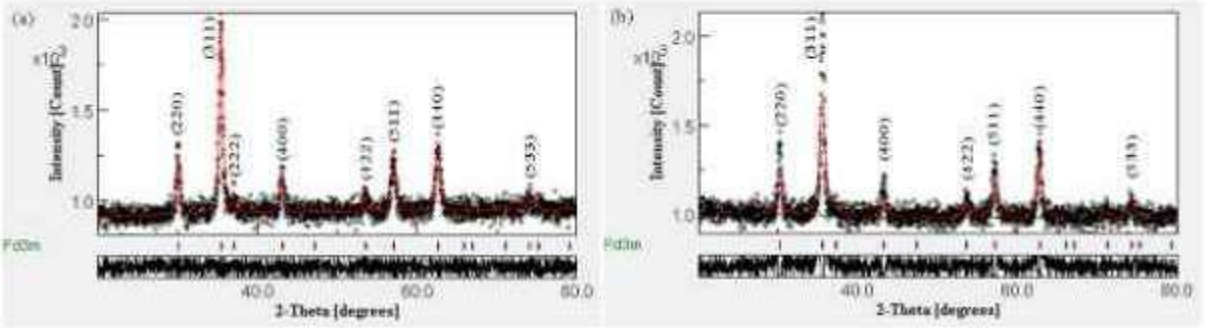

FIGURE 1. MAUD fitted XRD patterns of (a) NZCF and (b) LZCF nanoparticles

HRTEM micrographs are shown in Fig. 2a and b which shows that nanoparticles are mainly spherical in nature. The size of a particle as seen in the micrograph is about 16 nm for the NZCF sample and about 11 nm for the LZCF sample. The particles sizes are very close to the average crystallite dimensions obtained from Rietveld analysis. This fact suggests that the nanoparticles appeared in the micrographs are nothing but the nanocrystallites of the samples. The SEM micrograph of the sample LZCF/MWCNT is displayed in Fig. 2c. The nanoparticles are well integrated in the MWCNT matrix. Though only 10 % MWCNTs are taken but still MWCNTs are filling almost the entire micrograph because MWCNTs are very light compared to ferrite nanoparticles. As could be seen from the SEM micrograph, the ferrite nanoparticles are mostly agglomerated which is a signature of strong magnetic interaction among the ferrite nanoparticles.

R_L profile of the nanocomposites is displayed in Fig. 3a. The value of R_L for 1 mm thick layer of NZCF/MWCNT is − 22 dB at 15.24 GHz, which corresponds to 99.4 % absorption of incident MW. While, the value of R_L for 1 mm thick layer of LZCF/MWCNT is − 20.5 dB at 15.27 GHz which corresponds to 99.1 %

absorption. Obviously, NZCF/MWCNT exhibits greater shielding effect. Now, it is intended to explain the origin of MW absorption in ferrite/MWCNT nanocomposites so that the shielding effect could be improved further.

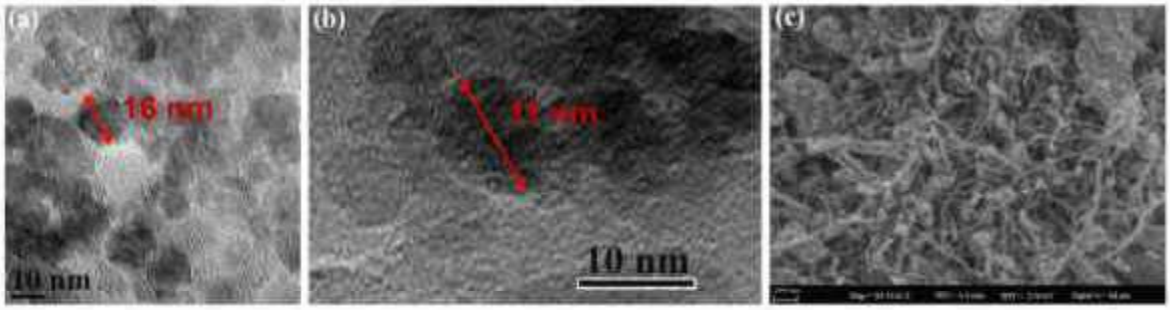

FIGURE 2. HRTEM micrographs of (a) NZCF and (b) LZCF nanoparticles; (c) SEM micrograph of LZCF/MWCNT

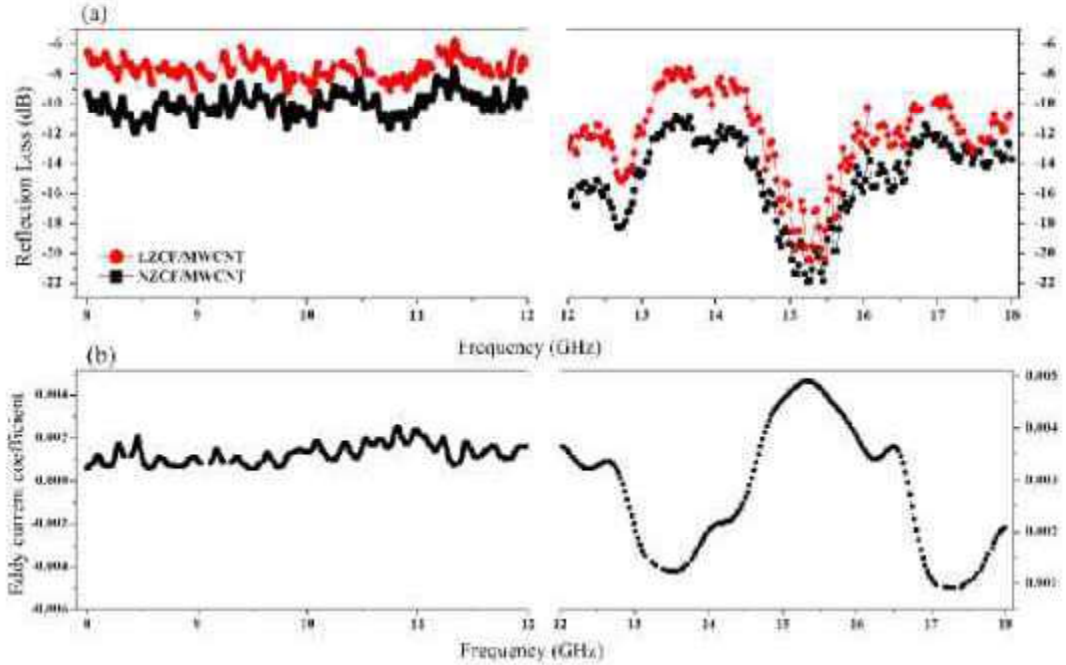

FIGURE 3. (a) Reflection loss profile of two nanocomposites in the frequency range8 – 18 GHz, (b) Eddy current coefficient of NZCF/MWCNT plotted as a function of frequency

MW absorption by a composite material is a combined effect of two kinds of loss phenomena, namely dielectric loss and magnetic loss. Reflection loss (R_L) is a measure of MW absorption and R_L of an absorbing layer of the nanocomposite terminated by a conductor is expressed by the formula [3]:

$$R_L(dB) = 20\log_{10}|(Z_{in}-1)/(Z_{in}+1)| \quad (1)$$

$$\text{where, } Z_{in} = \sqrt{\frac{\mu_r^*}{\varepsilon_r^*}}\tanh(\gamma t) \quad (2)$$

Here, $\gamma = \alpha + j\beta = j(2\pi f/c)\sqrt{\mu_r^*\varepsilon_r^*}$, $\mu_r^* = \mu' - j\mu''$, $\varepsilon_r^* = \varepsilon' - \varepsilon''$, α and β are attenuation constant and phase constant, respectively, f is the frequency of the MW, c is the speed of light in free space, μ_r^* is the complex permeability, ε_r^* is the complex permittivity, Z_{in} is the normalized input impedance at the absorbent surface and t is the thickness of the layer (1 mm). When MW falls on the surface of an absorbing layer, it is partially transmitted and partially reflected. The partially transmitted wave is reflected for the second time upon incidence on the surface of

the conductive plate, thereby generating multiple internal reflections. These internal reflections produce multiple waves that emerge from the absorber surface at 180° out of phase. At the matching frequency and matching thickness, the condition becomes so that the sum of the emerging waves cancel out the reflected EM wave at the air-interface on the surface of the absorbing layer and thus zero reflection occurs. Z_{in} is 1 at zero reflection and denotes the condition for maximum absorption. This can be achieved when the condition $|\mu_r^*| = |\varepsilon_r^*|$ is satisfied. Hence, to get maximum absorption, perfect matching between magnetic and dielectric losses is the essential criterion. In case of ferrite/MWCNTs nanocomposites, the magnetic loss arises from ferrites and dielectric loss arises from the MWCNTs.

When ferrite/MWCNTs nanocomposites are irradiated by MW, magnetic flux is flipped by the external field. The flux change produces a current which flows through the conducting path of MWCNTs. According to Lenz's law this current opposes its cause i.e. the change in flux density. Thus a strong loss of incident MWs arises in ferrite/MWCNTs nanocomposites. As both the ferrites are incorporated in MWCNT matrix, so the contribution from MWCNT could be considered same for both the nanocomposites. However, $\langle d_{cryst} \rangle$ of NZCF is smaller than that of LZCF, so incorporation would be better for NZCF nanoparticles. Thus more number of interfaces will be formed in NZCF/MWCNT nanocomposite which will act as space charge polarization sites and this will lead to a greater dielectric loss in NZCF/MWCNT nanocomposite.

On the other hand, the major contributing terms in magnetic loss are domain wall motion, Eddy current loss, natural and exchange resonances. In multi domain nanoparticles pinning sites present at grain boundaries, prevent domain wall motion and extra energy is required to keep domain walls moving across the grain boundaries which causes magnetic loss in multi domain nanoparticles. The single domain critical sizes for NZCF and LZCF are ~ 42 and 23 nm, respectively [1-2]. So, the nanoparticles considered here (17 and 19 nm, respectively) are mainly single domain, though a fraction of particles may be multi-domain because the size of nanoparticles couldn't be uniform and in single domain nanoparticles, magnetic loss is due to superparamagnetic (SPM) relaxation. However, domain loss contribution is significant only in MHz frequency range. The Eddy current loss depends on the conductivity of the composite and its thickness. In ferrites magnetic loss arising from Eddy current loss can be ignored because ferrites have high resistivity. Again, if magnetic loss arises only from Eddy current loss, then the Eddy current coefficient $\mu''(\mu')^{-2}f^{-1}$ should remain constant with the frequency variation because the Eddy current effect can be expressed by the equation [4]:

$$\mu'' \approx 2\pi\mu_0(\mu')^2\sigma t^2 f/3 \qquad (3)$$

where, μ_0 is the permeability of free space and σ is the conductivity. But from Fig. 3b, it is seen that Eddy current coefficient varies with frequency in the considered range. Thus at MW frequencies, natural and exchange resonances also contribute significantly in the magnetic loss.

CONCLUSION

In this report, ferrite/MWCNT nanocomposites are revealed as an effective MW shielding material over a wide range of frequency. It is seen that with a proper choice of the magnetic nanoparticles, ~ 99.4 % absorption of the incident MW is possible at a very high frequency (~ 15.24 GHz) in K_u-band. Mechanism behind the MW absorption of such nanocomposites is explained in detail with the finding that Ni substitution in Co substituted Zn ferrite is more effective for MW shielding purpose. Also, the techniques followed to prepare the nanoparticles and as well as the nanoparticles/MWCNT composites are very simple and cost effective. So these nanocomposites could be prepared in large scale and in near future, these nanocomposites will surely protect us from EM hazards.

ACKNOWLEDGMENT

I acknowledge Prof. Dr. Pabitra Kumar Chakrabarti, the Solid State Research Laboratory, the University of Burdwan for providing me laboratory facilities for sample preparation and other research facilities.

REFERENCES

1. M. Dalal, A. Das, D. Das, R. S. Ningthoujam and P. K. Chakrabarti, J. Magn. Magn. Mater. **460**, 12-27 (2018).
2. M. Dalal, J.M. Greneche, B. Satpati, T. B. Ghzaiel, F. Mazaleyrat, R.S. Ningthoujam and P. K. Chakrabarti, ACS Appl. Mater. Interfaces**9**, 40831 – 40845 (2017).

3. M.S. Cao, J. Yang, W.L. Song, D.Q. Zhang, B. Wen, H.B. Jin, Z.L. Hou and J. Yuan, ACS Appl. Mater. Interfaces**4**, 6948 – 6955 (2012).
4. M.M. Lu, M.S. Cao, Y.H. Chen, W.Q. Cao, J. Liu, H.L. Shi, D.Q. Zhang, W. Wang and J. Yuan, ACS Appl. Mater. Interfaces**7**, 19408 – 19415 (2015).

RESEARCH ARTICLE | JANUARY 12 2024

Anomalous electrical resistivity behaviourin Co-Ga near magnetic instability

Sk Mohammad Yasin ✉; V. Srinivas

AIP Conf. Proc. 2995, 020132 (2024)
https://doi.org/10.1063/5.0178113

Anomalous Electrical Resistivity Behaviourin Co-Ga Near Magnetic Instability

Sk Mohammad Yasin[1,a)] and V. Srinivas[2]

[1]*Department of Physics, Bejoy Narayan Mahavidyalaya, Itachuna Hooghly, West Bengal, 712147, India*
[2]*Department of Physics, Indian Institute of Technology Madras, Chennai, 600 036, India*

[a)]Corresponding author: yasin3587@gmail.com

Abstract. The temperature variation of electrical resistivity, $\rho(T)$,measurements of Co_xGa_{100-x}(x = 50, 54, 57 and 60)alloyshas beencarried out between 2-300 K. The compositions x = 50-57 show anomalousbehaviourcommonly not associatedwiththe crystallineintermetallic compounds. The $\rho(T)$ curve of the weaklymagneticequiatomic composition resemblessemiconductor-like nature, while a Kondo-like feature is near percolations threshold. The magnetic field dependent $\rho(T)$ indicates the presence of strong spin-disorder scatteringor spin fluctuations which is also responsible for high residual resistivity.The ferromagnetic composition (x =60) shows conventional Fermi liquid behaviour. Band structure calculationson thesecompositionscorroboratewellwithexperimentalresultspresentedhere.

INTRODUCTION

In non-crystalline material, extended electronic states close to the Fermi energy, E_F, can become partially localised if E_F happens to fall near a pseudo-gap or deep minimum in density of states (DOS). In such situations one can observe a high resistivity (ρ) with temperature dependence similar to that of tunnelling or hopping conduction and these processes are not limited to non-crystalline materials. In recent past there has been considerable interest in the electronic properties ofsuch materials due to theiranomalous but useful magnetic and electric properties[1, 2].This prompted us to investigate the electrical transport behaviour of Co_xGa_{100-x}alloys near equiatomic composition (x =50). The B2 phase in Co_xGa_{100-x} alloyspersists over awideCo concentration range (44 at.% to 65 at.% of Co). The antisitedefectsare responsible for the existence of magnetic moments in off-stoichiometricalloysfor Co concentration more than50 at. % [3]. Theband structure calculation on equiatomic Co-Ga revealed the presence of deep pseudo-gap in the density of states near Fermi energy[4]. Although, earlier authors observed anomaliesin the temperature variation of resistivity [4,5],it is not clear whether such anomalies are due to the variations in the DOS or presence of magnetic defects.On the other hand the magnetic long orderedstateevolves through intermediate cluster spin glass state [3, 6, 7]. We believe that the local inhomogeneities might be extremely important to understand the resistivity behaviour of these alloys. Therefore, from the magnetic phase diagram we purposefully selected three compositions; x =50, 54 and 60of Co_xGa_{100-x}having different magnetic states (paramagnetic, cluster spin glass and ferromagnetic) and x = 57, close to percolation threshold composition, to carry out the temperature dependent resistivity to unravel the questions on the transport anomalies.Further, elementary DOS calculations on equiatomic and nearby compositions were performed to support the analysis of the experimental data.

EXPERIMENTAL

The Co_xGa_{100-x} (x = 50, 54, 57 and 60) alloyswerepreparedfrom high purityelements Co(99.99%) and Ga(99.999%) by arc-meltingunder argon atmosphere. As preparedingotsweresealed in evacuated quartz ampules and annelaed at

66th DAE Solid State Physics Symposium
AIP Conf. Proc. 2995, 020132-1–020132-4; https://doi.org/10.1063/5.0178113
Published by AIP Publishing. 978-0-7354-4764-6/$30.00

Journal of Namibian Studies, 36 S2 (2023): 1566-1581 ISSN: 2197-5523 (online)

Social Developments Of Mughal India With Special Reference To Mobility Problems: A Historical Evaluation

Prithwis Kumar Biswas[1], Dr. Vimal Kumar Tiwari[2]

[1] Research Scholar, Department of History, Mansarovar Global University, Sehore, M.P., India.
[2] Research Guide, Department of History, Mansarovar Global University, Sehore, M.P., India.

ABSTRACT:

The major changes in Mughal India was migration. These moves were organised to take advantage of more plentiful employment opportunities. The immigrants to India brought their families and their traditions with them. Iranian and Turani immigrants settled in various parts of the Mughal Empire after coming to India. Their manner of life, social customs, and values were influenced by Indian society's traditions and customs. They made a substantial contribution to the growth of Indo-Mughal civilization and were absorbed into Indian culture. They significantly influenced the architecture, music, literature, painting, and other arts of Mughal India. In this article, social developments of Mughal India with special reference to mobility problems has been discussed.

Keywords: Social, Developments, Mughal, Mobility, Problems, India.

INTRODUCTION:

Persia and Central Asia are the ancestral homes of Iranians and Turks. Their culture was different from Indian culture in terms of language and sociopolitical practises. But after they arrived in India, Indian culture had an impact on them, which was visible in a variety of aspects of their social life, including food, clothes, court ceremonies, jewellery, etc.

SOCIAL MINGLINGINGS OF THE MIGRANTS (IRANIS AND TURANIS) AND LOCAL INHABITANTS:

Indian Journal of Psychology Book No.15 2024
ISSN: 0019-5553

The Rohingya crisis and South and South - East Asia

Prithwis Kumar Biswas, Assistant Professor, Department of History, Bejoy Narayan Mahavidyalaya, The University of Burdwan

Email: prithwis16ts@gmail.com

The Rohingya crisis is one of the most important issues in current international politics. The impact of this long-standing ethnic problem in Myanmar has not only affected Myanmar's internal politics, but also the politics of South and South East Asia. The Rohingya refugee crisis is one example of how horrific xenophobic persecution can be when it is government-sponsored. Hundreds of thousands of innocent Rohingyas have been displaced from their homeland and taken refuge in Bangladesh, India, Indonesia etc in South and South - East Asian countries amid the conflict between the Rohingya extremist organizations and the radical nationalist Burmese people and the Myanmar army and forced to live in extreme poverty, starvation, malnutrition and unhealthy environment. As a result, the Rohingya problem has transformed from an internal problem of Myanmar to an international problem and continues to influence the politics, society, culture and economy of South and Southeast Asian countries.

index word: Rohingya, Myanmar, Rakhine, Bangladesh, India, Indonesia, Malaysia United Nations.

The Rohingya are a minority group in Myanmar. Basically, they live in Rakhine (North Arakan) province on the eastern border of Myanmar. Most of the Rohingyas are Muslims, but some are Hindus. The Rohingyas are Bengali speaking and the Bengali language of Chittagong is similar to them. According to linguists, the word Rohingya comes from the word 'Rahm' (Rahamat). The Burmese complain that they are not residents of Myanmar, but illegal immigrants from Bangladesh. However, if we review the history, it can be seen that the Rohingyas arrived in the 8th century AD. At this time, Arakan was one of the centres of the huge international trade that took place in the Bay of Bengal sheltering Bengal. Due to this sea trade, Arab Muslim traders arrived in Arakan and under their influence, a part of the local people converted to Islam. This population of Arab origin preferred to live in the suburbs of Mruk U and Kayukta near Chittagong in Bengal.

In the fifteenth century, many Muslims from the Mughal Empire infiltrated Rakhine. At this time, King Nara Mekhala, an ally of the Mughals, encouraged immigration by employing Bengalis in various jobs. Narmekhla converted to Islam and ruled the state in Islamic style. The number of Bengalis in the Arakan royal court continued to increase and the area of Bengali settlements expanded. This trend increased during the reign of Emperor Aurangzeb. On the orders of the emperor, Subedar Shaista Khan of Bengal defeated the Arakanese and annexed the Mughal Empire in North Arakan. And encouraged Muslims to settle in these newly conquered territories. Later, the Buddhist dynasty took over the ruling power of Arakan, but kept the Mughal governance structure intact. As a result, Bengali settlements continued to spread in Arakan.2But the situation changed when the Burmese occupied Arakan in 1785.From this time, when the Buddhist Burmese attempted to liberate the Muslims in Arakan, conflict began. About 35,000 displaced Rohingyas have been forced to take shelter in British India due to this conflict.

In 1826, the British occupied Arakan through the First Anglo-Burmese War. The British government encouraged the settlement of Bengali farmers in the newly conquered areas with the aim of expanding agriculture. As a result, the number of Muslims in Arakan increased. According to the census of 1891, the number of Muslims in Arakan was 58,255, which increased to 178,647 in 1911.৩

The settlement of large numbers of peasants from British India provoked strong reactions among Buddhists in Rakhine and sowed the seeds of ethnic tension. 4 Although migration is a problem throughout Myanmar, the problem is most pronounced in Rakhine. In 1939, the British government formed a commission led by

Madhya Bharti
Humanities and Social Sciences
मध्य भारती
ISSN: 0974-0066

SUSTAINABLE DEVELOPMENT AND HEALTH- IN WEST-BENGAL.

Mrs. SOHINI NATH
Assistant Professor, Department of Economics, Bejoy Narayan Mahavidyalaya
Itachuna, Hooghly, The University of Burdwan., West Bengal, India.
E-mail: sohininath@rediffmail.com

ABSTRACT

"Sustainable Development"- a relevant term in today's world. This aspect and issues of development is concerned not only with the present but also the future generation. On the other hand "health" of the people of the country cannot be neglected or overlooked and as such can be thought of as a counterpart with development along with food, education and standard of living.

Providing proper health facilities and medical assistance to the people is a priority for any government be it Central or State. And when more than half of the population are poverty-ridden and vulnerable to a number of chronic diseases and illness for which the burden of medical expenses become unbearable, it becomes a grave matter of concern for the government. For sustainable development of a region or state or country so Health along with adequate food, appropriate education and pollution-free world has become so important.

The object of my paper is to see the prospects and challenges in Health Sector in the light of Sustainable Development with special reference to West Bengal.

INTRODUCTION

Sustainable Development- a very relevant term in Today's world. This aspect and issues of development is concerned not only with the present but also the future generation. On the other hand 'Health' of the people of the country cannot be neglected or overlooked and as such can be thought of as a counterpart with development along with food, education and standard of living.

SUSTAINABLE DEVELOPMENT AND HEALTH

Providing health facilities and medical assistance to the people is a priority for any Central or State government. And when more than half of the population are poverty-ridden and vulnerable to a number of chronic diseases and illness for which the burden of medical expenses become unbearable becomes a grave matter of concern for the government. Thus for Sustainable Development of a state or country health along with adequate food and proper education has become so much important.

Now Sustainable Development is referred to as the idea that human beings should sustain by meeting their basic needs, while also making sure that the future generations are able to meet their basic needs. The desired result is a state of society where living conditions and resources are used to continue to meet human needs without undermining the integrity and stability of the natural system. Sustai